Flavio Leandro de Souza
Edson Roberto Leite *Editors*

Nanoenergy

Nanotechnology Applied for Energy Production

Springer

Nanoenergy

Flavio Leandro de Souza
Edson Roberto Leite
Editors

Nanoenergy

Nanotechnology Applied for Energy Production

Springer

Editors
Flavio Leandro de Souza
Centro de Ciências Naturais e Humanas
Universidade Federal do ABC
Santo André
Brazil

Edson Roberto Leite
CCET, Depart. de Química
Universidade Federal de Sao Carlos
São Carlos, SP
Brazil

ISBN 978-3-642-31735-4 ISBN 978-3-642-31736-1 (eBook)
DOI 10.1007/978-3-642-31736-1
Springer Heidelberg New York Dordrecht London

Library of Congress Control Number: 2012944973

Printed on acid-free paper

Springer is part of Springer Science+Business Media (www.springer.com)

Preface

Today, the world urgently needs alternative sources of environmentally sustainable energy supply for rapid industrial development and for consumption, such as in China. Indeed, it has become crucial for the future of humanity to find clean and safe methodologies to produce alternative energy for avoiding the growing global warming effect and urban air pollution. As a consequence, to reach this purpose it is necessarily to create new materials to build devices for renewable energy. In the past decade, funding agencies and governmental programs were created worldwide to give the scientific community support to find and develop new materials and devices for alternative energy production. In this context, this book tries to give an overview of the main developments in Brazil and its contribution to produce a clean and alternative source of energy. This book written by leading experts in major fields of physics, chemistry, and material sciences in Brazil covers the fundamental use of semiconductors, organic, and inorganic materials to build devices that directly convert solar irradiation into hydrogen and electricity, the latest development of biofuel cell and low temperature fuel cell devices using nanomaterials, as well as the latest advances on lithium-ion batteries and nickel–metal hydride batteries. This book consists of seven chapters which address in detail the fundamental importance of nanomaterials on the device performance and efficiency. The first three chapters concern an overview of the main contribution of research in development of a photoelectrochemical device which directly converts solar irradiation into electricity and hydrogen. This book begins with a chapter by Nogueira and Freitas summarizing the recent progress on the incorporation of inorganic semiconductor nanoparticles and metal nanoparticles into organic solar cells. The improvement caused by nanoparticles insertion on organic solar cell and its efficiency are discussed. In Chap. 2, Souza and Polo describe the recent advances in the developments on *tris*-heteroleptic ruthenium dye-sensitizers and its impact on dye-sensitized solar cells, efficiency. In addition, this chapter also gives an overview of natural dyes promptly obtained from several fruits or flowers in a very simple way which are also being employed as semiconductor sensitizers to produce these devices at a low cost. Souza and Leite present the recent advances on chemical synthesis to obtain a very promising semiconductor to be used as

photoanode in a photoelectrochemical device. This chapter illustrates a general discussion on solid–liquid interface, photoelectrochemical device performance due to a variety of nanostructured morphologies prepared by chemical methods and the main features of molecular oxygen evolution mechanism (OER) from water oxidation under solar light irradiation.

The next two chapters give readers the recent progress and fundamental discussion on producing an efficient fuel cell working at low temperature based on nanomaterials and interface of biomolecule immobilized on nanostructure surface. Olyveira and Crespilho describe in this chapter recent studies using biological materials immobilized on nanostructured film surface to generate electricity. The main focus of this chapter is how to build biofuel cells with high power density, controlling the enzyme immobilization methodologies and stability. Lima and Cantane present a development of a new class of electrocatalysts for application on low temperature fuel cells. This chapter discusses the main challenges of oxygen reduction reaction (ORR), and of the ethanol oxidation reaction (EOR) for proton and anion exchange membrane electrolytes. Also, the performance and test stability for some ORR electrocatalysts are included.

Finally, the last two chapters are dedicated to contextualize the readers on the advances in development of lithium-ion batteries and nickel–metal hydride batteries with the use of nanomaterials. Huguenin and Torresi describe the main advances resulting from the use of sol–gel route to produce V_2O_5 xerogel, nanocomposites of V_2O_5, and polymer cathodes for lithium-ion batteries. This chapter reviews the importance of structural features for better understanding of lithium-ion insertion/deinsertion, and their influence on electrochemical properties and charge capacity. Also, the use of nanomaterial on lithium-ion batteries is discussed. A chapter focusing on novel hydrogen storage materials and fundamental aspects for using nickel–metal hydride (Ni–MH) as rechargeable batteries is discussed by Santos and Ticianelli. The recent progress on developments of anode materials, with special emphasis on the nanostructured Mg alloys, its challenges, and perspectives are reviewed.

We are thankful to our current authors for their valuable contribution. We hope that this book gives an important contribution for understanding the urgency of the world to develop a new and efficient device for supplying the current necessity of humanity to have a clean and sustainable source of energy. In addition, our expectations to aid a wide scientific community to understand the actual progress was only possible due to consolidation of nanoscience and nanotechnology.

Santo André, Brazil, May 2012

Prof. Dr. Flavio Leandro de Souza
Prof. Dr. Edson Roberto Leite

Contents

Incorporation of Inorganic Nanoparticles into Bulk Heterojunction Organic Solar Cells

Jilian N. de Freitas and Ana Flávia Nogueira

Abstract Organic solar cells are among the most promising devices for cheap solar energy conversion. The classical device consists of a bulk heterojunction of a conjugated polymer/fullerene network. Many research groups have focused on the replacement of the fullerene derivative with other materials, especially inorganic nanoparticles, due to their easily tunable properties, such as size/shape, absorption/emission and charge carrier transport. In this chapter, we highlight recent progress on the incorporation of inorganic semiconductor nanoparticles and metal nanoparticles into organic solar cells. The role of these nanoparticles in the improvement of photocurrent, voltage and efficiency is discussed.

1 Introduction

There is a continuously growing demand for clean and renewable energy, impelled by the need of bringing electricity to remote areas and due to an increase in world's population, which requires more (and safer) energy, at the same time minimizing the impacts on Earth and nature. Solar energy is considered a promising alternative to fulfill these aims.

For many decades the photovoltaic industry has been dominated by solid-state devices based mainly on silicon [1]. The energy conversion efficiency of the best

J. N. de Freitas (✉) · A. F. Nogueira (✉)
Laboratory of Nanotechnology and Solar Energy, Chemistry Institute,
University of Campinas (UNICAMP), P. O. Box 6154
Campinas-SP 13083-970, Brazil
e-mail: jfreitas@gmail.com

A. F. Nogueira
e-mail: anaflavia@iqm.unicamp.br

F. L. de Souza and E. R. Leite (eds.), *Nanoenergy*,
DOI: 10.1007/978-3-642-31736-1_1,

monocrystalline Si photovoltaic cells is ~25 % [2, 3], which is very close to its theoretical limit of 31 % [4]. However, the manufacturing of Si-based devices is very expensive due to the requirements for high purity crystalline semiconductor substrates [5]. Such drawbacks results in the high cost associated with solar energy exploration [6]. In order to increase the share of photovoltaic technology, especially considering the application of devices in low-scale consumer goods, such as cells phones, laptops, energetic bags and clothes, etc., the development of low-cost devices is extremely necessary.

In this scenario, organic solar cells (OSC) appear as very interesting candidates. Since these devices are usually assembled with organic semiconductors, either small molecules or polymers, they show great promise due to the synthetic variability of organic materials, their low-temperature of processing (similar to that applied to common plastics), and the possibility of producing lightweight, flexible, easily manufactured and inexpensive solar cells. Moreover, the high optical absorption coefficients of conducting polymers, in comparison to silicon, provide the possibility of preparation very thin (100–200 nm) solar cells.

Recent progress in the field of OSC has led to a device with the maximum efficiency of 7.4 % [7]. In order to further enhance the competitiveness of OSC with other technologies, efficiency and long term stability remain crucial issues. The photocurrent in these solar cells is limited by the light-harvesting capability of the individual molecules or polymers in the device. The synthesis of new low band gap polymers has been intensively studied for the purpose of overcoming this drawback [8], but it is a complicated matter since changing the band gap energy usually changes the energetic value of the highest occupied molecular orbital (HOMO), which have unfavourable implications on the open circuit voltage. Morphology is also important in this context since it impacts directly on charge transport, and an intimate contact between donor and acceptor materials on a nanoscale range is difficult to achieve due to phase separation. A better understanding of the processes at the nanoscale level, particularly those in layer-to-layer interfaces, is needed, and the exact role of phase separation remains the subject of active research.

To overcome some of these drawbacks, different types of acceptor materials have been applied in the photoactive layer of OSC, such as carbon nanotubes and inorganic semiconductor nanoparticles. When at least one component is replaced by an inorganic counterpart, these devices are referred to as hybrid solar cells (HSC). Figure 1 shows the structure and dimensions of nanomaterials typically used in OSC and HSC.

The use of inorganic nanoparticles in optoelectronic devices has some advantages, mainly related to the versatility of these materials, which often can be easily synthesized in a great variety of sizes and shapes, according to the desired properties. Usually, the so-called inorganic “nanoparticles” are structures that present at least one dimension between 1 and 100 nm. Since these materials are very small, their properties such as absorption, emission, electron affinity, etc, depend on the size (diameter) of the nanoparticle. For example, as the nanoparticle’s diameter decreases, the absorption maximum is blue-shifted, as a result of a

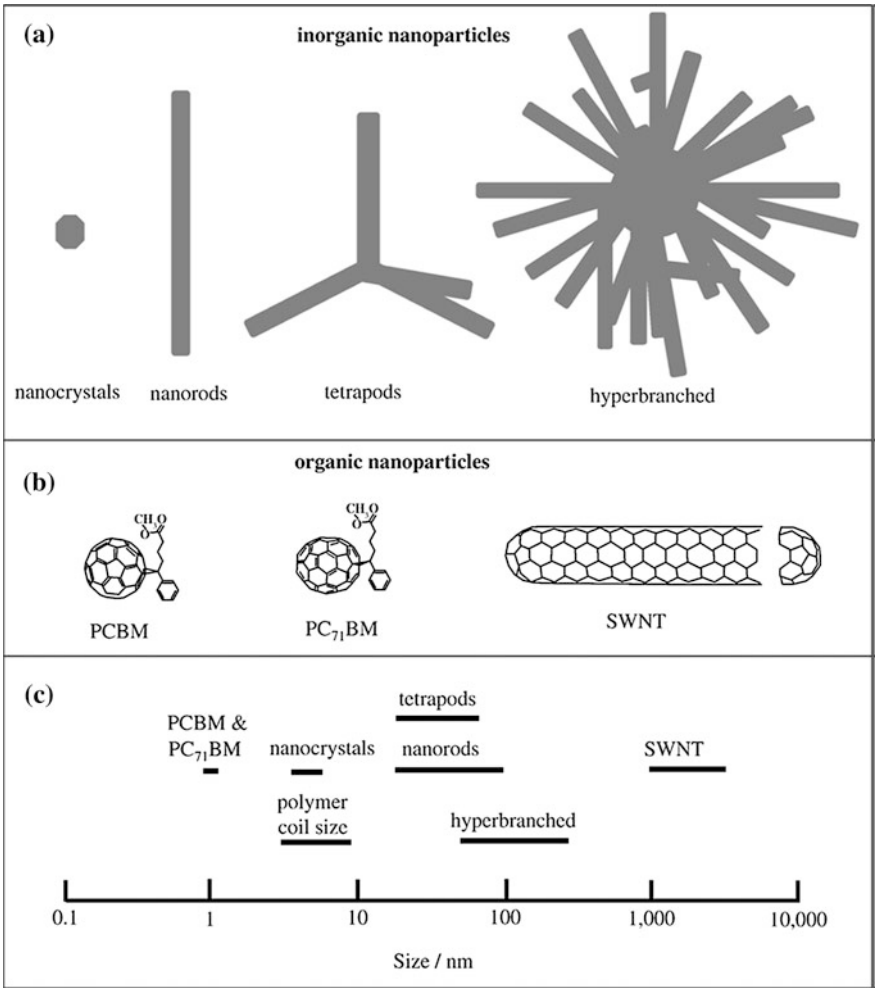

Fig. 1 Structural depictions and approximate dimensions of nanomaterials used in polymer photovoltaic cells. The structures shown in (**a**) are for CdSe nanoparticles. The structures shown in (**b**) are for carbon-based nanomaterials used in OSC. The size ranges shown in (**c**) are estimates based on literature reports for these materials. Reprinted with permission from Ref [23]

change in the band gap level due to the quantum confinement effect. Besides the quantum size effect, inorganic nanoparticles have the advantage that they can be easily synthesized in a great variety of shapes, such as spheres, prisms, rods, wires, and even larger and more complex structures, such as tetrapods or hyperbranched nanocrystals. For these materials, not only the optical properties but also the solubility can be controlled by varying size or shape of the nanostructures. Figure 2 shows examples of metal nanoparticles with various shapes and sizes, and the absorption characteristics of colloidal solutions of these nanoparticles [9].

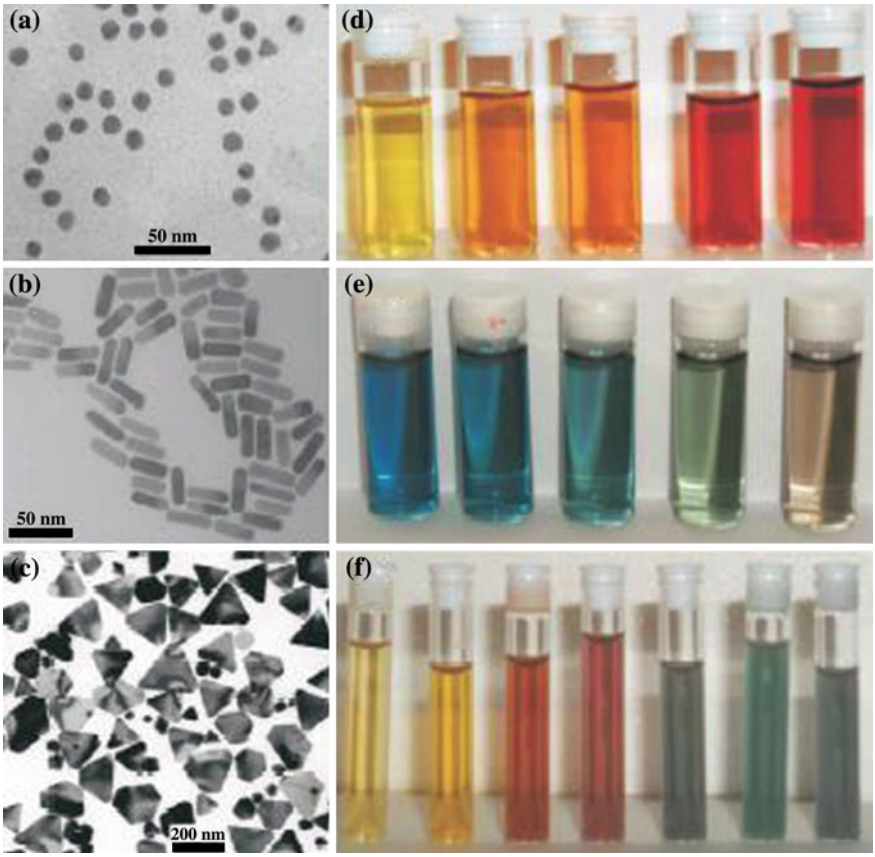

Fig. 2 (*Left*) Transmission electron micrographs of Au nanospheres and nanorods (**a**, **b**) and Ag nanoprisms (**c**). (*Right*) Photographs of colloidal dispersions of AuAg alloy nanoparticles with increasing Au concentration (**d**), Au nanorods of increasing aspect ratio (**e**) and Ag nanoprisms with increasing lateral side (**f**). Reprinted with permission from Ref [9]

In this chapter, recent progress on the application of inorganic nanoparticles in OSC is discussed. The chapter is divided into three sections: the first contains basic concepts of the assembly and principle of operation of classical OSC; the second and third parts review recent results on OSC containing inorganic semiconductor nanoparticles and metal nanoparticles, respectively. Reviews on the synthesis and properties of semiconductor nanoparticles [10–15], and metal nanoparticles [16–21], as well as other reviews on the application of inorganic nanoparticles in optoelectronic devices [22–24] can be found elsewhere.

2 Organic Solar Cells

The first OSC was developed by Tang [25] in 1986. This device consisted of a thin, two-layer film fabricated from copper phthalocyanine and a perylene tetracarboxylic derivative deposited between two electrodes, and presented $\sim$1 % efficiency. Since then, different types of organic materials have been applied in OSC, such as anthracene, perylene, porphyrins, phthalocyanines, fullerenes, carbon nanotubes, graphene, oligomers, conducting polymers and mixtures of materials.

Organic semiconductors differ from inorganic semiconductors in many aspects. The charge carriers generated in a photoactive organic material are not spontaneously dissociated but form a bound electron–hole pair (exciton) due to relatively high-binding energies (of the order 400 meV [26]), in comparison to a few meV observed for inorganic semiconductors. This is a consequence of the low electric permittivity and localized electron and hole wave functions in organic semiconductors, enhancing the Coulomb attraction between electron and hole [27]. The noncovalent electronic interactions between organic molecules are weak compared to the strong interatomic electronic interactions of covalently bonded inorganic semiconductor materials like silicon, so the electron's wave function is spatially restricted, allowing it to be localized in the potential well of its conjugate hole (and vice versa). The result is that a tightly bound electron–hole pair (Frenkel exciton or mobile excited state) is the usual product of light absorption in organic semiconductors [28]. Therefore, in conjugated polymers at room temperature only approximately 10 % of the photoexcitations are spontaneously dissociated into free charge carriers [29]. The typical lifetime of excitons is hundreds of picoseconds [30], after which they recombine radiatively or non-radiatively. In consequence, the energy conversion efficiency (η) of pure conjugated polymer-based solar cells is typically 1–2 % [31]. In order to enhance this efficiency one should combine polymers with a suitable electron acceptor material, to provide an efficient dissociation of excitons and separation of the charge carriers. This also allows the transport of the electrons and holes in the separate materials with a low probability of recombination.

Classical OSC are based on the combination of an electron donor/hole transporting material, usually conducting polymers or small organic molecules, and an electron acceptor/electron transporting material, usually fullerene (C_{60}) and its derivatives. Since light absorption results in the formation of excitons, these devices are also known as excitonic solar cells [32]. The small exciton diffusion length observed in organic semiconductors (i.e., 10–20 nm [33]), leads to the fact that only the excitons generated near the interface can effectively split. The energetic differences in the electron affinity and ionization potential of the two organic materials give rise to the driving force for exciton splitting at the interface. On the other hand, films of the order of $\sim$100–200 nm are required to absorb a significant fraction of the incident light. The overall processes occurring in polymer/fullerene OSC are represented in Fig. 3, and may be described as follows:

- Absorption of photons.
- Generation of exciton pairs in the photoactive material.

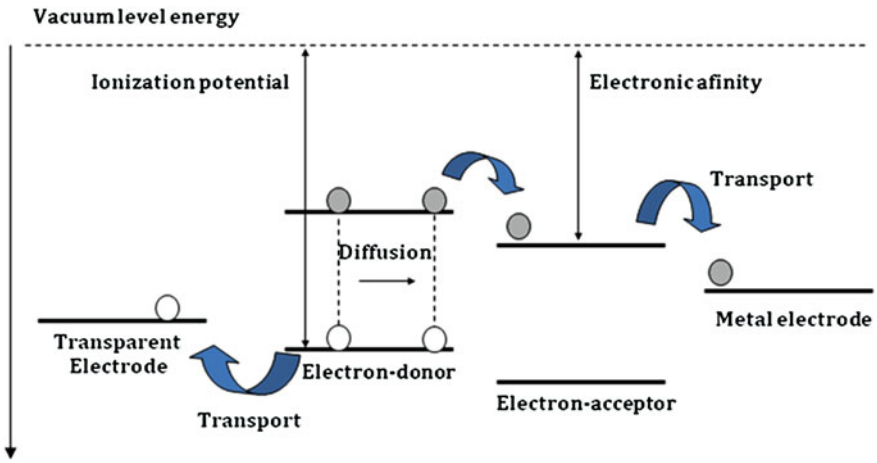

Fig. 3 Simplified energy diagram and the main steps of the photovoltaic process in a typical OSC. The incident photon creates an electron–hole pair (exciton). The exciton diffuses to the interface between the donor and acceptor materials, where it is separated into free charges. These charges need to be transported and collected on the respective electrodes to produce a photocurrent

- Diffusion of excitons in the photoactive material towards the donor/acceptor interface.
- Dissociation of excitons and separation of the charge carriers at the boundary between donor and acceptor materials.
- Transport of the holes and electrons to the electrodes.
- Collection of the holes and electrons by the electrodes.

Due to the excitonic nature of these devices, bilayer OSC, where two layers of different materials are co-deposited on top of each other, usually show lower efficiency due to the small interface for exciton dissociation [34]. Bulk heterojunction (BHJ) OSC, where the two materials are organized in an interpenetrated network, present an elegant form of minimizing the problems of exciton dissociation. In 1995 it was shown that using this approach, the performance of OSC could be significantly improved [35, 36]. The nanoscale mixtures of two components allow the interface formation throughout all the film extension, thus the photogenerated excitons rapidly split before recombination.

The development of BHJ architecture and the discovery of photoinduced electron transfer from polymers to C_{60} [37] were the breakthrough for the development of more efficient OSC. The photoinduced charge transfer in these materials is irreversible and very fast ($\sim$45 fs), with efficiencies of $\sim$100 % [38], while the recombination process is very slow (on the order of μs–ms) [39].

Figure 4a shows the scheme of a classical BHJ OSC device. Indium tin oxide (ITO) coated glass is used as conductive, transparent substrate. ITO is perhaps the most suitable electrode to be in contact with the conducting polymer due to its high work function and optical transparency. This substrate is usually covered with a

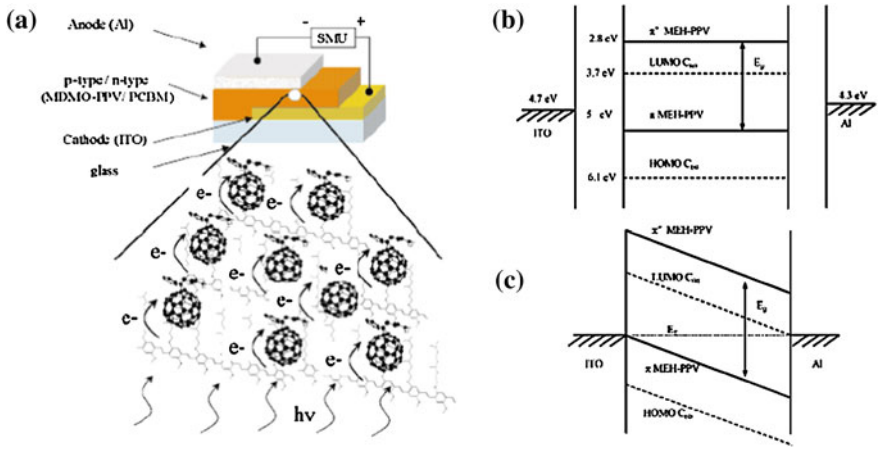

Fig. 4 Formation of a bulk heterojunction and subsequent photo-induced electron transfer inside such a composite formed from the interpenetrating donor/acceptor network plotted with the device structure for such a kind of junction (**a**). The diagrams with the energy levels of a MDMO-PPV/C_{60} bulk heterojunction system (as an example) under flat band conditions (**b**) and under short circuit conditions (**c**) do not take into account possible interfacial layers at the metal/semiconductor interface. Reprinted with permission from Ref. [43]

layer of a commercially available highly conducting polymer blend of poly(3,4-ethylene-dioxy)-thiophene:polystyrene-sulfonic acid (PDEOT:PSS). This material is known to increase the work function of the electrode (the work functions are ~4.7 eV [40] and ~5 eV [41] for ITO and PEDOT:PSS, respectively). In contrast, the top electrode should be a metal of low work function, such as Al, Mg or Ca, to allow transport of electrons and injection into the metal. A thin layer of LiF is usually employed to improve the electron injecting process [42]. The selected metal should also provide an ohmic contact with the semiconductor.

A crucial parameter for charge separation is the alignment of the energy levels of the materials. A schematic band diagram for the polymer/fullerene system, placed between two collecting electrodes is shown in Fig. 4b, c. It is energetically favorable when the energies of the HOMO and the lowest unoccupied molecular orbital (LUMO) of the conducting polymer lie at higher values than the HOMO and LUMO of fullerene, respectively. This ensures that electrons from the polymer are accepted by the fullerene, whereas holes remain in the polymer. An appropriate alignment of the energy levels is also important at the interfaces between conducting polymer and the hole collecting electrode, and between fullerene and the metal electrode.

The driving force for selective transport of electrons and holes to the opposite electrodes is attributed to a built-in potential [44]. As in the metal-insulator-metal model described by Parker [45], the difference between the work functions of the collecting electrodes induces the formation of an electric field, responsible for a selective charge transport. The diffusion concept was also used to explain selective charge transport. This concept considers that charge carrier transport is induced by concentration gradients, associated with the use of selective electrodes [46]. Both

concepts have in common the fact that charge transport is directed by the asymmetry of the electrodes. Gregg and Hanna [47] proposed a model where charge transport is assigned to the chemical potential gradient, formed by charge generation at the interface.

Morphology also plays a crucial role in BHJ OSC [48–52]. An efficient generation of charges depends on the formation of an uniform interface in the exciton diffusion length, which is favored by a homogenous mixture of the components, while efficient charge transport to the electrodes depends on the formation of percolation pathways from the interface to the respective electrode, favored by a certain degree of phase separation. Also, to achieve efficient charge transport, the concentration of the acceptor material (i.e., fullerene derivative) must be high in most cases.

Since both charge carriers exist in the heterojunction, there is a possibility that they might recombine before reaching the electrodes. There are two possible paths for recombination: (i) bimolecular recombination, where the electron and hole originated from the dissociation of a singlet exciton recombine with each other; and (ii) the recombination of electrons or holes deriving from the dissociation of different excitons. Although a large interface is good for exciton splitting, it also enhances the recombination of charges. Recombination is also strongly influenced by unbalanced hole and electrons mobilities. For the materials routinely employed in OSC, the electron mobility exceeds hole mobility by two or more orders of magnitude. Therefore, the improvement of hole transport mobility in polymers is an important parameter to improve the photovoltaic performance [53]. The recombination is also enhanced if the charge transport towards the electrodes is hindered by the domain boundaries between the electron donating and accepting materials [54], leading to a strongly morphology-dependent behavior.

In excitonic solar cells, the dark current is usually governed by a mechanism different from the photocurrent. The dark current is limited by charge carrier injection at the electrodes, while the photocurrent derives from interfacial exciton dissociation. In organic semiconductors with low degrees of impurities, the dark current can be many orders of magnitude lower than the photocurrent under forward bias [47].

Photocurrent (or short-circuit current, Jsc) is considered to be proportional to light-harvesting, since broader light absorption should give rise to increased exciton generation. Most materials used in OSC strongly absorb light in the spectral range below 600 nm. Thus, a way to improve the photocurrent and, in consequence, the efficiency, is to develop new materials with improved light-harvesting. Photocurrent also depends on film nanomorphology (a balance between charge separation, transport and recombination), as discussed before.

The open circuit voltage (Voc) in OSC is directly related to the energy difference of the HOMO level of the donor and the LUMO level of the acceptor components [55–57]. Sharber et al. [58] proposed a relationship between Voc and the values of the HOMO (E_{HOMO}) energy level of the conducting polymer and the LUMO (E_{LUMO}) energy level of the fullerene derivative (Eq. 1, where e is the elemental charge).

$$\mathrm{Voc} = (1/e)(\mathrm{E_{HOMO}(polymer)} - \mathrm{E_{LUMO}(fullerene)}) - 0.3\,\mathrm{V} \quad (1)$$

Gadisa et al. [59] observed a linear relation of Voc with the HOMO energy level of the conducting polymer employed in the heterojunction. On the other hand, Yamanari et al. [60] did not observe any direct relation of Voc and HOMO values. These reports suggest that Voc in OSC is mainly related to the electronic structure of the acceptor, which may be tuned by molecular engineering. The value of Voc is also influenced by an interfacial factor associated with different morphologies of composite films [61].

The influence of the metal electrode on Voc and on overall device performance has been investigated by many authors [62–65]. The insensitivity of voltage behavior on the electrode characteristics reported by some authors was ascribed to the Fermi level pinning between metal electrodes and fullerenes via charged interfacial states [55]. However, other authors have shown that Voc depends on the work function of the electrodes for the cases where a Schottky junction is formed, and is independent of this parameter when an ohmic contact is established [62]. Ramsdale et al. [63] reported a linear relation of Voc with the metal electrode work function in bilayer devices. The dependency of Voc on the work function of a PEDOT:PSS based electrode was also shown, where the voltage values could be manipulated by different doping of the electrode at different levels [66].

In 2001, Shaheen et al. [67] reported, for the first time, a 2.5 % efficiency for a BHJ OSC assembled with [6,6]-phenyl C_{61}-butyric acid methyl ester (PCBM) and poly[2-methoxy-5-(3,7-dimethyloctyloxy)]-1,4-phenylenevinylene (MDMO-PPV). By changing the film deposition conditions and the concentration of PCBM the efficiency was increased to 2.9 % [68]. When MDMO-PPV was substituted with poly(3-hexylthiophene) (P3HT), over 3 % efficiency was obtained [69, 70]. This further increase in efficiency when using P3HT is related to the improved light-harvesting and charge transport of this material in comparison to MDMO-PPV and other poly(p-phenylene vinylene) derivatives used before [53, 71–73]. A better control of the nanomorphology of the P3HT/PCBM film obtained by changing the solvent and the introduction of post-production treatment (annealing) further improved the efficiency of such devices [74, 75]. Annealing is considered to contribute to increase photocurrent in the following ways: (i) crystallization of PCBM and P3HT [76–80], which improves the light absorption and charge transport, and (ii) increase in the yield of dissociated charges, correlated with a decrease in P3HT's ionization potential [81].

The addition of small alkyl thiol molecules or other additives [82, 83], the use of low band gap conjugated polymers [8, 84] in combination with $PC_{71}BM$, and optimization of device design (i.e., Tandem solar cells) [85, 86] further improved the power conversion efficiency of these devices, that recently reached $\sim$7 % of efficiency [7, 74, 87, 88]. However, some factors still need to be improved, such as nanoscale control of morphology and phase separation, mismatches with the solar spectrum, adjustments of the HOMO energies of the semiconducting polymers, and stability issues.

3 Semiconductor Nanoparticles in Organic Solar Cells

Considering the specific application in solar cells, inorganic semiconductor nanoparticles have interesting characteristics: (i) easily tunable optical properties; (ii) high extinction coefficients; (iii) high intrinsic dipole moments, which may contribute to the separation of charges; and (iv) multiple exciton generation, i.e., the absorption of one single photon may generate more than one exciton [89–94]. Films of inorganic semiconductor nanoparticles also present very high charge transport characteristics [95]. On the other hand, some difficulties are often observed when trying to use inorganic materials in photovoltaics, such as poor interaction with polymers and phase separation, which keep the efficiencies of such devices below 3 %.

Hybrid solar cells assembled with the substitution of fullerenes by a vast variety of inorganic semiconductor nanoparticles, such as $CuInS_2$ [96–98], PbS [99, 100], PbSe [101, 102], Ge [103], InP [104] and even Si [105], have been investigated as promising alternatives. Probably, the most used materials in these hybrid solar cells are the CdE nanostructures (E = S, Se, Te). Therefore, this section will focus on the use of these materials in solar cells.

In 2002, Huynh et al. [106] combined CdSe spherical nanoparticles of 7 nm and CdSe nanorods (7 nm × 60 nm) with P3HT and observed that the maximum incident photon-to-current efficiency (IPCE) value was increased from ~20 to ~55 % when nanospheres were substituted by nanorods. The best device presented Jsc of 5.7 mA cm^{-2}, Voc of 0.7 V and FF of 40 %, with power conversion efficiency of 1.7 %. Later, it was found that by optimizing the solvent mixture used during film deposition, even higher IPCE values could be obtained [107, 108]. Other CdSe structures, such as tetrapods [109, 110] and hyperbranched nanocrystals [111] have also been used in combination with P3HT or MDMO-PPV, resulting in devices with efficiencies around 1–2 %. Sun et al. [110] compared the performance of solar cells assembled with CdSe nanorods or tetrapods and observed that the branched nanoparticles lead to more efficient devices. The elongated and branched nanoparticles provide more extended electric pathways, resulting in more efficient devices. In 2005, Sun et al. [112] used CdSe tetrapods in combination with P3HT and films spin-cast from 1,2,4-trichlorobenzene solutions resulted in devices with efficiencies of 2.8 %, which is among the highest values reported for this kind of device. Recently, the record efficiency of 3.2 % was reported by Dayal et al. [113] for a bulk heterojunction solar cell assembled with CdSe tetrapods and a low band gap polymer.

Some attempts to make hybrid solar cells using spherical CdSe nanoparticles resulted in low efficiency devices (<1 %). In 2006, Choi et al. [114] reported hybrid solar cells based on a mixture of CdSe nanoparticles of 5 nm with P3HT or poly(1-methoxy-4-(2-ethylhexyloxy-2,5-phenylenevinylene)) (MEH-PPV) and obtained Jsc of 2.16 μA cm^{-2}, Voc of 1.0 V, FF of 20 % and η of 0.05 % for the best case. In 2007, Tang et al. [115] used spherical nanoparticles covered with 2-mercaptoacetic acid in solar cells in combination with MEH-PPV. The devices

delivered Jsc of only 2.6 μA cm^{-2}, Voc of 0.58 V and FF of 28 %. Han et al. [116] used spherical CdSe nanoparticles crystallized in *zinc blend* structure, with 4.5 nm of diameter, covered with 1-octadecene and oleic acid and combined with the polymer MEH-PPV in solar cells. After annealing (thermal treatment), the devices delivered Jsc of 2.0 mA cm^{-2}, Voc of 0.90 V, FF of 47 % and η of 0.85 %. Recently, a record efficiency of 2 % obtained by using the combination of spherical CdSe nanoparticles with P3HT, was reported by Zhou et al. [117]. These authors achieved this efficiency by treating the nanoparticles with hexanoic acid, which removed the excess of surfactants accumulated around the quantum dot surfaces.

Table 1 summarizes the data reported for hybrid BHJ solar cells by different authors. As a general trend, the reported photocurrent and efficiency values vary significantly in quantum dots-based BHJ solar cells. This arises from problems inherent to the nanoparticle/polymer systems, such as poor dispersion properties of nanoparticles in solution and the phase separation frequently observed when films are formed. The presence of capping molecules on the nanoparticle surface, used to prevent aggregation during the synthesis, usually increases the solubility of these nanoparticles and their physical interaction with the polymer matrix, but also hinders charge transfer and the charge transport processes. All these parameters are crucial because they affect both the operation and the reproducibility of the solar cells.

Figure 5 shows the structures of P3HT, MDMO-PPV, a conducting polymer containing fluorene and thiophene units (PFT) and CdSe nanoparticles with 4.0 nm of preferential diameter, covered with trioctylphosphine oxide (TOPO). The absorption characteristics of films of these materials and solutions of CdSe nanoparticles with different sizes are shown in Fig. 6. It can be seen that the absorption of MDMO-PPV or PFT and CdSe are complementary. Thus, it would be expected that, for hybrid cells assembled with the combination of these materials, both the polymer and the inorganic nanoparticles would contribute to increase light-harvesting.

Solar cells assembled with the mixture of TOPO-capped CdSe nanoparticles and PFT delivered low values of photocurrent and fill factor (Jsc $\sim$ 150 μA cm^{-2}, FF $\sim$ 0.25) [122]. The low Jsc and FF indicated poor diode behavior for these systems, probably caused by poor electrical contacts at the interfaces and losses by recombination during charge transport. All these effects were possibly caused by a poor interaction between the polymer and CdSe, with the formation of phase separation or heterogeneous morphologies, or by a poor charge transfer process and/or poor charge transport. On the other hand, the devices showed very high open circuit voltage values (Voc $\sim$ 0.6–0.8 V). As discussed in the previous section, for this kind of device Voc depends directly on the energetic difference between the HOMO of the polymer (−5.4 eV for PFT) and the LUMO of the electron acceptor material. Therefore, the high Voc observed in devices assembled with CdSe were attributed to a more favorable energy of the LUMO level of CdSe in comparison to the LUMO of PCBM [122]. Also, Huynh et al. [123] found that, similar to the OSC cells, for hybrid solar cells Voc is not directly dependent on the difference of the work functions of the

Table 1 Performance parameters for a series of bulk heterojunction hybrid solar cells assembled with inorganic semiconductor nanoparticles and polymers

Active layer	Nanoparticle structure	Solvent	Jsc/mA cm^{-2}	Voc/V	FF/%	η/%	IPCE (max)/%	References
CdSe/PCPDTBT	Tetrapods	$CHCl_3$/py/TCB	9.02	0.674	51.5	3.13	55	[113]
CdSe/P3HT	Nanorods (5 × 65 nm)	$CHCl_3$/py/TCB	8.79	0.62	50	2.6	60	[108]
CdSe/MDMO-PPV	Tetrapods	$CHCl_3$/py/TCB	6.42	0.76	44	2.4	52	[112]
CdSe/APFO-3	Branched	Xylene	7.23	0.95	38	2.4	44	[127]
CdSe/P3HT	Hyperbranched	$CHCl_3$/py	7.00	0.60	50	2.2	23	[111]
CdSe/P3HT	Nanocrystals (5.5 nm)	DBC	5.80	0.623	56	2.0	50	[117]
CdSe/MDMO-PPV	Tetrapods	$CHCl_3$/py/DCB	7.30	0.65	35	1.8	45	[110]
CdSe/P3HT	Nanorods (7 × 60 nm)	$CHCl_3$/py	5.70	0.70	40	1.7	54	[106]
CdSe/P3HT-NH_2	Nanorods (7 × 30 m)	$CHCl_3$/py	5.80	0.57	40	1.4	–	[131]
CdSe/PF-PFT/PCBM	Nanocrystals (4 nm)	Toluene	5.00	0.68	39	1.3	–	[122]
Si/P3HT	Nanocrystals (3–5 nm)	DCB	3.30	0.75	46	1.15	26	[105]
CdSe/MEH-PPV	Tetrapods	$CHCl_3$/py/CB	2.86	0.69	46	1.13	47	[109]
CdS/P3HT	Nanocrystals	CB	3.54	0.61	33.3	0.72	36.5	[118]
PbS/MEH-PPV	Nanocrystals	CB	0.13	1.00	28	0.70	21	[100]
CdSe/MEH-PPV	Nanocrystals (3–5 nm)	CB/py	1.64	0.95	41.6	0.647	–	[116]
PbS/ PDTPQx	Nanocrystals	–	4.20	0.38	34	0.55	24	[102]
CdS/PBT	Nanorods	–	0.52	0.84	31	0.38	–	[119]
PbSe/P3HT	Nanocrystals (∼6 nm)	–	1.08	0.35	37	0.14	1.3 (at 805 nm)	[101]
CdSe/P3HT	Nanocrystals (5.5 nm)	$CHCl_3$/py	0.002	1.00	20	0.05	∼0.1	[114]
PbS/P3HT	Nanocrystals	$CHCl_3$	0.30	0.35	35	0.04	2.8	[99]
CdSe-PVK/P3HT	Nanocrystals	DCB	0.385	0.166	31.30	0.020	–	[146]
CdSe/PA_2	Nanorods	$CHCl_3$/py	0.147	0.264	28.4	0.011	–	[120]
CdSe/MEH-PPV	Nanocrystals (5 nm)	$CHCl_3$	0.05	0.50	26	0.6 (at 514 nm)	12	[124]
CdSe/P3HT	Nanorods (7 × 60 nm)	$CHCl_3$/py	–	–	–	–	59	[107]
$CuInSe_2$/P3HT	Nanocrystals (15–20 nm)	Toluene	0.30	1.00	50	–	–	[97]

(continued)

Table 1 (continued)

Active layer	Nanoparticle structure	Solvent	Jsc/mA cm^{-2}	Voc/V	FF/%	η/%	IPCE (max)/%	References
CdSe/MEH-PPV	Nanocrystals	$CHCl_3$	0.003	0.58	28	–	–	[115]
InP/P3HT	Nanowires	TCB	0.003	0.20	41	–	–	[104]
Ge/P3HT	Nanowires (1–5 μm)	$CHCl_3$	–	–	–	–	4	[103]

The results listed correspond to the highest efficiency device reported by different authors

CB chlorobenzene, *DCB* 1,2-dichlorobenzene, *TCB* 1,2,4-trichlorobenzene, *py* pyridine, *PCBM* [6,6]-phenyl C_{61}-butyric acid methyl ester, *APFO-3* poly(2,7-(9,9-dioctyl-fluorene)-*alt*-5,5-(4′,7′-di-2-thienyl-2′,1′,3′-benzothiadiazole)), *MDMO-PPV* poly[2-methoxy-5-(3,7-dimethyloctyloxy)]-1,4-phenylenevinylene, *MEH-PPV* poly(1-methoxy-4-(2-ethylhexyloxy-2,5-phenylenevinylene)), *P3HT* poly(3-hexylthiophene), *PA_2* poly(2-(2-(4-octylthiophen2-yl)thiophen-3-yl)acetic acid), *PBT* polybithiophene, *PCPDTBT* poly[2,6-(4,4-bis-(2-ethylhexyl)-4*H*-cyclopenta[2,1-*b*;3,4-*b*′]dithiophene)-*alt*-4,7-(2,1,3-benzothiadiazole)], *PDTPQx* poly(2,3-didecyl-quinoxaline-5,8-diyl-*alt*-*N*-octyldithieno[3,2-*b*;2′,3′-*d*]pyrrole), *PF-PFT* poly[(9,9-dihexyl-9H-fluorene-2,7-diyl)-1,2-ethenediyl-1,4-phenylene-1,2-ethenediyl]-co-[(9,9-dihexyl-9H-fluorene-2,7-diyl)-1,2-ethenediyl-2,5-thiophene-1,2-ethenediyl], *PVK* poly(*N*-vinylcarbazole)

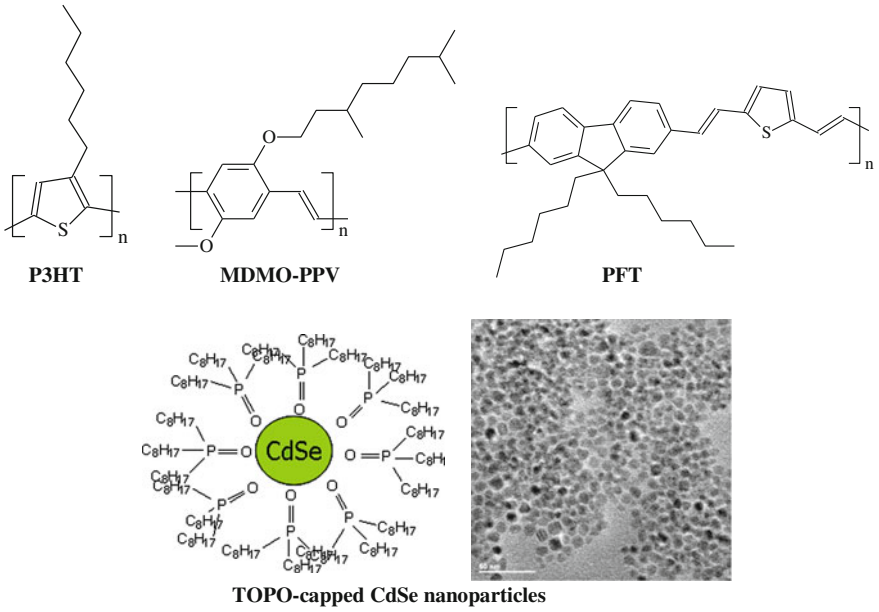

Fig. 5 Structures of the polymers P3HT. MDMO-PPV and PFT, and high-resolution transmission electron microscopy image (scale bar = 50 nm) of CdSe nanoparticles covered with trioctylphosphine oxide (TOPO). More information about PFT characteristics can be found elsewhere [121]

collecting electrodes because of the Fermi level pinning of metal electrode to the surface states close to the lowest unoccupied energy level of the semiconductor.

Generally, it is accepted that the presence of TOPO hinders efficient charge transfer and may also prevent charge transport through hopping in the nanoparticle phase (inter-particle charge transport) [124, 125], leading to devices with low Jsc, FF and efficiency. However, a few papers have shown the quenching of polymer emission by interaction with CdSe nanoparticles, and this may be considered as a first indication of the existence of charge transfer between these materials, either by the injection of electrons (from the polymer to CdSe) or by injection of holes (from CdSe to the polymer) [126–130]. Some authors used transient spectroscopy to prove that efficient charge injection processes occur between inorganic nanoparticles and conjugated polymers [126, 127]. The polymer structure (especially concerning the presence of bulky ramifications) and the nature of the surfactant molecules on the nanoparticle surfaces seem to play a major role in the effectiveness of the photoinduced charge transfer processes in these hybrid systems [129].

Phase separation is another phenomenon frequently observed in polymer-nanoparticle hybrid systems, and may lead to the formation of nanomorphologies where the nanoparticles are organized in “islands”, dispersed in a polymer “sea”. This also causes poor charge transport in the CdSe phase. For polymer/CdSe mixtures, the best photovoltaic responses are obtained when 60–90 wt % of

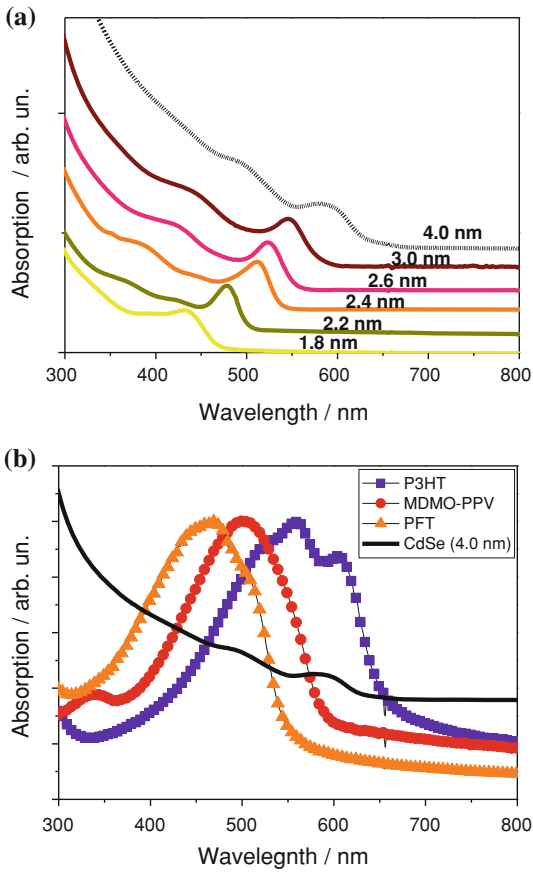

Fig. 6 Absorption spectra of **a** toluene solutions of CdSe nanoparticles with different sizes and **b** CdSe nanoparticles with 4.0 nm of preferential diameter and P3HT, MDMO-PPV or PFT films. More information about PFT characteristics can be found elsewhere [121]

nanoparticles are incorporated into the polymer matrix [111, 131]. For the same concentration of CdSe nanoparticles dispersed in a polymer matrix, a percolation network is more easily formed in the case of larger nanoparticles [124]. Thus, the morphological effects influence the charge transport, also affecting the photocurrent of these devices.

Considering these factors, many authors have focused on modifications of the nanoparticles surface, in order to obtain better dispersions in the composites with polymers. Ligand exchange is a routinely used process, and is a powerful tool to change the properties of the nanoparticles. For example, the exchange of TOPO/dodecylamine with 3-mercaptopropionic acid quenches the band edge emission and enhances the deep trap emission [132], while ligand exchange with 1,2-ethanedithiol or 1,2-ethanediamine significantly improved the exciton dissociation yield and/or charge carrier mobility [133].

Generally, the use of pyridine as capping ligand is widely accepted. These molecules have great affinity for the CdSe surface, and therefore easily replace the bulky surfactants usually employed in the synthesis, such as phosphonic acid and phosphine

oxide derivatives. The advantage of pyridine is that the smaller radius of these molecules allows a better interaction between nanoparticles and polymers, therefore facilitating charge transfer, leading to devices with higher efficiencies [22, 128]. On the other hand, some authors reported that the use of pyridine has led to the formation of agglomerates of CdSe, which might damage film morphology [114]. Recently, Lokteva et al. [134] reported the impact of single and multiple pyridine treatments on oleic acid-capped CdSe nanoparticles properties. Interestingly, repeated pyridine treatment was found to lead to more complete ligand exchange, which in turn enabled more efficient charge transfer, but at the same time the performance of the solar cells was found to be reduced. The authors correlated that fact with the increased aggregation tendency of repeatedly pyridine-treated particles, which negatively influenced the morphology, as well as with a larger amount of surface defects in particles stabilized by the weak pyridine ligand shell.

Two elegant approaches have been used in pursuit of high quality CdSe-polymer composites. The first consists in modification of the nanoparticle surface via ligand exchange with oligomers [135–137]. Sih et al. [138] synthesized a series of oligothiophenes containing thiol, which were used to functionalize the surface of CdSe nanorods previously functionalized with tetradecylphosphonic acid via ligand exchange. The authors observed that the emission characteristics of the nanorods depended on the number of oligothiophenes attached to the surface. Oligothiophene molecules containing aniline also have been used to passivate CdSe nanoparticles previously capped with thiol or carbonyl groups via ligand exchange [139].

The second approach consists of directly grafting conducting polymers to the nanoparticle, or grafting of a monomer followed by polymerization [140–143]. To this end, Zhang et al. [144] passivated CdSe nanorods with molecules containing thiol groups and aryl bromides. Afterwards, P3HT derivatives containing vinylic groups in the chains were reacted with the aryl bromides via Heck coupling. The nanocomposite obtained was compared to the one obtained by a simple physical mixture of P3HT and CdSe, revealing a better dispersion of the inorganic nanoparticles in the grafted materials, as well as an improved charge transfer behavior. Xu et al. [145] performed a similar approach, attaching P3HT to CdSe nanoparticles via Heck coupling and observed similar improvements in the composite morphology and charge transfer processes. Recently, poly(*N*-vinylcarbazole) (PVK) was grafted onto CdSe nanoparticles (CdSe-PVK) via the atom transfer radical polymerization of *N*-vinylcarbazole with OH-capped-CdSe previously reacted with 2-bromoisobutyryl bromide [146]. The photovoltaic properties of devices assembled with P3HT were improved by using PVK-CdSe in comparison to OH-capped CdSe, due to enhanced compatibility between P3HT and PKV-CdSe, as seen with atomic force microscopy (AFM) images.

All-inorganic nanocrystals composed of CdSe/ZnS and PbS capped with metal chalcogenide complexes, such as $Sn_2S_6^{4-}$, have been prepared recently [147]. These types of ligands can be used to increase the solubility of semiconductor nanoparticles in polar media, such as water, formamide and dimethylsulfoxide.

Besides the combination of CdSe with polymers, this material has also been widely used as sensitizer [148–154] or co-sensitizer [155, 156] for TiO_2 in

dye-sensitized solar cells (DSSC). The charge injection from CdSe into the conduction band of TiO_2 is a fast, efficient process. Similar behavior has been reported for CdSe (or PbSe) and ZnO [157, 158]. Efficient charge (or energy) transfer from CdSe to a series of organic dyes has also been shown [159–161]. The same approach has been shown for other materials, such as $CuInS_2$ [162], Ag_2S [163] and Sb_2S_3 [164]. The highest efficiency of 5 % was reported for a solid-state DSSC assembled with TiO_2/ Sb_2S_3 /P3HT [164]. The combination of CdSe with other nanoparticles, such as CdS [165–167], CdTe [168], ZnS [169] and SiO_2 [170], as sensitizers for DSSC has also been shown.

Charge transfers from CdSe to multi-walled carbon nanotubes [171, 172], and from CdTe to single-walled carbon nanotubes [173] have also been reported. Recently, energy transfer from CdSe/ZnS nanocrystals to graphene sheets was reported [174]. The ability of TOPO-capped CdSe nanoparticles to absorb light and inject electrons in C_{60} has also been shown by Biebersdorf et al. [175]. Advantage might be taken from these types of interaction. In a recent work, our group proposed the combination of CdSe nanoparticles with both PFT and PCBM, originating a ternary-component-based system. In these ternary systems, it is expected that, upon the incidence of light, both PFT and CdSe might absorb photons and generate excitons, which might result in electron transfer from the polymer to CdSe or PCBM, and from CdSe to PCBM, or hole injections from CdSe to the polymer. Hole transport is accomplished by the polymer, while the electrons are transported in the PCBM phase. Despite the fact that such systems are very interesting, there are only a few studies of ternary systems including polymer, PCBM and inorganic nanoparticles mixed as bulk heterojunctions [122, 176].

Figure 7 shows the current–voltage (J–V) characteristics and IPCE curves obtained for solar cells assembled with ternary mixtures of PFT/CdSe/PCBM, using nanoparticles with different sizes (2.0, 3.0 or 4.0 nm), keeping the CdSe:PCBM ratio constant at 1:1 wt %. The results obtained for devices assembled with the binary mixtures PFT/PCBM and PFT/CdSe (4.0 nm) are also presented for comparison. The overall FF values observed for the ternary systems, although higher than that observed for the two-component based solar cells, are still low ($\sim$30 %). This might be related to poor light-absorption and limited charge transport observed for the polymer used in this work (absorption maximum at 430 nm, and hole mobility $\sim 10^{-6}$ cm^2 V^{-1} s^{-1} for PFT [121]).

In general it was observed that Voc increases when CdSe nanoparticles are incorporated into the PFT/PCBM system, as a result of the more favorable energy of the LUMO level of CdSe in comparison to the LUMO of PCBM. In a previous work we observed that the concentration of CdSe in the ternary mixtures also affects Voc: the higher the concentration of CdSe, the higher is Voc [122]. The fact that Voc is sensitive to the presence of CdSe nanoparticles indicates that the new interface created after addition of this material is effective, and probably contributes somehow to charge generation processes.

The photocurrent is also dependent on the concentration of CdSe. There seems to be an optimum condition (CdSe:PCBM 1:1 wt % ratio) at which Jsc is much higher [122]. Considering that the TOPO-capped CdSe used has poor charge transport

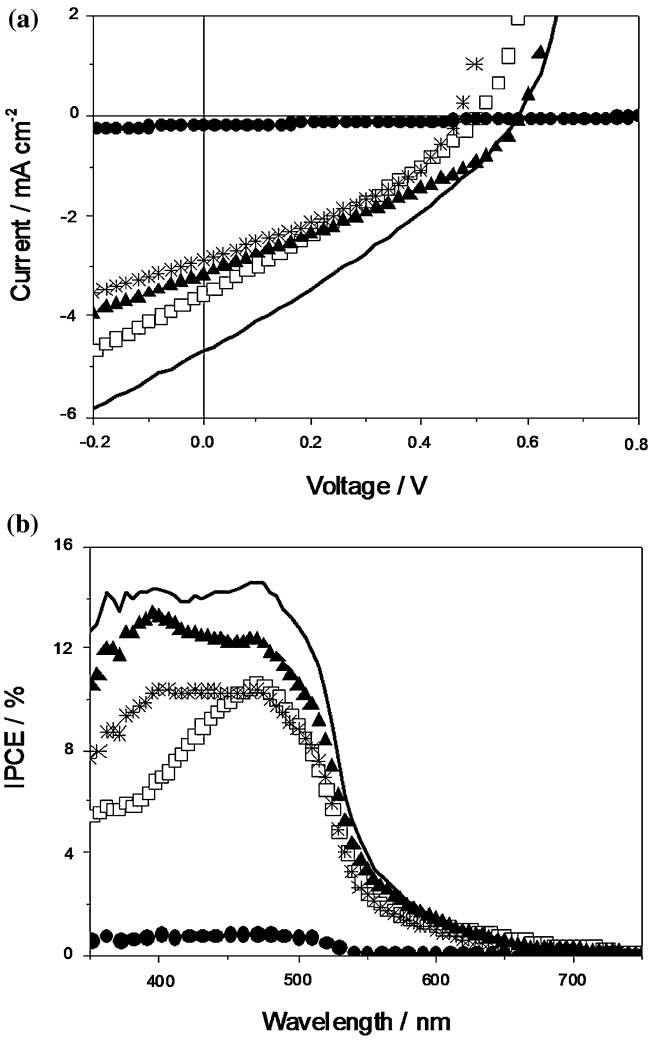

Fig. 7 J–V curves at 100 mW cm^{-2} (**a**) and IPCE spectra (**b**) of solar cells (active area ~ 0.1 cm^2) assembled with (□) PFT/PCBM, (●) PFT/CdSe (size = 4.0 nm), or ternary mixtures PFT/PCBM/CdSe containing nanoparticles with preferential diameters (*) 2.0 nm, (▲) 3.0 nm, or (—) 4.0 nm: For the ternary mixtures, the CdSe:PCBM ratio was kept constant at 1:1 wt %. For all samples the total amount of PCBM and/or CdSe was kept constant at 80 wt % (20 wt % of polymer). Reprinted with permission from Ref. [177]

ability, the improvement in Jsc for a specific condition/concentration of materials could be explained by the following: the increase in CdSe content leads to an increase in light-absorption (more excitons are generated and split, since CdSe is expected to inject charges into PCBM); on the other hand, the decrease in PCBM concentration damages the electron transport to the aluminum electrode. Therefore, there is a

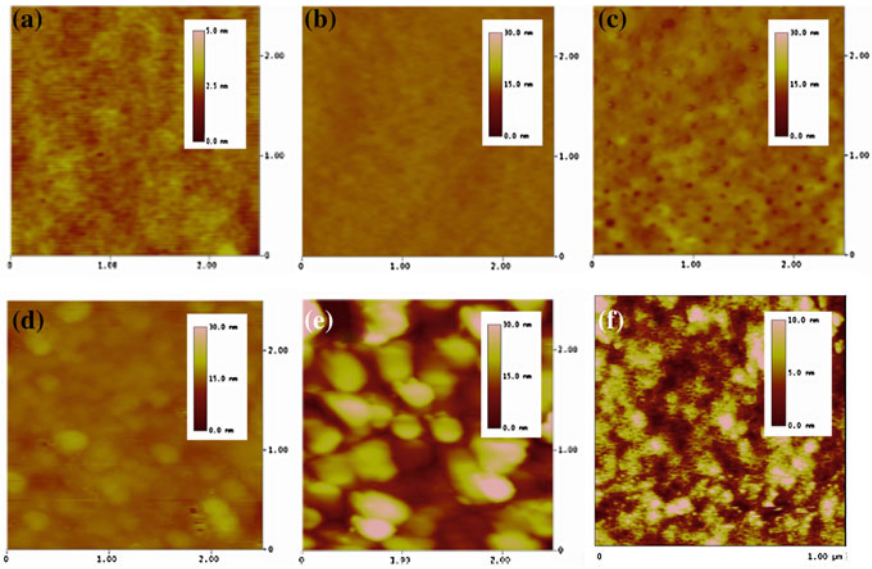

Fig. 8 AFM images obtained in the tapping mode for films of PFT containing 80 wt % of **a** PCBM, **b** PCBM:CdSe (2.0 nm), **c** PCBM:CdSe (3.0 nm), **d** PCBM:CdSe (4.0 nm), **e** CdSe (4.0 nm) and films of **f** pure CdSe film (4.0 nm), deposited onto PEDOT:PSS covered ITO-glass substrates. For the ternary component mixtures, the PCBM:CdSe ratio was kept constant at 1:1 wt %. The scan area is (2.5 μm × 2.5 μm). The scale indicates (**a**) 5 nm, (**b**–**e**) 30 nm, or (**f**) 10 nm. Reprinted with permission from Ref. [177]

compromise between the generation of more charges and their effective transport, reflected by the optimum concentration of CdSe and PCBM in the active layer.

Photocurrent is strongly dependent on the CdSe size, as shown in Fig. 7a. A decrease in Jsc is observed when smaller nanoparticles are used (preferential diameters of 2.0 or 3.0 nm). When larger nanoparticles are used (preferential diameter of 4.0 nm) an increase in Jsc was observed compared to the device assembled with PFT/PCBM only, leading to a significant enhancement of efficiency from 0.5 to 0.8 %.

In these ternary systems, CdSe nanoparticles may contribute to current generation in two different ways: (i) increasing light-harvesting, since this material strongly absorbs visible light; or (ii) changing film morphology. The contribution of CdSe in light-harvesting can be seen in the IPCE curves (Fig. 7b). It is evident that the addition of CdSe increases the IPCE values and also changes the curve profile in the low wavelength region (below 450 nm). However, if this contribution in light-harvesting was the main effect, the addition of CdSe would lead to an increase in the Jsc of the device in all cases, even for smaller nanoparticles. The results suggest that a morphologic effect is more likely to have caused changes in Jsc and efficiency.

The morphologic effect can be seen in Fig. 8, where the AFM images obtained for films of PFT/PCBM, PFT/CdSe, and ternary mixtures PFT/CdSe/PCBM (1:1 wt % CdSe:PCBM ratio) with nanoparticles of different sizes are displayed.

The polymer concentration was kept constant in all samples. These images show that the morphology of the PFT/PCBM film is very smooth, while for the sample composed of PFT/CdSe it is much rougher. Also, for each different nanoparticle size the morphology changes drastically despite the fact that the same material concentrations are used. The surface becomes rougher when the size of CdSe nanoparticles increases. In principle, rougher surfaces could be related to the formation of larger aggregates of CdSe, or phase separation with the formation of a CdSe layer in the surface. The AFM image obtained for films of pure CdSe (4.0 nm of preferential diameter, for example) show that the nanoparticle aggregates are smaller and the surface roughness is lower compared to the characteristics of the film of PFT/PCBM/CdSe (4.0 nm), suggesting that the surface of the ternary system is not mainly composed of pure CdSe. This is an indication that the nanoparticles might be distributed throughout the polymer/PCBM phase and do not suffer extended phase separation at the surface in the ternary systems.

The morphologic effect could also be observed in high-resolution transmission electron microscopy (HRTEM) images and optical microscopy images, as shown in previous works [122, 177]. Both the increases in CdSe nanoparticle concentration or size increase the agglomeration of CdSe, at the same time decreasing the agglomeration and the crystallite sizes of PCBM. The morphology changes observed are clearly related to the improvement in efficiency after the incorporation of CdSe nanoparticles in the PFT/PCBM mixture, especially when larger nanoparticles are used.

The effects of CdSe incorporation on the morphology of "standard" P3HT/PCBM mixtures were also investigated. Figure 9 displays AFM images for films of P3HT/PCBM (50 wt % of PCBM) and P3HT/PCBM/CdSe (size = 4.0 nm, PCBM:CdSe 1:1 wt %, total amount of 50 wt %) with and without post-production treatment: annealing was carried out in air, for 10 min at 110 °C.

After annealing, the root mean square (RMS) surface roughness of P3HT/PCBM film increases from 1.6 to 4.4 nm. Most reports show that surface roughness of P3HT/PCBM films increase after annealing, due to demixing and formation of P3HT crystalline regions and PCBM aggregates [80, 178, 179]. On the other hand, a few papers observed the opposite trend [180, 181]. These differences are attributed to different conditions of film preparation (solvent used, concentration of PCBM, fast or slow cooling/drying, time and temperature of annealing, etc.) [74, 180, 182]. After introduction of CdSe the RMS surface roughness is considerably increased to 10.6 nm. Annealing of the ternary system leads to the formation of larger agglomerates (RMS $\sim$ 15.9 nm), probably related to phase separation of CdSe [176].

The absorption characteristics of these films were also investigated. As expected, annealing induces the reorganization and crystallization of P3HT, resulting in a redshift of the absorption maxima and in the appearance of shoulders related to vibronic transitions. The addition of CdSe causes a similar effect in the absorption characteristics, probably related to the change in morphology induced by the presence of these nanoparticles. The annealing of the P3HT/PCBM/CdSe

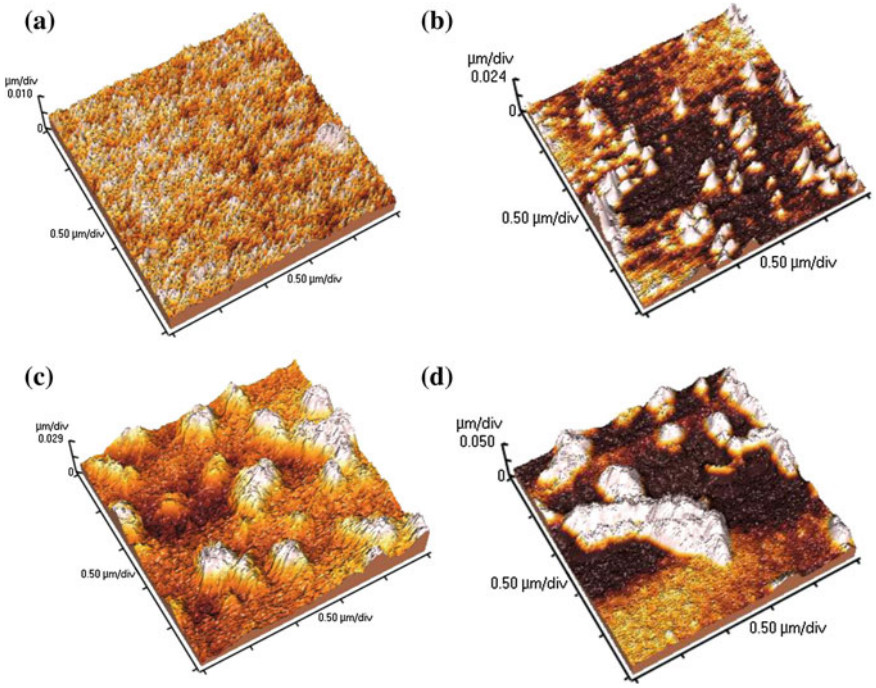

Fig. 9 AFM images obtained in the tapping mode for films of (**a**, **b**) P3HT/PCBM and (**c**, **d**) P3HT/PCBM/CdSe (4.0 nm), deposited onto PEDOT:PSS covered ITO-glass substrates, (**a**, **c**) before and (**b**, **d**) after annealing. The scan area is (2.5 µm × 2.5 µm)

film does not lead to further significant changes in the absorption characteristics of the polymer in this system.

Interestingly, in most cases the incorporation of CdSe into P3HT/PCBM devices causes loss of performance. This behavior is different from that observed for PFT/PCBM/CdSe systems. Photophysical measurements revealed that the difference observed for the devices with polymers P3HT and PFT could be associated with different polymer-nanoparticle interactions [183]. The higher content of thiophene units in the P3HT polymer contributes significantly to the formation of a complex between this polymer and CdSe and to the deactivation of electron transfer process between the polymer and PCBM. In this type of complex, electrons can be transferred from P3HT to the CdSe and, since the TOPO-capped CdSe nanoparticles are poor charge carriers, electrons can be trapped on their surface, not being collected by the electrodes. From this perspective, only the P3HT segments not complexed with CdSe would be free to perform an effective electron transfer to PCBM, as the CdSe acts as a trap for most of electrons from P3HT. For PFT systems, since this polymer has fluorene units in its segments, the possibility of formation of a complex with CdSe is reduced. In other words, in PFT/PCBM/CdSe devices both the polymer and CdSe nanoparticles are more available to interact with PCBM, which is responsible for the transport of

electrons. In P3HT/PCBM/CdSe devices, the main interaction is between the polymer and CdSe, and PCBM remains isolated, not being able to carry on the electron transport [183].

These results show that these kinds of systems are very promising and also very complex. Advantage should be taken of the versatility of inorganic nanoparticles and their interactions with different materials, such as fullerenes, polymers and metal oxides, in order to improve even further the efficiency of hybrid devices.

4 Metal Nanoparticles in Organic Solar Cells

Similar to the case of inorganic semiconductor nanoparticles, metal nanoparticles also show optical properties strongly dependent on size and shape. For example, bulk gold looks yellow in reflected light, while thin Au films look blue in transmission, and this color changes as the nanoparticle sizes are decreased. These characteristics of metal nanoparticles can be used to change the properties of their surrounding media. An interesting example is the Lycurgus Cup [184], which possesses the unique feature of changing color depending upon the light in which it is viewed: it looks green in reflected light and looks red when a light is shone from inside and is transmitted through the glass. This effect is attributed to the presence of Au and Ag nanoparticles in the glass.

The optical properties of small metal nanoparticles are actually dominated by collective oscillation of the conduction electrons, resulting from interaction with the electromagnetic field. A restoring force in the nanoparticles tries to compensate for this, resulting in a unique resonance wavelength [185]. These effects are called surface plasmon resonance [186], and correspond to the frequency of oscillation of conduction electrons in response to the alternating electric field of incident electromagnetic radiation. Figure 10 illustrates this phenomenon. The oscillation wavelength depends on many factors, including the particle size and shape, and the local dielectric environment [187–190]. In addition, when nanoparticles are sufficiently close together, interactions between neighboring particles arise. For elongated particles (1D systems), the resonance wavelength depends on the orientation of the electric field, giving two oscillations, transverse and longitudinal, as illustrated in Fig. 10. The longitudinal oscillation is very sensitive to the aspect ratio of the particles [191], leading to color changes.

Metal nanoparticles can exhibit strong surface plasmon resonances localized at UV, visible and near infrared wavelengths. However, only a few metals, such as Au, Ag and Cu, possess plasmon resonances in the visible spectrum, which give rise to intense colors [186, 192, 193].

Surface plasmons decay radiatively or non-radiatively, giving rise to scattering or absorption of light. Light scattering from metal nanoparticles near their local surface plasmon excitation is a promising way to increase light absorption in solar cells. The strong interaction of photons with metal nanoparticles induces the formation of an electromagnetic field in the regions near these particles.

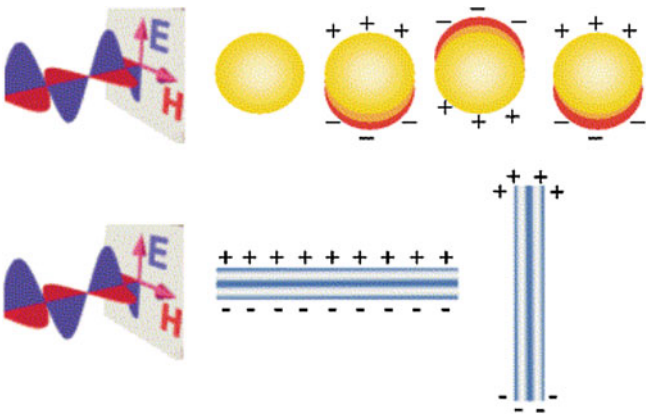

Fig. 10 (*Top*) Schematic drawing of the interaction of the electromagnetic radiation with a metal nanosphere. A dipole is induced, which oscillates in phase with the electric field of the incoming light. (*Bottom*) Transverse and longitudinal oscillation of electrons in a metal nanorod. Reprinted from Ref. [9]

If a semiconductor is located in the surroundings, for example, the absorption of light by this material may be increased, resulting in increased exciton generation. Besides, the excitons may split at the interface semiconductor-metal nanoparticle due to the electromagnetic field. These effects are expected to improve the photocurrent in solar cells.

In recent years, metal nanoparticles have been shown to improve the performance of silicon-based solar cells [194–204], GaAs solar cells [205], and quantum well solar cells [206]. For these inorganic devices, the principal method of enhancement is scattering of incident light, which increases light-trapping and can potentially reduce reflection. For metal nanoparticles situated on the front surface of a device, the nanoparticles must scatter light into the device (i.e., in the forward direction) to reduce reflection, and must scatter at oblique angles to improve light-trapping. Any light absorbed by the nanoparticle is lost as heat, so absorption should be minimized. If the nanoparticles are strongly absorbing and/or back-scattering they will decrease the device efficiency.

The incorporation of Au or Ag nanoparticles in TiO_2 [207–214] or ZnO [215–217] nanostructures, particularly aiming at the application in DSSC, has also been demonstrated. The contact between bulk gold and bulk TiO_2 can form a Schottky barrier of $\sim$1.0 eV [194, 218], which can be difficult for electrons to overcome, thus making interfacial charge separation unfavorable. However, electron transfer from Au nanoparticles to the conduction band of TiO_2 was observed by transient absorption spectroscopy [209, 219]. Photoexcited electrons can be also transferred from Au nanoparticles to the ZnO conduction band. The Schottky barrier at the ZnO/Au interface blocks the electron transfer back from ZnO to the dye and electrolyte, and thus increases the electron density of the ZnO conduction band [216]. For TiO_2 based DSSC, there are a few different mechanisms, which may be

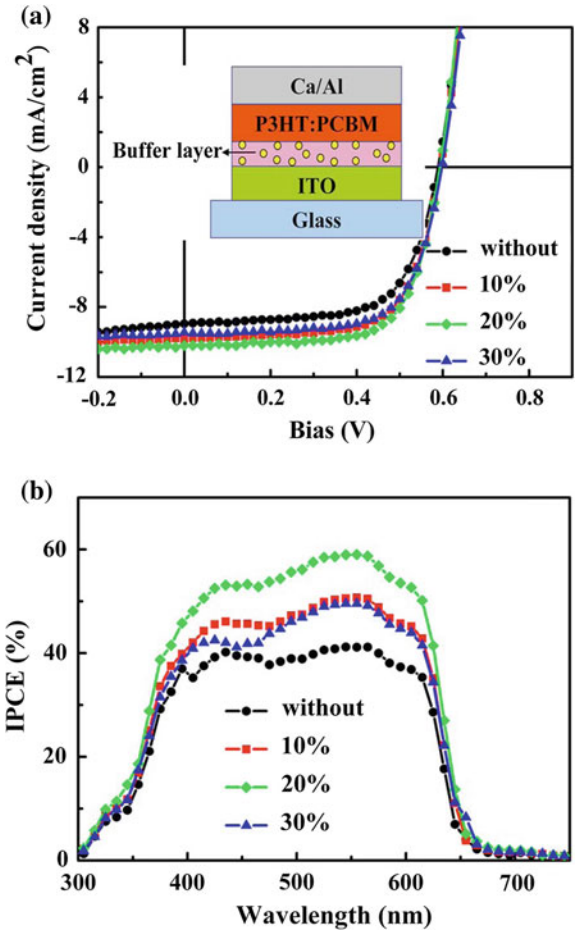

Fig. 11 **a** J–V characteristics, recorded under 100 mW cm^{-2}, of devices incorporating PEDOT:PSS doped with various concentrations of Au nanoparticles solutions: without doping (○); 10 % (■); 20 % (◆) and 30 % Au nanoparticles solution doping (▲); **b** corresponding IPCE curves of these devices. *Inset* Schematic representation of the device assembly. Reprinted with permission from Ref. [236]

considered as candidates for the plasmonic contribution to short circuit current [207]:

- Internal plasmon decay into energetic electron–hole pairs in the metal nanostructure, followed by subsequent charge carrier injection over, or tunneling through, the Schottky barrier between the metal and semiconductor substrate.
- Direct near-field coupling to electronic transitions in the dye molecules.
- Near-field coupling to TiO_2 band gap transitions.
- Far-field scattering leading to prolonged optical path and, in particular, coupling to wave guided modes in thin TiO_2 film.

The interactions of Ag and Au metal nanoparticles with many different molecules and materials have been observed, which may account for the development of new types of plasmonic solar cells. For example, Schottky diode junctions were formed between CdS nanowires and Au nanowires and delivered 0.92 mA cm^{-2}

of current under one sun illumination [220]. The incorporation of Au nanowires within nanocrystalline CdSe increases the extraction of photogenerated carriers, and the photoresponse of CdSe/Au hybrid materials can be controlled by changing the conductivity of the Au nanowires [221]. Electron-transfer was also observed for Au-CdS core-shell nanocrystals. The as-synthesized Au-CdS nanocrystals exhibited superior photocatalytic performance under visible light illumination compared to other relevant commercial materials, demonstrating their potential as an effective visible-light-driven photocatalysts [222].

Remarkable enhancement in the photocurrent action and fluorescence excitation spectra was observed for porphyrin and phthalocyanine when considerable amounts of Ag nanoparticles were deposited onto the ITO electrode. Raman scattering measurements suggested the effects of enhanced electric fields resulting from localized surface plasmon resonance and light scattering on the photocurrent enhancement [223].

The addition of Au nanoclusters to P3HT resulted in an increased photoluminescence, explained by polymer chain separation induced by the presence of the nanoparticles [224]. Addition of Au to a blue light emitting polymer also resulted in enhanced luminescent stability [225]. Parfenov et al. [226] reported that Ag nanoparticles increase photoluminescence efficiency through increasing the exciton decay time of the surrounded fluorophore. Saranthy et al. [227] observed fluorescence enhancement of poly(3-octylthiophene) (P3OT) that is near the Ag nanoparticles by means of a near-field scanning optical microscope experiment. The fluorescence of Au/MEH-PPV nanocomposites was changed by over an order of magnitude by controlling the Au particle size, the spatial distribution of nanoparticles throughout the MEH-PPV host, and the ligand chain layer thickness. Smaller particles were more efficient at quenching. As the ligand chain length increased, the quenching became less efficient [228].

Considering the application in OSC specifically, metal nanoparticles have been explored in different approaches: (i) in the metal electrode for collection of electrons (i) as a buffer layer, (ii) as an interfacial layer, or (iii) in the bulk heterojunction.

Au and Ag evaporated films have been widely used as metal-electrodes for charge collection in OSC [229, 230]. Usually, the use of these metals is associated with decreased Voc in comparison to Al cathodes. However, Au/LiF/Al layered cathodes showed 20–30 % improved Jsc and η over devices without Au. The introduction of a nanotextured Au thin film was observed to increase the absorption of a P3HT/PCBM thin film through plasmon-assisted localization of the electromagnetic field of the incident light [231].

Electron transfer from metal to C_{60} was reported [232–234] and the interaction between Ag and C_{60} is considered stronger than that between Au and C_{60}. On the one hand, this interaction allows strategies such as the use of a Ag or Au layer before the metal cathode [231]. On the other hand, in BHJ OSC some authors consider that this effect may be responsible for a Voc drop observed when large amounts of nanoparticles are used, since they might reduce the electron affinity of C_{60} [247].

The incorporation of metal nanoparticles as buffer layer in OSC is perhaps the most used approach [235–239]. Chen et al. [236] demonstrated improvement in

device performance after adding various concentrations of Au nanoparticles into the PEDOT:PSS layer, as shown in Fig. 11. The average Au particle size estimated from scanning electron microscopy was ~30–40 nm. The buffer layer was prepared by spin-coating a mixture of a Au nanoparticles solution with the PEDOT:PSS solution on top of the ITO substrate. The reference device prepared with pristine PEDOT:PSS exhibited a Voc of 0.59 V, Jsc of 8.95 mA cm^{-2}, a FF of 65.9 % and efficiency of 3.48 %. After the addition of Au nanoparticles to the buffer layer, the values of Voc remained unchanged, but FF was improved. The maximum efficiency of 4.19 % was obtained using 20 % Au (Jsc = 10.18 mA cm^{-2}, FF = 69.8). Further increases in the concentration of the metal nanoparticles to 30 % led to a decrease in the value of Jsc, due to enhanced backward scattering and/or increased resistivity of the buffer layer. The trends in IPCE follow those for the values of Jsc, as can be seen in Fig. 11b. The authors suggested that the surface plasmon resonance increased not only the rate of exciton generation, but also the probability of exciton dissociation [236].

In a similar way, Au nanostructures were fabricated through the layer-by-layer deposition of Au nanorods onto the ITO substrates and transformed into nanodots through a thermally-induced shape transition. The incorporation of plasmonic Au nanodots on the ITO surface was found to result in an increase in the power conversion efficiency of P3HT/PCBM devices from 3.04 to 3.65 %. The strong coupling between the organic excitons and plasmons of the Au nanostructures results in more efficient charge transfer in the BHJ system [237].

Ag nanoparticles of ~13 nm were electrodeposited onto the ITO and covered with PEDOT:PSS as buffer layer in a P3HT/PCBM device. The overall power conversion efficiency was increased from 3.05 to 3.69 %, mainly because of the improved photocurrent density, as a result of enhanced absorption of the photoactive conjugated polymer due to the high electromagnetic field strength in the vicinity of the excited surface plasmons. Improved IPCE was also observed at wavelength regions longer than 400 nm, related to the surface plasmon resonance band of electrodeposited Ag nanoparticles [238].

Ag nanoparticle layers were fabricated using vapor-phase deposition on ITO electrodes and the influence of the Ag film thickness in P3HT/PCBM solar cells was investigated. The highest increase in Jsc was observed for devices incorporating 2 nm of Ag, and, as the film thickness was increased, a downward trend in Jsc was observed. The efficiency was found to improve by a factor of 1.7 (from 1.3 to 2.2 %). The Voc decreased slightly with increasing Ag layer, related to a decrease in the work function of the transparent electrode [239].

Tvingstedt et al. [240] demonstrated the effects of a metal grating in an inverted BHJ OSC assembled with polyfluorene derivatives and PCBM. An increase of photocurrent was observed at the resonant position of the surface plasmon when this band has higher energy than the band gap of the absorbing polymer.

The beneficial effects in photocurrent and device efficiency from the plasmon resonance of Au, Ag or Cu nanoparticles as buffer layers have been shown for OSC assembled with Cu-based phthalocyanines [241–243] and Zn-based phthalocyanines [244]. The exploration of these metals as interfacial layers in tandem

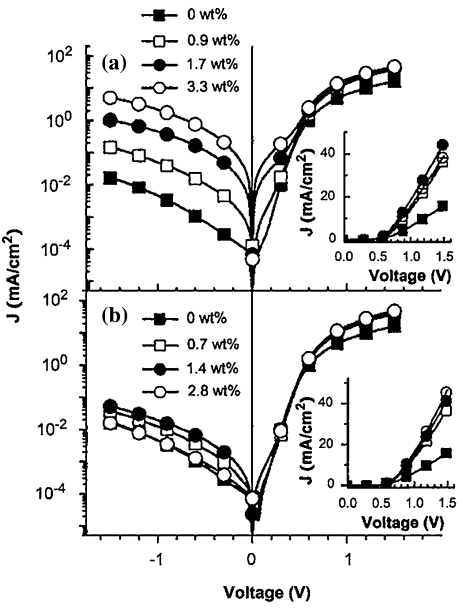

Fig. 12 J–V characteristics in the dark of P3OT/C_{60} solar cells containing: **a** Ag and **b** Au nanoparticles. Reprinted from Ref. [247]

OSC devices assembled with small organic molecules [245, 246] was also shown to be successful. Yakimov et al. [245] reported significant enhancement in photovoltaic efficiency of a tandem device containing Ag nanoparticles in the middle of two photoactive layers. The optical intensity near the Ag nanoparticle was significantly enhanced due to scattering [246].

The incorporation of Au or Ag nanoparticles in the BHJ active layer, on the other hand, has been much less explored. In fact, only a few papers can be found reporting this approach [247–252] and there has been some controversy about the effect of these nanoparticles in BHJ OSC.

In 2005, Kim and Carroll [247] reported the incorporation of Au (size ~6 nm) or Ag (size ~5 nm) nanoparticles stabilized with dodecylamine in the P3OT/C_{60} active layer. The BHJ was prepared from a chlorobenzene co-solution of all the materials. The authors showed an increase in the electrical conductivity of the films upon the incorporation of the nanoparticles, observed from J–V characteristics in the dark (Fig. 12). They proposed that hole transfer occurs from P3OT to Ag or Au, attributed to the "dopant" states introduced by the metal nanoparticles in the band gap of the polymer. These authors also showed that the contribution to light absorption enhancement was minimal, less than 10 %. Despite the different plasmon absorption of the two nanoparticles (443 nm for Ag and 523 nm for Au), they did not observe significant changes in the absorption spectra. The best efficiency was obtained using Ag nanoparticles.

In 2008, Park et al. [248] added small amounts of Au nanoparticles (size ~3–6 nm) to the BHJ of P3HT/PCBM. The films were prepared by adding different amounts of a toluene solution containing the nanoparticles to a

Table 2 Performance parameters reported by different authors for OSC containing metal nanoparticles in the bulk heterojunction

Active layer	Film thickness/active area	NP size/passivation	NP concentration/solvent	PV parameters	References
P3OT/C_{60}	–/0.19 cm^2	–	–/CB	Jsc = 5.1 mA cm^{-2} Voc = 0.55 V FF = 0.32 η = 1.1 %	[247]
P3OT/C_{60}/Au	150 nm/0.19 cm^2	5.3 ± 1.1/DDA	1.7 wt %/CB	Jsc = 5.9 mA cm^{-2} Voc = 0.56 FF = 0.41 η = 1.7 %	[247]
P3OT/C_{60}/Ag	150 nm/0.19 cm^2	6.1 ± 1.3/DDA	1.4 wt %/CB	Jsc = 6.2 mA cm^{-2} Voc = 0.56 V FF = 0.43 η = 1.9 %	[247]
P3HT/PCBM	110 nm/0.09 cm^2	–	–/CB	Jsc = 6.15 mA cm^{-2} Voc = 0.61 V FF = 0.37 η = 1.43 %	[248]
P3HT/PCBM/Au	110 nm/0.09 cm^2	3–6 nm	3×10^{-7} wt %/CB + toluene	Jsc = 9.17 mA cm^{-2} Voc = 0.61 V FF = 0.38 η = 2.17 %	[248]
P3HT/PCBM	90 nm/0.07 cm^2	–	–/CB	Jsc = 8 mA cm^{-2} Voc = 0.6 FF = 0.45 η = 2.5 %	[250]
P3HT/PCBM/Au	80 nm/0.07 cm^2	3.7 nm/P3HT	3 wt %/CB	Jsc = 6.0 mA cm^{-2} Voc = 0.54 V FF = 0.35 η = 1.5 %	[250]

(continued)

Table 2 (continued)

Active layer	Film thickness/active area	NP size/passivation	NP concentration/solvent	PV parameters	References
P3HT/PCBM/Au	75 nm/0.07 cm^2	3.7 nm/P3HT	16 wt %/CB	Jsc = 2.6 mA cm^{-2} Voc = 0.40 V FF = 0.35 η = 0.4 %	[250]
P3HT/PCBM	70 nm/0.04 cm^2	–	–/CB	Jsc = 9.7 mA cm^{-2} Voc = 0.65 FF = 0.52 η = 3.2 %	[250]
P3HT/PCBM/Au	90 nm/0.04 cm^2	7.0 nm/DDA	3 wt %/CB	Jsc = 10.8 mA cm^{-2} Voc = 0.59 FF = 0.46 η = 2.9 %	[250]
P3HT/PCBM/Au	85 nm/0.06 cm^2	7.0 nm/DDA	52 wt %/CB	Jsc = 5.3 mA cm^{-2} Voc = 0.27 FF = 0.25 η = 0.4 %	[250]
P3HT/PCBM	65 nm/0.05 cm^2	–	–/CB + py	Jsc = 8.7 mA cm^{-2} Voc = 0.62 FF = 0.45 η = 2.4 %	[250]
P3HT/PCBM/Au	45 nm/0.08 cm^2	15 nm/py	23 wt %/CB + py	Jsc = 7.1 mA cm^{-2} Voc = 0.42 FF = 0.31 η = 1.1 %	[250]
P3HT/PC_{71}BM/Au	220 nm/9.84 mm^2	70 nm/–	5 wt %/DCB	Jsc = 11.18 mA cm^{-2} Voc = 0.63 FF = 0.61	[252]

(continued)

Table 2 (continued)

Active layer	Film thickness/active area	NP size/passivation	NP concentration/solvent	PV parameters	References
PCDTBT/$PC_{71}BM$/Au	120 nm/9.84 mm^2	70 nm/–	5 wt %/DCB + CB	Jsc = 11.16 mA cm^{-2} Voc = 0.89 FF = 0.65 η = 6.45 %	[252]
Si-PCPDTBT/$PC_{71}BM$/Au	150 nm/9.84 mm^2	70 nm/–	5 wt %/DCB	Jsc = 13.13 mA cm^{-2} Voc = 0.57 FF = 0.61 η = 4.54 %	[252]

CB chlorobenzene, *DCB* dichlorobenzene, *DDA* dodecyl amine, *NP* nanoparticles, *P3HT* poly(3-hexylthiophene), *P3OT* poly(3-octylthiophene), *PCBM* [6,6]-phenyl C_{61}–butyric acid methyl ester, *$PC_{71}MB$* [6,6]-phenyl C_{71}–butyric acid methyl ester, *PCDTBT* poly[N-9″ -hepta-decanyl-2,7-carbazole-alt-5,5-(4′ ,7′ -di-2-thienyl-2′ ,1′ ,3′ -benzothiadiazole), *PV* photovoltaic, *py* pyridine, *Si–PCPDTBT* poly{[4, 4′ -bis(2-ethylhexyl) dithieno(3,2-b;2′ ,3′ -d)silole]-2,6-diyl-alt-[4,7-bis(2-thienyl)-2,1,3-benzothiadiazole]-5,5′ -diyl}

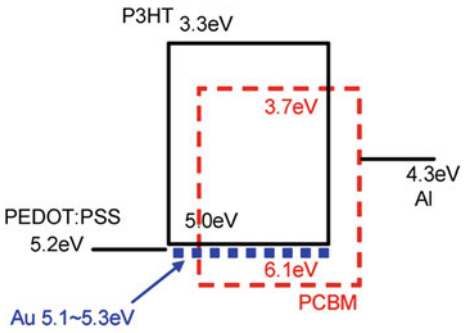

Fig. 13 Energy levels of HOMO and LUMO of P3HT and PCBM, and work function of Au, PEDOT:PSS and Al. Reprinted with permission from Ref. [248]

chlorobenzene solution of P3HT/PCBM, and then annealed at 120 °C for 30 min under nitrogen. As opposed to the work of Carroll and Kim [247], the authors did not observe enhanced dark conductivity for this system. Under illumination, increased efficiency was observed at small Au contents, which was mainly related to an improvement in photocurrent. Voc and FF remained almost the same. At a weight fraction of 6.25×10^{-8} Au nanoparticles/P3HT, about 50 % enhancement was shown in efficiency (from 1.43 to 2.17 %). They attributed the increase in Jsc to improved light-harvesting, although only a smooth change was observed in the absorption spectra.

As illustrated in Fig. 13, there is a small barrier for hole injection at the PEDOT:PSS contact [248]. Thus, one might consider that the Au nanoparticles might assist such injection (and therefore, charge collection) at the electrode in these systems, especially in cases where the concentration of these particles is large.

In 2009, Shen et al. [249] and Duche et al. [250] investigated the influence of Ag nanoparticles on the light-absorption characteristics of OSC by theoretical simulations. Shen et al. [249] found that near field enhancement is the main reason for absorption enhancement in the active layer, and that the optimum conditions are dependent both on the film thickness and the nanoparticle size. For a thin film (33 nm) of P3HT/PCBM, nanoparticles with diameters of $\sim$24 nm are necessary for optimum absorption enhancement. These conditions would lead to an enhancement factor of 1.56, which should compensate and bring the performance close to that expected for a much thicker device prepared without metal nanoparticles. Duche et al. [250] compared the modeling results with experimental results for MEH-PPV/PCBM BHJ OSC. Enhanced absorption of light up to 50 % was experimentally obtained in a 50 nm-thick layer including silver nanospheres with a diameter of 40 nm, in agreement with the high values expected from calculations.

In 2010, Topp et al. [251] investigated the incorporation of different amounts of P3HT-capped, dodecyl amine-(DDA)-capped, or pyridine-capped Au nanoparticles into P3HT/PCBM mixtures. The use of Au directly stabilized with P3HT seems to be a promising approach to incorporate these materials in OSC without further addition of organic components. Besides, one could expect that P3HT ligands strongly bound to Au nanoparticles might lead to direct electron transfer from the polymer to Au.

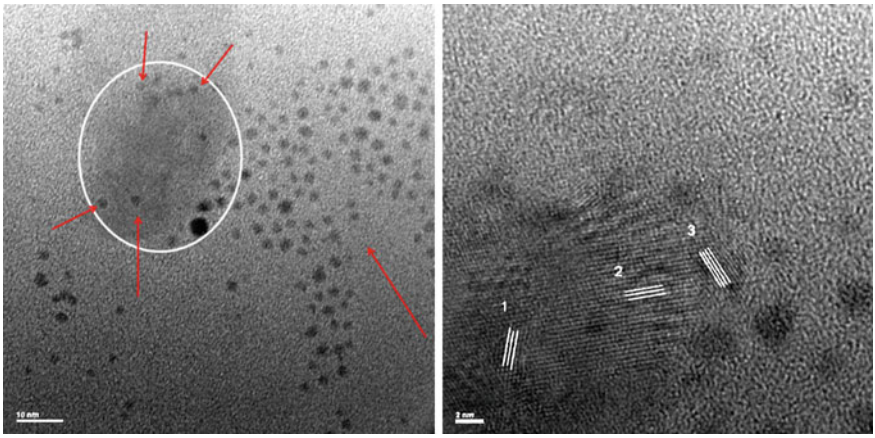

Fig. 14 HRTEM images obtained for the P3HT/PCBM/Au nanoparticles system, containing 1 wt % of Au. (*Left*) *White circle* indicates the PCBM region, while *red arrows* indicate Au nanoparticles dispersed in the P3HT matrix and in the PCBM domain. (*Right*) The high resolution image shows PCBM crystallites oriented in distinct directions, as indicated by the *white lines* (regions 1, 2 and 3) (Color figure online)

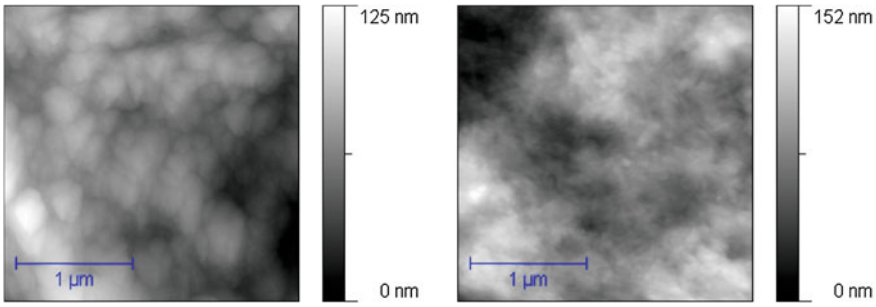

Fig. 15 AFM images in the tapping-mode for (*left*) P3HT/PCBM and (*right*) P3HT/PCBM/Au nanoparticle films

However, the authors reported a slightly decrease in performance (see Table 2) after addition of 3 wt % of P3HT-capped Au nanoparticles, and a strong decrease of performance after addition of 16 wt % of this material. No significant changes were observed in the absorption spectra, suggesting that the absorption was dominated by the polymer (even at 16 wt % of Au), and there was no disruption in the crystalline order of P3HT. The field effect mobility of holes was estimated to be the same ($\sim 1 \times 10^{-4}$ cm^2 V^{-1} s^{-1}) before and after Au incorporation. Photoinduced absorption spectroscopy was used to investigate charge transfer between P3HT and Au nanoparticles. The authors found no indications for Au-enhanced formation of long-lived polarons in P3HT, although these results are very noisy and therefore should be interpreted carefully. Since other effects were ruled out, the authors

suggested that the loss of performance in these devices may be explained by a quenching of the excited state of the polymer in the presence of Au. Phase segregation was not excluded, although the authors consider this unlikely due to the strong interaction between the S-containing polymer and Au. OSC assembled with 3 or ~50 wt % of dodecyl amine-stabilized Au nanoparticles also showed decreased performance, attributed to the ligand shell which is an insulating barrier for charge transport, as evidenced in J–V characteristics in the dark (the current under forward bias was reduced after introduction of Au). Interestingly, the cells containing DDA-capped Au nanoparticles seemed to be better than those containing P3HT-capped Au nanoparticles. This is in agreement with the proposed mechanism, where the quenching of the excited state in the polymer was the main cause for performance loss in the P3HT-capped Au nanoparticle system, while the presence of the DDA shell reduces the quenching probability. In a third approach, the authors used pyridine-capped Au nanoparticles, following strategies typically used for BHJ OSC containing CdSe nanoparticles. This approach did not improve the efficiency of devices after incorporation of Au nanoparticles, probably related to the quenching of the excited state and to Au segregation phenomena.

In 2011, Wang et al. [252] demonstrated positive effects arising from addition of 5 wt % of larger Au nanoparticles (size ~70 nm) into BHJ OSC composed of mixtures of polymer/$PC_{71}BM$. The improvement in Jsc, FF and IPCE resulted from a combination of enhanced light absorption caused by the light scattering of Au nanoparticles and improved charge transport. The authors also found that the increase in device efficiency depend in detail on the size of the metal nanoparticles and the weight ratio of these materials in the BHJ film.

Table 2 summarizes the results obtained by different authors for BHJ OSC before and after incorporation of Au or Ag nanoparticles into the active layer.

From Table 2 it is evident that there is some controversy between the results involving metal nanoparticle incorporation into BHJ OSC reported by different authors. Interestingly, none of these papers investigated systematically a possible morphological effect introduced by the presence of metal nanoparticles. As observed in polymer/PCBM/CdSe BHJ OSC (Sect. 3), morphology can be expected to play a crucial role in BHJ OSC containing metal nanoparticles as well.

In an earlier work, Conturbia showed that in fact the morphology of the P3HT/PCBM system is significantly changed upon incorporation of Au nanoparticles [253]. Figure 14 shows HRTEM images of a P3HT/PCBM/Au system containing 1 wt % of Au nanoparticles. In Fig. 14a it can be seen that the Au nanoparticles are distributed both in the polymer and in the PCBM domains, while Fig. 14b shows in higher magnification the presence of large PCBM domains/crystallites in the sample. The PCBM domain shown is estimated to have ~40 nm. The d-spacing of the nanocrystals at different orientations shown in regions 1, 2 and 3 correspond to 0.26, 0.28 and 0.19 nm. These results are similar to those found by Reyes-Reyes et al. [254] for P3HT/PCBM unannealed films containing high concentrations of PCBM, or films containing low concentrations of PCBM, annealed for short times. These authors correlated the aspect of the PCBM crystallites with device efficiency. The size and shape of PCBM crystallites seem to be

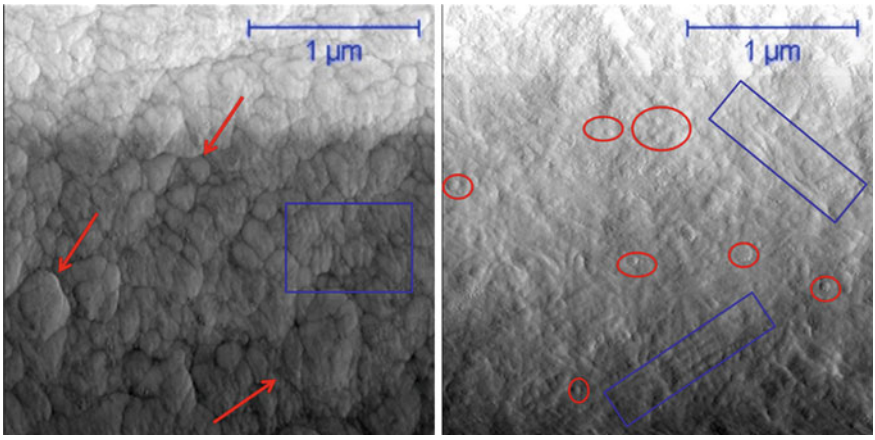

Fig. 16 AFM images in the phase-mode for (*left*) P3HT/PCBM and (*right*) P3HT/PCBM/Au nanoparticles films. (*Left*) The *red arrows* indicate large P3HT aggregates (mainly amorphous phase), while the *blue rectangle* indicates an area with fibrillar structures (associated with P3HT crystalline phase). (*Right*) *Red circles* indicate possible PCBM domains, while *blue rectangles* indicate areas with fibrillar structures (P3HT crystallites)

affected by annealing time and temperature [254] and also by the solvent and solvent evaporation ratio during film deposition [255]. We suggest that incorporation of Au nanoparticles may also affect somehow the crystallization of PCBM.

AFM images in the tapping mode are shown in Fig. 15. The RMS surface roughness is estimated to be 21 and 26 nm for P3HT/PCBM and P3HT/PCBM/Au films, respectively, deposited from 1,2,4-trichlorobenzene. Some authors have associated an observed increase in roughness in AFM images with a higher organization of P3HT chains [74, 80, 181]. Figure 16 shows AFM images of the same regions obtained in the phase mode. These figures show the different morphological aspects between the samples with and without Au nanoparticles. For example, in Fig. 16a the presence of large agglomerates can be seen, possibly attributed to the amorphous phase of P3HT. In some points it is possible to see fibrillar structures, attributed to crystalline regions of P3HT. In Fig. 16b (P3HT/PCBM/Au sample) the presence of fibrillar structures is more evident, and there are highly ordered regions, with anisotropy, suggesting that this sample is richer in P3HT crystallites [256]. In this image, well defined regions with $\sim$50 nm dimensions can be seen, which are associated to PCBM crystallites/domains, in agreement with the PCBM phases observed in HRTEM. These results suggest that the morphologic changes induced by incorporation of Au nanoparticles may act both in the way of organization/crystallization of PCBM and of P3HT, and this parameter could be responsible for improving or decreasing the device efficiency.

An interesting aspect of these systems, as observed by Conturbia [253], is that the incorporation of Au nanoparticles does not seem to disrupt the crystalline structure of P3HT (the alpha-axis orientation signal of the polymer in X-ray diffractograms was the same before and after Au incorporation). Also, the absorption characteristics of

the film are dominated by the characteristics of P3HT, and remain almost unchanged after addition of Au [253]. These data are in agreement with the observations reported by Park et al. [248] for X-ray patterns and absorption characteristics of P3HT/PCBM containing small amounts of Au nanoparticles.

From all the data discussed, we suggest that the performance of BHJ OSC containing Au nanoparticles depends strongly on the morphology of the film. Although a careful analysis was not carried out considering the effects of the nanoparticle concentration and size, one could expect these parameters to affect morphology and, therefore, solar cell performance.

5 Conclusions and Perspectives

In this review, recent results on the incorporation of inorganic nanoparticles into organic solar cells were highlighted. Such materials are not only easily synthesized in a great variety of sizes and shapes, but also possess important optical features that can be explored in improving the photocurrent and efficiency of solar cells. In this sense, semiconductor quantum dots, such as CdSe, may act as electron acceptors, at the same time contributing to increase light-harvesting, generating more charge carriers in the active layer. Metal nanoparticles, especially Au and Ag, are more suitable to act as light scattering structures in the buffer layer.

One of the main drawbacks associated with the use of inorganic nanoparticles in organic solar cells is the presence of bulky organic molecules (surfactants) on the surface of the nanoparticles, which prevent their aggregation but also hinder the charge transfer and charge transport processes. Much work still needs to be done to change the nanoparticles surface in order to improve their dispersion in polymer matrices. An interesting and elegant approach shown recently is to use quantum dots as sensitizers in polymer/fullerene mixtures, where they may contribute to the generation of free charge carriers and, at the same time, extend the phase separation in the active layer, leading to a more favorable morphology between the polymer and fullerene derivative. Such systems have been shown to be very promising and also very complex, and might be the future of highly efficient hybrid polymer solar cells.

Considering metal nanoparticles, the effects of the incorporation of these materials into polymer/fullerene mixtures is still controversial. Some authors have shown an improvement of device efficiency when adding small amounts of Au or Ag nanoparticles into the bulk heterojunction, attributed to an enhancement of charge carrier transport. On the other hand, other authors found that the incorporation of these materials decreased device efficiency. Interestingly, the morphology effect induced in the solar cell active layer by these nanoparticles has not yet been systematically investigated. This is an important parameter, which should be further explored, since it may clarify the reasons for different performances found in such devices. Meanwhile, the use of metal nanoparticles as buffer

layers under the active layer has been shown to be a promising way of exploring the optical and electronic properties of these materials in organic solar cells.

Acknowledgments The authors acknowledge FAPESP (fellowship 2009/15428-0) and CNPq for financial support, LME/LNNano/CNPEM for the technical support during the HR-TEM work, Prof. N. Serdar Sariciftci, Prof. Mônica A. Cotta, João H. Clerice and Giovanni Conturbia for scientific discussions, and Prof. Carol Collins for English revision.

References

1. Fthenakis V, Alsema E (2006) Photovoltaics energy payback times, greenhouse gas emissions and external costs: 2004—early 2005 status. Prog Photovolt 14:275–280
2. Zhao J, Wang A, Altermatt P, Green MA (1995) 24 percent efficient silicon solar-sells with double-layer antireflection coatings and reduced resistance loss. Appl Phys Lett 66:3636–3638
3. Zhao J, Wang A, Green MA, Ferrazza F (1998) 19.8 % efficient "honeycomb" textured multicrystalline and 24.4 % monocrystalline silicon solar cells. Appl Phys Lett 73:1991–1993
4. Shockley W, Queisser HQ (1961) Detailed balance limit of efficiency of p-n junction solar cells. J Appl Phys 32:510–519
5. Knapp K, Jester T (2001) Empirical investigation of the energy payback time for photovoltaic modules. Sol Energy 71:165–172
6. Goetzberger A, Luther J, Willeke G (2002) Solar cells: past, present, future. Sol Energy Mater Sol Cells 74:1–11
7. Liang Y, Xu Z, Xia J, Tsai S-T, Wu Y, Li G, Ray C, Yu L (2010) For the bright future-bulk heterojunction polymer solar cells with power conversion efficiency of 7.4 %. Adv Mater 22:E135–E138
8. Heeger AJ (2010) Semiconducting polymers: the third generation. Chem Soc Rev 39:2354–2371
9. Liz-Marzán LM (2004) Nanometals: formation and color. Mater Today 7:26–31
10. Scholes GD, Rumbles G (2006) Excitons in nanoscale systems. Nat Mater 5:683–696
11. Xia Y, Yang P, Sun Y, Wu Y, Mayers B, Gates B, Yin Y, Kim F, Yan H (2003) One-dimensional nanostructures: synthesis, characterization, and applications. Adv Mater 15:353–389
12. Manna L, Sher EC, Alivisatos AP (2002) Shape control of colloidal semiconductor nanocrystals. J Clust Sci 13:521–532
13. Cozzoli PD, Pellegrino T, Manna L (2006) Synthesis, properties and perspectives of hybrid nanocrystal structures. Chem Soc Rev 35:1195–1208
14. Biju V, Itoh T, Anas A, Sujith A, Ishikawa M (2008) Semiconductor quantum dots and metal nanoparticles: syntheses, optical properties, and biological applications. Anal Bioanal Chem 391:2469–2495
15. Moriarty P (2001) Nanostructured materials. Rep Prog Phys 64:297–381
16. Sau TK, Rogach AL (2010) Nonspherical noble metal nanoparticles: colloid-chemical synthesis and morphology control. Adv Mater 22:1781–1804
17. Sau TK, Rogach AL, Jäckel F, Klar TA, Feldmann J (2010) Properties and applications of colloidal nonspherical noble metal nanoparticles. Adv Mater 22:1805–1825
18. Henzie J, Lee J, Lee MH, Hasan W, Odom TW (2009) Nanofabrication of plasmonic structures. Annu Rev Phys Chem 60:147–165
19. Eustis S, El-Sayed MA (2006) Why gold nanopartilces are more precious than pretty gold: noble metal surface plasmon resonance and its enhancement of the radiative and nonradiative properties of nanocrystals of different shapes. Chem Soc Rev 35:209–217

20. Noguez C, Garzon IL (2009) Optically active metal nanoparticles. Chem Soc Rev 38:757–771
21. Zhang JZ, Noguez C (2008) Plasmonic optical properties and applications of metal nanostructures. Plasmonics 3:127–150
22. Arici E, Meissner D, Schaffler F, Sariciftci NS (2003) Core/shell nanomaterials in photovoltaics. Int J Photoenergy 5:199–208
23. Saunders BR, Turner ML (2008) Nanoparticle-polymer photovoltaic cells. Adv Colloid Interface Sci 138:1–23
24. Skompska M (2010) Hybrid conjugated polymer/semiconductor photovoltaic cells. Synth Met 160:1–15
25. Tang CW (1986) 2-layer organic photovoltaic cell. Appl Phys Lett 48:183–185
26. Meskers SCJ, Huebner M, Oestreich M, Baessler H (2001) Dispersive relaxation dynamics of photoexcitations in a polyfluorene film involving energy transfer: experiment and Monte Carlo simulations. J Phys Chem B 105:9139–9149
27. Mayer AC, Scully SR, Hardin BE, Rowell MW, McGehee MD (2007) Polymer-based solar cells. Mater Today 10:28–33
28. Pope M, Swenberg CE (1999) Electronic processes in organic crystals and polymers, 2nd edn. Oxford University Press, New York
29. Miranda PB, Moses D, Heeger AJ (2001) Ultrafast photogeneration of charged polarons in conjugated polymers. Phys Rev B 64:081201-1–081201-4
30. Harrison NT, Hayes GR, Phillips RT, Friend RH (1996) Singlet intrachain exciton generation and decay in poly(p-phenylenevinylene). Phys Rev Lett 77:1881–1884
31. Yu G, Zhang C, Heeger AJ (1994) Dual function semiconducting polymer devices—light-emitting and photodetecting diodes. Appl Phys Lett 64:1540–1542
32. Gregg BA (2003) Excitonic solar cells. J Phys Chem B 107:4688–4698
33. Savenije TJ, Warman JM, Goossens A (1998) Visible light sensitisation of titanium dioxide using a phenylene vinylene polymer. Chem Phys Lett 287:148–153
34. Nelson J (2002) Organic photovoltaic films. Curr Opin Solid State Mater Sci 6:87–95
35. Yu G, Gao J, Hummelen JC, Wudl F, Heeger AJ (1995) Polymer photovoltaic cells—enhanced efficiencies via a network of internal donor-acceptor heterojunctions. Science 270:1789–1791
36. Halls JJM, Walsh CA, Greenham NC, Marseglia EA, Friend RH, Moratti SC, Holmes AB (1995) Efficient photodiodes from interpenetrating polymer networks. Nature 376:498–500
37. Sariciftci NS, Smilowitz L, Heeger AJ, Wudl F (1992) Photoinduced electron-transfer from a conducting polymer to buckminsterfullerene. Science 258:1474–1476
38. Brabec CJ, Zerza G, Cerulo G, De Silvestri S, Luzatti S, Hummelen JC, Sariciftci NS (2001) Tracing photoinduced electron transfer process in conjugated polymer/fullerene bulk heterojunctions in real time. Chem Phys Lett 340:232–236
39. Nogueira AF, Montanari I, Nelson J, Durrant JR, Winder C, Sariciftci NS, Brabec CJ (2003) Charge recombination in conjugated polymer/fullerene blended films studied by transient absorption spectroscopy. J Phys Chem B 107:1567–1573
40. Kim JS, Granström M, Friend RH, Johansson N, Salaneck WR, Daik R, Feast WJ, Cacialli F (1998) Indium-tin oxide treatments for single- and double-layer polymeric light-emitting diodes: the relation between the anode physical, chemical, and morphological properties and the device performance. J Appl Phys 84:6859–6870
41. Koch N, Kahn A, Ghijsen J, Prieaux JJ, Schwartz S, Johnson RL, Elschner A (2003) Conjugated organic molecules on metal versus polymer electrodes: demonstration of a key energy level alignment mechanism. Appl Phys Lett 82:70–72
42. Brabec CJ, Shaheen SE, Winder C, Sariciftci NS, Denk P (2002) Effect of LiF/metal electrodes on the performance of plastic solar cells. Appl Phys Lett 80:1288–1290
43. Brabec CJ, Sariciftci NS, Hummelen JC (2001) Plastic solar cells. Adv Funct Mater 11:15–26
44. Malliaras GG, Salem JR, Brock PJ, Scott JC (1998) Photovoltaic measurement of the built-in potential in organic light emitting diodes and photodiodes. J Appl Phys 84:1583–1587

45. Markvart T, Castafier L (2005) Principles of solar cell operation. In: Markvart T, Castafier L (eds) Solar cells: materials, manufacture and operation. Elsevier, Amsterdam
46. Meissner D, Ronstalski J (2001) Photovoltaics of interconnected networks. Synth Met 121:1551–1552
47. Gregg BA, Hanna MC (2003) Comparing organic to inorganic photovoltaic cells: theory, experiment, and simulation. J Appl Phys 93:3605–3614
48. Hoppe H, Glatzel T, Niggemann M, Schwinger W, Schaeffler F, Hinsch A, Lux-Steiner MC, Sariciftci NS (2006) Efficiency limiting morphological factors of MDMO-PPV:PCBM plastic solar cells. Thin Solid Films 511:587–592
49. Hoppe H, Niggemann M, Winder C, Kraut J, Hiesgen R, Hinsch A, Meissner D, Sariciftci NS (2004) Nanoscale morphology of conjugated polymer/fullerene-based bulk-heterojunction solar cells. Adv Funct Mater 14:1005–1011
50. Rispens MT, Meetsma A, Rittberger R, Brabec CJ, Sariciftci NS, Hummelen JC (2003) Influence of the solvent on the crystal structure of PCBM and the efficiency of MDMO-PPV:PCBM "plastic" solar cells. Chem Commun 17:2116–2118
51. Gebeyehu D, Brabec CJ, Padinger F, Fromherz T, Hummelen JC, Badt D, Schindler H, Sariciftci NS (2001) The interplay of efficiency and morphology in photovoltaic devices based on interpenetrating networks of conjugated polymers with fullerenes. Synth Met 118:1–9
52. Yang X, Alexeev A, Michels MAJ, Loos J (2005) Effect of spatial confinement on the morphology evolution of thin poly(p-phenylenevinylene)/methanofullerene composite films. Macromolecules 38:4289–4295
53. Choulis SA, Nelson J, Kim Y, Poplavskyy D, Kreouzis T, Durrant JR, Bradley D (2003) Investigation of transport properties in polymer/fullerene blends using time-of-flight photocurrent measurements. Appl Phys Lett 83:3812–3814
54. Snaith HJ, Arias AC, Morteani AC, Silva C, Friend RH (2002) Charge generation kinetics and transport mechanisms in blended polyfluorene photovoltaic devices. Nano Lett 2:1353–1357
55. Brabec CJ, Cravino A, Meissner D, Saricftci NS, Fromherz T, Rispens MT, Sanchez L, Hummelen JC (2001) Origin of the open circuit voltage of plastic solar cells. Adv Funct Mater 11:374–380
56. Brabec CJ (2004) Organic photovoltaics: technology and market. Sol Energy Mater Sol Cells 83:273–292
57. Brabec CJ, Cravino A, Meissner D, Sariciftci NS, Rispens MT, Sanchez L, Hummelen JC, Fromherz T (2002) The influence of materials work function on the open circuit voltage of plastic solar cells. Thin Solid Films 403:368–372
58. Sharber MC, Mühlbacher D, Koppe M, Denk P, Waldauf C, Heeger AJ, Brabec CJ (2006) Design rules for donors in bulk-heterojunction solar cells—towards 10 % energy-conversion efficiency. Adv Mater 18:789–794
59. Gadisa A, Svensson M, Andersson M, Inganäs O (2004) Correlation between oxidation potential and open-circuit voltage of composite solar cells based on blends of polythiophenes/fullerene derivative. Appl Phys Lett 84:1609–1611
60. Yamanari T, Taima T, Sakai J, Saito K (2009) Origin of the open-circuit voltage of organic thin-film solar cells based on conjugated polymers. Sol Energy Mater Sol Cells 93:759–761
61. Liu J, Shi Y, Yang Y (2001) Solvation-induced morphology effects on the performance of polymer-based photovoltaic devices. Adv Funct Mater 11:420–424
62. Mihailetchi VD, Blom PWM, Hummelen JC, Rispens MT (2003) Cathode dependence of the open-circuit voltage of polymer:fullerene bulk heterojunction solar cells. J Appl Phys 94:6849–6854
63. Ramsdale CM, Barker JA, Arias AC, MacKenzie JD, Friend RH (2002) The origin of the open-circuit voltage in polyfluorene-based photovoltaic devices. J Appl Phys 92:4266–4270
64. Eo YS, Rhee HW, Chin BD, Yu J-W (2009) Influence of metal cathode for organic photovoltaic device performance. Synth Met 159:1910–1913

65. Alem S, Gao J, Wantz G (2009) Photovoltaic response of symmetric sandwich polymer cells with identical electrodes. J Appl Phys 106:044505-1–044505-5
66. Frohne H, Shaheen S, Brabec CJ, Müeller D, Sariciftci NS, Meerholz K (2002) Influence of the anodic work function on the performance of organic solar cells. Chem Phys Chem 3:795–799
67. Shaheen SE, Brabec CJ, Saricftci NS, Padinger F, Fromherz T, Hummelen JC (2001) 2.5% efficient organic plastic solar cells. Appl Phys Lett 78:841–843
68. Alem S, de Bettignies R, Nunzi J-M, Cariou M (2004) Efficient polymer-based interpenetrated network photovoltaic cells. Appl Phys Lett 84:2178–2180
69. Schilinsky P, Waldauf C, Brabec CJ (2002) Recombination and loss analysis in polythiophene based bulk heterojunction photodetectors. Appl Phys Lett 81:3885–3887
70. Padinger F, Rittberger R, Sariciftci NS (2003) Effects of postproduction treatment on plastic solar cells. Adv Funct Mater 13:85–88
71. Dennler G, Mozer AJ, Juska G, Pivrikas A, Osterbacka R, Fucnsbauer A, Sariciftci NS (2006) Charge carrier mobility and lifetime versus composition of conjugated polymer/fullerene bulkheterojunction solar cells. Org Electron 7:229–234
72. Kline RJ, Mcgehee MD, Kadnikova EN, Liu J, Fréchet JM (2003) Controlling the field-effect mobility of regioregular polythiophene by changing the molecular weight. Adv Mater 15:1519–1522
73. Hoppe H, Sariciftci NS (2004) Organic solar cells: an overview. J Mater Res 19:1924–1945
74. Li G, Shrotriya V, Huang J, Yao Y, Moriarty T, Emery K, Yang Y (2005) High-efficiency solution processable polymer photovoltaic cells by self-organization of polymer blends. Nat Mater 4:864–868
75. Yang X, Loos J, Veenstra SC, Verhees WJH, Wienk MM, Kroon JM, Michaels MAJ, Janssen RAJ (2005) Nanoscale morphology of high-performance polymer solar cells. Nano Lett 5:579–583
76. Erb T, Zhokkavets U, Gobsch G, Raleva S, Stühn B, Schilinsky P, Waldauf C, Brabec CJ (2005) Correlation between structural and optical properties of composite polymer/fullerene films for organic solar cells. Adv Funct Mater 15:1193–1196
77. Zhokhavets U, Erb T, Hoppe H, Gobsch G, Sariciftci NS (2006) Effect of annealing of poly(3-hexylthiophene)/fullerene bulk heterojunction composites on structural and optical properties. Thin Solid Films 496:679–682
78. Reyes-Reyes M, Kim K, Dewald J, López-Sandoval R, Avadhanula A, Curran S, Carroll DL (2005) Meso-structure formation for enhanced organic photovoltaic cells. Org Lett 7:5749–5752
79. Ma W, Yang C, Gong X, Lee K, Heeger AJ (2005) Thermally stable, efficient polymer solar cells with nanoscale control of interpenetrating network morphology. Adv Funct Mater 15:1617–1622
80. Li G, Shrotriya V, Yao Y, Yang Y (2005) Investigation of annealing effects and film thickness dependence of polymer solar cells based on poly(3-hexylthiophene). J Appl Phys 98:043704-1–043704-5
81. Clarke TM, Ballantyne AM, Nelson J, Bradley DDC, Durrant JR (2008) Free energy control of charge photogeneration in polythiophene/fullerene solar cells: the influence of thermal annealing on P3HT/PCBM blends. Adv Funct Mater 18:4029–4035
82. Moon JS, Takacs CJ, Cho S, Coffin RC, Kim H, Bazan GC, Heeger AJ (2010) Effect of processing additive on the nanomorphology of a bulk heterojunction material. Nano Lett 10:4005–4008
83. Privikas A, Stadler P, Neugebauer H, Sariciftci NS (2008) Substituting the postproduction treatment for bulk-heterojunction solar cells using chemical additives. Org Electron 9:775–782
84. Peet J, Heeger AJ, Bazan GC (2009) "Plastic" solar cells: self-assembly of bulk heterojunction nanomaterials by spontaneous phase separation. Acc Chem Res 42:1700–1708
85. Ameri T, Dennler G, Lungenschmied C, Brabec CJ (2009) Organic tandem solar cells: a review. Energy Environ Sci 2:347–363

86. Helgesen M, Sondergaard R, Krebs FC (2010) Advanced materials and processes for polymer solar cell devices. J Mater Chem 20:36–60
87. Kim JY, Lee K, Coates NE, Moses D, Nguyen TQ, Dante M, Heeger AJ (2007) Efficient tandem polymer solar cells fabricated by all-solution processing. Science 317:222–225
88. Wong WY, Wang XZ, He Z, Djurišić AB, Yip CT, Cheung KY, Wang H, Mak CSK, Chan WK (2007) On the efficiency of polymer solar cells. Nat Mater 6:704–705
89. Nozik AJ (2010) Nanoscience and nanostructures for photovoltaics and solar fuels. Nano Lett 10:2735–2741
90. Nozik AJ (2008) Multiple exciton generation in semiconductor quantum dots. Chem Phys Lett 457:3–11
91. Nozik AJ (2002) Quantum dot solar cells. Physica E 14:115–120
92. Nozik AJ, Beard MC, Luther JM, Law M, Ellingson RJ, Johnson JC (2010) Semiconductor quantum dots and quantum dot arrays and applications of multiple exciton generation to third-generation photovoltaic solar cells. Chem Rev 110:6873–6890
93. Rabani E, Baer R (2010) Theory of multiexciton generation in semiconductor nanocrystals. Chem Phys Lett 496:227–235
94. Beard MC, Midgett AG, Hanna MC, Luther JM, Hughes BK, Nozik AJ (2010) Comparing multiple exciton generation in quantum dots to impact ionization in bulk semiconductors: implications for enhancement of solar energy conversion. Nano Lett 10:3019–3027
95. Kang MS, Sahu A, Norris DJ, Frisbie D (2010) Size-dependent electrical transport in CdSe nanocrystal thin films. Nano Lett 10:3727–3732
96. Arici E, Sariciftci NS, Meissner D (2003) Hybrid solar cells based on nanoparticles of CuInS2 in organic matrices. Adv Funct Mater 13:165–171
97. Arici E, Hoppe H, Schaffler F, Meissner D, Malik MA, Sariciftci NS (2004) Morphology effects in nanocrystalline $CuInSe_2$-conjugated polymer hybrid systems. Appl Phys A Mater Sci Process 79:59–64
98. Arici E, Hoppe H, Schaffler F, Meissner D, Malik MA, Sariciftci NS (2004) Hybrid solar cells based on inorganic nanoclusters and conjugated polymers. Thin Solid Films 451:612–618
99. Günes S, Fritz KP, Neugebauer H, Sariciftci NS, Kumar S, Scholes GD (2007) Hybrid solar cells using PbS nanoparticles. Sol Energy Mater Sol Cells 91:420–423
100. Watt AAR, Blake D, Warner J, Thomsen EA, Tavenner EL, Rubinsztein-Dunlop H, Meredith P (2005) Lead sulfide nanocrystal: conducting polymer solar cells. J Phys D Appl Phys 38:2006–2012
101. Cui DH, Xu J, Zhu T, Paradee G, Ashok S, Gerhold M (2006) Harvest of near infrared light in PbSe nanocrystal-polymer hybrid photovoltaic cells. Appl Phys Lett 88:183111-1–183111-3
102. Noone KM, Strein E, Anderson NC, Wu P-T, Jenekhe SA, Ginger DS (2010) Broadband absorbing bulk heterojunction photovoltaics using low-bandgap solution-processed quantum dots. Nano Lett 10:2635–2639
103. Du Pasquier A, Mastrogiovanni DDT, Klein LA, Wang T, Garfunkel E (2007) Photoinduced charge transfer between poly(3-hexylthiophene) and germanium nanowires. Appl Phys Lett 91:183501-1–183501-3
104. Novotny CJ, Yu ET, Yu PKL (2008) InP nanowire/polymer hybrid photodiode. Nano Lett 8:775–779
105. Liu C-Y, Holman ZC, Kortshagen UR (2009) Hybrid solar cells from P3HT and silicon nanocrystals. Nano Lett 9:449–452
106. Huynh WU, Dittmer JJ, Alivisatos AP (2002) Hybrid nanorod-polymer solar cells. Science 295:2425–2427
107. Huynh WU, Dittmer JJ, Libby WC, Whiting GL, Alivisatos AP (2003) Controlling the morphology of nanocrystal-polymer composites for solar cells. Adv Funct Mater 13:73–79
108. Sun BQ, Greenham NC (2006) Improved effciency of photovoltaics based on CdSe nanorods and poly(3-hexylthiophene) nanofibers. Phys Chem Chem Phys 8:3557–3560
109. Zhou Y, Li YC, Zhong HZ, Hou JH, Ding YQ, Yang CH, Li YF (2006) Hybrid nanocrystal/polymer solar cells based on tetrapod-shaped $CdSe_xTe_{1-x}$ nanocrystals. Nanotechnology 17:4041–4047

110. Sun BQ, Marx E, Greenham NC (2003) Photovoltaic devices using blends of branched CdSe nanoparticles and conjugated polymers. Nano Lett 3:961–963
111. Gur I, Fromer NA, Chen C-P, Kanaras AG, Alivisatos AP (2007) Hybrid solar cells with prescribed nanoscale morphologies based on hyperbranched semiconductor nanocrystals. Nano Lett 7:409–414
112. Sun BQ, Snaith HJ, Dhoot AS, Westenhoff S, Greenham NC (2005) Vertically segregated hybrid blends for photovoltaic devices with improved efficiency. J Appl Phys 97:014914-1–014914-6
113. Dayal S, Kopidakis N, Olson DC, Ginley DS, Rumbles G (2010) Photovoltaic devices with a low band gap polymer and CdSe nanostructures exceeding 3% efficiency. Nano Lett 10:239–242
114. Choi S-H, Song HJ, Park IK, Yum J-H, Kim S-S, Lee SH, Sung Y-E (2006) Synthesis of size-controlled CdSe quantum dots and characterization of CdSe-conjugated polymer blends for hybrid solar cells. J Photochem Photobiol A 179:135–141
115. Tang A-W, Teng F, Jui H, Gao Y-H, Hou Y-B, Liang C-J, Wang Y-S (2007) Investigation on photoconductive properties of MEH-PPV/CdSe-nanocrystal nanocomposites. Mater Lett 61:2178–2181
116. Han LL, Qin DH, Jiang X, Liu YS, Wang L, Chen JW, Cao Y (2006) Synthesis of high quality zinc-blende CdSe nanocrystals and their application in hybrid solar cells. Nanotechnology 17:4736–4742
117. Zhou YF, Riehle FS, Yuan Y, Schleiermacher H-F, Niggemann M, Urban GA, Krüger M (2010) Improved efficiency of hybrid solar cells based on non-ligand-exchanged CdSe quantum dots and poly(3-hexylthiophene). Appl Phys Lett 96:013304-1–013304-3
118. Leventis HC, King SP, Sudlow A, Hill MS, Molloy KC, Haque SA (2010) Nanostructured hybrid polymer-inorganic solar cell active layers formed by controllable in situ growth of semiconducting sulfide networks. Nano Lett 10:1253–1258
119. Xi DJ, Zhang H, Furst S, Chen B, Pei Q (2008) Electrochemical synthesis and photovoltaic property of cadmium sulfide-polybithiophene interdigitated nanohybrid thin films. J Phys Chem C 112:19765–19769
120. Aldakov D, Jiu T, Zagorska M, de Bettignies R, Jouneau P-H, Pron A, Chandezon F (2010) Hybrid nanocomposites of CdSe nanocrystals distributed in complexing thiophene-based copolymers. Phys Chem Chem Phys 12:7497–7505
121. de Freitas JN, Pivrikas A, Nowacki BF, Akcelrud LC, Sariciftci NS, Nogueira AF (2010) Investigation of new PPV-type polymeric materials containing fluorene and thiophene units and their application in organic solar cells. Synth Met 160:1654–1661
122. de Freitas JN, Grova IR, Akcelrud LC, Arici E, Sariciftci NS, Nogueira AF (2010) The effects of CdSe incorporation into bulk heterojunction solar cells. J Mater Chem 20:4845–4853
123. Huynh WU, Dittmer JJ, Teclemariam N, Milliron DJ, Alivisatos AP, Barnham KWJ (2003) Charge transport in hybrid nanorod-polymer composite photovoltaic cells. Phys Rev B 67:115326-1–115326-12
124. Greenham NC, Peng XG, Alivisatos AP (1996) Charge separation and transport in conjugated-polymer/semiconductor-nanocrystal composites studied by photoluminescence quenching and photoconductivity. Phys Rev B 54:17628–17637
125. Ginger DS, Greenham NC (2000) Charge injection and transport in films of CdSe nanocrystals. J Appl Phys 87:1361–1368
126. Lin Y-Y, Chen C-W, Chang J, Lin TY, Liu IS, Su W-F (2006) Exciton dissociation and migration in enhanced order conjugated polymer/nanoparticle hybrid materials. Nanotechnology 17:1260–1263
127. Wang P, Abrusci A, Wong HMP, Svensson M, Andersson MR, Greenham NC (2006) Photoinduced charge transfer and efficient solar energy conversion in a blend of a red polyfluorene copolymer with CdSe nanoparticles. Nano Lett 6:1789–1793
128. Ginger DS, Greenham NC (1999) Charge separation in conjugated-polymer/nanocrystal blends. Synth Met 101:425–428
129. Ginger DS, Greenham NC (1999) Photoinduced electron transfer from conjugated polymers to CdSe nanocrystals. Phys Rev B 59:10622–10629

130. Kucur E, Riegler J, Urban G, Nann T (2004) Charge transfer efficiency in hybrid bulk heterojunction composites. J Chem Phys 121:1074–1079
131. Liu JS, Tanaka T, Sivula K, Alivisatos AP, Fréchet JMJ (2004) Employing end-functional polythiophene to control the morphology of nanocrystal-polymer composites in hybrid solar cells. J Am Chem Soc 126:6550–6551
132. Baker DR, Kamat PV (2010) Tuning the emission of CdSe quantum dots by controlled trap enhancement. Langmuir 13:11272–11276
133. Talforn E, Moysidou E, Abellon RD, Savenije TJ, Goossens A, Houtepen AJ, Siebbeles LDA (2010) Highly photoconductive CdSe quantum-dot films: influence of capping molecules and film preparation procedure. J Phys Chem C 114:3441–3447
134. Lokteva I, Radychev N, Witt F, Borchert H, Parisi J, Kolny-Olesiak J (2010) Surface treatment of CdSe nanoparticles for application in hybrid solar cells: the effect of multiple ligand exchange with pyridine. J Phys Chem C 114:12784–12791
135. Querner C, Reiss P, Bleuse J, Pron A (2004) Chelating ligands for nanocrystals' surface functionalization. J Am Chem Soc 126:11574–11582
136. Milliron DJ, Gur L, Alivisatos AP (2005) Hybrid organic: nanocrystal solar cells. MRS Bull 30:41–44
137. Advincula RC (2006) Hybrid organic-inorganic nanomaterials based on polythiophene dendronized nanoparticles. Dalton Trans 23:2778–2784
138. Sih BC, Wolf M (2007) CdSe nanorods functionalized with thiol-anchored oligothiophenes. J Phys Chem C 111:17184–17192
139. Aldakov D, Querner C, Kervella Y, Jousselme B, Demadrille R, Rossitto E, Reiss P, Pron A (2008) Oligothiophene-functionalized CdSe nanocrystals: preparation and electrochemical properties. Microchim Acta 160:335–344
140. Skaff H, Sill K, Emrick T (2004) Quantum dots tailored with poly(para-phenylene vinylene). J Am Chem Soc 126:11322–11352
141. Odoi MY, Hammer NI, Sill K, Emrick T, Barnes MD (2006) Observation of enhanced energy transfer in individual quantum dot-oligophenylene vinylene nanostructures. J Am Chem Soc 128:3506–3507
142. Pokrop R, Pamula K, Deja-Drogomirecka S, Zagorska M, Reiss P, Louarn G, Chandezon F, Pron A (2010) Molecular hybrids of CdSe semiconductor nanocrystals with terthiophene carboxylic acid or its polymeric analogue. Mater Chem Phys 123:756–760
143. Shallcross RC, D'Ambruoso GD, Pyun J, Armstrong NR (2010) Photoelectrochemical processes in polymer-tethered CdSe nanocrystals. J Am Chem Soc 132:2622–2632
144. Zhang QL, Russel TP, Emrick T (2007) Synthesis and characterization of CdSe nanorods functionalized with regioregular poly(3-hexylthiophene). Chem Mater 19:3712–3716
145. Xu J, Wang J, Mitchell M, Mukherjee P, Jeffries-EL M, Petrich JW, Lin Z (2007) Organic-inorganic nanocomposites via directly grafting conjugated polymers onto quantum dots. J Am Chem Soc 129:12828–12833
146. Wang T-L, Yang C-H, Shieh Y-T, Yeh A-C, Juan L-W, Zeng HC (2010) Synthesis of new nanocrystal-polymer nanocomposite as the electron acceptor in polymer bulk jeterojunction solar cells. Eur Polym J 46:634–642
147. Kovalenko MV, Bodnarchuk MI, Zaumseil J, Lee J-S, Talapin DV (2010) Expanding the chemical versatility of colloidal nanocrystals capped with molecular metal chalcogenide ligands. J Am Chem Soc 132:10085–10092
148. Robel J, Kuno M, Kamat PV (2007) Size-dependent electron injection from excited CdSe quantum dots into TiO_2 nanoparticles. J Am Chem Soc 129:4136–4137
149. Kongkanand A, Tvrdy K, Takechi K, Kuno M, Kamat PV (2008) Quantum dot solar cells. Tuning photoresponse through size and shape control of CdSe-TiO_2 architecture. J Am Chem Soc 130:4007–4015
150. Kamat PV (2008) Quantum dot solar cells. Semiconductor nanocrystals as light harvesters. J Phys Chem C 112:18737–18753
151. Baker DR, Kamat PV (2009) Photosensitization of TiO_2 nanostructures with CdS quantum dots: particulate versus tubular support architectures. Adv Funct Mater 19:805–811

152. Bang JH, Kamat PV (2010) Solar cells by design: photoelectrochemistry of TiO_2 nanorod arrays decorated with CdSe. Adv Funct Mater 20:1970–1976
153. Sambur JB, Riha SC, Choi D, Parkinson BA (2010) Influence of surface chemistry on the binding and electronic coupling of CdSe quantum dots to single crystal TiO_2 surfaces. Langmuir 26:4839–4847
154. Shin K, il Seok S, Im SH, Park JH (2010) CdS or CdSe decorated TiO_2 nanotube arrays from spray pyrolysis deposition: use in photoelectrochemical cells. Chem Commun 46:2385–2387
155. Mora-Seró I, Likodimos V, Gimenez S, Martínez-Ferrero E, Albero J, Palomares E, Kontos AG, Falaras P, Bisquert J (2010) Fast regeneration of CdSe quantum dots by Ru dye in sensitized TiO_2 electrodes. J Phys Chem C 114:6755–6761
156. Shalom M, Albero J, Tachan Z, Martinez-Ferrero E, Zaban A, Palomares E (2010) Quantum dot-bilayer-sensitized solar cells: breakng the limits imposed by the low absorbance of dye monolayers. J Phys Chem Lett 1:1134–1138
157. Luo L, Lv G, Li B, Hu X, Jin L, Wang J, Tang Y (2010) Formation of aligned ZnO nanotube arrays by chemical etching and coupling with CdSe for photovoltaic application. Thin Solid Films 518:5146–5152
158. Timp BA, Zhu X-Y (2010) Electronic energy alignment at the PbSe quantum dots/ZnO (1010) interface. Surf Sci 604:1335–1341
159. Huang J, Huang Z, Yang Y, Zhu H, Lian T (2010) Multiple exciton dissociation in CdSe quantum dots by ultrafast electron transfer to adsorbed methylene blue. J Am Chem Soc 132:4858–4864
160. Guchhait A, Rath AK, Pal AJ (2009) Hybrid core-shell nanoparticles: photoinduced electron-transfer for charge separation and solar cell applications. Chem Mater 21:5292–5299
161. Narayanan SS, Sinhá SS, Verma PK, Pal SK (2008) Ultrafast energy transfer from 3-mercaptopropionic acid capped CdSe/ZnS QDs to dye-labelled DNA. Chem Phys Lett 463:160–165
162. Li T-L, Teng H (2010) Solution synthesis of high-quality $CuInS_2$ quantum dots as sensitizers for TiO_2 photoelectrodes. J Mater Chem 20:3656–3664
163. Tubtimtae A, Wu K-L, Tung H-Y, Lee M-W, Wang GJ (2010) Ag_2S quantum dot-sensitized solar cells. Electrochem Commun 12:1158–1160
164. Chang JA, Rhee JH, Im SH, Lee YH, Kim H, Seok SI, Nazeeruddin MK, Grätzel M (2010) High-performance nanostructured inorganic-organic heterojunction solar cells. Nano Lett 10:2609–2612
165. Gao X-F, Sun W-T, Ai G, Peng L-M (2004) Photoelectric performance of TiO_2 nanotube array photoelectrodes cosensitized with CdS/CdSe quantum dots. Appl Phys Lett 96:153104-1–153104-3
166. Huang S, Zhang Q, Huang X, Guo X, Deng M, Li D, Luo Y, Shen Q, Toyoda T, Meng Q (2010) Fibrous CdS/CdSe quantum dot co-sensitized solar cells based on ordered TiO_2 nanotube arrays. Nanotechnology 21:375201-1–375201-7
167. Talgorn E, Abellon RD, Kooyman PJ, Piris J, Savenije TJ, Goossens A, Houtepen AJ, Siebbeles LDA (2010) Supercrystals of CdSe quantum dots with high charge mobility and efficient electron transfer to TiO_2. ACS Nano 4:1723–1731
168. Kniprath R, Rabe JP, McLeskey JT Jr, Wang D, Kirstein S (2009) Hybrid photovoltaic cells with II-VI quantum dot sensitizers fabricated by layer-by-layer deposition of water-soluble components. Thin Solid Films 518:295–298
169. Hamada M, Nakanishi S, Itoh T, Ishikawa M, Biju V (2010) Blinking suppression in CdSe/ZnS single quantum dots by TiO_2 nanoparticles. ACS Nano 4:4445–4454
170. Liu Z, Miyauchi M, Uemura Y, Cui Y, Hara K, Zhao Z, Sunahara K, Furube A (2010) Enhancing the performance of quantum dots sensitized solar cell by SiO_2 surface coating. Appl Phys Lett 96:233107-1–233107-3
171. Deepa M, Gakhar R, Joshi AG, Singh BP, Srivastava AK (2010) Enhanced photoelectrochemistry and interactions in cadmium selenide-functionalized multiwalled carbon nanotube composite films. Electrochim Acta 55:6731–6742

172. Zhang L, Jia Y, Wang S, Li Z, Ji C, Wei J, Zhu H, Wang K, Wu D, Shi W, Fang Y, Cao A (2010) Carbon nanotube and CdSe nanobelt Schottky junction solar cells. Nano Lett 10:3583–3589
173. Schulz-Drost C, Sgobba V, Gerhardsm C, Leubner S, Calderon RMK, Ruland A, Guldi DM (2010) Innovative inorganic-organic nanohybrid materials: coupling quantum dots to carbon nanotubes. Angew Chem Int Ed 49:6425–6429
174. Chen Z, Berciaud S, Nukolls C, Heinz TF, Brus LE (2010) Energy transfer from individual semiconductor nanocrystals to graphene. ACS Nano 4:2964–2968
175. Biebersdorf A, Dietmuller R, Susha AS, Rogach AL, Poznyak SK, Talapin DV, Weller H, Klar TA, Feldmann J (2006) Semiconductor nanocrystals photosensitize C-60 crystals. Nano Lett 6:1559–1563
176. Chen H-Y, Lo MKF, Yang G, Monbouquette HG, Yang Y (2008) Nanoparticle-assisted high photoconductive gain in composites of polymer and fullerene. Nat Nanotechnol 3:543–547
177. de Freitas JN, Nogueira AF (2010) Hybrid nanostructured solar cells based on the incorporation of inorganic nanoparticles in polymer-fullerene mixtures. In: Tsakalakos L (ed) Proceedings of SPIE, vol 7772. The International Society for Optical Engineering, San Diego, p 77721K. doi:10.1117/12.862510
178. Xue B, Vaughan B, Poh C-H, Burke KB, Thomsen L, Stapleton A, Zhou X, Bryant GW, Belcher W, Dastoor PC (2010) Vertical stratification and interfacial structure in P3HT:PCBM organic solar cells. J Phys Chem C 114:15797–15805
179. Huang Y-C, Liao Y-C, Li S-S, Wu M-C, Chen C-W, Su W-F (2009) Study of the effect of annealing process on the performance of P3HT/PCBM photovoltaic devices using scanning-probe microscopy. Sol Energy Mater Sol Cells 93:888–892
180. Dante M, Peet J, Nguyen T-Q (2008) Nanoscale charge transport and internal structure of bulk heterojunction conjugated polymer/fullerene solar cells by scanning probe microscopy. J Phys Chem C 112:7241–7249
181. Zhao Y, Xie Z, Qu Y, Geng Y, Wang L (2007) Solvent-vapor treatment induced performance enhancement of poly(3-hexylthiophene):methanofullerene bulk heterojunction photovoltaic cells. Appl Phys Lett 90:043504-1–043504-3
182. Watts B, Belcher WJ, Thomsen L, Ade H, Dastoor PC (2009) A quantitative study of PCBM diffusion during annealing of P3HT:PCBM blend films. Macromolecules 42:8392–8397
183. Alves JPD, de Freitas JN, Almeida LCP, Atvars TDZ, Nogueira AF (2011) Photophysical and photovoltaic properties of a polymer-fullerene system with CdSe nanoparticles (Submitted for publication)
184. http://www.britishmuseum.org/explore/highlights/highlight_objects/pe_mla/t/the_lycurgus_cup.aspx. Accessed 10 Jan 2011
185. Henglein A (1993) Physical properties of small metal particles in solution—microelectrode reactions, chemisorption, composite metal particles, and the atom-to-metal transition. J Phys Chem 97:5457–5471
186. Kreibig U, Vollmer M (1996) Optical properties of metal clusters. Springer, Berlin
187. Kelly KL, Coronado E, Zhao LL, Schatz GC (2003) The optical properties of metal nanoparticles: the influence of size, shape, and dielectric environment. J Phys Chem B 107:668–677
188. Mulvaney P (1996) Surface plasmon spectroscopy of nanosized metal particles. Langmuir 12:788–800
189. Underwood S, Mulvaney P (1994) Effect of the solution refractive-index on the color of gold colloids. Langmuir 10:3427–3430
190. Ung T, Liz-Marzan LM, Mulvaney P (2001) Optical properties of thin films of Au@SiO2 particles. J Phys Chem B 105:3441–3452
191. Link S, El-Sayed MA (1999) Spectral properties and relaxation dynamics of surface plasmon electronic oscillations in gold and silver nanodots and nanorods. J Phys Chem B 103:8410–8426

192. Alvarez MM, Khoury JT, Schaaff TG, Shafigullin MN, Vezmar I, Whetten RL (1997) Optical absorption spectra of nanocrystal gold molecules. J Phys Chem B 101:3706–3712
193. Kreibig U, Genzel L (1985) Optical-absorption of small metallic particles. Surf Sci 156:678–700
194. Schaadt DM, Feng B, Yu ET (2005) Enhanced semiconductor optical absorption via surface plasmon excitation in metal nanoparticles. Appl Phys Lett 86:063106-1–063106-3
195. Catchpole KR, Polman A (2008) Plasmonic solar cells. Opt Express 16:21739–21800
196. Akimov YA, Koh WS (2010) Resonant and nonresonant plasmonic nanoparticle enhancement for thin-film silicon solar cells. Nanotechnology 21:235201-1–235201-6
197. Pillai S, Catchpole KR, Trupke T, Green MA (2007) Surface plasmon enhanced silicon solar cells. J Appl Phys 101:093105-1–093105-8
198. Hägglund C, Zäch M, Petersson G, Kasemo B (2008) Electromagnetic coupling of light into a silicon solar cell by nanodisk plasmons. Appl Phys Lett 92:053110-1–053110-3
199. Akimov YA, Koh WS, Ostrikov K (2009) Enhancement of optical absorption in thin-film solar cells through the excitation of higher-order nanoparticle plasmon modes. Opt Express 17:10195–10205
200. Temple TL, Mehanama GDK, Reehal HS, Bagnall DM (2009) Influence of localized surface plasmon excitation in silver nanoparticles on the performance of silicon solar cells. Sol Energy Mater Sol Cells 93:1978–1985
201. Akimov YA, Ostrikov K, Li EP (2009) Surface plasmon enhancement of optical absorption in thin-film silicon solar cells. Plasmonics 4:107–113
202. Ferry VE, Verschuuren MA, Li HBT, Verhagen E, Walters RJ, Schropp REI, Atwater HA, Polman A (2010) Light trapping in ultrathin plasmonic solar cells. Opt Express 18:A237–A245
203. Pala RA, White J, Barnard E, Liu J, Brongersma ML (2009) Design of plasmonic thin-film solar cells with broadband absorption enhancements. Adv Mater 21:3504–3509
204. Catchpole KR, Polman A (2008) Design principles for particle plasmon enhanced solar cells. Appl Phys Lett 93:191113-1–191113-3
205. Nakayama K, Tanabe K, Atwater HA (2008) Plasmonic nanoparticle enhanced light absorption in GaAs solar cells. Appl Phys Lett 93:121904-1–121904-3
206. Pryce IM, Koleske DD, Fischer AJ, Atwater HA (2010) Plasmonic nanoparticle enhanced photocurrent in GaN/InGaN/GaN quantum well solar cells. Appl Phys Lett 96:153501-1–153501-3
207. Hägglund C, Zach M, Kasemo B (2008) Enhanced charge carrier generation in dye sensitized solar cells by nanoparticle plasmons. Appl Phys Lett 92:013113-1–013113-3
208. Standridge SD, Schatz GC, Hupp JT (2009) Distance dependence of plasmon-enhanced photocurrent in dye-sensitized solar cells. J Am Chem Soc 131:8407–8409
209. Du L, Furube A, Yamamoto K, Hara K, Katoh R, Tachiya M (2009) Plasmon-induced charge separation and recombination dynamics in gold-TiO_2 nanoparticle systems: dependence on TiO_2 particle size. J Phys Chem C 113:6454–6462
210. Sudeep PK, Takechi K, Kamat PV (2007) Harvesting photons in the infrared. Electron injection from excited tricarbocyanine dye (IR-125) into TiO_2 and Ag@TiO_2 core-shell nanoparticles. J Phys Chem C 111:488–494
211. Kathiravan A, Kumar PS, Renganathan R, Anandan S (2009) Photoinduced electron transfer reactions between meso-tetrakis(4-sulfonatophenyl)porphyrin and colloidal metal-semiconductor nanoparticles. Colloids Surf A 333:175–181
212. Grätzel M (2003) Solar cells to dye for. Nature 421:586–587
213. McFarland EW, Tang J (2003) A photovoltaic device structure based on internal electron emission. Nature 421:616–618
214. Hussain AM, Neppolian B, Kim SH, Kim JY, Choi H-C, Lee K, Park S-J, Heeger AJ (2009) Improved performance of polymer light-emitting diodes with nanocomposites. Appl Phys Lett 94:073306-1–073306-3
215. Dhas V, Muduli S, Lee W, Han S-H, Ogale S (2008) Enhanced conversion efficiency in dye-sensitized solar cells based on ZnO bifunctional nanoflowers loaded with gold nanoparticles. Appl Phys Lett 93:243108-1–243108-3

216. Chen ZH, Tang YB, Liu CP, Leung YH, Yun GD, Chen LM, Wang YQ, Bello I, Zapien JA, Zhang WJ, Lee CS, Lee ST (2009) Vertically aligned ZnO nanorod arrays sensitized with gold nanoparticles for Schottky barrier photovoltaic cells. J Phys Chem C 113:13433–13437
217. Peh CKN, Ke L, Ho GW (2010) Modification of ZnO nanorods through Au nanoparticles surface coating for dye-sensitized solar cells applications. Mater Lett 64:1372–1375
218. Jakob M, Levanon H, Kamat PV (2003) Charge distribution between UV-irradiated TiO_2 and gold nanoparticles: determination of shift in the Fermi level. Nano Lett 3:353–358
219. Furube A, Du L, Hara K, Katoh R, Tachiya M (2007) Ultrafast plasmon-induced electron transfer from gold nanodots into TiO2 nanoparticles. J Am Chem Soc 129:14852–14853
220. Guduru S, Singh VP, Rajaputra S, Mishra S, Mangu R, St Omer I (2010) Characteristics of gold/cadmium sulfide nanowire Schottky diodes. Thin Solid Films 518:1809–1814
221. Haberer ED, Joo JH, Hodelin JF, Hu EL (2009) Enhanced photogenerated carrier collection in hybrid films of bio-templated gold nanowires and nanocrystalline CdSe. Nanotechnology 29:415206-1–415206-7
222. Yang T-T, Chen W-T, Hsu Y-J, Wei KH, Lin TY, Lin TW (2010) Interfacial charge carrier dynamics in core-shell Au-CdS nanocrystals. J Phys Chem C 114:11414–11420
223. Arakawa T, Munaoka T, Akiyama T, Yamada S (2009) Effects of silver nanoparticles on photoelectrochemical responses of organic dyes. J Phys Chem C 113:11830–11835
224. Nicholson PG, Ruiz V, Macpherson JV, Unwin PR (2005) Enhanced visible photoluminescence in ultrathin poly(3-hexylthiophene) films by incorporation of Au nanoparticles. Chem Commun 12:1052–1054
225. Park JH, Lim YT, Park OO, Kim JK, Yu J-W, Kim YC (2004) Polymer/gold nanoparticle nanocomposite light-emitting diodes: enhancement of electroluminescence stability and quantum efficiency of blue-light-emitting polymers. Chem Mater 16:688–692
226. Parfenov A, Gryczynski I, Malicka J, Geddes CD, Lakowicz JR (2003) Enhanced fluorescence from fluorophores on fractal silver surfaces. J Phys Chem B 107:8829–8833
227. Saranthy KV, Narayan KS, Kim J, White JO (2000) Novel fluorescence and morphological structures in gold nanoparticle-polyoctylthiophene based thin films. Chem Phys Lett 318:543–548
228. Chen XC, Green PF (2010) Control of morphology and its effects on the optical properties of polymer nanocomposites. Langmuir 26:3659–3665
229. Li F, Zhou Y, Zhang F, Liu X, Zhan Y, Fahlman M (2009) Tuning work function of noble metals as promising cathodes in organic electronic devices. Chem Mater 21:2798–2802
230. Nakamura M, Yang C, Tajima K, Hashimoto K (2009) High-performance polymer photovoltaic devices with inverted structure prepared by thermal lamination. Sol Energy Mater Sol Cells 93:1681–1684
231. Chen X, Zhao C, Rothberg L, Ng MK (2008) Plasmon enhancement of bulk heterojunction organic photovoltaic devices by electrode modification. Appl Phys Lett 93:123302-1–123302-3
232. Tjeng LH, Hesper R, Heessels ACL, Heers A, Jonkman HT, Sawatzky GA (1997) Development of the electronic structure in a K-doped C-60 monolayer on a Ag(111) surface. Solid State Commun 103:31–35
233. Hunt MRC, Modesti S, Rudolf P, Palmer RE (1995) Charge-transfer and structure in C_{60} adsorption on metal-sufaces. Phys Rev B 51:10039–10047
234. Chase SJ, Bacsa WS, Mitch MG, Pilione LJ, Lannin JS (1992) Surface-enhanced Raman-scattering and photoemission of C_{60} on noble-metal surfaces. Phys Rev B 46:7873–7877
235. Morioka R, Yasui K, Ozawa M, Odoi K, Ichikawa H, Fujita K (2010) Anode buffer layer containing Au nanoparticles for high stability organic solar cells. J Photopolym Sci Technol 23:313–316
236. Chen F-C, Wu J-L, Lee C-L, Hong Y, Kuo C-H, Huang MH (2009) Plasmonic-enhanced polymer photovoltaic devices incorporating solution-processable metal nanoparticles. Appl Phys Lett 95:013305-1–013305-3
237. Lee JH, Park JH, Kim JS, Lee DY, Cho K (2009) High efficiency polymer solar cells with wet deposited plasmonic gold nanodots. Org Electron 10:413–420

238. Kim S-S, Na S-I, Jo J, Kim D-Y, Nah Y-C (2008) Plasmon enhanced performance of organic solar cells using electrodeposited Ag nanoparticles. Appl Phys Lett 93:073307-1–073307-3
239. Morfa AJ, Rowlen KL, Reilly TH III, Romero MJ, van de Lagemaat J (2008) Plasmon-enhanced solar energy conversion in organic bulk heterojunction photovoltaics. Appl Phys Lett 92:013504-1–013504-3
240. Tvingstedt K, Persson N-K, Inganas O, Rahachou A, Zozoulenko IV (2007) Surface plasmon increase absorption in polymer photovoltaic cells. Appl Phys Lett 91:113514
241. Stenzel O, Stendal A, Voigtsberger K, von Borczykowski C (1995) Enhancement of the photovoltaic conversion efficiency of copper phthalocyanine thin-film devices by incorporation of metal-clusters. Sol Energy Mater Sol Cells 37:337–348
242. Mapel JK, Singh M, Baldo MA, Celebi K (2007) Plasmonic excitation of organic double heterostructure solar cells. Appl Phys Lett 90:121102-1–121102-3
243. Lindquist NC, Luhman WA, Oh S-W, Holmes RJ (2008) Plasmonic nanocavity arrays for enhanced efficiency in organic photovoltaic cells. Appl Phys Lett 93:123308-1–123308-3
244. Westphalen M, Kreibig U, Rostalski J, Luth H, Meissner D (2000) Metal cluster enhanced organic solar cells. Sol Energy Mater Sol Cells 61:97–105
245. Yakimov A, Forrest SR (2002) High photovoltage multiple-heterojunction organic solar cells incorporating interfacial metallic nanoculsters. Appl Phys Lett 80:1667–1669
246. Rand BP, Peumans P, Forrest SR (2004) Long-range absorption enhancement in organic tandem thin-film solar cells containing silver nanoclusters. J Appl Phys 96:7519–7526
247. Kim K, Carroll DL (2005) Roles of Au and Ag nanoparticles in efficiency enhancement of poly(3-octylthiophene)/C_{60} bulk heterojunction photovoltaic devices. Appl Phys Lett 87:203113-1–203113-3
248. Park M, Chin BD, Yu J-W, Chun M-S, Han S-H (2008) Enhanced photocurrent and efficiency of poly(3-hexylthiophene)/fullerene photovoltaic devices by the incorporation of gold nanoparticles. J Ind Eng Chem 14:382–386
249. Shen H, Bienstman P, Maes B (2009) Plasmonic absorption enhancement in organic solar cells with thin active layers. J Appl Phys 106:073109-1–073109-5
250. Duche D, Torchio P, Escoubas L, Monestier F, Simon J-J, Flory F, Mathian G (2009) Improving light absorption in organic solar cells by plasmonic contribution. Sol Energy Mater Sol Cells 93:1377–1382
251. Topp K, Borchert H, Johnen F, Tunc AV, Knipper M, von Hauff E, Parisi J, Al-Shamery K (2010) Impact of the incorporation of Au nanoparticles into polymer/fullerene solar cells. J Phys Chem A 114:3981–3989
252. Wang DH, Kim DY, Choi KW, Seo JH, Im SH, Park JH, Park OO, Heeger AJ (2011) Enhancement of donor–acceptor polymer bulk heterojunction solar cell power conversion efficiencies by addition of au nanoparticles. Angew Chem Int Ed 50:1–6
253. Conturbia GLC (2009) Células solares baseadas em nanotubos de carbono modificado e nanopartículas de ouro. Dissertation, Universidade Estadual de Campinas
254. Reyes-Reyes M, López-Sandoval R, Arenas-Alatorre J, Garibay-Alonso R, Carroll DL, Lastras-Martinez A (2007) Methanofullerene elongated nanostructure formation for enhanced organic solar cells. Thin Solid Films 516:52–57
255. Yang X, van Duren JKK, Rispens MT, Hummelen JC, Hanssen RAJ, Michels MAJ, Loos J (2004) Crystalline organization of a methanofullerene as used for plastic solar-cell applications. Adv Mater 16:802–806
256. Hugger S, Thomann R, Heinzel T, Thurn-Albrecht T (2004) Semicrystalline morphology in thin films of poly(3-hexylthiophene). Colloid Polym Sci 282:932–938

Nanomaterials for Solar Energy Conversion: Dye-Sensitized Solar Cells Based on Ruthenium (II) *Tris*-Heteroleptic Compounds or Natural Dyes

Juliana dos Santos de Souza, Leilane Oliveira Martins de Andrade and André Sarto Polo

Abstract The worldwide energy demand is growing and the development of sustainable power generation is a critical issue. Among several possibilities, dye-sensitized solar cells, DSSCs, have emerged as a promising device to meet the energy needs as an environmentally friendly alternative and investigation for academic and technological improvement of DSSCs are being carried out. One of the most important components of this device is the dye-sensitizer, since it is responsible for the sunlight harvesting and electron injection, the first steps of energy conversion. Herein, we review the developments on *tris*-heteroleptic ruthenium dye-sensitizers, which have been gaining much attention on the last years due to the possibility of modulating their photochemical and photophysical properties of the complex by using different ligands. Besides synthetic compounds, natural dyes have also been employed as semiconductor sensitizers for these devices and are also reviewed. These dyes can lower the device production costs since they can be promptly obtained from fruits or flowers in a very simple way. Among numerous classes of natural dyes, anthocyanins have been the most investigated ones and gained special attention in this work.

1 Aims and Scope

Dye-sensitized solar cells, DSSCs, gained much attention since it is a simple and cheap device capable of converting the sunlight into electricity through a regenerative photoelectrochemical process. DSSCs overall efficiency attained 11 % and it is estimated to last around 20 years. Besides the economic advantages, these

J. d. S. de Souza (✉) · L. O. M. de Andrade · A. S. Polo
Centro de Ciências Naturais e Humanas, Universidade Federal do ABC, Rua Santa Adélia 166, Santo André, SP 09210-170, Brazil
e-mail: andre.polo@ufabc.edu.br

F. L. de Souza and E. R. Leite (eds.), *Nanoenergy*,
DOI: 10.1007/978-3-642-31736-1_2,

devices can be transparent and allows their use for distinct architectonic purposes, such as facades of buildings. DSSCs are based on a nanocrystalline mesoporous semiconductor films sensitized by dyes, which are responsible for light harvesting and electron transfer, these processes, start the energy conversion and are directly responsible for its overall efficiency.

This chapter aims to review a specific class of synthetic dye, the *tris*-heteroleptic ruthenium sensitizers, which have been attracting much attention on the last years due to the possibility of tune their spectroscopic and electrochemical properties as well as to improve the stability of the device. The recent advances on the use of natural dyes as semiconductor sensitizers, from 2003 to 2010, are also reviewed.

2 Introduction

The use of fossil fuel based technologies is the major responsible for the continuous increase in the pollution and in the concentration of greenhouse gases. Renewable sources must have higher contribution on the energetic matrix in providing more energy available for the humanity in a short period, having low environmental impact [1, 2]. The interest on the conversion of environmentally friendly energy sources led to the development of several devices that took the advantage of the continuous evolution on several fields of research, which can result in new materials for already developed devices. For instance, the performance of direct methanol fuel cells, a well known technology [3, 4] was improved due to the development of nanomaterials especially designed for the energy conversion process [5, 6] and their evolution allows the use of light to boost the process through a synergic arrangement [7–10].

The use of sunlight has been gaining much attention due to its abundance. For instance, it is possible to supply human energy needs up to 2050 covering only 0.16 % of the earth surface with 10 % efficiency solar devices [1, 11]. There are several investigations on the conversion of sunlight in substances with more chemical energy than the reactants in a process that mimics the photosynthesis; this approach is known as artificial photosynthesis [12]. Most recently, the investigation on this research field is being called solar fuels and several papers were published describing photochemical approaches to produce high energy content substances, or fuels, from simple reactants such as water or CO_2 [13–19].

Great interest is dedicated to an especially attractive, the Dye-sensitized solar cells, DSSC, since they are capable of converting the sunlight into electricity based on photoelectrochemical principles. The materials employed for the construction of these new solar cells are common and cheap and the procedures do not require controlled environment, thus clean rooms or any other sophisticated control can be avoided, consequently a very low production cost is estimated (less than 1 € per Wp) [20]. The use of new nanomaterials allows interesting features of these devices, such as transparency, possibility to have distinct colors, among others. These characteristics are very interesting for new applications of solar cells, since

it can substitute glass windows and promote the co-generation of energy, or for any other architecture design.

Albeit the possible use of sensitization effect for solar energy conversion is known for a long time [21], the breakthrough of these solar cells was in 1991 when B. O'Reagan and M. Grätzel published the use of nanocrystalline and mesoporous TiO_2 film [22]. This film enhanced the light absorption due to its sponge-like characteristic which increases the surface area. The nanocrystallinity plays an important role on the electron injection and transport in these devices [23].

Since the paper of 1991, this field has been growing very fast and all the aspects of these solar cells are investigated [24–27]. In this review, the focus is on the development of *tris*-heteroleptic ruthenium (II) dyes as well as the use of natural extracts as a source of sensitizers. The absorption spectra and photoelectrochemical parameters published for these compounds since 2003 will be reviewed and discussed.

2.1 Dye-Sensitized Solar Cells: Principles and Operation

Dye-sensitized solar cells are prepared in a sandwich arrangement and are comprised by two electrodes, the photoanode and the counter-electrode, Fig. 1. The photoanode is a conducting glass covered by a mesoporous and nanocrystalline TiO_2 film, sensitized by the dye-sensitizers. The counter electrode is a conducting glass covered by a thin film of catalyst, such as platinum or graphite. Between these electrodes is placed a mediator layer, usually a solution of I_3^-/I^- in nitriles.

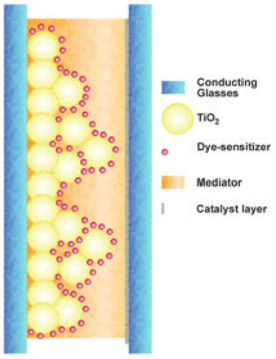

Fig. 1 Schematic arrangement of a dye-sensitized solar cell

In order to promote the energy conversion, the sunlight is harvested by the dye-sensitizers leading to an excited-state capable of inject an electron into the semiconductor conducting band. The oxidized dye is immediately regenerated by the mediator and the injected electron percolates through the semiconductor film, reaches the conducting glass and flows by the external circuit to the counter-electrode. The counter electrode is responsible for regenerating the oxidized specie of the mediator, reducing it by a catalyzed reaction using electrons from the

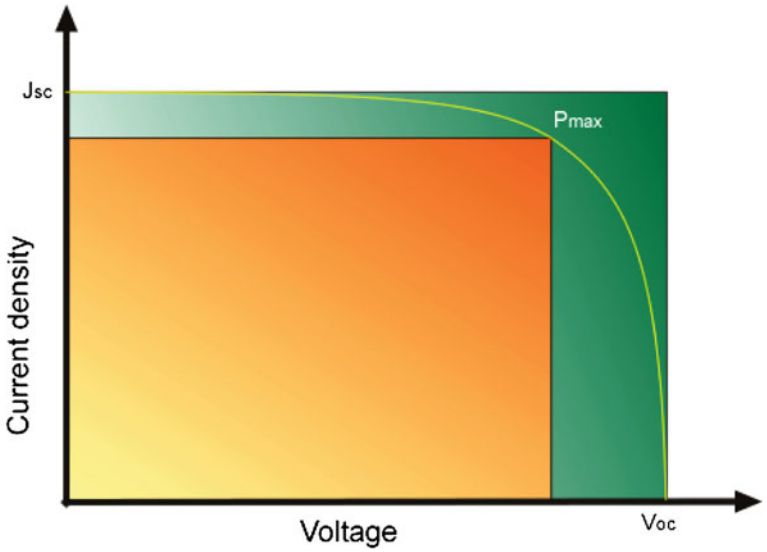

Fig. 2 Schematic current–voltage curve

external circuit. Since there is not a permanent chemical change for dye-sensitized solar cells, the estimated lifetime of these devices is 20 years [23].

2.2 Performance Experiments

Dye-sensitized solar cells are evaluated by several experimental approaches. For instance, the recombination processes or electron injection dynamics are investigated by time-resolved experiments [27–35], information about electron transport and electrical characteristics of TiO_2 film can be obtained by electrochemical impedance spectroscopy [36]. Among several experiments used in evaluation of DSSCs, two experiments play an important role for investigation of dye performance, the current–voltage curves and photocurrent action spectra. Due to their importance, they are detailed in the next sections.

2.2.1 Current–voltage (IxV) Curves

Current–voltage curves allow the access to one of the most important information about the prepared solar cells, the overall efficiency, η. Other important parameters such as the short circuit current density, J_{sc}, open-circuit potential, V_{oc}, and fill factor, ff, are also determined by this experiment. In most cases, IxV curves determined experimentally for dye-sensitized solar cells are similar to the schematic one, Fig. 2.

Short-circuit current density, J_{SC}, and open-circuit potential, V_{OC}, are the values determined by the intersection of IxV curve to the current density axis. The voltage at this axis is zero, the short-circuit condition, thus the current is named for this condition. Analogous idea is applied for the determination of open-circuit potential, since the current at voltage axis is zero, open circuit condition.

The maximum power output of a DSSC, P_{max}, is the highest value obtained for the multiplication of current density and voltage for each point of the IxV curve and can be graphically expressed as the area covered by the orange rectangle in of Fig. 2. On the other hand, the multiplication of V_{OC} by J_{SC} results in the maximum power output possible to be achieved for this DSSC and it can also be represented by the green rectangle of Fig. 2. The fill-factor, ff, is named for the amount of the green rectangle which is filled by the orange one and. Thus ff express the electrical losses of DSSCs. Mathematically, ff can be determined by the ratio of P_{max} and the multiplication of J_{SC} by V_{OC}, Eq. 1.

$$ff = \frac{P_{max}(mW \cdot cm^{-2})}{J_{sc}(mA.cm^{-2}) \cdot Voc(V)} \tag{1}$$

Under simulated solar irradiation condition (1 sun = P_{irr} = 100 mW cm^{-2}), the overall efficiency, η_{Cell}, can be determined by dividing P_{max} by the total incident light power, P_{irr}, Eq. 2, resulting in the percentage amount of solar light converted in electrical Output.

$$\eta\% = \frac{P_{max}}{P_{irr}} \cdot 100\ \% \tag{2}$$

2.2.2 Photocurrent Action Spectra

Photocurrent action spectra exhibit the photoelectrochemical behavior of solar cells as a function of wavelength. For each wavelength can be determined the incident photon-to-current conversion efficiency, IPCE, and the spectra are valuable to analyze the performance of new dyes prepared. IPCE values can be determined by a relationship that considers the energy and intensity of the incident light, the J_{SC} and Planck's constant, Eq. 3.

$$IPCE(\lambda) = \frac{J_{sc}}{P_{irr} \cdot e} \cdot \frac{hc}{\lambda} \tag{3}$$

J_{sc} Short-circuit photocurrent density (A m^{-2});
h Planck's constant (J s);
c Speed of light (m s^{-1});
λ Irradiation wavelength (nm);
P_{irr} Power of the incident light (W m^{-2});
e Elementary charge (C).
For practical purposes, this equation can be simplified to Eq. 4.

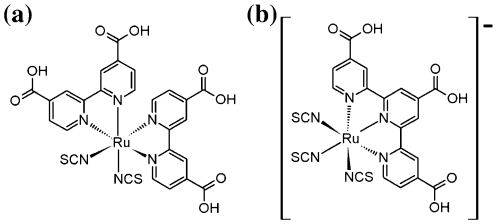

Fig. 3 Structures of the N3 (**a**) and black-dye (**b**) sensitizers

$$IPCE\ \%\ (\lambda) = \left(1239.8 \cdot \frac{J_{sc}(mA \cdot cm^{-2})}{P_{irr}(mW \cdot cm^{-2})\lambda(nm)}\right) \cdot 100\ \% \tag{4}$$

IPCE values are also related to some important parameters for DSSCs, such as light harvesting efficiency, LHE, electron injection quantum efficiency, Φ_{EI}, and the efficiency of collecting electrons in the external circuit, η_{EC}, Eq. 5 [37]. The simple measurements, such as J_{SC} and P_{irr} allow the access to important information such as the electron injection quantum yield.

$$IPCE(\lambda) = LHE\Phi_{E1}\eta_{EC} \tag{5}$$

Photocurrent action spectra are valuable experiments to evaluate new dye-sensitizers since it is possible to directly associate the absorption response of the dye with the conversion efficiency. This is valuable information for design new sensitizers.

2.3 Molecular Engineering

The design of new dye-sensitizers is based on joining in just one specie components capable of performing specific tasks. Using different ligands it is possible to have excellent light harvesting, electron injection on semiconductor conducting band and fast regeneration by the mediator. A new molecule to be employed in DSSCs should fulfill some basic requirements such as having an intense absorption on the visible region, which corresponds to 44 % of the incident sunlight on the earth's surface, having an anchoring group capable of promoting the chemical adsorption onto TiO_2 surface, improving the electronic coupling between dye and semiconductor interface.

The first DSSC that exhibited $\eta > 10$ % employed *cis*-di(isothiocyanato)bis-(2,2′-bipyridyl-4,4′-dicarboxylic acid)ruthenium(II), N3 as dye-sensitizer [38]. after this dye, the complex *mer*-tri(isothiocyanato)(2,2′,2′'-terpyridyl-4,4′,4′'-tricarboxylic acid)ruthenium(II), black-dye was prepared and also successfully used as sensitizer [39], Fig. 3.

Due to the outstanding performance of N3 and black-dye as dye-sensitizers, they can be used as models for molecular engineering of new dyes. Their chemical attachment onto TiO_2 surface through the carboxylic acid groups of the 2,2′-

bipyridine or of the 2,2′,2′’-terpyridine ligands. Particularly, the 4,4′-dicarboxylic acid-2,2′-bipyridine anchoring ligand is been widely employed among several other possible groups investigated and it has been considered the best one for ruthenium(II) sensitizers [40]. This ligand allows intimate electronic coupling between the dye excited state wavefunction and the semiconductor conducting band. Its lowest unoccupied orbital, LUMO, is the lowest one of the coordination compound and facilitates an efficient electronic transfer of excited dye molecules and Titania nanocrystals [41].

Great influence on the absorption spectra and molar absorptivities of compounds; emission maxima and quantum yields, as well as excited state lifetimes, in addition to the redox properties was observed as a function of the degree of protonation of the carboxylic acids of the ligand. These changes are directly responsible for the increase on photovoltaic performance of solar cells sensitized by N719, Fig. 4, which is the di-deprotonated N3 specie [42]. As a natural consequence, the use of compounds having one or more deprotonated carboxylic groups in the $dcbH_2$ has been increasing [32, 41, 43–48].

Fig. 4 Structure of N719

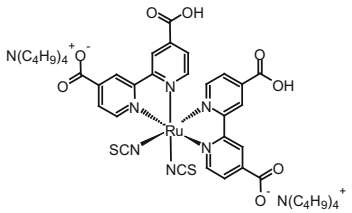

In the case of N3, consequently of N719, the presence of two $dcbH_2$ ligands results in absorption spectra which overlaps the visible region of the incident sunlight. The absorption bands have high molar absorptivity ($\varepsilon \sim 10^4$ L mol^{-1} cm^{-1}), typical of metal-to-ligand charge transfer transitions, $MLCT_{d\pi Ru\text{-}\pi^*dcbH2}$. The high molar absorptivity improves the light harvesting efficiency, allowing the absorption of almost all incidents light in a few micrometers of optical length of the TiO_2 film. Besides the bipyridine, the two isothiocyanate ligands in these complexes are valuable to promote the stabilization of the t_{2g} orbitals and result in a fine tuning of the energy levels of the complex.

3 Ruthenium *Tris*-Heteroleptic Complexes

The knowledge acquired understanding the structure of the N3 dye can be used for the development of several other complexes by using the molecular engineering [49]. Among several classes of compounds developed, ruthenium *tris*-heteroleptic complexes have been gaining attention on the last years due to the possibility to modulate their properties, just changing one of the polypyridinic ligand. This approach is very interesting for the development of new sensitizers.

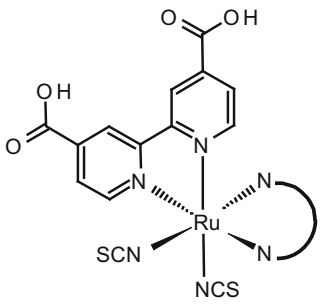

Fig. 5 General structure of cis-[Ru(dcbH$_2$)(L)(NCS)$_2$] dyes

There are several classes of ruthenium *tris*-heteroleptic compounds described by the general formula *cis*-[Ru(dcbH$_2$)(L)(NCS)$_2$], Fig. 5, since each new ligand L and its derivatives can be a new class. In this work, our focus will be on 2,2′-bipyridine derivatives and 1,10-phenanthroline derivatives, even that several other compounds of this general formula is known [34, 50–52].

3.1 2,2′-Bipyridine Derivative Ligands

The search for high-efficiency ruthenium(II) dyes focused on the development of complexes having high molar absorptivity, mainly in visible and near infra-red region [53, 54]. A good light harvesting yield and a reduction on the film thickness, which implies in reduction of transport losses in the nanoporous environment, resulting in higher open-circuit potentials and more efficient devices [55, 56]. Another approach is the development of dye-sensitizers capable of improving the lifetime performance of a dye-sensitized solar cell.

The first *tris*-heteroleptic ruthenium compounds investigated as dye sensitizers are based on 2,2′-bipyridine derivatives and it is possible to observe three different approaches, following the bipyridine substituent. These subclasses are the amphiphilic, donor-antenna and thiophene compounds.

3.1.1 Amphiphilic Compounds

In 2003, a thermally stable DSSC was disclosed employing the amphiphilic Z907 sensitizer. Using this dye was possible to prepare stable devices under prolonged thermal stress at 80°. However, the molar extinction coefficient of this sensitizer is somewhat lower than that of the standard N719 dye. Meanwhile, a compromise between efficiency and high temperature stability has been noted for the Z907 sensitizer [57]. Subsequently, the concept of developing a high molar extinction coefficient, amphiphilic ruthenium sensitizer, was followed by other groups, with a motivation to enhance device efficiency [34, 58–61]. The absorption properties as well as the performance parameters determined for

ruthenium *tris*-heteroleptic complexes having amphiphilic derivatives of 2,2′-bipyridine are listed in Table 1.

The absorption spectra of amphiphilic compounds usually exhibit two MLCT bands in the visible region, typical of ruthenium *bis*-bipyridyl compounds. Molar absorptivity values listed on Table 1 are similar to those determined for the complexes N3 or N719. This behavior is expected since the aliphatic substituents do not have significant influence in the chromophoric properties of the complexes.

Amphiphilic ruthenium *tris*-heteroleptic dye-sensitizers exhibit lower photoelectrochemical performance than determined for N3. The highest efficiency achieved by this class of dyes is 8.6 % [59]. The advantage of these compounds is their long-term stability. These amphiphilic heteroleptic sensitizers have the ground-state pKa of 4,4′-dicarboxy-2,2′-bipyridine higher than determined for N3, enhancing the chemical adsorption of the complex onto the TiO_2 surface [60, 62, 63]. The structure of amphiphilic ligands decreases the charge density on the sensitizer, resulting in less electrostatic repulsion and results in higher amount of dye adsorbed. The hydrophobic substituent of 2,2′-bipyridine does not allow the presence of water molecules close to TiO_2 surface, improving the stabilization of solar cells toward water-induced desorption of the dye. The redox potentials of these complexes are shifted toward a more positive electrochemical potential in comparison to the N3 sensitizer, increasing the reversibility of the ruthenium III/II couple, leading to higher electrochemical stability [60, 62, 63].

3.1.2 Donor-Antenna Compounds

Complexes prepared with donor-antenna substituents of 2,2′-bipyridine are an approach to improve the light absorption at the same time that the hydrophobic character is enhanced. The use of aromatic substituents can have this function since the aromaticity increases the light absorption and the existence of the hydrophobic chain allows the protection to dye desorption caused by water. The spectral and photoelectrochemical parameters of this class of dyes are listed in Table 2.

In most cases it is observed higher molar absorptivities values in comparison to amphiphilic compounds or N3 or N719 dyes which can be ascribed to an extended π-cloud delocalized in the substituent. The higher light harvesting efficiency results directly in higher IPCE values as well as overall efficiency of the solar cell, Tables 2.

There are a few investigations on the use of π-excessive heteroaromatic rings as end-groups in substituted bpy ligands [43, 44, 64]. The use of conjugated π-excessive heteroaromatic rings as end-substituents donors directs the electron injection in the excited state and enhances the oscillator strength resulting in significant increases in the short circuit photocurrent [54].

The higher molar absorptivity in the visible region can be understood by the influence of the different delocalised π-systems integrated in the bipyridyl donor-antenna ligands. The reason for the lower absorption of the standard N719 dye in this region is the absence of any these groups [56].

Table 1 Absorption properties and photoelectrochemical performance of ruthenium (II) *tris*-heteroleptic compounds having amphiphilic derivatives of 2,2′-bipyridine

Abbreviation	Structure	Absorption properties		Photoelectrochemical performance					References
		Solvent	λ_{MAX}/nm ($\varepsilon_{MAX}/10^4$ L mol^{-1}cm^{-1})	V_{OC}/V	J_{SC}/mA cm^{-2}	$IPCE_{MAX}$ (%) (λ/nm)	ff	η_{cell} (%)	
Z907	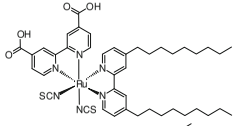	Ethanol	295 (4.24); 312 (3.01); 385 (1.09); 526 (1.16)	0.73	12.5	80 (540)	0.67	6.2	[57]
CS9	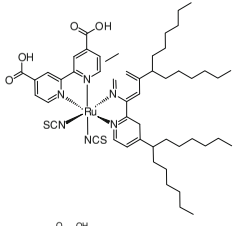	DMF	296 (4.17); 366 (1.03); 518 (0.7)	0.63	14.59	60 (540)	0.62	5.68	[58]
WP-1[a]	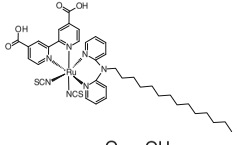	1:1 acetonitrile : tert-butanol	426; 526 (8.7)	0.756	15.5	80 (530)	0.7	8.2	[34]
NMK-2[a]	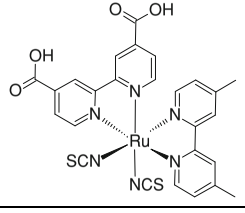	Ethanol	295 (4.54); 312 (3.35); 383 (1.13); 524 (1.16)	0.7	14.7	–	–	6.8	[59]

(continued)

Table 1 (continued)

Abbreviation	Structure	Absorption properties		Photoelectrochemical performance					References
		Solvent	λ_{MAX}/nm ($\varepsilon_{MAX}/10^4$ L mol^{-1}cm^{-1})	V_{OC}/V	J_{SC}/mA cm^{-2}	$IPCE_{MAX}$ (%) (λ/nm)	ff	η_{cell} (%)	
NMK-3[a]	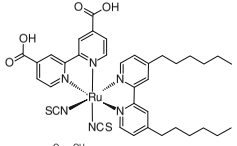	Ethanol	296 (4.26); 312 (3.2); 384 (1.01); 525 (1.11)	0.7	15.5	–	–	7.4	[59]
NMK-5[a]	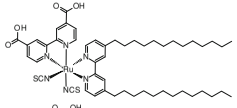	Ethanol	296 (4.21); 312 (3.02); 384 (1.08); 525 (1.15)	0.75	16.2	90	–	8.6	[59]
KC-8[a]	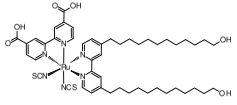	DMF	297 (4.54); 309 (2.74); 370 (1.25); 522 (1.26)	0.673	17.13	86	0.72	8.3	[60]

[a] These compounds were named after the initials of the first author of the reference cited

Table 2 Absorption properties and photoelectrochemical performance of ruthenium (II) *tris*-heteroleptic compounds having donor-antenna derivatives of 2,2′-bipyridine

Abbreviation	Structure	Absorption properties		Photoelectrochemical performance					References
		Solvent	λ_{MAX}/nm ($\varepsilon_{MAX}/10^4$ L mol^{-1}cm^{-1})	V_{OC}/ V	J_{SC}/ mA cm^{-2}	$IPCE_{MAX}$ (%) (λ/ nm)	ff	η_{cell} (%)	
LXJ1	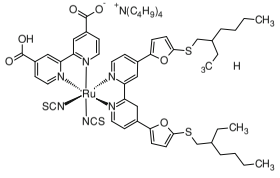	DMF	309 (4.7), 353 (3.3), 549 (1.84)	0.715	16.50	83.7 (550)	0.745	8.80	[43]
IJ-1	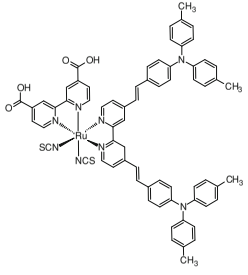	Ethanol	218; 308 (5.0); 432 (4.3), 536 (1.9)	0.748	19.2	87	0.72	10.3	[55]
KW-2[a]	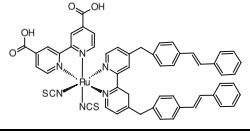	DMF	310 (4.86); 373 (7.95); 550 (2.22)	0.685	3.42	–	0.42	0.99	[56]

(continued)

Table 2 (continued)

Abbreviation	Structure	Absorption properties		Photoelectrochemical performance					References
		Solvent	λ_{MAX}/nm ($\varepsilon_{MAX}/10^4$ L mol^{-1}cm^{-1})	V_{OC}/V	J_{SC}/mA cm^{-2}	$IPCE_{MAX}$ (%) (λ/nm)	ff	η_{cell} (%)	
KW-3[a]	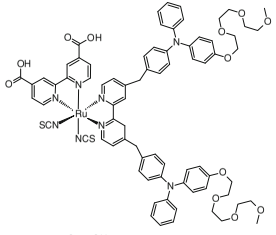	MetOH + 1 wt % KOH	307 (8.13); 429 (5.34); 524 (3.09)	0.735	4.03	–	0.46	1.37	[56]
KW-4[a]	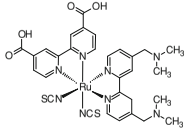	1:1 H_2O:DMF + 1wt % KOH	307 (3.88); 381 (1.28); 526 (1.13)	0.635	2.15	–	0.42	0.58	[56]
KW-5[a]	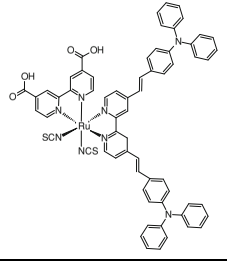	1:1 H_2O:DMF + 1wt % KOH	304 (6.25); 423 (5.47); 544(2.27)	0.715	4.30	–	0.43	1.31	[56]

(continued)

Table 2 (continued)

Abbreviation	Structure	Absorption properties		Photoelectrochemical performance					References
		Solvent	λ_{MAX}/nm ($\varepsilon_{MAX}/10^4$ L mol^{-1}cm^{-1})	V_{OC}/V	J_{SC}/mA cm^{-2}	$IPCE_{MAX}$ (%) (λ/nm)	ff	η_{cell} (%)	
C105	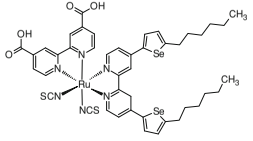	DMF	309 (3.90); 353 (3.2); 420(1.84); 550 (1.84)	0.747	18.9	95 (520)	0.744	10.06	[64]
HRD-1	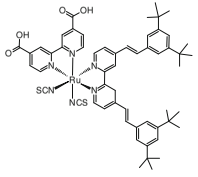	DMF	543 (1.93)	0.59	10.9	60	0.78	4.93	[62]
HRD-2	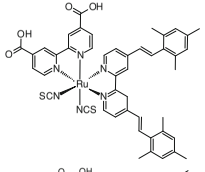	DMF	532 (1.61)	0.60	10.5	64	0.78	4.91	[62]
HRS-2	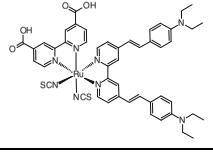	Ethanol	431 (5.93); 542 (2.81)	0.697	17.47	85 (552)	0.711	8.65	[63]

(continued)

Table 2 (continued)

Abbreviation	Structure	Absorption properties		Photoelectrochemical performance					References
		Solvent	λ_{MAX}/nm ($\varepsilon_{MAX}/10^4$ L mol^{-1}cm^{-1})	V_{OC}/V	J_{SC}/mA cm^{-2}	$IPCE_{MAX}$ (%) (λ/nm)	ff	η_{cell} (%)	
C102	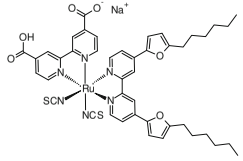	DMF	305; 341; 407; 547(1.68)	0.740	17.80	82 (550)	–	9.5	[44]
AB-1[a]	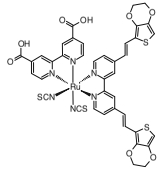	Ethanol	314; 388; 538 (1.6)	0.663	19.1	87	0.72	9.1	[54]
N945	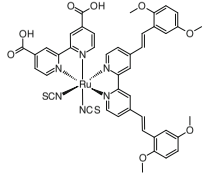	1:1 acetonitrile : tert-butanol	400 (3.4); 550 (1.9)	0.728	17.96	61	0.71	9.29	[76]

(continued)

Table 2 (continued)

Abbreviation	Structure	Absorption properties		Photoelectrochemical performance					References
		Solvent	λ_{MAX}/nm ($\varepsilon_{MAX}/10^4$ L mol^{-1}cm^{-1})	V_{OC}/V	J_{SC}/mA cm^{-2}	$IPCE_{MAX}$ (%) (λ/nm)	ff	η_{cell} (%)	
KCS-1[a]	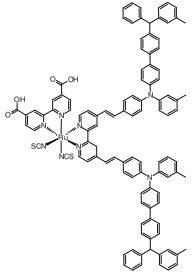	DMF	310 (8.49); 440 (5.34); 540 (2.67)	0.757	9.6	–	0.35	3.4	[77]
K-19	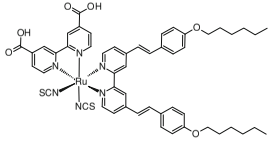	DMF	310 (5.0); 350 (4.8); 410 (1.8); 545 (1.8)	0.718	13.2	–	0.745	7.1	[32]
K-73	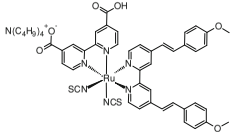	DMF	310; 350; 410; 545	0.748	17.22	85 (540)	0.649	9.5	[32]
Z-910	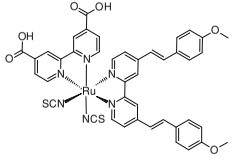	Acetonitrile	410 (1.7); 543 (1.69)	0.777	17.2	87 (520)	0.764	10.2	[33]

(continued)

Table 2 (continued)

Abbreviation	Structure	Absorption properties		Photoelectrochemical performance					References
		Solvent	λ_{MAX}/nm ($\varepsilon_{MAX}/10^4$ L mol^{-1}cm^{-1})	V_{OC}/V	J_{SC}/mA cm^{-2}	$IPCE_{MAX}$ (%) (λ/nm)	ff	η_{cell} (%)	
KC-5[a]	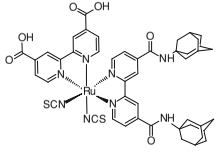	DMF	313 (3.88); 392 (1.17); 537 (1.19)	0.695	15.8	75	0.66	7.01	[60]
KC-6[a]	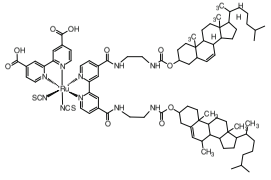	DMF	314 (3.36); 390 (1.11); 531 (1.12)	0.676	15.47	63	0.71	7.42	[60]
KC-7[a]	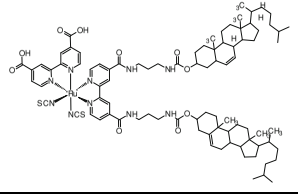	DMF	312 (3.39); 393 (1.12); 533 (1.21)	0.676	16.11	79	0.7	7.62	[60]

[a] These compounds were named after the initials of the first author of the reference cited

3.1.3 Thiophene Compounds

Ruthenium(II) sensitizers having 2,2′-bipyridine with thiophene substituents have higher molar absorptivity than observed for the previous classes of compounds. For instance, the compound KW-1 has $\varepsilon_{515} = 3.56$ L mol^{-1} cm^{-1} [56], much higher than the ones determined for N3 or N719 dyes. As it is observed for the donor-antenna class of compounds, the higher light harvesting efficiency results in higher IPCE values and consequently improve overall performance of the solar cell, Table 3.

Ruthenium(II) thiophene compounds gained special attention after C101 dye has set a new DSSC efficiency record of 11.3–11.5 % and became the first sensitizer to triumph over the well-known N3 dye [44]. In comparison to its analogues C102 or C105, in which the thiophene is replaced by furan, or selenophene, respectively, the molar absorptivity increases in the order of Se > S > O. This sequence it is consistent with the electropositivity trend and the size of the heteroatoms of five-member conjugated units. The LUMO energy sequence of the spectator ligand is O > S > Se, which explain this behavior [64].

Another important dye employing thiophene derivatives is CYC-B1, which exhibts a remarkably high light-harvesting capacity of up to 2.12x10^4 L mol^{-1} cm^{-1} [40]. After the development of the CYC-B1 dye, several ruthenium dyes were synthesized by incorporating thiophene derivatives into the ancillary ligand and DSSC cells based on these dyes exhibited excellent photovoltaic performances [45, 46, 65, 66].

The extensive use of polythiophene is due to its similarity to a *cis*-polyacetylene chain bridged with sulfur atoms. The "bridging sulfur atoms" could effectively provide aromatic stability to the polyacetylene chain while preserving the desirable physical properties, such as high charge transport. The facile functionalization of thiophene groups also offers relatively efficient synthetic solutions to solubility, polarity, and energetic tuning. Furthermore, sulfur has greater radial extension in its bonding than the second-row elements, such as carbon. Therefore, thiophene is a more electron-rich moiety and incorporation of thiophene onto bipyridine ligands raises the energy levels of the metal center and the LUMO of the ligands [67]. As a consequence, the band resulting from charge transfer from the metal center to the anchoring ligand is redshifted, and upon illumination of the sample, the electrons on the metal center are transferred to the anchoring dcbH_2 ligand, where electrons can move to the outer circuit through the TiO_2 particles more efficiently [40].

3.2 1,10-Phenanthroline Derivative Ligands

Besides 2,2′-bipyridine derivatives, 1,10-phenanthroline and its derivatives is gaining attention to be used in *cis*-[Ru(dcbH_2)(L)(NCS)$_2$] sensitizers. Their similarity to 2,2′-bipyridine and the advantage of having an extended π-conjugated structure led to a great potential to be employed as ancillary ligands [68]. This

Table 3 Absorption properties and photoelectrochemical performance of ruthenium (II) *tris*-heteroleptic compounds having thiophene derivatives of 2,2′-bipyridine

Abbreviation	Structure	Absorption properties		Photoelectrochemical performance					References
		Solvent	λ_{MAX}/nm ($\varepsilon_{MAX}/10^4$ L mol^{-1}cm^{-1})	V_{OC}/ V	J_{SC}/ mA cm^{-2}	$IPCE_{MAX}$ (%) (λ/nm)	ff	η_{cell} (%)	
CYC-B1	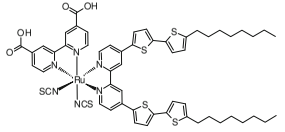	DMF	312 (3.58); 400 (4.64); 553 (2.12)	0.65	23.92	77.5	0.55	8.54	[40]
CYC-B3	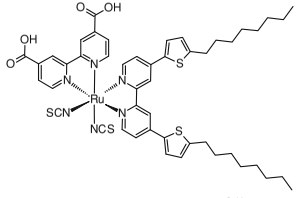	DMF	350; 400; 544 (1.57)	0.669	15.7	64.1 (520)	0.705	7.39	[65]
CYC-B7	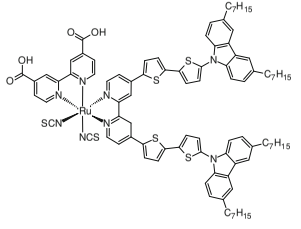	DMF	345 (3.55), 412 (4.35), 551 (2.19)	0.788	17.4	76 (530)	0.654	8.96	[66]
CYC-B11	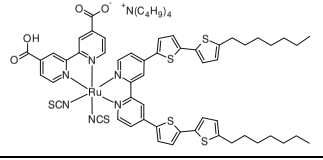	DMF	305(4.5), 388(5.40), 554 (2.42)	0.714	16.1	95 (580)	0.69	7.9	[45]

(continued)

Table 3 (continued)

Abbreviation	Structure	Absorption properties		Photoelectrochemical performance					References
		Solvent	λ_{MAX}/nm ($\varepsilon_{MAX}/10^4$ L mol^{-1}cm^{-1})	V_{OC}/ V	J_{SC}/ mA cm^{-2}	$IPCE_{MAX}$ (%) (λ/nm)	ff	η_{cell} (%)	
CYC-B13	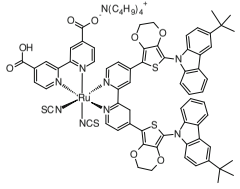	DMF	295 (8.6); 397 (3.4); 547 (1.93)	0.728	10.26	90 (550)	0.68	5.1	[46]
C101	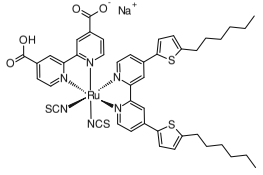	DMF	305; 341; 407; 547 (1.75)	0.746	5.42	89 (580)	0.833	11.3	[44]
C104	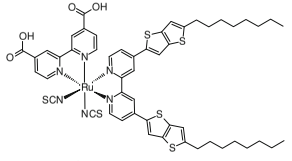	DMF	312 (5.4); 368 (4.5); 553 (2.05)	0.76	17.87	85 (580)	0.776	10.53	[61]
C106	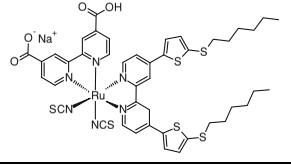	DMF	310 (3.95); 348 (3.1); 550 (1.87)	0.749	18.28	90 (520-640)	0.772	10.57	[41]

(continued)

Table 3 (continued)

Abbreviation	Structure	Absorption properties		Photoelectrochemical performance					References
		Solvent	λ_{MAX}/nm ($\varepsilon_{MAX}/10^4$ L mol^{-1}cm^{-1})	V_{OC}/ V	J_{SC}/ mA cm^{-2}	$IPCE_{MAX}$ (%) (λ/nm)	ff	η_{cell} (%)	
KW-1[a]	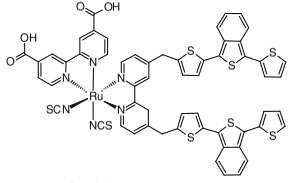	DMF	301 (4.58); 369 (3.51); 515 (3.56)	0,625	1.06	–	0,46	0,31	[56]
RT-1[a]	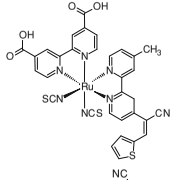	DMF	301 (3.04); 368 (2.28); 529 (1.41)	0.58	6.0	–	0.70	2.45	[78]
RT-2[a]	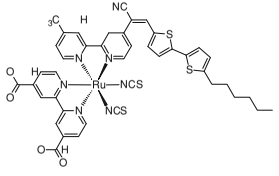	DMF	300 (4.34); 445 (2.88); 551 (1.68)	0.57	5.3	–	0.75	2.84	[78]
RT-3[a]	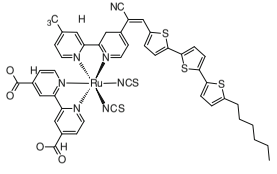	DMF	305 (4.56); 388 (3.15); 563 (2.76)	0.54	4.5	–	0.76	1.85	[78]

(continued)

Table 3 (continued)

Abbreviation	Structure	Absorption properties		Photoelectrochemical performance					References
		Solvent	λ_{MAX}/nm ($\varepsilon_{MAX}/10^4$ L mol^{-1}cm^{-1})	V_{OC}/ V	J_{SC}/ mA cm^{-2}	$IPCE_{MAX}$ (%) (λ/nm)	ff	η_{cell} (%)	
C107	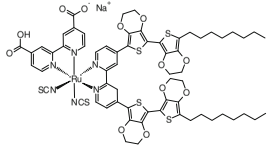	DMF	310 (3.9); 453 (5.43); 552 (2.8)	0.739	19.8	92 (550)	0.751	10.7	[47]
SJW-E1	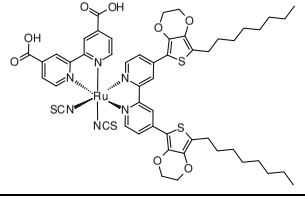	DMF	310; 360; 546 (1.87)	0.669	21.6	72.6 (550)	0.626	9.02	[65]

[a] These compounds were named after the initials of the first author of the reference cited

Table 4 Absorption properties and photoelectrochemical performance of ruthenium (II) *tris*-heteroleptic ruthenium compounds having 1,10-phenanthroline derivatives

Abbreviation	Structure	Absorption properties		Photoelectrochemical performance					References
		Solvent	λ_{MAX}/nm ($\varepsilon_{MAX}/10^4$ L mol^{-1}cm^{-1})	V_{OC}/V	J_{SC}/mA cm^{-2}	IPCE$_{MAX}$ (%) (λ/nm)	ff	η_{cell} (%)	
YS5	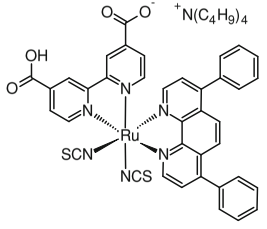	DMF	283(5.68), 308 (3.95), 362 (0,81), 522 (1.71)	0.749	14.52	64.6 (540)	0.557	6.05	[48]
AR25	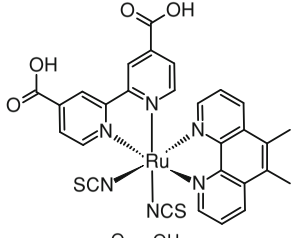	DMF	420; 518(6.58)	0.69	9.6	61 (520)	0.39	2.6	[69]
NOK-1[a]	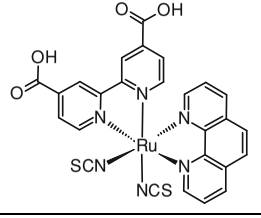	0.01 M NaOH aqueous solution	267 (5.7); 309 (2.9); 400 (1.0); 492(1.2)	0.65	15.3	74	0.67	6.7	[70]

(continued)

Table 4 (continued)

Abbreviation	Structure	Absorption properties		Photoelectrochemical performance					References
		Solvent	λ_{MAX}/nm ($\varepsilon_{MAX}/10^4$ L mol^{-1}cm^{-1})	V_{OC}/V	J_{SC}/mA cm^{-2}	IPCE$_{MAX}$ (%) (λ/nm)	ff	η_{cell} (%)	
NOK-2[a]	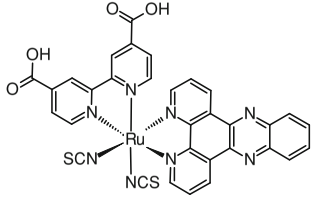	0.01 M NaOH aqueous solution	275 (5.7); 310 (3.5); 374 (1.8); 492 (1.1)	0.62	11.7	54	0.73	5.3	[70]

[a] These compounds were named after the initials of the first author of the reference cited

Table 5 Absorption maxima and photoelectrochemical performance of natural dye-sensitized solar cells reported since 2003

Extract of	Dye	Medium	λ_{max} (nm)	V_{OC} (V)	J_{SC} (mA cm^{-2})	ff	η_{cell} (%)	References
Red-cabbage	Anthocyanin	Water	550	0.52	0.68	0.70	0.50	[79]
Rosella flower	Anthocyanin	Water	520	0.404	1.63	0.57	0.37	[80]
Blue pea flower	Anthocyanin	Water	580, 620	0.372	0.37	0.33	0.05	[80]
Canna indica flower	Anthocyanin	Water and Ethanol	513	0.54	0.82	0.59	0.29	[81]
		TiO_2	530	–	–	–	–	
Salvia splendens flower	Anthocyanin	Water and Ethanol	507	0.558	0.7	0.61	0.26	[81]
		TiO_2	516	–	–	–	–	
Cowberry	Anthocyanin	Water and Ethanol	522	0.556	0.4	0.54	0.13	[81]
		TiO_2	531	–	–	–	–	
Solanum nigrum	Anthocyanin	Water and Ethanol	539	0.54	1.01	0.51	0.31	[81]
		TiO_2	564	–	–	–	–	
Rhododendron arboretum zeylanicum	Anthocyanin	Ethanol	538	0.4020	1.15	0.637	0.29	[82]
Sesbania grandiflora Scarlet	Anthocyanin	Ethanol	544	0.4067	4.40	0.569	1.02	[82]
Hibiscus rosasinensis	Anthocyanin	Ethanol	534	0.4003	4.04	0,633	1.02	[82]
Hibiscus surattensis	Anthocyanin	Ethanol	545	0.3921	5.45	0.535	1.14	[82]
Nerium oleander	Anthocyanin	Ethanol	539	0.4088	2.46	0.591	0.59	[82]
Ixora macrothyrsa	Anthocyanin	Ethanol	537	0.4031	1.31	0.568	0.30	[82]
Black rice	Anthocyanin	Ethanol	560	0.551	1.142	0.52	–	[83]
Rosa xanthina	Anthocyanin	Ethanol	560	0.492	0.637	0.52	–	[83]
Maple leaves	Anthocyanin	Ethanol	536	0.65	1.0	0.60	0.4	[84]
Red Sicilian orange	Anthocyanin	Water	515	0.340	3.84	0.5	–	[85]
Skin of eggplant	Anthocyanin	Water	522	0.350	3.40	0.4	–	[85]
Skin of jaboticaba	Anthocyanin	Ethanol	535	0.66	2.6	0.62	–	[86]
		TiO_2	560	–	–	–	–	
Calafate fruit	Anthocyanin	Water	525	0.47	6.2	0.36	–	[86]
		TiO_2	545	–	–	–	–	
Raw beet	Betalain	TiO_2	470	0.22	2.00	0.51	0.19	[87]
		Water	535	–	–	–	–	

(continued)

Table 5 (continued)

Extract of	Dye	Medium	λ_{max} (nm)	V_{OC} (V)	J_{SC} (mA cm^{-2})	ff	η_{cell} (%)	References
Red Turnip	Betalain	Water	484, 536	0.425	9.5	0.37	1.7	[75]
		TiO_2	450	–	–	–	–	
Wild silician prickly pear	Betalain	TiO_2	460	0.375	8.20	0.38	1.19	[75]
Kelp	Chlorophyll	Ethanol	460	0.441	0.433	0.62	–	[83]
Wormwood	Chlorophyll	Ethanol	432	0.67	2.3	0.56	0.9	[84]
Bamboo leaves	Chlorophyll	Ethanol	432	0.67	1.9	0.56	0.7	[84]
Pomegranate leaves	Chlorophyll	Ethanol	412, 665	0.560	2.05	0.52	0.597	[88]
Curcumin	Polyphenol	Ethanol	430	0.53	0.53	0.72	0.41	[79]
Red-perilla	–	–	–	0.51	0.39	0.67	0.27	[79]
Erythrina	Carotenoid	Ethanol	451	0.484	0.776	0.55	–	[83]
Capsicum	Carotenoid	Ethanol	455	0.412	0.225	0.63	–	[83]
Achiode seed	Carotenoid	Chloroform	440, 475, 500	0.56	0.53	0.66	0.19	[89]

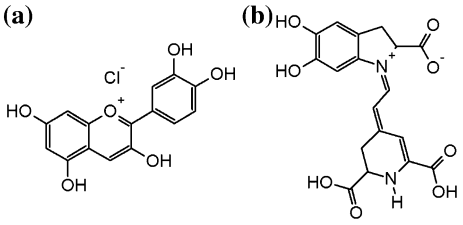

Fig. 6 Structure of anthocyanidin, a flavinic ion of anthocyanin (**a**) and betanidin (**b**), a betalain compound

class of compounds still having few complexes reported in DSSCs, and their spectral as well as photoelectrochemical parameters are listed in Table 4.

The use of phenanthroline derivatives in ruthenium(II) sensitizers leads to properties favorable to the energy conversion processes and can increase on the of DSSCs, which have shown promising results [48, 69, 70].

The comparison on the properties of the complex NOK-1 [70] with N3 indicates that the substitution of the 2,2′-bipyridine derivative by 1,10-phenanthroline does not exhibit better performance or absorption properties. On the other hand, the recently reported complex YS5 exhibits a higher absorbance and also had better performance than the complex N719 under the same condition [48], indicating that this is a promising class of compounds to be investigated.

4 Natural Dyes

Faster, cheaper, low-energy way alternative for ruthenium sensitizers are natural dyes and these compounds has been gaining much attention. Natural dyes can be obtained from fruits, flowers or leaves and are suitable for educational purposes [71, 72] or are an environmentally friendly alternative for dye production since a long-term stability of DSSC using these sensitizers have been demonstrated recently [73].

The absorption properties and photoelectrochemical performance of natural dye-sensitized solar cells reported since 2003 are listed in Table 5.

The most investigated class of natural dyes is the anthocyanins, commonly found in red-purplish fruits or flowers, Fig. 6. These, even other sensitizers have also been investigated [74].

Betalain from raw beet, Red Turnip and Wild silician prickly pear have also been used as natural sensitizers and they have been presented a good photoelectrochemical response, however these cells have low V_{OC}, with overall efficiency up to 1.7 % and reasonable stability [75].

Other classes of natural dyes, such as chlorophyll, polyphenol etc. were also investigated, but the photoelectrochemical parameters were not as good as those observed for anthocyanins or betalains.

5 Conclusion

The energy needs will be supplied by alternative sources and dye-sensitized solar cells are one of the most promising ones for this application since it is cheap and environmentally friendly device. The investigation on dye-sensitizers is fundamental issue on the development of these devices and one of the most promising alternatives is the use of ruthenium *tris*-heteroleptic dyes sensitizers to modulate or enhance their photoelectrochemical performance. The investigation on natural extracts to be employed as dye sensitizers has also been attracting much attention in the last years. They can be an alternative to further reduction of the production costs of these revolutionary devices.

Acknowledgments The authors would like to acknowledge to CNPq (577256/2008-4), FAPESP (2011/11717-8) and UFABC for financial support.

References

1. Cook TR et al (2010) Solar energy supply and storage for the legacy and nonlegacy worlds. Chem Rev 110(11):6474–6502
2. Nocera DG (2009) Chemistry of personalized solar energy. Inorg Chem 48(21):10001–10017
3. Carrette L, Friedrich KA, Stimming U (2000) Fuel cells: principles, types, fuels, and applications. Chem Phys Chem 1(4):162–193
4. Cameron D, Holliday R, Thompson D (2003) Gold's future role in fuel cell systems. J Power Sour 118(1–2):298–303
5. Lemos SG et al (2007) Electrocatalysis of methanol, ethanol and formic acid using a Ru/Pt metallic bilayer. J Power Sour 163(2):695–701
6. Freitas RG et al (2007) Methanol oxidation reaction on $Ti/RuO_{2(x)}Pt_{(1-x)}$ electrodes prepared by the polymeric precursor method. J Power Sour 171(2):373–380
7. Polo AS et al (2011) Pt-Ru-TiO2 photoelectrocatalysts for methanol oxidation. J Power Sour 196(2):872–876
8. Gu C, Shannon C (2007) Investigation of the photocatalytic activity of TiO2-polyoxometalate systems for the oxidation of methanol. J Mol Catal A Chem 262(1–2):185–189
9. Drew K et al. (2005) boosting fuel cell performance with a semiconductor photocatalyst: TiO_2/Pt-Ru hybrid catalyst for methanol oxidation. J Phys Chem B 109(24):11851–11857
10. Kamat PV (2007) Meeting the clean energy demand: nanostructure architectures for solar energy conversion. J Phys Chem C 111(7):2834–2860
11. Armaroli N, Balzani V (2007) The future of energy supply: challenges and opportunities. Angew Chem Int Ed Engl 46(1–2):52–66
12. Meyer TJ (1989) Chemical approaches to artificial photosynthesis. Acc Chem Res 22(5):163–170
13. Dubois DL (2009) Development of molecular electrocatalysts for CO2 reduction and H2 production/oxidation. Acc Chem Res 42(12):1974–1982
14. Morris AJ, Meyer GJ, Fujita E (2009) Molecular approaches to the photocatalytic reduction of carbon dioxide for solar fuels. Acc Chem Res 42(12):1983–1994
15. Concepcion JJ et al (2009) Making oxygen with ruthenium complexes. Acc Chem Res 42(12):1954–1965
16. Walter MG et al (2010) Solar water splitting cells. Chem Rev 110(11):6446–6473

17. Caramori S et al (2010) Photoelectrochemical behavior of sensitized TiO_2 photoanodes in an aqueous environment: application to hydrogen production. Inorg Chem 49(7):3320–3328
18. Koike K et al (2009) Architecture of supramolecular metal complexes for photocatalytic CO2 reduction: III: effects of length of alkyl chain connecting photosensitizer to catalyst. J Photochem Photobiol A Chem 207(1):109–114
19. Takeda H et al (2008) Development of an efficient photocatalytic system for CO_2 reduction using rhenium (i) complexes based on mechanistic studies. J Am Chem Soc 130(6):2023–2031
20. Kroon JM et al (2007) Nanocrystalline dye-sensitized solar cells having maximum performance. Prog Photovolt Res Appl 15(1):1–18
21. Tributsch H (1972) Reaction of excited chlorophyll molecules at electrodes and in photosynthesis*. Photochem Photobiol 16(4):261–269
22. O'Regan B, Gratzel M (1991) A low-cost, high-efficiency solar cell based on dye-sensitized colloidal TiO2 films. Nature 353(6346):737–740
23. Grätzel M (2001) Photoelectrochemical cells. Nature 414(6861):338–344
24. Katoh R et al (2004) Kinetics and mechanism of electron injection and charge recombination in dye-sensitized nanocrystalline semiconductors. Coord Chem Rev 248(13–14):1195–1213
25. Gregg BA (2004) Interfacial processes in the dye-sensitized solar cell. Coord Chem Rev 248(13–14):1215–1224
26. Galoppini E (2004) Linkers for anchoring sensitizers to semiconductor nanoparticles. Coord Chem Rev 248(13–14):1283–1297
27. Anderson NA, Lian T (2004) Ultrafast electron injection from metal polypyridyl complexes to metal-oxide nanocrystalline thin films. Coord Chem Rev 248(13–14):1231–1246
28. Asbury JB et al (2003) Parameters affecting electron injection dynamics from ruthenium dyes to titanium dioxide nanocrystalline thin film. J Phys Chem B 107(30):7376–7386
29. Anderson NA, Ai X, Lian T (2003) Electron injection dynamics from Ru polypyridyl complexes to ZnO nanocrystalline thin films. J Phys Chem B 107(51):14414–14421
30. Garcia CG et al (2002) Electron injection versus charge recombination in photoelectrochemical solar cells using cis-$[(dcbH_2)_2Ru(CNpy)(H_2O)]Cl_2$ as a nanocrystalline TiO_2 sensitizer. J Photochem Photobiol A Chem 151(1–3):165–170
31. Garcia CG et al (2002) Time-resolved experiments in dye-sensitized solar cells using $[(dcbH_2)_2Ru(ppy)_2](ClO_4)_2$ as a nanocrystalline TiO_2 sensitizer. J Photochem Photobiol A Chem 147(2):143–148
32. Kuang DB et al (2006) High molar extinction coefficient heteroleptic ruthenium complexes for thin film dye-sensitized solar cells. J Am Chem Soc 128(12):4146–4154
33. Wang P et al (2004) Stable new sensitizer with improved light harvesting for nanocrystalline dye-sensitized solar cells. Adv Mat 16(20)1806–1811
34. Wang P et al (2004) Amphiphilic polypyridyl ruthenium complexes with substituted 2,2 '-dipyridylamine ligands for nanocrystalline dye-sensitized solar cells. Chem Mater 16(17):3246–3251
35. Pelet S, Moser J-E, Gratzel M (2000) Cooperative effect of adsorbed cations and iodide on the interception of back electron transfer in the dye sensitization of nanocrystalline TiO2. J Phys Chem B 104(8):1791–1795
36. Patrocinio AOT, Paterno LG, Iha NYM (2010) Role of polyelectrolyte for layer-by-layer compact TiO2 films in efficiency enhanced dye-sensitized solar cells. J Phys Chem C 114(41):17954–17959
37. Murakami Iha NY, Garcia CG, Bignozzi CA (2003) Dye-sensitized photoelectrochemical solar cells. In: Nalwa HS (Ed.) Handbook of photochemistry and photobiology. American Scientific Publishers, Stevenson Ranch, p 49–82
38. Nazeeruddin MK et al (1993) Conversion of ligth to electricity by cis-X_2bis(2,2′-Bipyridyl-4,4′-Dicarboxylate)Ruthenium(II) charge-transfer sensitizers (X = Cl^-, Br^-, I^-, CN^-, and SCN^-) on nanocrystalline TiO_2 electrodes. J Am Chem Soc 115(14):6382–6390
39. Nazeeruddin MK, Gratzel M (2001) Separation of linkage isomers of trithiocyanato (4,4′,4″-tricarboxy-2,2′,6,2″-terpyridine)ruthenium(II) by pH-titration method and their application in nanocrystalline TiO2-based solar cells. J Photochem Photobiol A Chem 145(1–2):79–86

40. Chen CY et al (2006) A ruthenium complex with superhigh light-harvesting capacity for dye-sensitized solar cells. Angew Chem Int Ed 45(35):5822–5825
41. Cao YM et al (2009) Dye-sensitized solar cells with a high absorptivity ruthenium sensitizer featuring a 2-(Hexylthio)thiophene conjugated bipyridine. J Phys Chem C 113(15):6290–6297
42. Nazeeruddin MK et al (2003) Investigation of sensitizer adsorption and the influence of protons on current and voltage of a dye-sensitized nanocrystalline TiO2 solar cell. J Phys Chem B 107(34):8981–8987
43. Lv XJ, Wang FF, Li YH (2010) Studies of an extremely high molar extinction coefficient ruthenium sensitizer in dye-sensitized solar cells. Acs Appl Mat Interfaces 2(7):1980–1986
44. Gao F et al (2008) Enhance the optical absorptivity of nanocrystalline TiO2 film with high molar extinction coefficient ruthenium sensitizers for high performance dye-sensitized solar cells. J Am Chem Soc 130(32):10720–10728
45. Chen CY et al (2009) Highly efficient light-harvesting ruthenium sensitizer for thin-film dye-sensitized solar cells. ACS Nano 3(10):3103–3109
46. Chen CY et al (2009) New ruthenium sensitizer with carbazole antennas for efficient and stable thin-film dye-sensitized solar cells. J Phys Chem C 113(48):20752–20757
47. Yu QJ et al (2009) An extremely high molar extinction coefficient ruthenium sensitizer in dye-sensitized solar cells: the effects of pi-conjugation extension. J Phys Chem C 113(32):14559–14566
48. Sun YL et al (2010) Viable alternative to N719 for dye-sensitized solar cells. ACS Appl Mater Interfaces 2(7):2039–2045
49. Polo AS, Itokazu MK, Murakami Iha NY (2004) Metal complex sensitizers in dye-sensitized solar cells. Coord Chem Rev 248(13–14):1343–1361
50. Jin Zhengzhe et al (2008) Triarylamine-functionalized ruthenium dyes for efficient dye-sensitized solar cells. ChemSusChem 1(11):901–904
51. Mitsopoulou CA et al (2007) Synthesis, characterization and sensitization properties of two novel mono and bis carboxyl-dipyrido-phenazine ruthenium(II) charge transfer complexes. J Photochem Photobiol A Chem 191:6–12
52. Huang WK et al (2010) Synthesis and electron-transfer properties of benzimidazole-functionalized ruthenium complexes for highly efficient dye-sensitized solar cells. Chem Commun 46(47):8992–8994
53. Wu SJ et al (2010) An efficient light-harvesting ruthenium dye for solar cell application. Dyes Pigm 84(1):95–101
54. Abbotto A et al (2008) Electron-rich heteroaromatic conjugated bipyridine based ruthenium sensitizer for efficient dye-sensitized solar cells. Chem Commun 42:5318–5320
55. Yum JH et al (2009) High efficient donor-acceptor ruthenium complex for dye-sensitized solar cell applications. Energy Environ Sci 2(1):100–102
56. Willinger K et al (2009) Synthesis, spectral, electrochemical and photovoltaic properties of novel heteroleptic polypyridyl ruthenium(II) donor-antenna dyes. J Mater Chem 19(30):5364–5376
57. Wang P et al (2003) A stable quasi-solid-state dye-sensitized solar cell with an amphiphilic ruthenium sensitizer and polymer gel electrolyte (vol 2, pg 402, 2003). Nat Mater 2(7):498–498
58. Sahin C et al (2008) Synthesis of an amphiphilic ruthenium complex with swallow-tail bipyridyl ligand and its application in nc-DSC. Inorg Chim Acta 361(3):671–676
59. Nazeeruddin MK et al (2004) Stepwise assembly of amphiphilic ruthenium sensitizers and their applications in dye-sensitized solar cell. Coord Chem Rev 248(13–14):1317–1328
60. Klein C et al (2004) Amphiphilic ruthenium sensitizers and their applications in dye-sensitized solar cells. Inorg Chem 43(14):4216–4226
61. Gao FF et al (2008) A new heteroleptic ruthenium sensitizer enhances the absorptivity of mesoporous Titania film for a high efficiency dye-sensitized solar cell. Chem Commun 23:2635–2637

62. Giribabu L et al (2009) High molar extinction coefficient amphiphilic ruthenium sensitizers for efficient and stable mesoscopic dye-sensitized solar cells. Energy Environ Sci 2(7):770–773
63. Jiang KJ et al (2008) Efficient sensitization of nanocrystalline TiO2 films with highmolar extinction coefficient ruthenium complex. Inorg Chim Acta 361(3):783–785
64. Gao FF et al (2009) Conjugation of selenophene with bipyridine for a high molar extinction coefficient sensitizer in dye-sensitized solar cells. Inorg Chem 48(6):2664–2669
65. Chen CY et al. (2007) A new route to enhance the light-harvesting capability of ruthenium complexes for dye-sensitized solar cells. Adv Mat 19(22):3888–3891
66. Li J-Y et al (2010) Heteroleptic ruthenium antenna-dye for high-voltage dye-sensitized solar cells. J Mater Chem 20(34):7158–7164
67. Zhu SS, Kingsborough RP, Swager TM (1999) Conducting redox polymers: investigations of polythiophene-Ru(bpy)(3)(n+) hybrid materials. J Mater Chem 9(9):2123–2131
68. Hara K et al (2001) Dye-sensitized nanocrystalline TiO2 solar cells based on ruthenium(II) phenanthroline complex photosensitizers. Langmuir 17(19):5992–5999
69. Reynal A et al (2008) A phenanthroline heteroleptic ruthenium complex and its application to dye-sensitised solar cells. Eur J Inorg Chem 12:1955–1958
70. Onozawa-Komatsuzaki N et al (2006) Molecular and electronic ground and excited structures of heteroleptic ruthenium polypyridyl dyes for nanocrystalline TiO2 solar cells. New J Chem 30(5):689–697
71. Smestad GP, Grätzel M (1998) Demonstrating electron transfer and nanotechnology: a natural dye-sensitised nanocrystalline energy converter. J Chem Educ 75(6):752–756
72. Smestad GP (1998) Education and solar conversion: demonstrating electron transfer. Sol Energy Mater Sol Cells 55(1–2):157–178
73. Patrocinio AOT, Iha NYM (2010) Toward sustainability: solar cells sensitized by natural extracts. Quim Nova 33(3):574–578
74. Zhang D et al. (2008) Betalin pigments for dye-sensitised solar cells. J Photochem Photobiol A Chem 195(1):72–80
75. Calogero G et al (2010) Efficient dye-sensitized solar cells using red turnip and purple wild sicilian prickly pear fruits. Int J Mol Sci 11(1):254–267
76. Nazeeruddin MK et al (2007) A high molar extinction coefficient charge transfer sensitizer and its application in dye-sensitized solar cell. J Photochem Photobiol A Chem 185(2–3):331–337
77. Karthikeyan CS et al (2007) Highly efficient solid-state dye-sensitized TiO2 solar cells via control of retardation of recombination using novel donor-antenna dyes. Sol Energy Mater Sol Cells 91(5):432–439
78. Ryu TI et al (2009) Synthesis and photovoltaic properties of novel ruthenium(ii) sensitizers for dye-sensitized solar cell applications. Bull Korean Chem Soc 30(10):2329–2337
79. Furukawa S et al (2009) Characteristics of dye-sensitized solar cells using natural dye. Thin Solid Films 518(2):526–529
80. Wongcharee K, Meeyoo V, Chavadej S (2007) Dye-sensitized solar cell using natural dyes extracted from rosella and blue pea flowers. Sol Energy Mater Sol Cells 91(7):566–571
81. Luo PH et al (2009) From salmon pink to blue natural sensitizers for solar cells: Canna indica L., Salvia splendens, cowberry and Solanum nigrum L. Spectrochim Acta A Mol Biomol Spectrosc 74(4):936–942
82. Fernando J, Senadeera GKR (2008) Natural anthocyanins as photosensitizers for dye-sensitized solar devices. Curr Sci 95(5):663–666
83. Hao SC et al (2006) Natural dyes as photosensitizers for dye-sensitized solar cell. Sol Energy 80(2):209–214
84. Jin EM et al. (2010) Photosensitization of nanoporous TiO2 films with natural dye. Physica Scripta T139
85. Calogero G, Di Marco G (2008) Red Sicilian orange and purple eggplant fruits as natural sensitizers for dye-sensitized solar cells. Sol Energy Mater Sol Cells 92(11):1341–1346

86. Polo AS, Murakami Iha NY (2006) Blue sensitizers for solar cells: natural dyes from Calafate and Jaboticaba. Sol Energy Mater Sol Cells 90(13):1936–1944
87. Zhang D et al (2008) Betalain pigments for dye-sensitized solar cells. J Photochem Photobiol A Chem 195(1):72–80
88. Chang H, Lo YJ (2010) Pomegranate leaves and mulberry fruit as natural sensitizers for dye-sensitized solar cells. Sol Energy 84(10):1833–1837
89. Gomez-Ortiz NM et al (2010) Dye-sensitized solar cells with natural dyes extracted from achiote seeds. Sol Energy Mater Sol Cells 94(1):40–44

Facile Routes to Produce Hematite Film for Hydrogen Generation from Photoelectro-Chemical Water Splitting

Flavio L. de Souza, Allan M. Xavier, Waldemir M. de Carvalho, Ricardo H. Gonçalves and Edson R. Leite

Abstract In this chapter, we brief review a recent progress in chemical synthesis used to prepare very promise material to be applied as photoanode in a PEC cell. We discuss the important parameters such as; the interface solid/liquid showing the different challenge that needs to be addressed for obtains higher semiconductor photoanode performance. In addition, we discuss the impact of a variety of morphology applied in a PEC cell to split water and generate hydrogen and oxygen molecular. Finally, we have pointed out the progress of molecular oxygen evolution mechanism from water oxidation under solar light irradiation.

1 Introduction

Energy from the sun can provide sufficient power for all of our energy needs, and a potentially efficient route to storing this energy is to convert sunlight into chemical energy in the form of chemical bonds which is a form of an artificial photosynthesis process. Considering the abundance of H_2O on the planet, water splitting is a natural pathway for artificial photosynthesis. Based on the pioneering work of Fujishima and Honda [1], worldwide research has focused on the conversion of sunlight into hydrogen as a clean and renewable energy source. In their classical

F. L. de Souza (✉) · A. M. Xavier · W. M. de Carvalho
Centro de Ciências Naturais e Humanas, Universidade Federal do ABC—UFABC, Santo André, São Paulo, Brasil
e-mail: flavio.souza@ufabc.edu.br

RicardoH. Gonçalves · E. R. Leite (✉)
Departamento de Química, Universidade Federal de São Carlos, São Carlos, São Paulo, Brasil
e-mail: leite@pq.cnpq.br

F. L. de Souza and E. R. Leite (eds.), *Nanoenergy*,
DOI: 10.1007/978-3-642-31736-1_3,

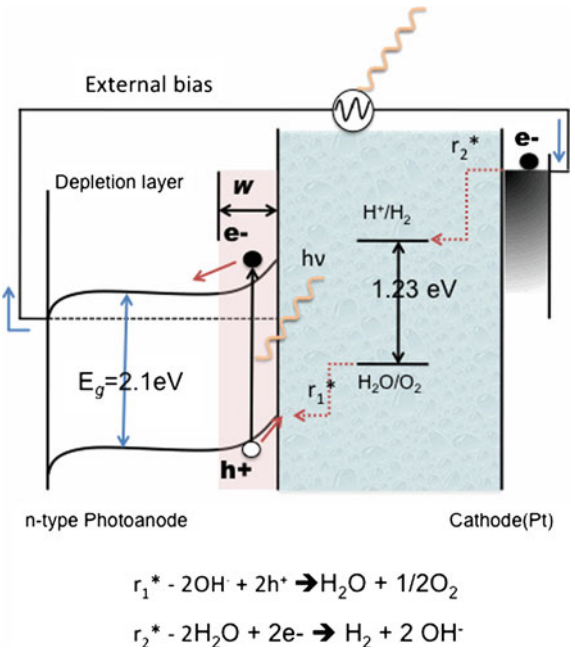

Fig. 1 Schematic representation of the n-type hematite photoanode energy diagram and reactions related to water splitting

work, the authors demonstrated that it is possible to induce water-splitting by light using a TiO_2 semiconductor as a photoanode. As in conventional water electrolysis, O_2 evolution occurs at the anode, H_2 evolution occurs at the cathode, and an aqueous electrolyte completes the current loop. One or both of the electrodes can be a photoactive semiconductor where a space-charge (depletion) layer is formed at the semiconductor/liquid junction (SCLJ). Under light irradiation a pair of electron-holes is generated. The photogenerated carriers are separated by the space-charge field, and the minority carriers (holes for an n-type photoanode) travel to the SCLJ to perform one half of the water splitting reaction. Figure 1 illustrates the energy diagram of an n-type photoanode and the reactions related to the water splitting.

However, TiO_2 has a wide band gap and hence is photoexcited by UV light only (which occupies 5 % of the solar spectrum). Nowadays, the main focus of the present research is to shift the activity of the photoanode into the visible region of the sunlight to increase the energy conversion efficiency [2–4]. Iron oxide (α-Fe_2O_3 or hematite) is a semiconductor material with a narrow band gap (approximately 2.1 eV) and very good electrochemical stability in water. These properties make this material especially attractive when used as a photoanode to split water into oxygen and hydrogen using sunlight. Theoretical calculations [5] suggest that this semiconductor has a maximum efficiency of 12.9 %; however, the reported water splitting efficiency for α-Fe_2O_3 is much lower [6–9]. Actually, there are several reasons for this discrepancy such as a small optical absorption coefficient, a rapid electron(e^-)-hole(h^+) recombination resulting in short carrier

diffusion lengths (in the range of 2–4 [10], 20 nm [11]) and slow surface reaction kinetics.

One approach to improve the conversion efficiency is the development of nanostructured α-Fe_2O_3 thin films [8, 12]. The introduction of the nanometric scale can improve the surface reaction kinetics by an increased interfacial reaction area and avoid the electron-hole recombination due to the short diffusion path of the hole up to the surface in a nanostructured material with a crystal size close to the diffusion length of the hole. This approach seems to be very attractive; however, the influence of the nanoscale structure in the optical absorption of α-Fe_2O_3 is questionable.

Many research groups worldwide have focused their research on the hematite photoanode to produce oxygen with a reduced anodic overpotential and to improve the overall solar-to-hydrogen conversion efficiencies. In general, these researchers have achieved significant breakthroughs in decreasing the overpotential and modifying the photoanode surface with the addition of precious metals such as iridium [13], platinum [14], ruthenium [15] or cobalt [16–19]. These chemical elements increase the oxygen kinetic evolution that captures the hole currents on the semiconductor liquid junction [13]. Despite excellent results and advances which have been reported, we believe that high efficiency depends strongly on the nanostructure [20], grain boundaries [21], reduction of lattice defects and crystallographic orientation. In this case, these structural challenges could be overcome using suitable preparation methods and experimental parameters.

Thus, we will describe in this chapter recent progress regarding the design of a hematite nanostructure and its impact on the photoelectrochemistry performance for water splitting. Here we will discuss several chemical approaches to prepare the hematite photoanode such as: sol–gel, colloidal deposition and hydrothermal processes.

2 Photoanode Processed by Sol–Gel Process

The sol–gel process is a wet-chemical technique widely used in the fields of material chemistry and thin films. This method is used primarily for the processing of materials (typically metal oxides) starting from a solution (*sol*) that acts as the precursor for an integrated network (or *gel*). Typical precursors are metal alkoxides, metal salts or even metal-complex compounds such as citrates. In a suitable solvent, these precursors undergo a series of chemical transformation which results in a gel. The sol–gel solution offers several advances for thin film deposition such as good chemical composition control, film thickness and microstructure control and a low sintering temperature.

A very interesting and suitable sol–gel process for thin film preparation is the solution deposition of a polymerizable precursor. This method was used by our research group to process several kinds of metal oxide thin films and facilitated the attainment of nanostructured films with good stoichiometric and thickness control

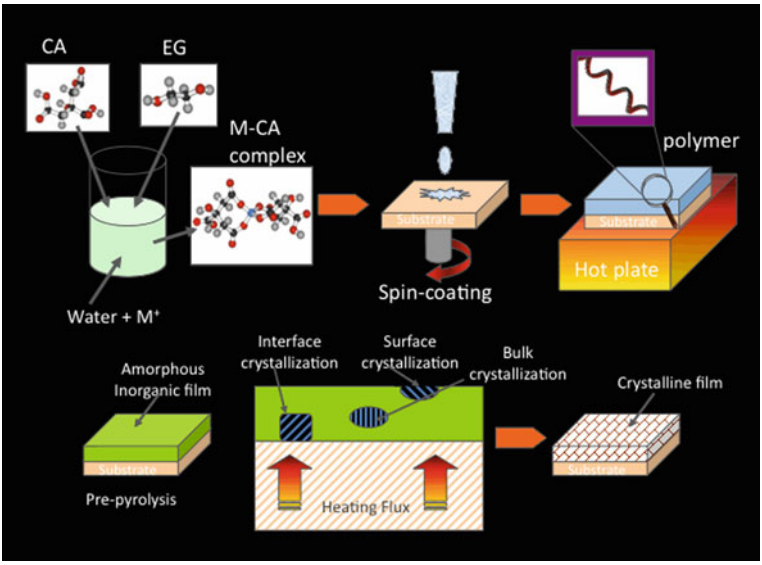

Fig. 2 Schematic illustration of the solution deposition of a polymerizable precursor for ceramic thin film processing

[22–24]. The process is based on the synthesis of a soluble polymeric precursor with the metals arrested in the polymeric chain. A hydrocarboxylic acid (such as citric acid) is used to chelate the ions of interest. Following this step, the addition of a glycol (such as ethylene glycol) leads to the formation of a soluble polyester. The polymerization processes, which are promoted by heating the mixture result in a homogeneous polymer where metal ions are uniformly distributed throughout the organic matrix. Figure 2 is a schematic representation of the solution deposition of a polymerizable precursor for ceramic thin film processing.

Recently, Souza et al. used this process to obtain a photoanode of undoped and Si-doped hematite thin films [25, 26]. In a typical synthesis procedure, citric acid ($[C_6H_8O_7]$) was dissolved in anhydrous ethyl alcohol and heated to a temperature of 60 °C. Then iron (III) nitrate ($[Fe(NO_3)_3.9H_2O]$) and tetra-ethyl-ortho-silicate ($TEOS\text{-}Si(CH_2CH_2OH)_4$) was mixed into the citric acid solution under constant stirring in a molar ratio of 3:1 ([citric acid]/[Fe + Si]). After homogenization of the solution containing Fe + (0.5 % wt) Si, ethylene glycol ($C_2H_6O_2$) was added to the mixture in a citric acid/ethylene glycol ratio of 60:40 wt %. The resulting solution was stirred and heated until it reached citrate polymerization by the polyesterification reaction. In this step, a high viscosity liquid was obtained. After the polymerization step, the viscosity was adjusted (decreased) by the addition of ethyl alcohol. The solution was deposited onto a transparent conducting glass substrate (FTO-Fluorine doped SnO_2 $R_\Omega < 15\Omega$/cm) where spin coating was conducted at a rotation speed of 7,000 rpm. After deposition, the substrate was heated on a hot plate at 50 °C for solvent evaporation and heat treated at 500 °C for 2 h for the film

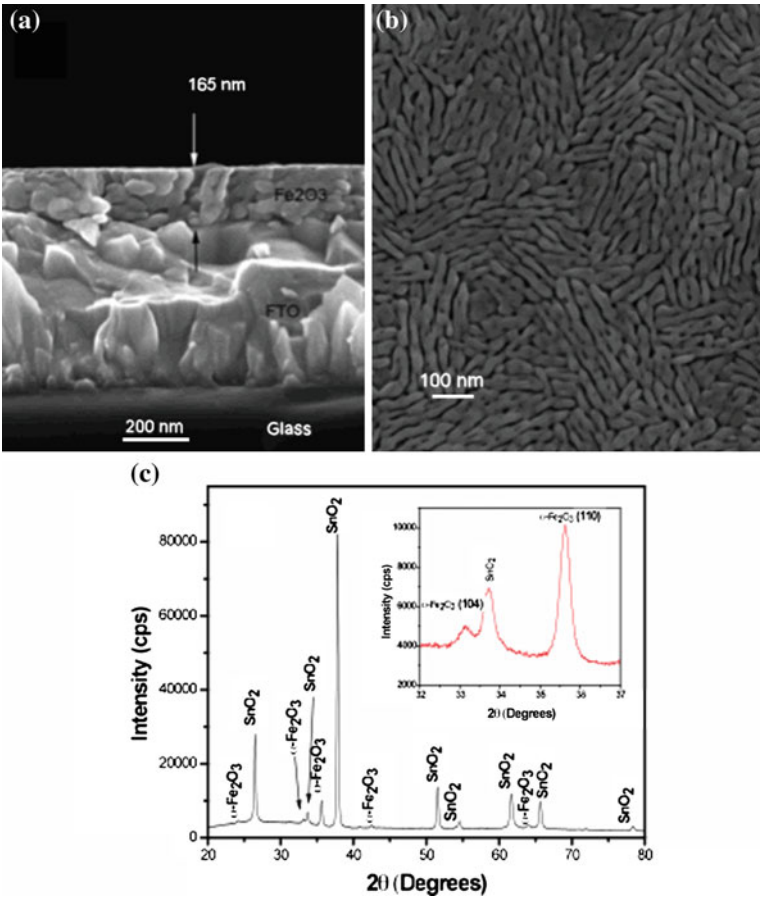

Fig. 3 SEM and XRD characterization of the hematite thin film processed by solution deposition of a polymerizable precursor: **a** Cross section SEM analysis; **b** top-view SEM analysis; **c** XRD analysis, using CuKα radiation

crystallization (at a heating and cooling rate of 1 °C/min). To control the film thickness, the solution viscosity was adjusted as well as the number of deposition layers. For instance, to obtain a film of 165 nm, four layers were deposited (with complete deposition cycle; i.e., deposition and heat treatment).

The deposition process produced orange-red transparent films. Figure 3 illustrates the scanning electron microscopy characterization of the cross section (see Fig. 3a) and the top-view analysis (see Fig. 3b) of typical films produced by this sol–gel process. A thin film with a uniform and continuous morphology is visible. The top view analysis exhibits the nanostructured nature of the film, with elongated grains and a diameter ranging from 20–30 nm and a length of 60–100 nm. However, the cross-section analysis suggests that the film is formed by several grain layers. This cross-section morphology is typical of films prepared

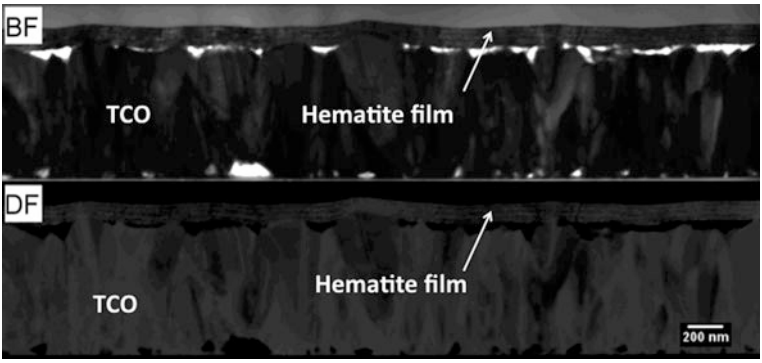

Fig. 4 Scanning-transmission electron microscopy (STEM) image of the hematite thin film processed by solution deposition of a polymerizable precursor: **a** *Bright* field (BF) image; **b** *dark* field (DF) image

by solution deposition and multiple deposition steps. An X-ray diffraction (XRD) pattern of the film (see Fig. 3c) exhibits the formation of a hematite phase with preferential orientation in the [110] axis vertical to the substrate (see inset of Fig. 1), even for the thinner film. This result indicates that the (001) plane is oriented vertical to the substrate. It is well know that the hematite presents a strong anisotropy in electronic conductivity. Actually the conductivity in the basal plane (001) is up to 4 orders of magnitude higher than the orthogonal planes [8], and this preferential orientation should facilitate the collection of electrons during the photooxidation process. A similar orientation was observed by several authors [6–9] using different deposition methods.

Despite the very nice microstructure and favorable crystallographic structure, this methodology did not result in a film with a high photocurrent [25, 26]. The highest photocurrent density observed for this film at 1.23 V_{RHE} was 3.4×10^{-5} A/cm^2. At 1.6 VRHE, this film had a photocurrent density of 1.5×10^{-4} A/cm^2. The main reasons for this low performance in terms of the photocurrent are the low film porosity and the very poor interface between the hematite film and the transparent conductor oxide film. As shown in the scanning-transmission electron microscopy (STEM) image in Fig. 4, good contact is visible in only few regions of the interface which resulted in a low electron collection by the transparent conducting oxide (TCO) film. As consequence, a high recombination rate between electrons and holes must occur to realize a low photocurrent.

3 Colloidal Deposition

Among several methodologies listed in the literature to produce hematite photoanodes, colloidal dispersion deposition has shown promising results [27]. This approach demands an analysis of important variables before the deposition

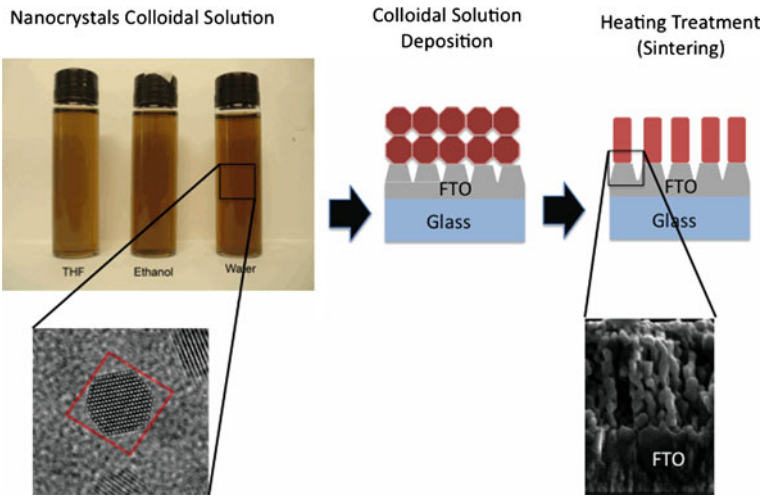

Fig. 5 Schematic representation of the colloidal deposition approach

and heat treatment processes; e.g., the surface chemical composition of the inorganic particle, the amount of organic material in the colloidal dispersion, the crystallinity and the morphology of nanoparticles. These features have strong influences on the formation of pure hematite that consequently affects the performance of water splitting. This process is displayed schematically in Fig. 5. The first step consists of the attainment of a colloidal solution of the nanocrystal to be deposited. Then the solution is deposited by traditional techniques such as spin or dip coating. The final step is film sintering. Recently, Gonçalves et al. [28] developed an interesting route to prepare a hematite photoanode, by using the colloidal deposition approach. In that research, the authors used a magnetite nanocrystal as the precursor for hematite. During the sintering process, the magnetite (Fe_3O_4) is transformed into hematite; the Fe_3O_4 transforms into gamma-maghemite γ-Fe_2O_3 at 200 °C, and γ-Fe_2O_3 is transformed into α-Fe_2O_3 (hematite) at 450 °C. This last reaction is critical because pure hematite is obtained just above the Neel point (725 °C) with a minimum amount of defects [19]. Thus, a sintering temperature that assures the complete elimination of the organic layer and oxidation of magnetite must be selected.

The magnetite colloidal approach produced orange-red transparent hematite films after sintering at 820 °C. Figure 6 illustrates cross-sectional (see Fig. 6a) and top-view (see Fig. 6b) analyses of the film morphology characterized by SEM. Figure 6a shows a film with a thickness of 930 nm and a typical columnar grain structure. Also, a good interface between the TCO and hematite film is apparent as well as the presence of an elongated porous which promotes the connection between the top of the hematite film and the TCO surface. Figure 6b (top-view analysis) exhibits the nanostructured nature of the film with elongated grains (a typical size of 50 nm) and open porosity, which characterizes a mesoporous

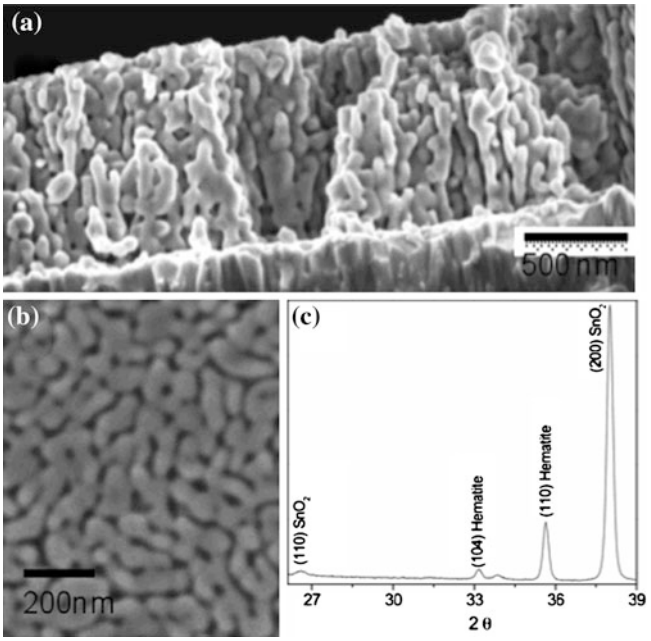

Fig. 6 SEM and XRD analysis of the hematite thin film prepared from the colloidal deposition of magnetite nanocrystals and sintered at 820 °C: **a** SEM cross-sectional analysis; **b** SEM top-view analysis; **c** XRD pattern

film. The XRD analysis of the film sintered at 820 °C (see Fig. 6c) exhibits the formation of a hematite phase with preferential orientation in the [110] axis vertical to the substrate. The crystallite size for the thicker film is calculated from XRD data and Scherrer's equation and considers the [110] plane at 36 nm which supports the FE-SEM top-view analysis.

Photoelectrochemical characterization shows that the approach developed by Gonçalves and co-authors produced a high performance hematite electrode for water photooxidation with an onset potential as low as 0.8 V_{RHE}. This value is comparable to the best results reported in the literature for a hematite photoanode modified with catalytic materials [13]. A high plateau of photocurrent (photocurrent density of 1.1 $mA.cm^{-2}$ at 1.23 V_{RHE}) is also observed, even for a film with a grain size in the range of 50 nm. The Mott-Schottky analysis of the hematite film clearly indicates this material possesses a favorable surface rather than an improvement of bulk properties. Lower overpotential and high photocurrent values are attributed to favorable surface properties of the hematite grains obtained by using a high temperature and an oxygen atmosphere during the sintering process. It was addressed two origins of unfavorable surface properties that contribute to the low photocurrent in a hematite photoanode: 1) induced surface reconstruction (at least partially) for a structure that has electrochemical properties very similar to Fe_3O_4 properties [28]. It is well established that Fe_3O_4 is not a good catalytic

material to promote water oxidation; [29, 30] and 2) a small intrinsic faradaic rate constant for the oxidation of water on Fe_2O_3 associated with trap levels at or near the surface. It is clear that the extensive grain growth process promoted by the high sintering temperature (higher than the Neel point) and oxygen must contribute to the stabilization of the surface, avoiding any structure similar to Fe_3O_4. Those treatments must also decrease the surface state recombination as well as the recombination in the depletion region. The reason for this modification is not clear and is under investigation; however, we can propose that the high sintering temperature under oxygen flow leads to a passivation of the surface trapping state due to the formation of an elongated textured hematite grain with a high fraction of (001) surface. In general, in relation to other hematite surfaces, it is accepted that the (001) surface is relatively inert (in water) for the protonation and deprotonation reactions needed for charge accumulation [31]. This behavior can be favorable in decreasing the hematite surface trapping state in a water-based electrolyte. Another important contribution of the Gonçalves works is the morphology of the photoanode. A columnar grain structure oriented in a favorable crystallographic orientation for electron collection and a mesoporous structure was obtained which permits the penetration of the electrolyte up to the TCO interface which must also contribute to the high photocurrent.

4 Hydrothermal Synthesis

As discussed in the previous sections, one of the most promising materials used as a photoanode in a photoelectrochemical cell to split water is iron oxide (α- Fe_2O_3) which has photocatalytic efficiency, high photocorrosion stability and electronic conductivity directly linked to crystal facets. Based on this argument, strategies to produce materials with oriented morphology onto substrates at the (001) crystallography facet are required to obtain better catalytic activity and electronic conductivity of hematite photoanodes. In the last two decades, significant progress has been achieved in hierarchical nanoarchitecture based on aqueous solution under hydrothermal conditions in a highly basic or acidic medium which is attractive to many research groups worldwide [32]. Particularly from this process, a one-dimensional (1D) nanostructure vertically oriented onto a substrate has been used as a great alternative to enhance photocatalytic properties of several metal oxides used as photoanodes [33–38]. To better illustrate the morphological advantages of a 1D nanostructure to overcome hematite limitations, an interesting schematic comparison between hematite films grown parallel and perpendicular onto the substrate, are depicted in the Fig. 7.

Usually, the nanostructured film composed of interconnected nanoparticles shows low photocatalytic efficiency due its high recombination rate between a photogenerate electron and a hole favorable for grain boundaries presence (see Fig. 7, left side). A 1D nanorod vertically oriented to the substrate is an alternative to overcome the short hole diffusion and/or inefficient electron collection scheme

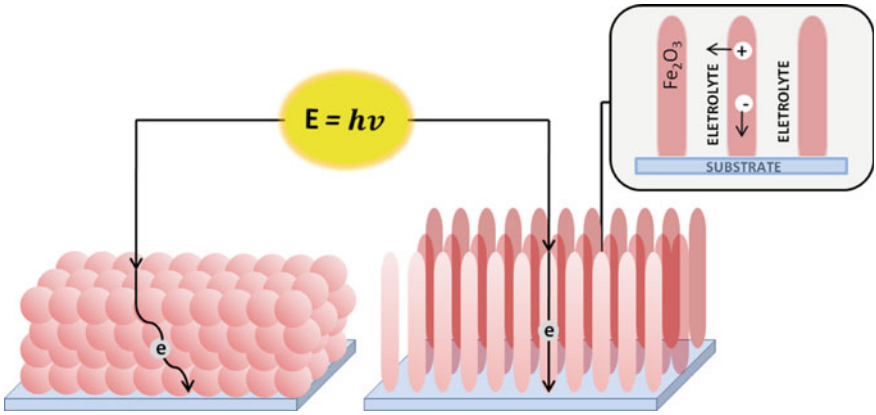

Fig. 7 Schematic representation of electron transport through hematite morphology grown parallel and orthogonal onto a conductor substrate. (Figure adapted from Ref. [37])

(see Fig. 7, right side). A zoom-in in Fig. 7 illustrates the desired morphology with a low number of structural defects leading to a very low recombination rate due its fast electron collection by a substrate and an efficient contact semiconductor/liquid favoring water oxidation (hole/liquid contact). This strategy may enhance the hematite performance and aid in overcoming its limitations.

Vayssieres and co-workers have created a very promising route based on a controllable aqueous chemical solution under hydrothermal conditions which is able to produce (in a single step) a wide gamut of metal oxide vertically oriented crystalline nanorod arrays onto a substrate [36]. Using the route called purpose built materials (*PBM*), Vayssieres et al. [36] produced hematite films and investigated the performance of this new materials product as a photoanode in a photoelectrochemical cell which shows the advantage of a 1D nanostructure as compared with an interconnected nanoparticle film. As expected, they verified that *PBM* films provide a more efficient transport and collection of photogenerated electrons through a designed path as compared with films constituted of sintered spherical particles. Their experiments involved a three configuration electrode cell, and their results and discussion take into account the effect of morphology, orientation, film thickness, electrolyte composition and dye sensitization. They demonstrated an improvement in the IPCE (incident photon-to-current conversion efficiency) of 100 and 7 times, respectively as compared with research conducted earlier on thin films with spherical particles [37, 38] with 0.1 M KI in water (pH 6.8) as the electrolyte which was illuminated either through the electrolyte/electrode interface or through the substrate ($F:SnO_2$)/electrode interface. In addition, they using the electrolyte with different pH from 6.8 to 12.0 also increased the IPCE by a factor of two. Since the first report using this promising *PBM* synthetic route [36–38], research effort has been dedicated to a better understanding and improvement of hematite-oriented nanorod performance in PEC systems.

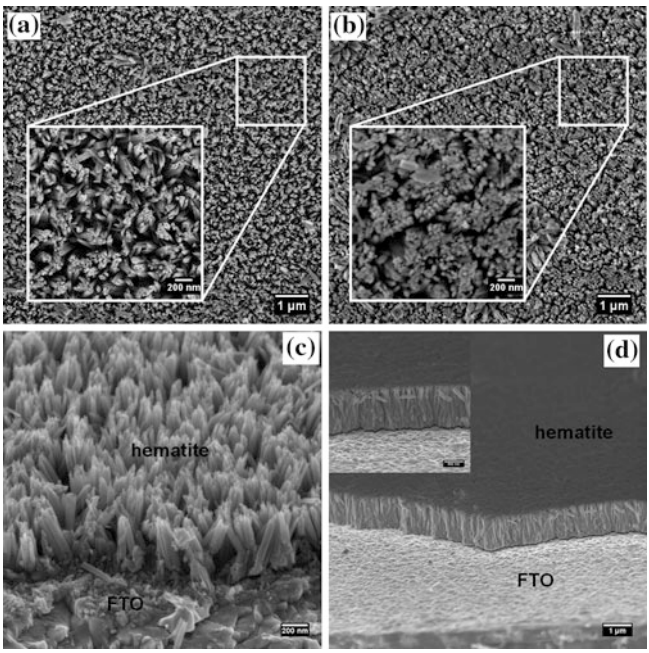

Fig. 8 SEM images of a hematite film: **a** and **b** Top-view: synthesized during 6 and 24 h under hydrothermal conditions and sintered at 390 °C, respectively; **c** and **d** cross-section of a corresponding film obtained after 6 and 24 h. A zoom-in of **d** illustrates the interface FTO-hematite

Recently, Carvalho et al. [35] reported a significant improvement in photocurrent response using the *PBM* method by employing the fundamental strategy to prepare better undoped hematite films and also to address and overcome real challenges. The photocurrent generated under the front side illumination using the developed photoanode was found to be three orders of magnitude higher as compared with the seminal work by Vayssieres [36–38] in the same applied condition: three electrode configuration cell, platinum foil as counter electrode, Ag/AgCl as a reference and NaOH, pH 13.6 as the electrolyte. In that research, the commercial substrate surface was cleaned several times before and after subjection to a thermal treatment at 390 °C for a few hours. Figure 8 illustrates the top-view and cross-section SEM image analysis of film morphology sintered at 390 °C for 1 h.

As expected, a high homogeneous film with a large nanorod distribution (see Fig. 8a and c) was obtained with a modified substrate as compared with the material reproduced from the original strategy [36] (see Fig. 8b and d). From the cross-section SEM images of films synthesized for 24 h (see Fig. 8d) and 6 h under hydrothermal conditions (Fig. 8c), the film thickness was estimated to be 450 nm. In addition, the distance between each rod given an open structure

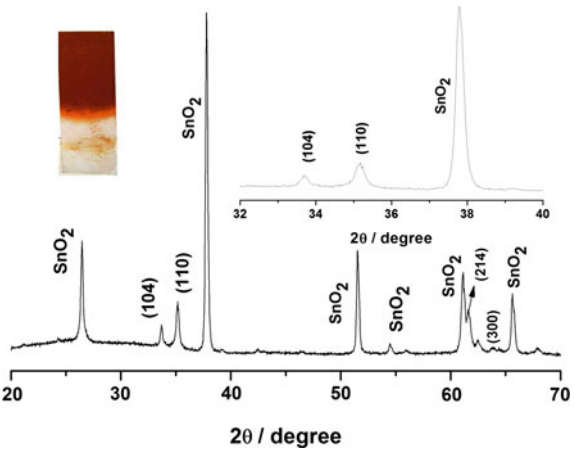

Fig. 9 XRD diffraction data of a hematite film under 6 h of hydrothermal condition and sintered at 390 °C for 1 h. Left side: Photo of obtained hematite film studied

provides a good interface between FTO-hematite films and was more efficiently achieved after 6 h of hydrothermal processing (see Fig. 8a and c).

Here the as-prepared film shows the oxy-hydroxide (β-FeOOH) crystallographic arrangement (details discussed in Ref. [35]). To obtain a pure hematite phase, all films are submitted to an additional thermal treatment at 390 °C for 1 h. The films acquire a typical red color from the hematite phase (see film aspect in Fig. 9). The XRD analysis of the film sintered at 390 °C for 1 h, (see Fig. 9) exhibits the typical indexed planes related to the formation of hematite (α-Fe_2O_3). The peaks identified in Fig. 9 assigned to SnO_2 (the cassiterite phase) is from the fluorine-doped SnO_2 (FTO) substrate. As extensively discussed in the literature [7, 8, 25, 28, 35, 39], an important requirement to extract better electronic interface FTO-hematite layers (to facilitate electron collection) is the preferential structure grown in the perpendicular plane of the (001) substrate. The inset in Fig. 9 illustrates that the hematite nanorod prepared by using the hydrothermal process exhibits preferential orientation in the [110] plane perpendicular to FTO as required.

Another requirement for any semiconductor to be employed in PEC systems is a high absorption of a solar irradiation spectrum. Carvalho showed that the film with red colored α-Fe_2O_3 nanorods exhibits strong absorption in the visible region which reaches the maximum value (see Fig. 10). The inset in Fig. 10 illustrates the comparison between the substrate before and after modification with 450 nm of deposited hematite film. As expected, the FTO substrate has very low absorption in the visible range; i.e., it does not significantly participate in the global photocurrent response during application in the PEC cell. Basically, hydrogen and oxygen are generated by an illuminated hematite film/liquid interface. Furthermore, from these data, indirect and direct electronic band gaps were calculated by considering the following equation: $(\alpha h\nu) = A_o(h\nu - E_g)^m$ where $h\nu$ is the photon energy (in eV), E_g is the optical band gap energy (in eV) and A_o and m are constants which depend on the kind of electronic transition where m is equal to 1/2 for a direct

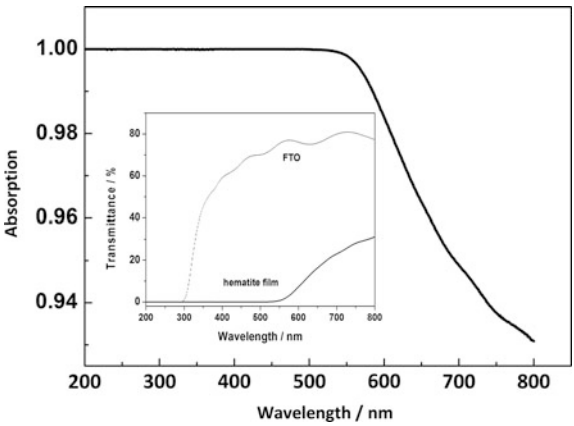

Fig. 10 Absorption versus wavelength spectra of FTO modified with hematite layer produced after 6 h under hydrothermal condition and sintered at 390 °C for 1 h. Inset: Curve of transmittance versus wavelength of FTO conductor substrate (520 nm) and FTO modified with hematite layer (450 nm)

allowed and 2 for an indirect forbidden transition. The values estimated were 1.95 and 2.1 eV, respectively, which is in good agreement with the literature [35–53].

Additionally, based on the excellent performance of the films prepared after 6 h under hydrothermal conditions and sintered at 390 °C, Carvalho et al. [35] reported a detailed study dedicated to the semiconductor/liquid interface using cyclic voltammetry (an electrochemical technique). As observed in SEM images, hematite films have a high surface area due to vertically oriented rods on a substrate which promotes excellent hole transport to the semiconductor surface. Hematite is an *n*-type semiconductor with Fermi energy closer to the conduction band than to the valence band.

Molecular oxygen evolution at the hematite surface is still an important challenge for the scientific community to overcome [54–61]. To better understand the formation of molecular oxygen on the hematite surface, cyclic voltammetric experiments of the pure and modified FTO substrate were conducted. FTO modified with a hematite layer was cycled several times (more than 100 cycles; see inset in Fig. 11a) through a basic medium (pH 13.6) with a potential window ranging from 0.8 to 0.8 V in dark conditions (Fig. 11). In this potential range, clearly there is an irreversible reduction peak at −0.5 V (see Fig. 11a). As expected, by varying the scan rate (v), the electrochemical reaction is limited by a charge-transfer [62–64] up to 500 $mV.s^{-1}$ which confirms that the electrochemical process originates from adsorbed groups at the nanorod surface. Surprisingly, this process appears only if the electrochemistry follows an anodic pathway (see inset in Fig. 11b); otherwise, it slowly disappears, and reveals the consumption of these species at the surface. Similar to a cathodic peak found here, this process has appeared in TiO_2 an electrode (in the context of dye-sensitized solar cells) which is attributed to the charging of surface states when there is also chemical capacitance in the semiconductor and space charge capacitance [65–81].

Several effects in the cathodic region were reported for nanostructured TiO_2 films [65–81] exhibiting several characteristic features; the dominant features are related to exponential densities of states (DOS) at negative potentials approaching

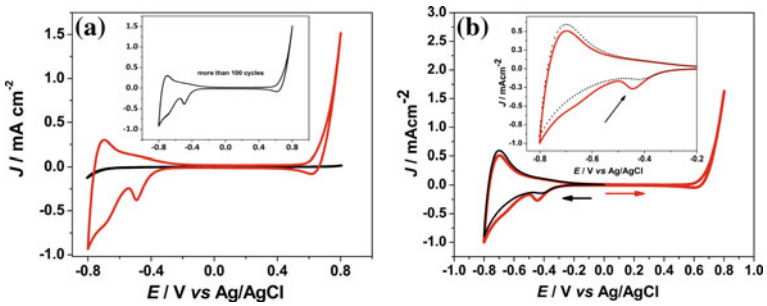

Fig. 11 Cyclic voltammograms under dark conditions at pH 13.6 (NaOH) of: **a** Pure FTO (*black line* (—)) and FTO-hematite (*red line* (-)). Inset: FTO-hematite performance during more than 100 cycles of stability; **b** FTO-hematite (*black line*) measured at a negative potential and FTO-hematite at a positive potential (*red line*). Inset: Zoomed-in image of the FTO-hematite in the negative region. All measurements were performed at 50 $mV.s^{-1}$ (23 °C ± 0.1 °C)

the conduction band potential. Bisquert et al. [80] reported that the symmetric and much less intense peak appears at less negative potentials (similar to the hematite at the −0.8 V region). These features are highly symmetric with respect to the voltage axis in good quality electrodes, although they sometimes appear as a distortion due to the IR drop. Also, it was reported that for a very negative potential scan where the electrochemical potential is close to the conduction band edge, the capacitance is controlled by both the Helmholtz capacitance at the inner surface and the film entrance into band unpinning [80, 82]. Furthermore, an additional peak at a more positive potential can appear (in our case, for hematite at −0.5 V) which was well established experimentally in 1995 by Gratzel et al. for nanostructured TiO_2 films [69].

However, in their research with hematite nanorods, Carvalho et al. [35] has assumed that the adoption of OH^- groups on the hematite surface shows an electrochemical behavior governed by a Nernstian equilibrium which is similar to the Nernstian H^+/OH^- equilibrium reported for nanostructured TiO_2 films [83–85]. This result is a strong indication that the electrocatalytic anodic process for molecular oxygen evolution is also undergoing a structural rearrangement step where some species of Fe(III) in the hematite crystalline structure have different energies from the energies in bulk nanorods. For the latter assumption, this effect should only occur in basic media when the OH^- ions are directly associated with the reaction mechanism. Carvalho et al. [35] proposed a simply way to verify the dependence of this reaction on OH^- ion concentration. They carried out the same electrochemical experiment at neutral KCl with a 0.1 $mol.L^{-1}$ electrolyte. As expected, no changes in the voltammetry profile were observed; only a decrease in the capacitive currents was observed in this case. Based on the experimental investigation, the authors suggested an intermediate slow step where Fe(III) forms an oxide/hydroxide intermediate before the molecular oxygen evolution. A complete mechanism proposed by them for oxygen evolution on a hematite nanorod film is shown in Eqs 3.1 and 3.2.

Step1: OH^- adsorption (*slow*)

$$4\alpha - Fe_2O_3 + 4OH^- \rightarrow 4\alpha - Fe_2O_3(OH)^-_{ads} \quad (3.1)$$

Step2: molecular oxygen evolution ($E = 0.38$ V)

$$4\alpha - Fe_2O_3(OH)^-_{ads} + 4hv \rightarrow 4\alpha - Fe_2O_3 + \uparrow O_2 + 2H^+ + 2H_2O + 2e^- \quad (3.2)$$

In summary, this additional step considers a slow intermediate reaction (formation of oxide/hydroxide) before the molecular oxygen evolution; other elementary steps in the detailed mechanism are unknown. Thus the OER mechanism proposed by Carvalho et al. [35] is an important contribution as one of several other mechanisms for different materials found in literature [86–94]. An excellent example is based on Tafel slopes as suggested by Trasatti et al. [91] where the molecular oxygen is liberated from two highly oxidized sites and deposited onto the semiconductor surface. Therefore, the latter proposed mechanism does not make any distinction between the intermediate oxygen that arises from the oxide lattice and from the water species. Finally for hematite nanorods developed by Carvalho et al. [35], both effects appear to be evident where the OH^- arising from the solution and the formation of oxide/hydroxide play important roles in water splitting.

Acknowledgments We gratefully acknowledge financial support from the Brazilian agencies of FAPESP (Grant No. 2010/02464-6), CAPES, CNPq (555855/2010-4), Instituto Nacional em Eletrônica Orgânica (INEO), NanoBioMed Brazilian Network (CAPES) and INCTMN.

References

1. Fujishima A, Honda K (1972) Electrochemical photolysis of water at a semiconductor electrode. Nature 238:37
2. Park JH, Kim S, Bard AJ (2006) Novel carbon-doped TiO_2 nanotube arrays with high aspect ratios for efficient solar water splitting. Nano Lett 6:24–28
3. Matsuoka M, Kitano M, Takeuchi M, Tsujimaru K, Anpo M, Thomas JM (2007) Photocatalysis for new energy production. Catal Today 122:51–61
4. Mor KG, Prakasam HE, Varghese OK, Shankar K, Grimes CA (2007) Vertically oriented Ti-Fe-O nanotube array films: towards a useful material architecture for solar spectrum water photolysis. Nano Lett 7(8):2356–2364
5. Murphy AB, Barnes PRF, Randeniya LK, Plumb IC, Grey IE, Horne MD, Glasscock JA (2006) Efficiency of solar water splitting using semiconductor electrodes. Int J Hydrogen Energy 31:1999–2017
6. Duret A, Gratzel M (2005) Visible light-induced water oxidation on mesoscopic α-Fe_2O_3 films made by ultrasonic spray pyrolysis. J Phys Chem B 109:17184–17191
7. Cesar I, Kay A, Gonzalez Martinez JA, Gratzel M (2006) Translucent thin film Fe_2O_3 photoanodes for efficient water splitting by sunlight: nanostructure-directing effect of si-doping. J Am Chem Soc 128(14):4582–4583
8. Kay A, Cesar I, Gratzel M (2006) New benchmark for water photooxidation by nanostructured α-Fe2O3 films. J Am Chem Soc 128(49):15714–15721

9. Glasscock JA, Barnes PRF, Plumb IC, Savvides N (2007) Enhancement of photoelectrochemical hydrogen production from hematite thin films by the introduction of Ti and Si. J Phys Chem C 111:16477–16488
10. Dare-Edwards MP, Goodnough JP, Hamnett A, Trevellick PR (1983) Electrochemistry and photoelectrochemistry of iron(III) oxide. J Chem Soc, Faraday Trans 79:2027–2041
11. Kennedy JH, Frese KW Jr (1978) Photooxidation of water at α-Fe_2O_3 electrodes. J Electrochem Soc 125(5):709–714
12. van de Krol R, Liang Y, Schoonman J (2008) Solar hydrogen production with nanostructured metal oxides. J Mater Chem 18:2311–2320
13. Tilley SD, Cornuz M, Sivula K, Gratzel M (2010) Light-induced water splitting with hematite: improved nanostructure and iridium oxide catalysis. Angew Chem Int Ed 49:6405–6408
14. Hu YS, Kleiman-Shwarsctein A, Forman AJ, Hazen D, Park J-N, McFarland EW (2008) Pt-doped alpha- Fe2O3 thin films active for photoelectrochemical water splitting. Chem Mater 20:3803–3805
15. Sartoretti CJ, Alexander BD, Solarska R, Rutkowska IA, Augustynski J (2005) Photoelectrochemical oxidation of water at transparent ferric oxide film electrodes. J Phys Chem B 109:13685–13692
16. Zhong DK, Sun J, Inumaru H, Gamelin DR (2009) Solar water oxidation by composite catalyst/α-Fe_2O_3 photoanodes. J Am Chem Soc 131:6086–6087
17. Kanan MW, Nocera DG (2008) In situ formation of an oxygen-evolving catalyst in neutral water containing phosphate and Co^{2+}. Science 321:1072–1075
18. Steinmiller EMP, Choi K-S (2009) Photochemical deposition of cobalt-based oxygen evolving catalyst on a semiconductor photoanode for solar oxygen production. PNAS 106(49):20633–20636
19. Shiroishi H, Nukaga M, Yamashita S, Kaneko M (2002) Efficient photochemical water oxidation by a molecular catalyst immobilized onto metal oxides. Chem Lett 31:488–489
20. Bjorkstbn U, Moser J, Gratzel M (1994) Photoelectrochemical studies on nanocrystalline hematite films. Chem Mater 6:858–863
21. Ahrned SM, Leduc J, Haller SF (1988) Photoelectrochemical and impedance characteristics of specular hematite. 1. photoelectrochemical parallel conductance, and trap rate studies. J Phys Chem B 92:6655–6660
22. Bouquet V, Bernardi MIB, Zanetti SM, Leite ER, Longo E, Varela JA, Viry MG, Perrin A (2000) Epitaxially grown $LiNbO_3$ thin films by polymeric precursor method. J Mater Res 15:2446–2453
23. Pontes FM, Leite ER, Mambrini GP, Escote MT, Longo E, Varela JÁ (2004) Very large dielectric constant of highly oriented Pb1-xBaxTiO_3 thin films prepared by chemical deposition. Appl Phys Lett 84(2):248–250
24. Mambrini GP, Leite ER, Escote MT, Chiquito AJ, Longo E, Varela JA, Jardim RF (2007) Structural, microstructural, and transport properties of highly oriented $LaNiO_3$ thin films deposited on $SrTiO_3$ (100) single crystal. J Appl Phys 102:043708
25. Souza FL, Lopes KP, Longo E, Leite ER (2009) The influence of the film thickness of nanostructured alpha-Fe(2)O(3) on water photooxidation. Phys Chem Chem Phys 11:1215–1219
26. Souza FL, Lopes KP, Longo E, Leite ER (2009) Nanostructured hematite thin film produced by spin-coating deposition solution: application in water splitting. Sol Energ Mat Sol Cells 93:362–368
27. Sivula K, Zboril R, Formal F, Robert R, Weidenkaff A, Tucek J, Frydrych J, Gratzel M (2010) Photoelectrochemical water splitting with mesoporous hematite prepared by a solution-based colloidal approach. J Am Chem Soc 132:7436–7444
28. Gonçalves RH, Lima BHR, Leite ER (2011) Magnetite colloidal nanocrystals: a facile pathway to prepare mesoporous hematite thin films for photoelectrochemical water splitting. J Am Chem Soc 133:6012–6019

29. Trasatti S (1980) Electrocatalysis by oxides—Attempt at a unifying approach. J Electroanal Chem 111:125–131
30. Walter MG, Warren EL, McKone JR, Boettcher SW, Mi Q, Santori EA, Lewis NS (2010) Solar water splitting cells. Chem Rev 110:6446–6473
31. Yanina SV, Rosso KM (2008) Linked reactivity at mineral-water interfaces through bulk crystal conduction. Science 320:218–222
32. Kronawitter CX, Vayssieres L, Shen S, Guo L, Wheeler DA, Zhang JZ, Antoun BR, Mao SS (2011) A perspective on solar-driven water splitting with all-oxide hetero-nanostructures. Energy Environ Sci 4:4889
33. Morrish R, Rahman M, Don MacElroy JM, Wolden CA (2011) Activation of hematite nanorod arrays for photoelectrochemical water splitting. Chem Sus Chem 4:474–479
34. Ling Y, Wang G, Reddy J, Wang C, Zhang JZ, Li Y (2012) The influence of oxygen content on the thermal activation of hematite nanowires. Angew Chem 51:1–7
35. Carvalho VAN, Luz RAS, Lima BH, Crespilho FN, Leite ER, Souza FL (2012) Highly oriented hematite nanorods arrays for photoelectrochemical water splitting. J Power Sources 205:525–529
36. Vayssieres L, Beermann N, Lindquist SE, Hagfeldt A (2001) Controlled aqueous chemical growth of oriented three-dimensional crystalline nanorod arrays: application to iron (III) oxides. Chem Mater 13(2):233–235
37. Beermann N, Vayssieres L, Lindquist SE, Hagfeldt A (2000) Photoelectrochemical studies of oriented nanorod thin films of hematite. J Electrochem Soc 147(7):2456–2461
38. Lindgren T, Wang H, Beermann N, Vayssieres L, Lindquist SE, Hagfeldt A (2002) Aqueous photoelectrochemistry of hematite nanorod-array Sol. Energy Mat Solar Cells 71(12):231–243
39. Cornuz M, Graetzel M, Sivula K (2010) Preferential orientation in hematite films for solar hydrogen production via water splitting. Chem Vap Deposition 16:291–295
40. Cherepy NJ, Liston DB, Lovejoy JA, Deng HM, Zhang JZ (1998) Ultrafast studies of photoexcited electron dynamics in γ- and α-Fe_2O_3 semiconductor nanoparticles. J Phys Chem B 102(5):770–776
41. Sivula K, Formal FL, Gratzel M (2009) WO_3—Fe_2O_3 photoanodes for water splitting: a host scaffold guest absorber approach. Chem Mater 21(13):2862–2867
42. Cesar IK, Sivula K, Kay A, Zboril R, Gratzel M (2008) Influence of feature size, film thickness, and silicon doping on the performance of nanostructured hematite photoanodes for solar water splitting. The J Phys Chem C 113(2):772–782
43. Kharisov BI, Kharissova OV, Yacaman MJ (2010) Nanostructures with animal-like shapes. Ind Eng Chem Res 49(18):8289–8309
44. Sun J, Zhong DK, Gamelin DR (2010) Composite photoanodes for photoelectrochemical solar water splitting. Energy Environ Sci 3(9):1252–1261
45. Andrade L, Cruz R, Ribeiro HA, Mendes A (2010) Impedance characterization of dye-sensitized solar cells in a tandem arrangement for hydrogen production by water splitting. Int J Hydrogen Energy 35(17):8876–8883
46. Frydrych J, Machala L, Hermanek M, Medrik I, Mashlan M, Tucek J, Pechousek J et al (2010) A nanocrystalline hematite film prepared from iron (III) chloride precursor. Thin Solid Films 518(21):5916–5991
47. Hahn NT, Ye H, Flaherty DW, Bard AJ, Mullins CB (2010) Reactive ballistic deposition of α-Fe_2O_3 thin films for photoelectrochemical water oxidation. ACSNANO 4(4):1977–1986
48. Li Y, Zhang JZ (2009) Hydrogen generation from photoelectrochemical water splitting based on nanomaterials. Laser Photonics Rev 4(4):517–528
49. Tahir AA, Upul Wijayantha KG, Yarahmadi SS, Mazhar M, McKee V (2009) Nanostructured α-Fe_2O_3 thin films for photoelectrochemical hydrogen generation. Chem Mater 21(16):3763–3772
50. Formal FL, Tétreault N, Cornuz M, Moehl T, Gratzel M, Sivula K (2011) Passivating surface states on water splitting hematite photoanodes with alumina overlayers. Chem Sci 2(4):737–743
51. Klahr BM, Hamann TW (2011) Current and voltage limiting processes in thin film hematite electrodes. The J Phys Chem C 115(16):8393–8399

52. McDonald KJ, Choi KS (2011) Photodeposition of Co-based oxygen evolution catalysts on α-Fe_2O_3 photoanodes. Chem Mater 23(7):1686–1693
53. Spray RL, McDonald KJ, Choi KS (2011) Enhancing photoresponse of nanoparticulate α-Fe_2O_3 electrodes by surface composition tuning. The J Phys Chem C 115(8):3497–3506
54. Lin Y, Zhou S, Sheehan SW, Wang D (2011) Nanonet-based hematite heteronanostructures for efficient solar water splitting. J Am Chem Soc 133(8):2398–2401
55. Sivula K, Formal FL, Gratzel M (2011) Solar water splitting: progress using hematite (α-Fe_2O_3) photoelectrodes. Chem Sus Chem 4(4):432–449
56. Pendlebury SR, Barroso M, Cowan AJ, Sivula K, Tang J, Gratzel M et al (2011) Dynamics of photogenerated holes in nanocrystalline α-Fe_2O_3 electrodes for water oxidation probed by transient absorption spectroscopy. Chem Commun 47(2):716–718
57. Wijayantha KGU, Yarahmadi SS, Peter LM (2011) Kinetics of oxygen evolution α-Fe_2O_3 photoanodes: a study by photoelectrochemical impedance spectroscopy. Phys Chem Chem Phys 13(12):5264–5270
58. Zhong DK, Cornuz M, Sivula K, Grätzel M, Gamelin DR (2011) Photo-assisted electrodeposition of cobalt-phosphate (Co-Pi) catalyst on hematite photoanodes for solar water oxidation. Energy Environ Sci 4(5):1759–1764
59. Dotan H, Sivula K, Gratzel M, Rothschild A, Warren SC (2011) Probing the photoelectrochemical properties of hematite (α-Fe_2O_3) electrodes using hydrogen peroxide as a hole scavenge. Energy Environ Sci 4(3):958–964
60. Chen J, Xu L, Li W, Gou X (2005) α-Fe_2O_3 nanotubes in gas sensor and lithium-ion battery applications. Adv Mater 17:582–586
61. Itoh K, Bockris JO (1984) Thin film photoelectrochemistry: iron oxide. J Electrochem Soc 131(6):1266–1271
62. Alencar WS, Crespilho FN, Zucolotto V, Oliveira ON Jr, Silva WC (2007) Influence of film architecture on the charge-transfer reactions of metallophthalocyanine layer-by-layer films. The J Phys Chem C 111(34):12817–12821
63. Crespilho FN, Ghica ME, Caridade CG, Oliveira ON Jr, Brett C (2008) Enzyme immobilisation on electroactive nanostructured membranes (ENM): optimised architectures for biosensing. Talanta 76(4):922–928
64. Brett CMA, Brett AMO (1993) Electrochemistry Principles, Methods and Applications. Oxford University Press, New York
65. Moser J, Gratzel M (1982) Photoelectrochemistry with colloidal semiconductors; laser studies of halide oxidation in colloidal dispersions of TiO_2 and α- Fe_2O_3. Helv Chim Acta 65(5):1436–1444
66. Gardner RFG, Sweett F, Tanner DW (1963) The electrical propertie of alpha ferric oxide—II. Ferric oxide of high purity. J Phys Chem Solids 24:1183–1196
67. Drissi SH, Abdelmoula RM, Génin JMR (1995) The preparation and thermodynamic properties of Fe(II)-Fe(III) hydroxide-carbonate (green rust 1); Pourbaix diagram of iron in carbonate-containing aqueous media. Corros Sci 37(12):2025–2041
68. Berverskog B, Puigdomenech I (1996) Revised pourbaix diagrams for iron at 25–300 °C. Corros Sci 38(12):2121–2135
69. Kavan L, Kratochvilova K, Gratzel M (1995) Study of nanocrystalline TiO_2 (anatase) electrode in the accumulation regime. J Electroanal Chem 394(12):93–102
70. Boschloo G, Fitzmaurice D (1999) Spectroelectrochemical investigation of surface states in nanostructured TiO_2 electrodes. J Phys Chem B 103(12):2228–2231
71. Wang H, Boschloo JHG, Lindstrom H, Hagfeldt A, Lindquist SE (2001) Electrochemical investigation of traps in a nanostructured TiO_2 film. J Phys Chem B 105(13):2529–2533
72. Fabregat-Santiago F, Mora-Seró I, Garcia-Belmonte G, Bisquert J (2003) Cyclic voltammetry studies of nanoporous semiconductors. Capacitive and reactive properties of nanocrystalline TiO_2 electrodes in aqueous electrolyte. J Phys Chem B 107(3):758–768
73. Bisquert J (2003) Chemical capacitance of nanostructured semiconductors: its origin and significance for nanocomposite solar cells. Phys Chem Chem Phys 5(24):5360–5364

74. Randriamahazaka H, Fabregat-Santiago F, Zaban A, García-Cañadas J, Garcia-Belmonte G, Bisquert J (2006) Chemical capacitance of nanoporous-nanocrystalline TiO_2 in a room temperature ionic liquid. Phys Chem Chem Phys 8(15):1827–1833
75. Tirosh S, Dittrich T, Ofir A, Grinis L, Zaban A (2006) Influence of ordering in porous TiO_2 layers on electron diffusion. J Phys Chem B 110(33):16165–16168
76. Mor GK, Varghese OK, Paulose M, Shankar K, Grimes CA (2006) A review on highly ordered, vertically oriented TiO_2 nanotube arrays: fabrication, material properties, and solar energy applications. Sol Energy Mater Sol Cells 90(14):2011–2075
77. Law M, Greene LE, Radenovic A, Kuykendall T, Liphardt J, Yang P (2006) ZnO-Al_2O_3 and ZnO-TiO_2 core-shell nanowire dye-sensitized solar cells. J Phys Chem B 110(45):22652–22663
78. Mora-Seró I, Fabregat-Santiago F, Denier B, Bisquert J, Tena-Zaera R, Elias J et al (2006) Determination of carrier density of ZnO nanowires by electrochemical techniques. Appl Phys Lett 89(20):203117–203119
79. Bisquert J (2008) Physical electrochemistry of nanostructured devices. Phys Chem Chem Phys 10(1):49–72
80. Bisquert J, Fabregat-Santiago F, Mora-Seró I, Garcia-Belmonte G, Barea EM, Palomares E (2008) A review of recent results on electrochemical determination of the density of electronic states of nanostructured metal-oxide semiconductors and organic hole conductors. Inorg Chim Acta 361(3):684–698
81. Bisquert J (2011) A variable series resistance mechanism to explain the negative capacitance observed in impedance spectroscopy measurements of nanostructured solar cells. Phys Chem Chem Phys 13(10):4679–4685
82. Bisquert J, Zabn Z (2003) The trap-limited diffusivity of electrons in nanoporous semiconductor networks permeated with a conductive phase. Appl Phys A Mater Sci Process 77(3):507–514
83. Leng WH, Zhang Z, Zhang ZQ, Cao CN (2005) Investigation of the kinetics of a TiO_2 photoelectrocatalytic reaction involving charge transfer and recombination through surface states by electrochemical impedance spectroscopy. J Phys Chem B 109(31):15008–15023
84. Levine S, Smith AL (1971) Theory of the differential capacity of the oxide/aqueous electrolyte interface. Discuss Faraday Soc 52:290–301
85. Healy TW, White LR (1978) Ionizable surface group models of aqueous interfaces. Adv Colloid Interface Sci 9(4):303–345
86. Walter MG, Warren EL, McKone JR, Boettcher SW, Mi Q, Santori EA, Lewis NS (2010) Solar water splitting cells. Chem Rev 110(11):6446–6473
87. Cook TR, Dogutan DK, Reece SY, Surendranath Y, Teets TS, Nocera DG (2010) Solar energy supply and storage for the legacy and nonlegacy worlds. Chem Rev 110(11):6474–6502
88. Bockris JO, Huq A (1956) The mechanism of the electrolytic evolution of oxygen on platinum. Proc Royal Soc London A 237:277–296
89. Zhong DK, Gamelin DR (2010) Photoelectrochemical water oxidation by cobalt catalyst ("Co-Pi") α-Fe_2O_3 composite photoanodes: oxygen evolution and resolution of a kinetic bottleneck. J Am Chem Soc 132(12):4202–4207
90. Lutterman DA, Surendranath Y, Nocera DG (2009) A self-healing oxygen-evolving catalyst. J Am Chem Soc 131(11):3838–3839
91. Trasatti S (1994) In: Lipkowski J, Ross PN (eds) The electrochemistry of novel materials.VCH Publishers, New York
92. Wohlfahrt-Mehrens M, Heitbaum J (1987) Oxygen evolution on Ru and RuO_2 electrodes studied using isotope labelling and on-line mass spectrometry. J Electroanal Chem Interfacial Electrochem 237(2):251–260
93. Willsau J, Wolter O, Heitbaum J (1985) Does the oxide layer take part in the oxygen evolution reaction on platinum? A DEMS study J Electroanal Chem 195(2):299–306
94. Hibbert DB, Churchill CR (1984) Kinetics of the electrochemical evolution of isotopically enriched gases. Part 2-$^{18}O^{16}O$ evolution on $NiCO_2O_4$ and $Li_xCo_{3-x}O_4$ in alkaline solution. J Chem Soc, Faraday Trans 1 Phys Chem Condens Phases 80(7):1965–1971

Biofuel Cells: Bioelectrochemistry Applied to the Generation of Green Electricity

Gabriel M. Olyveira, Rodrigo M. Iost, Roberto A. S. Luz and Frank N. Crespilho

Abstract Several studies published in the last decade have pointed to the use of enzymes and microorganisms in biocatalytic reactions to generate electricity. Enzymes and living organisms can be used in modified electrodes to build the so-called biofuel cells (BFCs). However, a deep understanding of the structure and biocatalytic properties after enzyme immobilization is still lacking because they are immobilized in the solid state and outside of their natural environment. Thus, based on biological molecules and nanostructure materials applied to BFCs, these current topics shall be reviewed here, and prospects for future development in these areas will be presented as well. Moreover, immobilization methodologies and enzyme stability systems that result in BFCs will also be presented. Finally, BFC power density and catalyst support will be widely discussed in this book chapter.

1 Introduction

The modern concept of clean energy generation continues from the last century, with much interest being placed on the search for alternative sources of energy. The continuous use of the combustion of natural gases or nonrenewable fossil fuels like petroleum for energy production is the biggest challenge towards the

G. M. Olyveira · R. A. S. Luz
Centro de Ciências Naturais e Humanas, Universidade Federal do ABC, CEP, Santo André, SP 09210-170 Brazil

R. M. Iost · F. N. Crespilho (✉)
Institute of Chemistry of São Carlos (IQSC), University of São Paulo (USP), São Carlos, 13560-970 Brazil
e-mail: frankcrespilho@iqsc.usp.br

F. L. de Souza and E. R. Leite (eds.), *Nanoenergy*,
DOI: 10.1007/978-3-642-31736-1_4, © Springer-Verlag Berlin Heidelberg 2013

development of new, sustainable, and pollutant-free technologies with which to meet the global energy demand [1, 2]. The electrochemical energy produced by redox reactions has been extensively studied during the last few decades as an alternative and more environmentally favorable energy resource [3]. These redox systems are included in batteries, fuel cells, electrochemical capacitors, and biofuel cells, which use different principles of energy storage and energy conversion [4–9]. Although batteries are capable of storing and converting chemical energy into electrical energy, fuel cells have made remarkable progress in many applications and provide a portable, clean, and more efficient energy generation without the combustion of fuels [9]. A fuel cell consists of two electrodes, called the anode and cathode, which are immersed in an electrolyte solution whose electrons are removed from an input fuel on the anode to generate electrical energy. Generally, for the majority of organic fuel compounds, the products generated are H_2O and CO_2, and chemical energy storage is significantly higher as compared to common batteries. In addition, the development of electrochemical devices has resulted in increased energy production by chemical reactions in fuel cells relative to conventional batteries [4, 8–9]. However, the operation of fuel cells requires non-selective and expensive metals as catalysts for the necessary chemical reactions.

The study of bioelectrochemical reactions originated from biological organisms gained attention in the 1780s when Galvani first demonstrated nerves contracting in a frog′s leg upon application of external energy produced by a static electricity generator [10]. The possibility to use microorganisms to generate energy was also consider a possible technology for use at 50s decade [6]. This so-called biological fuel cell, or biofuel cell (BFC), is a particular kind of biodevice that utilizes biological components, such as enzymes or microorganisms, as selective recognition elements for a specific molecule capable of producing electrical energy by electrochemical redox processes [11–19]. The BFC system is similar to traditional fuel cells and consists of an anode and cathode modified with biological molecules that are commonly separated by a semi-permeable membrane at two separate compartments in an electrolyte solution. When a specific fuel is introduced into the anodic compartment, the oxidation reaction takes place and the electrons produced at the anode are used to reduce other chemical species, like oxygen, at the cathode. However, the amount of electrical energy obtained from biological molecules is very low, which generates an inefficient current characteristic of BFCs.

Recent research on BFCs have expanded on the utilization of the first microbial fuel cell in 1912 by Potter and co-workers [20]. This study provided a simple example of energy generation by fermentation of microorganisms like bacteria in glucose media. These electrochemical biodevices based on biological components offer many advantages over traditional chemical fuel cells, such as their use of renewable [21, 22] and non-pollutant [23] fuels, and their ability to operate at low temperatures [24]. Despite these advantages, the performance of BFCs in terms of power energy density generated by biochemical reactions, their lifetimes as compared to conventional fuel cells, and their stability during operational measurement are all responsible for the intense research in this area over the last years. Moreover, the main focus is to utilize biological components, as opposed to metal

catalysts, to catalyze biochemical reactions and generate energy with implantable biodevices in live organisms, like the human body [22]. Since the first such experiment reported by Yahiro in 1964 [25], which used the enzyme glucose oxidase (GOx) as the biological component for the anode in devices operating with glucose as fuel [25–36], many advances have been made which focus on their various applications, such as portable power biochips, implantable biodevices, etc. [22]. In addition to their use of renewable fuels, the favorable and mild temperature operation conditions make BFCs an interesting route for future energy production.

In this chapter, we present an overview of enzyme- and microbial-based BFCs for power energy production, and we explore their main operation characteristics, enzymatic immobilization on electrodes, and nanostructured materials for BFC applications. The focus of this chapter is to establish the correlation between enzymatic kinetic processes and nanostructured materials, and to briefly describe their utilization in modified electrodes for BFC power energy generation. Finally, the main applications and perspectives are detailed.

2 BFCs for Power Energy Production

The development of biomolecules-based electrochemical devices has arisen due to wide interest in their potential application in many areas, such as amperometric biosensors [37, 38] and, in particular, implantable biodevices for energy generation or BFCs [22]. The basic principle behind the energy generation of BFCs is similar to that of conventional fuel cells. However, BFCs use a recognition element in conjunction with biomolecules such as enzymes or microorganisms to produce electrical current, whereas traditional fuel cells use metallic electrodes [5–7]. BFCs consist of two electrodes that can be separated or not by a semi-permeable membrane [39–47], as can be seen in Fig. 1. Firstly, species are oxidized on the anode surface, and the electrons produced are driven throughout an external circuit and finally reach the cathode electrode [48]. Generally, water is produced when electrons are combined with an oxidizing agent, such as oxygen, present in the environment [41].

Several approaches have been published, revealing a large number of electrode configurations that involve the utilization of organic/inorganic hybrid molecules [43, 49–53] in BFCs. As an example, Scodeller and co-workers [52] reported the use of purified *Trametes trogii* laccase as a biocatalyst for an oxygen redox reaction on biocathodes composed of layer-by-layer self-assembled laccase and osmium complexes on mercaptopropane-sulfonate modified gold electrodes. This work shows a relevant operating system based on the detection of H_2O_2 as a result of O_2 electroreduction and generated by laccase biocatalysis mediated by an osmium complex. On the other hand, Raitman and co-workers [53] electropolymerized polyaniline (PAni) and polyacrylic acid (PAA) on electrode surfaces resulting in PAni/PAA films. Then, an amino-FAD cofactor was covalently linked

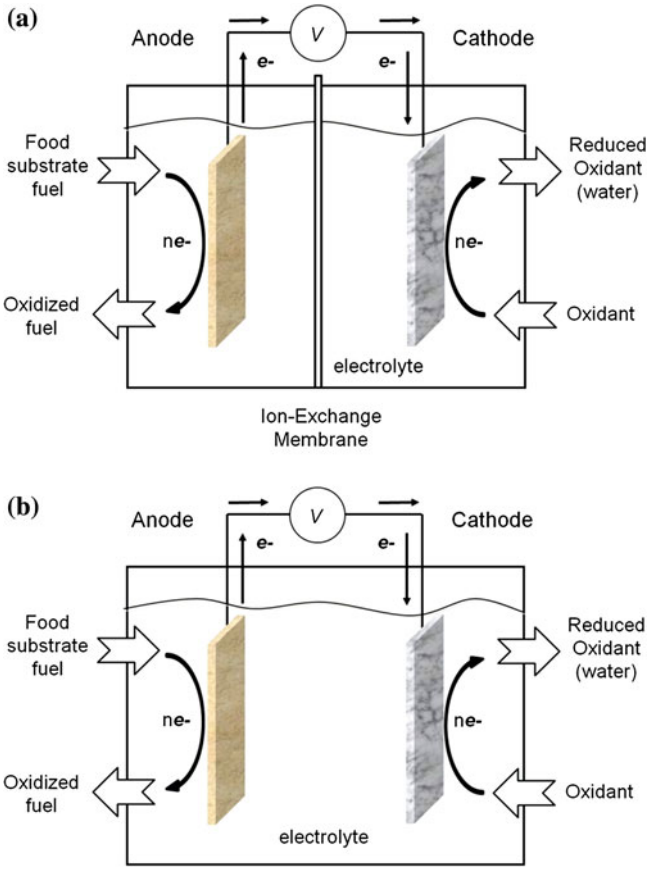

Fig. 1 Scheme of a general representation of two BFC configurations **a** with a semi-permeable membrane, and **b** in the absence of a membrane. The fuel is oxidized on the anode by a biological component, and the electrons released are transferred throughout an external circuit, which is associated with an oxidant element (usually O_2), to generate H_2O

to the PAA functional group chains, and apo-glucose oxidase was reconstituted on the FAD cofactor. The bioelectrocatalytic activation of the reconstituted enzyme was attributed to the appropriate alignment of the enzyme with respect to the electroactive PAni/PAA films, which in turn facilitated the electro-transfer between the cofactor site embedded in the enzyme and the electrode surface [53].

In addition to the use of enzymes, microorganisms like bacteria have also been extensively study as a new form of green and renewable energy generation [13–15, 54–62]. They posses several advantages over enzymes, such as complete oxidation of sugar components [19] and a decreased susceptibility to interfering agents [63] [69]. On the other hand, it is more difficult to access the energy produced inside these cell during the metabolic process. Conventional microbial-based BFCs are similar to other cell types and posses two electrodes (anode and cathode) separated

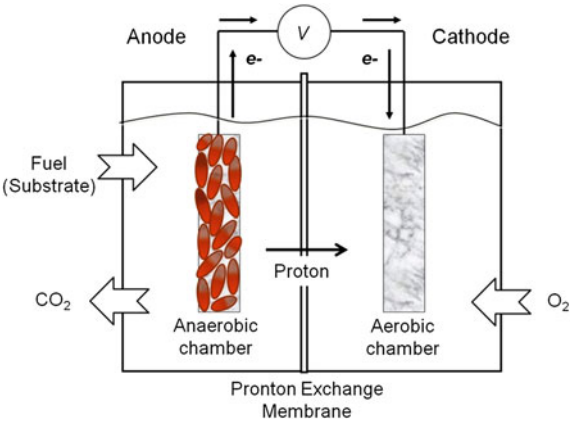

Fig. 2 A general schematic of a microbial-based BFC. The principle of power energy generation is similar to an enzymatic-based BFC

by a proton exchange membrane [39, 43, 46, 64, 65]. The oxidation of redox-active microorganisms occurs at the anode, while the cathode can be composed of a simple metal electrode. The functional activity of microorganisms facilitates the oxidation of organic compounds, which produces electrical energy that travels throughout an external circuit and generates water from the reduction of oxygen, while the proton exchange occurs via a semi-permeable membrane. A schematic configuration of a microbial BFC is presented in Fig. 2.

Many operational difficulties associated with BFCs, such as poor lifetime, low operation time, and poor stability, present big challenges associated with the large-scale application of this type of bioelectrochemical system [5, 7, 16, 18, 66]. Moreover, the main challenge today is to improve the biorecognition elements; to achieve this goal, much focus has been placed on searching for different electrode configurations based on nanostructured elements, which have provided several advances in BFC development. The next section examines these two kinds of BFCs in detail and summarizes some of the most important works reported in regards to the utilization of nanostructured materials for BFC applications.

3 Power Energy and Thermodynamics in BFCs

The electrical energy from biological cells can be generated by anodic/cathodic reactions from enzymatic biocatalytic processes or energetically favorable metabolic reactions on microorganisms [5, 6, 12–14, 16–18]. The evaluation of an electrochemical system's power density, which is commonly measured as the power generated per area or volume of electrochemical cell, is very important. Another crucial assessment is the evaluation of the energy generated by enzymatic and microbial BFCs to show the performance of many different kinds of electrode

configurations [5–7]. The cell voltage can be obtained by any electrochemical system, and is given by Eq. 1 [6].

$$E_{Cell} = E_C - E_A - \Sigma IR_e \tag{1}$$

where E_{Cell} represents the liquid potential generated by the biological cell and E_C and E_A represent the cathodic and anodic potential, respectively. The term ΣIR_e represents the sum of the internal potential losses of the electrochemical cell. The standard potential for a biological fuel cell can be represented by semi-reduction reactions in a semi-electrochemical cell, given by the Nernst Eq. (2) [67].

$$E_{Cell} = E_e^0 + \frac{RT}{nF}\log\left(\frac{[Ox]}{[\mathrm{Red}]}\right) \tag{2}$$

The liquid potential generated by an electrochemical cell can be calculated from the current generated by the electrochemical reactions. In this case, these residual potential generated ($E_{Cell} = E_C - E_A - \Sigma I\mathrm{Re}$) is given by Eq. 3.

$$\eta = E - E_e \tag{3}$$

where E_e corresponds to the equilibrium potential of the electrode. The optimization of the current density generated in an electrochemical cell can be obtained when the ohmic resistance (ΣIR_e) is at a minimum value. The configuration of electrodes on an electrochemical cell and their operation at low current densities are examples of how power generation can be optimized in BFCs. For several kinds of fuel cells, the power density generation is calculated from the residual potential of the cell and the current generated by electrochemical reactions per electrode area, according to Eq. 4 and 5.

$$P_{Cell} = E_{Cell}\int IdI \tag{4}$$

$$Power\,Density = \frac{P_{Cell}}{A} \tag{5}$$

The power density of BFC is dependent of the electrochemical parameters that can be obtained by polarization curves. The polarization properties of polarization curves for electrochemical cells is described by Butler-Volmer kinetics [68]. Generally, the Coulomb efficiency (ε_c) is used to evaluate the power generated in a microbial BFC and correlates the theoretical coulombs generated from the substrate and the maximum electron transfer to the electrode, as represented by Eq. 6 [14].

$$\varepsilon_c = \frac{M\int_0^t Idt}{Fbv_{An}\Delta COD} \tag{6}$$

where M represents the molar mass for oxygen (M = 32 g mol^{-1}), $\int_0^t Idt$ is the charge generated over the time period (t), F is the Faraday constant (96,485 C mol^{-1}), b is the number of electrons generated per mol of oxygen, v_{An} is the volume of the anode, and ΔCOD is the variation of oxygen demand for current density generated on microbial BFCs.

Several factors are responsible for power energy generation, and many efforts have been made in recent years to improve the performance of many kinds of BFCs. Nanostructures have been reported as interesting electrochemical approaches in conjunction with electron mediators to improve power performance in BFCs [70, 71]. Moreover, several of the nanostructured architectures investigated have provided successful advances on BFC development.

4 Nanostructured Materials Applied to Modified Electrodes and BFCs

Recent advances in nanostructured materials applied to electrochemistry have been responsible for an increase in developments in the field of bionanoelectrochemistry [7]. The development of nanostructures brings with it the possibility to control many material properties at the molecular level and, also, some interesting studies reports their impact in the environment [72,73]. Materials on the nanometer scale are characterized by their large surface area, which greatly influences their electrochemical properties; that is, electrochemical potential increases with reduction of the size of the material [74]. Several nanostructure materials have been applied to modified electrodes, such as metallic nanoparticles, carbon nanostructures, oxide nanoparticles, and many others. Carbon nanotubes represent one of the allotropic forms of carbon, and several works have reported their use in modified electrodes. Since their discovery in 1991 by Iijima and co-workers [75], carbon nanotubes have received great attention due to their unique electronic, electrochemical, and mechanic properties, as well as their potential application in many areas [76–78]. The electrochemical properties of carbon nanotubes have been extensively investigated in the last decade by Compton and co-workers [79–83], who have confirmed their high electrocatalytic activity. In general, their electroactivity was initially associated with their unique tubular structure; but recent studies have provided information about other iron impurities that improve their catalytic properties [80]. Britto and co-workers [84] reported a significant improvement in the electrochemical detection of dopamine by using carbon nanotubes prepared with bromoform. Another important approach was reported by Zhang and co-workers [85], which utilized carbon nanotubes for the amperometric detection of glucose. The carbon nanotubes provided an improvement in the current density response when GOx was immobilized on the electrode surface; the results were observed by direct electron transfer (DET) of the prosthetic group FAD by the enzyme GOx.

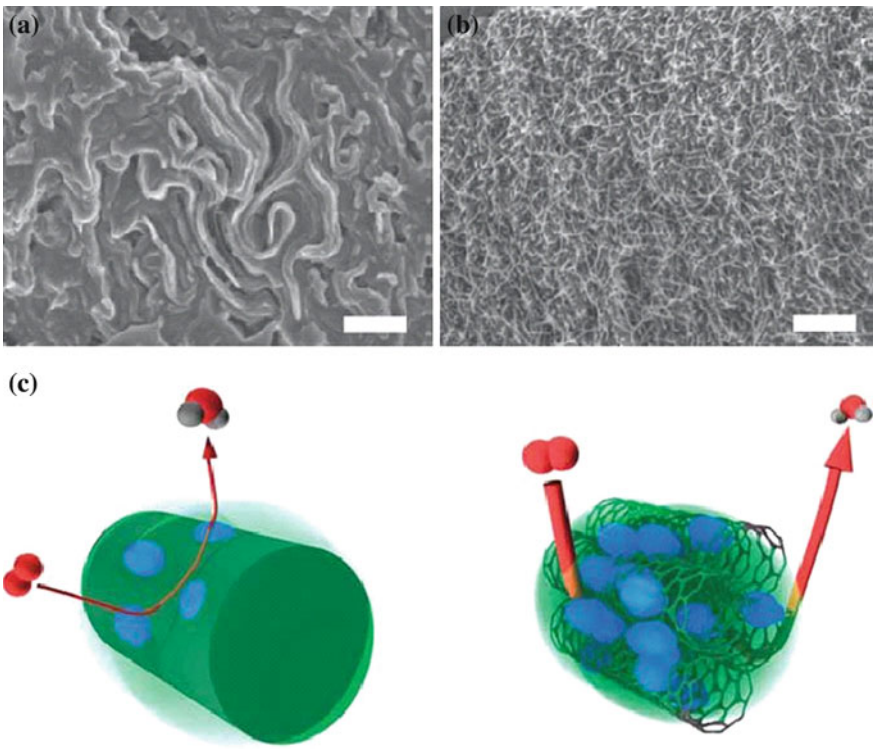

Fig. 3 SEM images of **a** CF and **b** CNT fiber. Schematic representation of oxygen reduction on **c** CF and **d** CNT fiber (the *green shade* represents the redox polymer and the *blue color* represents the enzymes). Reproduced from Ref. [86] with kind permission of Macmillan Publishers Limited

The use of carbon nanotubes in modified electrodes has also gained a lot of consideration for their application as recognition elements in BFCs [29, 31, 76, 78, 85–89]. Gao and co-workers [86] developed an electrode composite material based on carbon fibers (CFs) and oriented carbon nanotube (CNT) microwires for the electroreduction of oxygen. These results show that non-porous CFs have a relatively nonporous structure good for the diffusion of oxygen, whereas CNT microwires have a large porous surface which allows for the permeation of both electrolyte solutions and oxygen. In addition, the resistance of mass transfer along the porous materials can be reduced, generating a current density of 750 μA cm^{-2} and only a 20 % loss of their power density. Figure 3 show SEM images and a schematic of the diffusion of oxygen throughout porous microelectrodes.

Graphene-based nanomaterials are another important form of carbon materials, which are formed by a monolayer of carbon atoms and were first isolated in 2004 [90]. These nanomaterials present very interesting electronic and electrochemical properties, which depend strongly on their structure, orientation and properties associated with the presence of defects [91–94]. Usually, graphene-oxide is converted to the graphene form and utilized in modified electrodes for

electrochemical devices and biodevices, and plays an important role in heterogeneous electron transfer (HET). Recent studies demonstrate that the basal-plane of graphene sheets increases considerably the heterogeneous electron kinetic constant k (–0.01 cm s^{-1}) [95]. For this purpose, several studies have reported the preparation of modified electrode-based graphene. Moreover, the electrochemical properties of graphene allow for their inclusion in interesting applications such as biosensing [96–98], sensing [99, 100], and BFC development [42, 101].

Recently, Liu and co-workers [42] reported the use of the sol–gel method for immobilization of graphene nanosheets; they compared their results to carbon nanotubes which were used toward the development of a bioanode and biocathode for application in an enzymatic BFC. The electrochemical responses of graphene and carbon nanotubes demonstrate that the catalytic efficiency of graphene is twice that of carbon nanotubes, with a maximum power density of 24.3 μA cm^{-2} and a lifetime of 7 days.

5 Enzyme-Based Modified Electrodes Applied to BFCs

Biological redox reactions are known to be specific and occur in live organisms to accelerate several biochemical processes associated with metabolism [16, 18, 19]. Such biochemical reactions, or catalyzed enzymatic reactions, take place with specific enzymes of a particular nature that makes this biomolecules especially suitable for the determined application. Particularly, these enzymatic processes can be utilized to produce energy by coupled redox reactions that can be utilized in specific applications [17–19, 22, 28, 102–109]. For this purpose, enzymes with a metallic redox center are very interesting due to the possibility of participating in redox couple reactions as cofactors by a charge transfer with the electrode surface. Cofactors are, in most cases, organic molecules that transfer electrical charge between enzymes and the electrode surface, thereby allowing the charge to create a flow of current in the electrochemical system. However, biocatalysts present several advantages over metal catalysts, such environmentally-friendly conditions (e.g., mild temperature and pH) and advanced operation life time [110]. From another point of view, such biological systems allow energy generation from more complex fuels [12–14, 16, 18, 19]. Figure 4 shows a conventional configuration of an enzyme-based BFC operating with the oxidation of glucose on the anode by the enzyme glucose oxidase (GOx).

There are two types of BFCs according to this classification. The first is based on the type of product generated by the enzymatic reactions. In this type of BFCs, enzymes do not directly produce the energy originated by the biological processes. The products catalyzed by such enzymes are used as fuel for fuel cells, such as the generation of hydrogen as fuel by hydrogenase enzymes [23]. In the second type of BFCs, biological components are directly involved in energy production, which originates from biochemical reactions. The enzymes present on the anodic electrodes catalyze the oxidation of an organic species to generate a current that

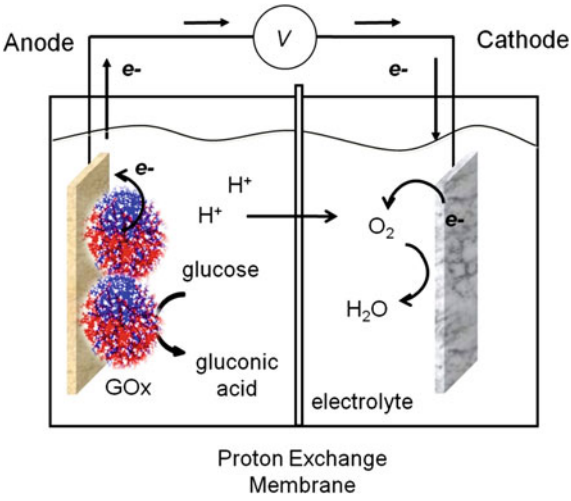

Fig. 4 Schematic representation of an enzyme-based BFC configuration. As an example of operation, glucose is oxidized with the enzyme GOx immobilized on the anode to generate H_2O on the cathode

depends directly on the enzymatic performance [50, 111, 112]. The key to this type of cell is to establish better communication between the enzymes and electrodes for an efficient electron transfer and a higher-than-usual current generated by the biocatalytic processes [50, 111, 112]. Enzymes are large biological molecules with redox properties that can be divided into three groups based on the localization of the enzymatic cofactors in the protein structure[17]. The first group is classified by the presence of nicotinamide adenine nucleotide ($NADH/NAD^+$) or nicotinamide adenine dinucleotide phosphate ($NADPH/NADP^+$) redox centers, which are weakly bound to the proteic structure of the enzyme that actuate directly on cellular electron transfer reactions. The second group of enzymes is classified as having redox centers at or near the periphery of their protein shell structure. Peroxidases and other copper enzymes belong to this group. Enzymes of the third group have redox centers that are strongly bound to the proteic structure and are located deep inside the enzyme or glycoprotein structure.

The major difficulty with these enzymatic redox catalysts is immobilizing the enzymes on solid electrodes and accessing the redox center localized deep inside the protein structure without the loss of their bioactivity properties. The use of these specific enzymes on electrode surfaces began many decades ago, when the first biodevices were studied to develop a biosensor with high selectivity and specificity [25]. The development of such devices brings about the possibility of studying electrochemical processes when biomolecules actuate out of their natural environments [18, 19, 113]. Although the redox enzymatic reactions can occur when enzymes are in contact with the solid electrode surfaces, they partly lose some of their bioactivity properties due to denaturation by the immobilization processes [18, 19, 113]. In fact, the main interest associated with the use of immobilization methods and developing biodevices that maximize the enzymatic biocatalysis is to better maintain the integrity of the enzyme structures by optimization of the electrode materials and immobilization methods. Biomolecules

such as enzymes can be immobilized on a substrate surface by physical or chemical adsorption [114–117]. Physical adsorption occurs as a result of a residual charge present on certain chemical groups of the enzymes, which causes spontaneous adsorption onto a substrate or molecule with the opposite residual structural charge. On the other hand, chemical adsorption is caused by the cross-linking of chemical groups on an enzyme's structure with other molecules on the substrate, or by the presence of bifunctional groups [38]. Although immobilization techniques are crucial in terms of providing better communication between the enzyme and electrode surface, many biological species undergo very slow heterogeneous electron transfer due to energy barriers associated with their proteic structure. One pathway to intensifying the charge transfer originated by bioelectrochemical reactions is to use mediated electron transfer [44, 46, 111, 118–121]. Electrochemical mediators are molecules that can easily and reversibly switch between oxidation states used to facilitate electron transfer processes between redox centers on enzymes and electrodes [44, 46, 111, 118–121]. This results in a better performance of the current generated in modified electrodes that can be applied to biosensors [118–120] and BFCs [44, 46, 111, 121]. Electrode preparation with most kinds of redox mediators, such as ferrocene [118, 122], Prussian blue [123, 124], 1,4-benzoquinone [26, 125], hexacyanoferrates (Co, Fe, Ni, Cu), etc., can improve current transport on the electrode surface by several orders of magnitude. Since their discovery in 1951 [126], ferrocene, along with its derivatives, is one of the most popular redox mediators used for amperometric [71, 127], potentiometric [128, 129], and immunosensor [130, 131] development. Several works have reported about the use of redox mediators to enhance charge transport in bioelectrochemical devices [44, 46, 71, 111, 118, 121, 122]. However, the redox mediator should be chosen such that its redox potential is as close as possible to that of the cofactor enzymes [16].

Several approaches have reported the utilization of nanostructured metallic materials, such as noble metal nanoparticles with redox mediators, to intensify the electrochemical response on modified electrodes [98, 131–134]. The synthesis of gold nanoparticles by organic molecules produces hybrids with very interesting electrochemical properties [131, 133, 134]. This involves the utilization of PAMAM dendrimers as gold nanoparticle stabilizing agents for the development of electroactive nanostructured membranes (ENMs) [70, 135, 136]. This system is based on the use of polyelectrolytes with opposite charges for the fabrication of self-assembled multilayer thin films of PSS and PAMAM-AuNPs with a cobalt hexacyanoferrate (CoHCF) mediator electrodeposited around the AuNPs to intensify the electron transfer on the electrode surfaces [70, 135, 136]. In other words, this concept can be extended to many other redox mediators. In addition, this electrochemical approach was successfully applied to a glucose amperometric biosensor, as reproduced in Fig. 5.

Another important approach was described by Katz and co-workers [137], with the use of the enzyme glucose oxidase (GOx) by the reconstitution of apo-GOx on charge-transporting wires consisting of a relay unit as the charge carrying element, and a flavin adenine dinucleotide cofactor (FAD) as a reconstitution site. In one configuration, pyrroloquinoline quinone (PQQ) was assembled on a gold electrode,

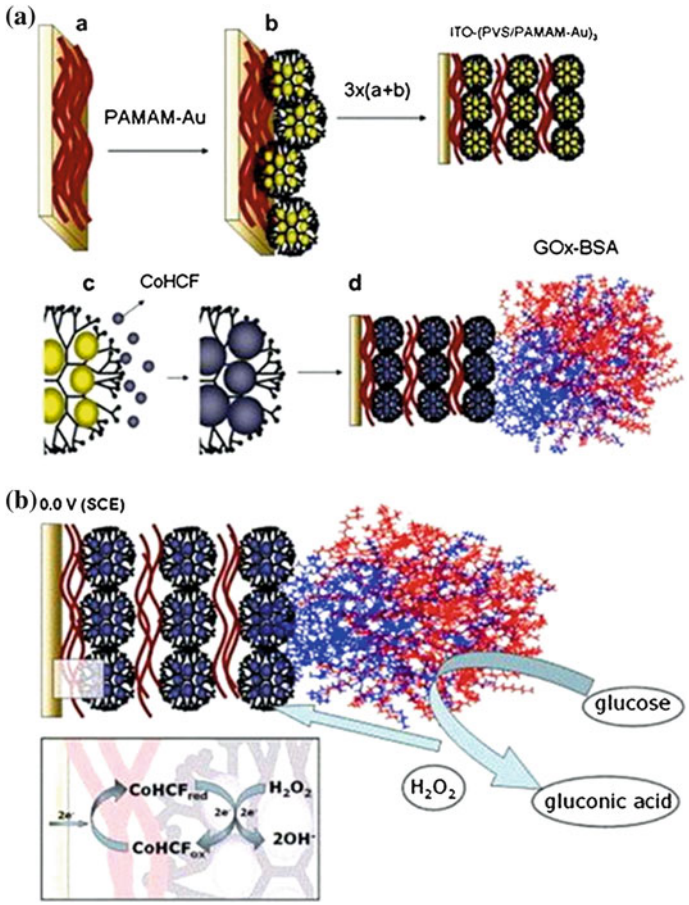

Fig. 5 (**A**) Schematic fabrication of layer-by-layer (LbL) films comprising PVS and PAMAM-Au. The sequential deposition of LbL multilayers was carried out by immersing the substrates alternately into **a** PVS and **b** PAMAM-Au solutions for 5 min per step. After deposition of three layers, an ITO-(PVS/PAMAM-Au)$_3$@CoHCF electrode was prepared by potential cycling **c**. The enzyme immobilization to produce ITO-(PVS/PAMAM-Au)$_3$@CoHCF-GOx **d** was carried out in a solution containing BSA, glutaraldehyde and GOx. (**B**) Schematic representation of the reaction of glucose at the ITO-(PVS/PAMAM-Au)$_3$@CoHCF-GOx electrode. Reproduced from Ref. [70] with kind permission of Elsevier

and N^6-(2-aminoethyl-flavinadenine dinucleotide) (amino-FAD) was covalently linked to the PQQ [137]. The reconstitution of apo-glucose oxidase on the surface-bound FAD site led to a structurally aligned enzyme monolayer immobilized on a gold electrode. This electrode configuration provided an efficient electrical communication between the redox enzyme center and the electrode, leading to an oxygen-insensitive amperometric glucose sensing. Figure 6 shows the preparation of the bioanode, applicable as a recognition element for glucose sensing.

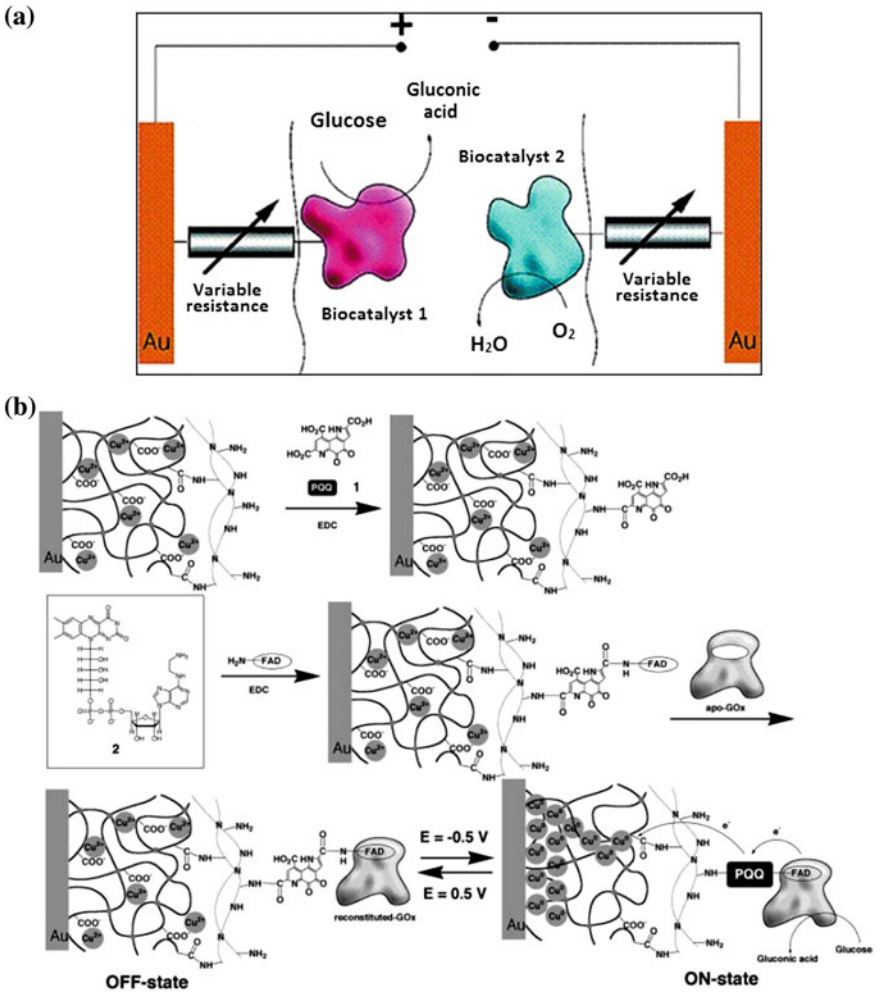

Fig. 6 **a** Schematic representation of the biocatalytic current generation of a BFC. **b** Stepwise covalent binding of PQQ (**1**) and N^6-(2-aminoethyl)-flavin adenine dinucleotide (**2**) to the polymer functionalized electrode, followed by the reconstitution of apo-glucose oxidase and the reversible activation and deactivation of the biocatalytic activity anode by the electrochemical reduction of the Cu^+-polymer film and the oxidation of the Cu^0-polymer film, respectively. Reproduced from Ref. [137]. Copyright@1999 American Chemical Society

6 Microbial-Based Modified Electrodes Applied to BFCs

The present potential application of bacteria and other microorganisms in energy storage originates from living cultures [54, 59, 60, 138, 139]. These living organisms, such as *Saccharomyces cerevisiae* or *Escherichia coli*, for example,

actuate on disintegration processes of organic molecules by biochemical reactions during metabolism to absorb necessary sources of energy [140]. The dependence of electrical energy generation on changes in temperature has also been evaluated. For this purpose, the utilization of environment culture provides for the microorganisms' growth and generates energy by the oxidation of organic fuels.

Microbial BFCs are basically composed of an anode, which facilitates oxidation processes by a microorganism, and a cathode, which facilitates the reduction of O_2 and generation of water [54, 55, 57, 61, 101, 141]. The two electrodes are separated by a semi-permeable membrane for the proton exchange that permits the flow of ions through the circuit. However, the major challenge is to establish better communication between electron transport inside the microorganism and the electrode surface [13, 15, 56, 59, 142]; the transfer of electrons across the microorganism membrane leads to a slow flux of ions and, consequently, generates low levels of energy at long times. The problem of current generation was partially resolved by utilization of redox mediators that are able to diffuse along the microbial membrane and transfer electrons to the anode electrode [111, 121]. Typically, a microbial fuel cell utilizing glucose as the organic fuel and a redox mediator operate according to the following reactions.

$$\text{Anodic reaction: } C_6H_{12}O_6 + H_2O \rightarrow CO_2 + 14e^- + 14H^+ \tag{7}$$

$$\text{Cathodic reaction: } 1/2O_2 + 2H^+ + 2e^- \rightarrow H_2O \tag{8}$$

$$\text{Mediator}_{Ox} + e^- \rightarrow \text{Mediator}_{Red} \tag{9}$$

On the other hand, several works have reported the utilization of microbial fuel cells without the use of redox mediators [58]. For example, Chaudhuri and co-workers [58] reported a new microorganism *Rhodoferax ferrireducens* capable of glucose oxidation, generating CO_2 without a redox mediator, and utilizing a graphite cathode to generate energy. The semi-electrochemical reactions took place with current energy generation in a microbial BFC. Many different configurations have been reported which vary according to the fuel or type of catalyst utilized. Fishilevich and co-workers [143] reported the use of GOx as the redox enzyme displayed on the surface of *Saccharomyces cerevisiae* (YSD-GOx fuel cells) in the anode compartment with methylene blue as the redox mediator. The reduction of oxygen was performed by the enzyme laccase at the cathode with 2,2′-azino-bis(3-ethylbenzothiazoline-6-sulfonic acid) (ABTS) as a redox mediator. This configuration demonstrated that GOx immobilized on a microorganism's surface can be used as another important approach in the development of BFCs (Fig. 7).

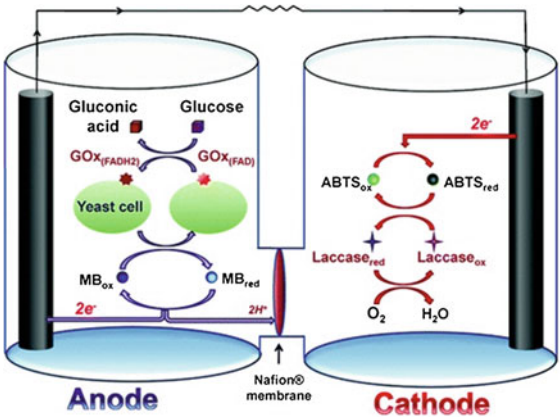

Fig. 7 Principle of operation of the YSD-GOx fuel cells. Reprinted with kind permission of Ref. [143]. Copyright@2009 American Chemical Society

7 Development of Biomimetic Electrodes Applied to BFCs

The search for novel BFC materials within the last decade has focused on the development of cells with components more suitable for producing energy with maximum performance. The concept of biomimetic systems has been reported as a new and interesting tool for the development of modified electrodes applied to BFCs [144, 145]. Enzymes are known to catalyze biochemical reactions with high specificity to a determined substance; the modern concept of biomimetic catalysts allows for the possible use of inorganic materials, as an example, as catalysts for specific chemical reactions and, at the same time, to be favorable for use as a biorecognition element applied to electrochemical devices. These kinds of systems are capable of being specific to certain chemical species due to their high affinity, and behave in a similar fashion to natural bimolecular receptors [144, 145]. These artificial receptors bring new possibilities and can be obtained by several methods that include obtaining biomolecule ligands [145] and the synthesis of nanostructures for application to a specific function [144]. As an example, the development of biomimetic cathodes for application in BFCs has been developed [144] by the synthesis of iron (III) nanoparticles stabilized on poly (diallyldimethylammonium) (PDAC) as a biomimetic nanostructured material for the reduction of H_2O_2. A metastable phase of iron oxide and iron hydroxide nanoparticles (PDAC-FeOOH/Fe_2O_3-NPs) has a quasi-reversible anodic/cathodic electrochemical process attributed to Fe^{3+}/Fe^{2+}, which produces high electrochemical catalytic activity for H_2O_2 at -0.29 to 0.39 V with a potential range of $\Delta E = 0.68$ V (Fig. 8).

The future behind biomimetic materials is very important for biomimetic electrochemical devices in which catalytic reactions can be performed without the use of enzymes. In addition, nanostructured biomimetic materials can be achieved by simple synthetic methods and bring new tools for the next generation of modified electrodes applicable to BFCs.

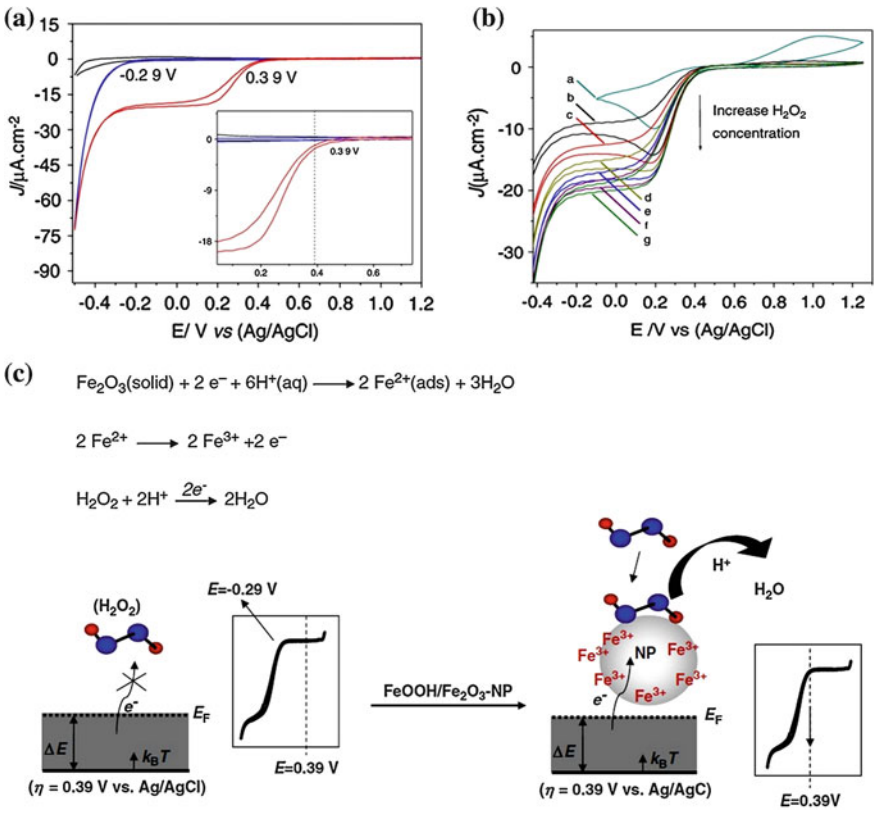

Fig. 8 **a** Cyclic voltammograms of ITO (*black line*) (0.1 mol L^{-1} H_2SO_4 + 11.6 µmol L^{-1} H_2O_2) in the presence (*red line*) and absence (*blue line*) of PDAC–FeOOH/Fe_2O_3-NPs. **b** Solution phase voltammetry of PDAC–Fe_2O_3-FeOOH-NPs at different concentrations of H_2O_2 ($a = 0.0$, $b = 1.16$, $c = 2.32$, $d = 3.48$, $e = 5.80$, $f = 9.12$ and $g = 11.67$ mol L^{-1}). **c** Proposed electrochemical mechanism for H_2O_2 reduction and schematic representation of the electrode process involving PDAC–FeOOH/Fe_2O_3-NPs. Reproduced from Ref. [144] with kind permission of Elsevier

8 Perspectives on Green Energy Generation and Future Applications

The modern and recent advances in BFC development for practical technological applications are still in an early stage, with barriers to overcome. However, their potential applications utilizing live organisms and implantable devices for energy generation are unquestionable. Enzymatic BFCs can be a promising tool for the development of new implantable devices; they also possess challenges for developing suitable and more efficient biodevices capable of producing power energy for many applications. An efficient method of enzymatic immobilization

and a more suitable modified electrode must be applied. Nanostructured materials applied to modified electrodes are an important strategy for bioanode development; metal nanoparticles, carbon nanotubes, and graphene are very interesting materials reported by several authors to provide better performance in the field of biological fuel cell development and a more suitable and biocompatible route for enzyme immobilization. Much attention is concentrated on the improvement of communication between the enzyme's redox center and the electrode surface. The use of redox mediators provides a key for the development of more suitable communication on modified electrodes. In addition, microbial fuel cells offer the possibility of using biological processes of microorganisms like bacteria to produce energy density at long times of operation and using organic molecules as fuel. One important approach has been developed which uses microbial BFCs utilizing glucose as a renewable fuel for power energy generation. On the other hand, biomimetic materials, such as metal oxide nanoparticles, have been used as an alternative for bioelectrode development.

Some applications for biological fuel cells are implantable biodevices and industrial reactors that use rejects, such as wastewaters, which depend on the concentration of biodegradable organic matter originating from some industries, as fuels for energy production. Thus, the biggest challenge is to develop such systems with a long lifetime of operation, high stability, and with sufficient power density to be used in technological applications. Moreover, the continuing research on biological systems conjugated with nanostructured materials, and studies on biological areas and electrochemical characteristics of biomolecules, need to be improved to a more rapid expansion of this new and clean generation of power energy.

References

1. Hubenova Y, Mitov M (2010) Potential application of Candida melibiosica in biofuel cells. Bioelectrochemistry 78:57–61
2. Giroud F, Gondran C, Gorgy K, Pellissier A, Lenouvel F, Cinquin P, Cosnier S (2010) A quinhydrone biofuel cell based on an enzyme-induced pH gradient. J Power Sour
3. Liu Y, Dong S (2007) A biofuel cell with enhanced power output by grape juice. Electrochem Commun 9:1423–1427
4. Katz E, Shipway AN, Willner I (2003) Biochemical fuel cells. Handbook of fuel cells—fundamentals, technology and applications, vol 1. Wiley, New York, pp 355–381
5. Katz E, Atanassov P (2010) Biofuel cells. Electroanalysis 22:723–724
6. Bullen RA, Arnot TC, Lakeman JB, Walsh FC (2006) Biofuel cells and their development. Biosens Bioelectron 21:2015–2045
7. Davis F, Higson SPJ (2007) Biofuel cells–recent advances and applications. Biosens Bioelectron 22:1224–1235
8. Heinzel A, Barragan VM (1999) A review of the state-of-the-art of the methanol crossover in direct methanol fuel cells. J Power Sour 84:70–74
9. Yamamoto O (2000) Solid oxide fuel cells: fundamental aspects and prospects. Electrochim Acta 45:2423–2435
10. Winter M, Brodd RJ (2004) What are batteries, fuel cells, and supercapacitors? Chem Rev 104:4245–4270

11. Wang X, Sjöberg-Eerola P, Eriksson JE, Bobacka J, Bergelin M (2010) The effect of counter ions and substrate material on the growth and morphology of poly (3,4-ethylenedioxythiophene) films: towards the application of enzyme electrode construction in biofuel cells. Synth Met 160:1373–1381
12. Zhao TS (2009) Micro fuel cells: principles and applications. Academic Press, Burlington
13. Franks AE, Nevin KP (2010) Microbial fuel cells, a current review. Energies 3:899–919
14. Logan BE, Hamelers B, Rozendal R, Schröder U, Keller J, Freguia S, Aelterman P, Verstraete W, Rabaey K (2006) Microbial fuel cells: methodology and technology. Environ Sci Technol 40:5181–5192
15. Rabaey K, Verstraete W (2005) Microbial fuel cells: novel biotechnology for energy generation. Trend Biotechnol 23:291–298
16. Atanassov P, Apblett C, Banta S, Brozik S, Barton SC, Cooney M, Liaw BY, Mukerjee S, Minteer SD (2007) Enzymatic biofuel cells. Electrochem Soc Interface 16:28–31
17. Hao YuE, Scott K (2010) Enzymatic biofuel cells—fabrication of enzyme electrodes. Energies 3:23–42
18. Cooney MJ, Svoboda V, Lau C, Martin G, Minteer SD (2008) Enzyme catalysed biofuel cells. Energy Environ Sci 1:320–337
19. Minteer SD, Liaw BY, Cooney MJ (2007) Enzyme-based biofuel cells. Curr Opin Biotechnol 18:228–234
20. Potter MC (1911) Electrical effects accompanying the decomposition of organic compounds. Proc R Soc B 84:260–276
21. Zebda A, Renaud L, Cretin M, Innocent C, Ferrigno R, Tingry S (2010) Membraneless microchannel glucose biofuel cell with improved electrical performances. Sens Actuators B: Chem 149:44–50
22. Barton SC, Gallaway J, Atanassov P (2004) Enzymatic biofuel cells for implantable and microscale devices. Chem Rev 104:4867–4886
23. Karyakin AA, Morozov SV, Karyakina EE, Varfolomeyev SD, Zorin NA, Cosnier S (2002) Hydrogen fuel electrode based on bioelectrocatalysis by the enzyme hydrogenase. Electrochem Commun 4:417–420
24. Arechederra RL, Treu BL, Minteer SD (2007) Development of glycerol/O2 biofuel cell. J Power Sour 173:156–161
25. Yahiro AT, Lee SM, Kimble DO (1964) Bioelectrochemistry: I. Enzyme utilizing bio-fuel cell studies. Biochimica et Biophysica Acta (BBA): Specialized Sect Biophys Subj 88:375–383
26. Nien PC, Wang JY, Chen PY, Chen LC, Ho KC (2010) Encapsulating benzoquinone and glucose oxidase with a PEDOT film: Application to oxygen-independent glucose sensors and glucose/O2 biofuel cells. Bioresour Technol 101:5480–5486
27. Courjean O, Gao F, Mano N (2009) Deglycosylation of glucose oxidase for direct and efficient glucose electrooxidation on a glassy carbon electrode. Angew Chem Int Ed 48:5897–5899
28. Gao F, Yan Y, Su L, Wang L, Mao L (2007) An enzymatic glucose/O2 biofuel cell: preparation, characterization and performance in serum. Electrochem Commun 9:989–996
29. Yan Y, Zheng W, Su L, Mao L (2006) Carbon-nanotube-based glucose/O2 biofuel cells. Adv Mater 18:2639–2643
30. Atanassov P, Colon F, Rajendran V (2004) Glucose–air enzymatic fuel cell. American Chemical Society, Washington, DC, p 207
31. Cai C, Chen J (2004) Direct electron transfer of glucose oxidase promoted by carbon nanotubes. Anal Biochem 332:75–83
32. Tsujimura S, Kano K, Ikeda T (2002) Glucose/O2 biofuel cell operating at physiological conditions. Denki Kagaku oyobi Kogyo Butsuri Kagaku 70:940–942
33. Pizzariello A, Stred'ansky M, Miertu S (2002) A glucose/hydrogen peroxide biofuel cell that uses oxidase and peroxidase as catalysts by composite bulk-modified bioelectrodes based on a solid binding matrix. Bioelectrochemistry 56:99–105

34. Katz E, Willner I, Kotlyar AB (1999) A non-compartmentalized glucose O2 biofuel cell by bioengineered electrode surfaces. J Electroanal Chem 479:64–68
35. Willner I, Katz E, Patolsky F, Bückmann AF (1998) Biofuel cell based on glucose oxidase and microperoxidase-11 monolayer-functionalized electrodes. J Chem Soc, Perkin Transac 2(1998):1817–1822
36. Willner I, Heleg-Shabtai V, Blonder R, Katz E, Tao G, Bückmann AF, Heller A (1996) Electrical wiring of glucose oxidase by reconstitution of FAD-modified monolayers assembled onto Au-electrodes. J Am Chem Soc 118:10321–10322
37. Bachas LG, Law SA, Gavalas V, Ball JC, Andrews R (2002) Development of amperometric biosensors by integrating enzymes with carbon nanotube sol-gel composites. Abstracts of Papers, 223rd ACS National Meeting, Orlando, FL, United States
38. Gregg BA, Heller A (1990) Cross-linked redox gels containing glucose oxidase for amperometric biosensor applications. Anal Chem 62:258–263
39. Ticianelli EA, Derouin CR, Redondo A, Srinivasan S (1988) Methods to advance technology of proton exchange membrane fuel cells. J Electrochem Soc 135:2209
40. Wang ZH, Wang CY, Chen KS (2001) Two-phase flow and transport in the air cathode of proton exchange membrane fuel cells. J Power Sour 94:40–50
41. Topcagic S, Minteer SD (2006) Development of a membraneless ethanol/oxygen biofuel cell. Electrochim Acta 51:2168–2172
42. Liu C, Alwarappan S, Chen Z, Kong X, Li CZ (2010) Membraneless enzymatic biofuel cells based on graphene nanosheets. Biosens Bioelectron 25:1829–1833
43. Akers NL, Moore CM, Minteer SD (2005) Development of alcohol/O2 biofuel cells using salt-extracted tetrabutylammonium bromide/Nafion membranes to immobilize dehydrogenase enzymes. Electrochim Acta 50:2521–2525
44. Barrière F, Ferry Y, Rochefort D, Leech D (2004) Targeting redox polymers as mediators for laccase oxygen reduction in a membrane-less biofuel cell. Electrochem Commun 6:237–241
45. Chen T, Barton SC, Binyamin G, Gao Z, Zhang Y, Kim HH, Heller A (2001) A miniature biofuel cell. J Am Chem Soc 123:8630–8631
46. Coman V, Vaz-Domínguez C, Ludwig R, Harreither W, Haltrich D, Lacey ALD, Ruzgas T, Gorton L, Shleev S (2008) A membrane-, mediator-, cofactor-less glucose/oxygen biofuel cell. Phys Chem Chem Phys 10:6093–6096
47. Kim HH, Mano N, Zhang Y, Heller A (2003) A miniature membrane-less biofuel cell operating under physiological conditions at 0.5 V. J Electrochem Soc 150:A209
48. Yue PL, Lowther K (1986) Enzymatic oxidation of C1 compounds in a biochemical fuel cell. Chem Eng J 33:B69–B77
49. Abad JM, Vélez M, Santamaría C, Guisán JM, Matheus PR, Vázquez L, Gazaryan I, Gorton L, Gibson T, Fernández VM (2002) Immobilization of peroxidase glycoprotein on gold electrodes modified with mixed epoxy-boronic acid monolayers. J Am Chem Soc 124:12845–12853
50. Inamuddin KM, Kim SI, So I, Kim SJ (2008) A conducting polymer/ferritin anode for biofuel cell applications. Electrochim Acta 54:3979–3983
51. Kim J, Grate JW (2003) Single-enzyme nanoparticles armored by a nanometer-scale organic/inorganic network. Nano Lett 3:1219–1222
52. Scodeller P, Carballo R, Szamocki R, Levin L, Forchiassin F, Calvo EJ (2010) Layer-by-layer self-assembled osmium polymer-mediated laccase oxygen cathodes for biofuel cells: the role of hydrogen peroxide. J Am Chem Soc 132:11132–11140
53. Raitman OA, Katz E, Bückmann AF, Willner I (2002) Integration of polyaniline/poly (acrylic acid) films and redox enzymes on electrode supports: an in situ electrochemical/surface plasmon resonance study of the bioelectrocatalyzed oxidation of glucose or lactate in the integrated bioelectrocatalytic systems. J Am Chem Soc 124:6487–6496
54. Aelterman P, Freguia S, Keller J, Verstraete W, Rabaey K (2008) The anode potential regulates bacterial activity in microbial fuel cells. Appl Microbiol Biotechnol 78:409–418

55. He Z, Angenent LT (2006) Application of bacterial biocathodes in microbial fuel cells. Electroanalysis 18:2009–2015
56. Sharma V, Kundu PP (2010) Biocatalysts in microbial fuel cells. Enzym Microb Technol 47(5):179–188
57. Oh S, Min B, Logan BE (2004) Cathode performance as a factor in electricity generation in microbial fuel cells. Environ Sci Technol 38:4900–4904
58. Chaudhuri SK, Lovley DR (2003) Electricity generation by direct oxidation of glucose in mediatorless microbial fuel cells. Nat Biotechnol 21:1229–1232
59. Logan BE, Regan JM (2006) Electricity-producing bacterial communities in microbial fuel cells. Trends Microbiol 14:512–518
60. Logan BE (2009) Exoelectrogenic bacteria that power microbial fuel cells. Nat Rev Microbiol 7:375–381
61. You S, Zhao Q, Zhang J, Liu H, Jiang J, Zhao S (2008) Increased sustainable electricity generation in up-flow air-cathode microbial fuel cells. Biosens Bioelectron 23:1157–1160
62. Li F, Sharma Y, Lei Y, Li B, Zhou Q (2010) Microbial fuel cells: the effects of configurations, electrolyte solutions, and electrode materials on power generation. Appl Biochem Biotechnol 160:168–181
63. Wook Lee J, Kjeang E (2010) A perspective on microfluidic biofuel cells. Biomicrofluidics 4:041301
64. Kerres JA (2001) Development of ionomer membranes for fuel cells. J Membr Sci 185:3–27
65. Du Z, Li H, Gu T (2007) A state of the art review on microbial fuel cells: a promising technology for wastewater treatment and bioenergy. Biotechnol Adv 25:464–482
66. Kim J, Jia H, Wang P (2006) Challenges in biocatalysis for enzyme-based biofuel cells. Biotechnol Adv 24:296–308
67. Brett CMA, Brett AMO, Brett A (1993) Electrochemistry: principles, methods, and applications. Oxford University Press, Oxford
68. Kharkats YI, Sokirko AV, Bark FH (1995) Properties of polarization curves for electrochemical cells described by Butler-Volmer kinetics and arbitrary values of the transfer coefficient. Electrochim Acta 40:247–252
69. Gil GC, Chang IS, Kim BH, Kim M, Jang JK, Park HS, Kim HJ (2003) Operational parameters affecting the performance of a mediator-less microbial fuel cell. Biosens Bioelectron 18:327–334
70. Crespilho FN, Ghica ME, Zucolotto V, Nart FC, Oliveira ON Jr, Brett C (2007) Electroactive nanostructured membranes (ENM): synthesis and electrochemical properties of redox mediator modified gold nanoparticles using a dendrimer layer by layer approach. Electroanalysis 19:805–812
71. Qiu JD, Zhou WM, Guo J, Wang R, Liang RP (2009) Amperometric sensor based on ferrocene-modified multiwalled carbon nanotube nanocomposites as electron mediator for the determination of glucose. Anal Biochem 385:264–269
72. Colvin VL (2003) The potential environmental impact of engineered nanomaterials. Nat Biotechnol 21:1166–1170
73. Huczko A (2000) Template-based synthesis of nanomaterials. Appl Phys A Mater Sci Process 70:365–376
74. Park MS, Kang YM, Wang GX, Dou SX, Liu HK (2008) The effect of morphological modification on the electrochemical properties of SnO_2 nanomaterials. Adv Funct Mater 18:455–461
75. Iijima S (1991) Helical microtubules of graphitic carbon. Nature 354:56–58
76. Baughman RH, Zakhidov AA, De Heer WA (2002) Carbon nanotubes—the route toward applications. Science 297:787
77. Thostenson ET, Ren Z, Chou TW (2001) Advances in the science and technology of carbon nanotubes and their composites: a review. Compos Sci Technol 61:1899–1912
78. Wang J (2005) Carbon-nanotube based electrochemical biosensors: a review. Electroanalysis 17:7–14

79. Banks CE, Compton RG (2005) Exploring the electrocatalytic sites of carbon nanotubes for NADH detection: an edge plane pyrolytic graphite electrode study. Analyst 130:1232–1239
80. Banks CE, Crossley A, Salter C, Wilkins SJ, Compton RG (2006) Carbon nanotubes contain metal impurities which are responsible for the "electrocatalysis" seen at some nanotube modified electrodes. Angew Chem Int Ed 45:2533–2537
81. Banks CE, Davies TJ, Wildgoose GG, Compton RG (2005) Electrocatalysis at graphite and carbon nanotube modified electrodes: edge plane sites and tube ends are the reactive sites. Chem Commun 7:829–841
82. Streeter I, Wildgoose GG, Shao L, Compton RG (2008) Cyclic voltammetry on electrode surfaces covered with porous layers: an analysis of electron transfer kinetics at single-walled carbon nanotube modified electrodes. Sens Actuators B: Chem 133:462–466
83. Wildgoose GG, Banks CE, Leventis HC, Compton RG (2006) Chemically modified carbon nanotubes for use in electroanalysis. Microchim Acta 152:187–214
84. Britto PJ, Santhanam KSV, Ajayan PM (1996) Carbon nanotube electrode for oxidation of dopamine. Bioelectrochem Bioenerg 41:121–125
85. Zhang WD, Zhao YD, Chen H, Luo QM (2002) Direct electron transfer of glucose oxidase molecules adsorbed onto carbon nanotube powder microelectrode. Anal Sci 18:939–941
86. Gao F, Viry L, Maugey M, Poulin P, Mano N (2010) Engineering hybrid nanotube wires for high-power biofuel cells. Nature Commun 1:1–7
87. Zheng W, Li Q, Su L, Yan Y, Zhang J, Mao L (2006) Direct electrochemistry of multi copper oxidases at carbon nanotubes noncovalently functionalized with cellulose derivatives. Electroanalysis 18:587–594
88. Guiseppi-Elie A, Lei C, Baughman RH (2002) Direct electron transfer of glucose oxidase on carbon nanotubes. Nanotechnology 13:559
89. Xue H, Sun W, He B, Shen Z (2003) Single-wall carbon nanotubes as immobilization material for glucose biosensor. Synth Met 135:831–832
90. Horiuchi S, Gotou T, Fujiwara M, Asaka T, Yokosawa T, Matsui Y (2004) Single graphene sheet detected in a carbon nanofilm. Appl Phys Lett 84:2403
91. Geim AK, Novoselov KS (2007) The rise of graphene. Nat Mater 6:183–191
92. Hashimoto A, Suenaga K, Gloter A, Urita K, Iijima S (2004) Direct evidence for atomic defects in graphene layers. Nature 430:870–873
93. Li D, Müller MB, Gilje S, Kaner RB, Wallace GG (2008) Processable aqueous dispersions of graphene nanosheets. Nat Nanotechnol 3:101–105
94. Stankovich S, Dikin DA, Dommett GHB, Kohlhaas KM, Zimney EJ, Stach EA, Piner RD, Nguyen SBT, Ruoff RS (2006) Graphene-based composite materials. Nature 442:282–286
95. Pumera M, Ambrosi A, Chng ELK, Poh HL (2010) Graphene for electrochemical sensing and biosensing. Trends Anal Chem 29:954–965
96. Kang X, Wang J, Wu H, Aksay IA, Liu J, Lin Y (2009) Glucose oxidase-graphene-chitosan modified electrode for direct electrochemistry and glucose sensing. Biosens Bioelectron 25:901–905
97. Shan C, Yang H, Song J, Han D, Ivaska A, Niu L (2009) Direct electrochemistry of glucose oxidase and biosensing for glucose based on graphene. Anal Chem 81:2378–2382
98. Wu H, Wang J, Kang X, Wang C, Wang D, Liu J, Aksay IA, Lin Y (2009) Glucose biosensor based on immobilization of glucose oxidase in platinum nanoparticles/graphene/chitosan nanocomposite film. Talanta 80:403–406
99. Dan Y, Lu Y, Kybert NJ, Luo Z, Johnson ATC (2009) Intrinsic response of graphene vapor sensors. Nano Lett 9:1472–1475
100. Fowler JD, Allen MJ, Tung VC, Yang Y, Kaner RB, Weiller BH (2009) Practical chemical sensors from chemically derived graphene. ACS Nano 3:301–306
101. Logan B, Cheng S, Watson V, Estadt G (2007) Graphite fiber brush anodes for increased power production in air-cathode microbial fuel cells. Environ Sci Technol 41:3341–3346
102. Colmati F, Yoshioka SA, Silva V, Varela H, Gonzalez ER (2007) Enzymatic based biocathode in a polymer electrolyte membrane fuel cell. Int J Electrochem Sci 2:195–202

103. Ramanavicius A, Kausaite A, Ramanaviciene A (2008) Enzymatic biofuel cell based on anode and cathode powered by ethanol. Biosens Bioelectron 24:761–766
104. Jia H, Zhu G, Vugrinovich B, Kataphinan W, Reneker DH, Wang P (2002) Enzyme carrying polymeric nanofibers prepared via electrospinning for use as unique biocatalysts. Biotechnol Prog 18:1027–1032
105. Bunte C, Prucker O, Konig T, Ruhe J (2009) Enzyme containing redox polymer networks for biosensors or biofuel cells: a photochemical approach. Langmuir 26:6019–6027
106. Taqieddin E, Amiji M (2004) Enzyme immobilization in novel alginate-chitosan core-shell microcapsules. Biomaterials 25:1937–1945
107. Rege K, Raravikar NR, Kim DY, Schadler LS, Ajayan PM, Dordick JS (2003) Enzyme-polymer- single walled carbon nanotube composites as biocatalytic films. Nano Lett 3:829–832
108. Wang P, Sheng Dai SD, Tsao AY, Davison BH (2001) Enzyme stabilization by covalent binding in nanoporous sol-gel glass for nonaqueous biocatalysis. Biotechnol Bioeng 74:249–255
109. de la Garza L, Jeong G, Liddell PA, Sotomura T, Moore TA, Moore AL, Gust D (2003) Enzyme-based photoelectrochemical biofuel cell. J Phys Chem B 107:10252–10260
110. Daniel DK, Das Mankidy B, Ambarish K, Manogari R (2009) Construction and operation of a microbial fuel cell for electricity generation from wastewater. Int J Hydrogen Energy 34:7555–7560
111. Alferov SV, Tomashevskaya LG, Ponamoreva ON, Bogdanovskaya VA, Reshetilov AN (2006) Biofuel cell anode based on the Gluconobacter oxydans bacteria cells and 2, 6-dichlorophenolindophenol as an electron transport mediator. Russ J Electrochem 42:403–404
112. Miyake T, Oike M, Yoshino S, Yatagawa Y, Haneda K, Kaji H, Nishizawa M (2009) Biofuel cell anode: NAD +/glucose dehydrogenase-coimmobilized ketjenblack electrode. Chem Phys Lett 480:123–126
113. Ivanov I, Vidakovi -Koch T, Sundmacher K (2010) Recent advances in enzymatic fuel cells: experiments and modeling. Energies 3:803–846
114. Bullock C (1995) Immobilised enzymes. Sci Prog 78:119–134
115. Kennedy JF, Melo EHM, Jumel K (1990) Immobilized enzymes and cells. Chem Eng Prog 86:81–89
116. Tischer W, Kasche V (1999) Immobilized enzymes: crystals or carriers? Trend Biotechnol 17:326–335
117. Tischer W, Wedekind F (2000) Biocatalysis: from discovery to application. Springer-Verlag, Berlin, p 254
118. Okawa Y, Nagano M, Hirota S, Kobayashi H, Ohno T, Watanabe M (1999) Tethered mediator biosensor. Mediated electron transfer between redox enzyme and electrode via ferrocene anchored to electrode surface with long poly (oxyethylene) chain. Biosens Bioelectron 14:229–235
119. Smolander M, Livio HL, Räsänen L (1992) Mediated amperometric determination of xylose and glucose with an immobilized aldose dehydrogenase electrode. Biosens Bioelectron 7:637–643
120. Wang J, Mo JW, Li S, Porter J (2001) Comparison of oxygen-rich and mediator-based glucose-oxidase carbon-paste electrodes. Anal Chim Acta 441:183–189
121. Picioreanu C, Katuri KP, van Loosdrecht MCM, Head IM, Scott K (2010) Modelling microbial fuel cells with suspended cells and added electron transfer mediator. J Appl Electrochem 40:151–162
122. Hodak J, Etchenique R, Calvo EJ, Singhal K, Bartlett PN (1997) Layer-by-layer self-assembly of glucose oxidase with a poly (allylamine) ferrocene redox mediator. Langmuir 13:2708–2716
123. Karyakin AA, Gitelmacher OV, Karyakina EE (1995) Prussian blue-based first-generation biosensor. A sensitive amperometric electrode for glucose. Anal Chem 67:2419–2423
124. Ricci F, Palleschi G (2005) Sensor and biosensor preparation, optimisation and applications of Prussian Blue modified electrodes. Biosens Bioelectron 21:389–407

125. Nakano K, Nakamura K, Iwamoto K, Soh N, Imato T (2009) Positive-feedback-mode scanning electrochemical microscopy imaging of redox-active DNA-poly (1, 4-benzoquinone) conjugate film deposited on carbon fiber electrode for micrometer-sized hybridization biosensor applications. J Electroanal Chem 628:113–118
126. Kealy TJ, Pauson PL (1951) A new type of organo-iron compound. Nature 168:1039–1040
127. Merchant SA, Tran TO, Meredith MT, Cline TC, Glatzhofer DT, Schmidtke DW (2009) High-sensitivity amperometric biosensors based on ferrocene-modified linear poly (ethylenimine). Langmuir 25:7736–7742
128. Ishige Y, Takeda S, Kamahori M (2010) Direct detection of enzyme-catalyzed products by FET sensor with ferrocene-modified electrode. Biosens Bioelectron 26(4):1366–1372
129. Kato R, Sato A, Yoshino D, Hattori T (2011) Electrochemical sensing of anions and heparin by an alkyl-chain ferrocene cationic surfactant. Anal Sci 27:61–66
130. Kwon SJ, Yang H, Jo K, Kwak J (2008) An electrochemical immunosensor using p-aminophenol redox cycling by NADH on a self-assembled monolayer and ferrocene-modified Au electrodes. Analyst 133:1599–1604
131. Qiu JD, Liang RP, Wang R, Fan LX, Chen YW, Xia XH (2009) A label-free amperometric immunosensor based on biocompatible conductive redox chitosan-ferrocene/gold nanoparticles matrix. Biosens Bioelectron 25:852–857
132. De Cuyper M, Joniau M (1992) Binding characteristics and thermal behaviour of cytochrome-C oxidase, inserted into phospholipid-coated, magnetic nanoparticles. Biotechnol Appl Biochem 16:201
133. Mukhopadhyay K, Phadtare S, Vinod VP, Kumar A, Rao M, Chaudhari RV, Sastry M (2003) Gold nanoparticles assembled on amine-functionalized Na-Y zeolite: a biocompatible surface for enzyme immobilization. Langmuir 19:3858–3863
134. Zhang S, Wang N, Yu H, Niu Y, Sun C (2005) Covalent attachment of glucose oxidase to an Au electrode modified with gold nanoparticles for use as glucose biosensor. Bioelectrochemistry 67:15–22
135. Crespilho FN, Ghica ME, Gouveia-Caridade C, Oliveira ON Jr, Brett C (2008) Enzyme immobilisation on electroactive nanostructured membranes (ENM): optimised architectures for biosensing. Talanta 76:922–928
136. Siqueira JR Jr, Crespilho FN, Zucolotto V, Oliveira ON Jr (2007) Bifunctional electroactive nanostructured membranes. Electrochem Commun 9:2676–2680
137. Katz E, Filanovsky B, Willner I (1999) A biofuel cell based on two immiscible solvents and glucose oxidase and microperoxidase-11 monolayer-functionalized electrodes. New J Chem 23:481–487
138. Lewis K (1966) Symposium on bioelectrochemistry of microorganisms. IV. Biochemical fuel cells. Microbiol Mol Biol Rev 30:101
139. Park DH, Zeikus JG (2000) Electricity generation in microbial fuel cells using neutral red as an electronophore. Appl Environ Microbiol 66:1292
140. Ishikawa M, Yamamura S, Takamura Y, Sode K, Tamiya E, Tomiyama M (2006) Development of a compact high-density microbial hydrogen reactor for portable bio-fuel cell system. Int J Hydrogen Energy 31:1484–1489
141. Cheng S, Liu H, Logan BE (2006) Power densities using different cathode catalysts (Pt and CoTMPP) and polymer binders (Nafion and PTFE) in single chamber microbial fuel cells. Environ Sci Technol 40:364–369
142. Schröder U, Nießen J, Scholz F (2003) A generation of microbial fuel cells with current outputs boosted by more than one order of magnitude. Angew Chem 115:2986–2989
143. Fishilevich S, Amir L, Fridman Y, Aharoni A, Alfonta L (2009) Surface display of redox enzymes in microbial fuel cells. J Am Chem Soc 131:12052–12053
144. Martins MVA, Bonfin C, da Silva WC, Crespilho FN, (2010) Iron (III) nanocomposites for enzyme-less biomimetic cathode: A promising material for use in biofuel cells. Electrochem Commun 12:1509–1512
145. Sokic-Lazic D, Minteer SD (2008) Citric acid cycle biomimic on a carbon electrode. Biosens Bioelectron 24:939–944

Recent Advances on Nanostructured Electrocatalysts for Oxygen Electro-Reduction and Ethanol Electro-Oxidation

Fabio H. B. Lima and Daniel A. Cantane

Abstract In this chapter, we review the development of electrocatalysts for electrochemical reactions that take place in low temperature fuel cells. It is focused on the oxygen reduction reaction (ORR), and on the ethanol oxidation reaction (EOR) for proton and anion exchange membrane electrolytes. For the ORR, which takes place at the fuel cell cathode, the major problem is the low platinum mass-activity, and its low long-term stability. In this manuscript, it is reviewed the activity of a new class electrocatalysts that are composed by platinum sub-monolayer deposited on metal nanoparticles, including the correlation of their activity with the center of the Pt d-band. Finally, it is presented stability tests for some ORR electrocatalysts. For the ethanol electro-oxidatation (EOR), on platinum-based electrocatalysts, in required conditions of ethanol concentration and temperature for practical applications, the reaction undergoes parallel reactions, producing acetaldehyde, and acetic acid as major products, instead of CO_2, reducing drastically the fuel cell efficiency. So, the central challenge for the EOR is the development of more efficient nanostructured electrocatalysts. The recent achievements for the EOR, catalyzed by different nanostructured materials, are presented for acid and alkaline media.

F. H. B. Lima (✉) · D. A. Cantane
Institute of Chemistry of Sao Carlos, University of Sao Paulo, Sao Paulo, Brazil
e-mail: fabiohbl@iqsc.usp.br

F. L. de Souza and E. R. Leite (eds.), *Nanoenergy*,
DOI: 10.1007/978-3-642-31736-1_5,

1 Introduction

1.1 Initial Considerations

Fuel Cells are electrochemical energy conversion devices that transform the chemical energy of a fuel into electrical energy. These devices work as a regular galvanic cell, with the exception that the fuel is supplied externally. Low temperature fuel cells, as proton exchange membrane fuel cells (PEMFCs), can be used in a large range of power applications. For the particular case of portable applications, methanol is widely proposed as possible fuel. The direct oxidation of methanol in fuel cells has been widely investigated, where the usage of carbon-supported Pt-Ru bimetallic nanoparticles have been presented high activity, and high faradaic conversion efficiency to CO_2. However, methanol is toxic, possesses large miscibility with water, and it is not a renewable fuel, which bring serious disadvantages for application on commercial devices. On the other hand, ethanol is an attractive fuel for direct alcohol fuel cell (DAFC), since it can be produced by fermentation of sugar-containing raw materials from agriculture. This is particularly interesting for countries like Brazil, where ethanol is already produced in large scale, and distributed by gas station networks, in order to fuel internal combustion engines of regular cars.

Despite several advances in recent years, the existing fuel cell technology still has two main drawbacks: the inadequate efficiency of energy conversion and the high Pt content of the electrocatalysts. The last one is the main problem associated with the cathode, where the oxygen reduction, generally, from the air, takes place. In order to overcome these problems, intensity research has been conducted. So, in this text, we will review, briefly, some published works that aimed at developing more active and efficient electrocatalysts for the ethanol electro-oxidation, and oxygen electro-reduction reaction for low temperature fuel cells, operating in acid and alkaline electrolyte.

2 Oxygen Reduction Electrocatalysis

The oxygen reduction reaction (ORR) can be represented as follows in acidic and alkaline electrolyte [1]:

A. "Direct" four-electron pathway:

Alkaline Electrolyte:

$$O_2 + 2\ H_2O + 4\ e^- \rightarrow 4\ OH^- \quad E_0 = 0.401V \tag{1}$$

Acid Electrolyte:

$$O_2 + 4\ H^+ + 4\ e^- \rightarrow 2\ H_2O \quad E_0 = 1.229V \tag{2}$$

B. "Series" pathway:
Alkaline Electrolyte:

$$O_2 + H_2O + 2\ e^- \rightarrow HO_2^- + OH^- \quad E_0 = -0.065V \tag{3}$$

Followed by the peroxide electroreduction:

$$HO_2^- + H_2O + 2\ e^- \rightarrow 3\ OH^- \quad E_0 = 0.867V \tag{4}$$

Or by a decomposition reaction:

$$2\ HO_2^- \rightarrow 2\ OH^- + O_2 \tag{5}$$

Acid Electrolyte:

$$O_2 + 2\ H^+ + 2\ e^- \rightarrow H_2O_2 \quad E_0 = 0.67V \tag{6}$$

Followed by:

$$H_2O_2 + 2\ H^+ + 2\ e^- \rightarrow 2\ H_2O \quad E_0 = 1.77V \tag{7}$$

Or by:

$$2\ H_2O_2 \rightarrow 2\ H_2O + O_2 \tag{8}$$

On Pt-based electrocatalysts, some evidences suggest that the first electron transfer or the O_2 adsorption with the simultaneous electron transfer and the proton addition is the rate determining step [2, 3].

$$O_2 + Pt \rightarrow Pt\text{ - - - }O_2 \tag{9}$$

Followed by and electrochemical step:

$$Pt\text{ - - - }O_2 + H^+ + e^- \rightarrow \text{products} \tag{10}$$

(the difference to the alkaline electrolyte is that the hydrogen atom for the O–H bond formation comes from the water molecules of the electrolyte, instead of H_3O^+ species).

From the kinetic point of view, the other steps are less important, since they take place after the rate determining step. The transfer of the second electron, with the addition of a second proton, generates OH or hydrogen peroxide species. The peroxide can diffuse to the bulk of the solution electrolyte and the reaction terminates with a process of 2 electrons. One additional transfer of 2 electrons and 2 protons involving OH or H_2O_2 completes the reduction via 4 electrons, resulting in H_2O (for the case of acidic media). So, the reaction via 4 electrons, wherein it is of major interest since it involves higher number of electrons per O_2 molecule, has to deal with the O–O bond breaking and the O–H bond formation, as represented below [4, 5]:

$$O_2 \rightarrow O + O \tag{11}$$

$$O + H \rightarrow OH \tag{12}$$

Thus, electrocatalysts for the ORR have to present electronic structures that result in adsorption forces that strike these two competing steps: while strong adsorption lead a facilitated O–O bond breaking, weak adsorption tend to facilitate the O–H bond formation (hydrogen addition). This produces the so-called "volcano" plot of the activity as a function of the adsorption strength on the catalyst surface [4, 5].

Nørskov et al. [6, 7] introduced the *d*-band model. This model correlates the *d*-band density of electronic states of a metal with its ability to form chemisorption bonds, which better rationalizes the catalytic activity of the metal catalysts. According to this model, as the *d*-band center shifts up, a distinctive anti-bonding state appears above the Fermi level. The anti-bonding states above the Fermi level are empty, and the bond becomes increasingly stronger as their number increase. Thus, strong bonding occurs if the anti-bonding states are shifted up though the Fermi level (and become empty), and weak bonding occurs if anti-bonding states are shifted down through the Fermi level (and become filled). Since an adsorption step is involved in the mechanism of O_2 reduction, the *d*-band structure of a metal catalyst is considered an important parameter determining the kinetic of a particular reaction. So, this evidences that it can be expected some correlation between the electrocatalyst *d*-band center and its electrocatalytic activity for the ORR.

A particularly difficult problem of the ORR electrocatalysis is the high loss in potential, which is a substantial source of the decline in the efficiency of fuel cells. Another drawback is the high Pt loading in cathode or the low mass-activity (current per mass of active metal) in the regular Pt-based electrocatalysts [8, 9]. Thus, the research in the ORR electrocatalysis aims at developing better electrocatalysts in order to reduce the cathode overpotential and the total mass of Pt.

2.1 Singlecrystals and bulk alloys

In a recent work, Lima et al. [5] studied the kinetics of the ORR in alkaline electrolyte in well-ordered single-crystal surfaces of Au(111), Ag(111), Pd(111), Rh(111), Ir(111), and Ru(0001), and on nanoparticles of these metals supported on high-surface-area XC-72 Vulcan carbon. Figure 1a shows the volcano curves obtained for Au(111), Ag(111), Pd(111), Rh(111), Ir(111), and Ru(0001) single-crystals surfaces, and Fig. 1b shows the curves obtained for carbon-supported nanoparticles of these same metals. As can be observed, the nature of the metal has a pronounced effect on the kinetics of the ORR. The results show that Pt has the higher electrocatalytic activity, both as a single-crystal and carbon-supported metal nanoparticle. The limiting current densities (not shown) for Pt, Pd, Rh, and, at lower potentials, for Ir and Ru, have similar values, signifying that the ORR is dominated mainly by a four-electron reduction process in that potential region [2]. With Au, the limiting current for the ORR is half of that for the other metals, which indicates that the O_2 reduction on Au occurs via 2 electrons (the reaction stops at the peroxide stage), in accordance to a previous work [3, 4].

The activity of Pt monolayers, deposited on five different single-crystal surfaces using the Cu UPD technique [10], were investigated in acid and in alkaline

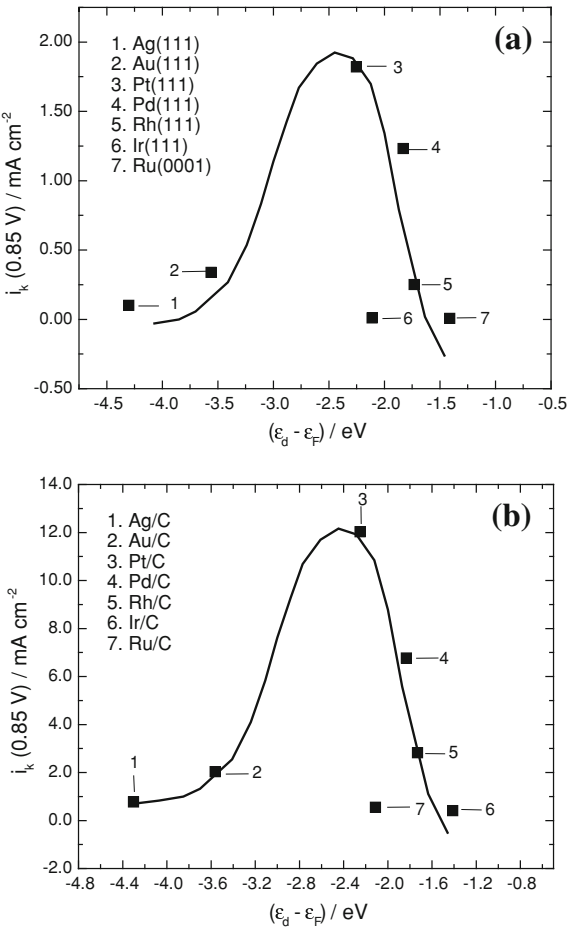

Fig. 1 Kinetic currents (j_k) at 0.80 V for O_2 reduction on the different metal single-crystals and on carbon-supported metal nanoparticles, in 0.1 mol L^{-1} NaOH solution as functions of the metal *d*-band center (ε_d-ε_F; relative to the Fermi level). Published with the permission of the publisher [5]

electrolyte [5, 11, 12], and the ORR polarization curves are presented in Fig. 2a, b. As it can be seen, the Pt monolayer electrocatalysts exhibited support-induced tunable activity by properly selecting the substrate, in which the activity of a Pt monolayer can be enhanced through structural and electronic effects. It can be observed that the most active of all surfaces is Pt_{ML}/Pd(111), and the least active is Pt_{ML}/Ru(0001). The plots of the kinetic current on the platinum monolayers on various substrates at 0.8 V as a function of the calculated *d*-band center, ε_d, generated a volcano-like curve, with Pt_{ML}/Pd(111) showing the maximum activity (Fig. 3).

The modification of the electronic and chemical properties of Pt(111) surfaces by subsurface 3*d* transition metals was studied using density-functional theory [13]. In each case investigated, the Pt surface *d*-band was broadened and lowered in energy by interactions with the subsurface 3*d* metals, resulting in weaker dissociative adsorption energies of hydrogen and oxygen on these surfaces. The

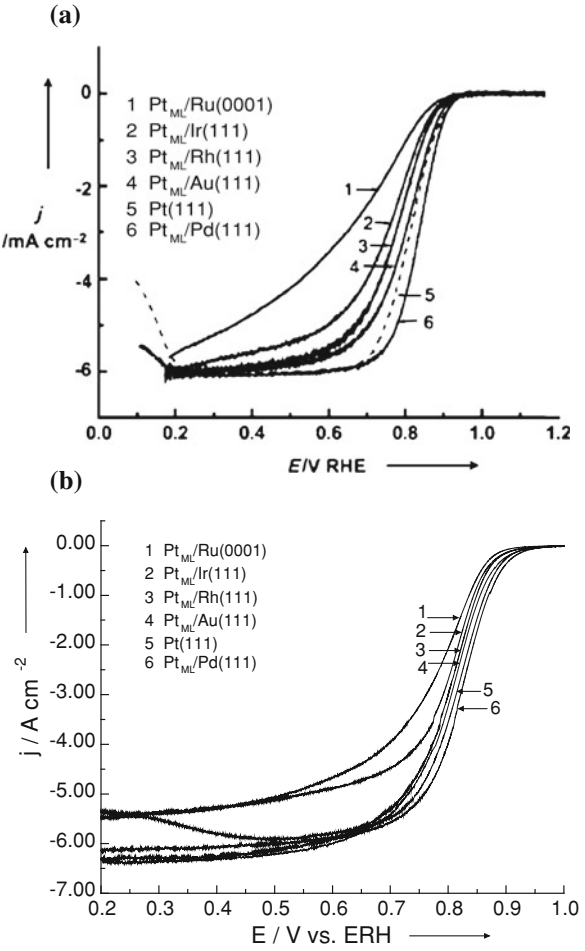

Fig. 2 Polarization curves for O_2 reduction on Pt monolayers on Ru(0001), Ir(111), Rh(111), Au(111), and Pd(111) in a 0.1 mol L^{-1} $HClO_4$ (**a**) and NaOH 0.1 mol L^{-1} electrolyte (**b**) on a disk electrode at room temperature. For comparison, the curve for Pt(111) in acid media from Ref. [18] is shown. The rotation rate: 1600 rpm; sweep rate: 0.02 Vs^{-1} (0.05 Vs^{-1} for Pt(111)) (**a**) and 5 mV s^{-1} (**b**). (Published with permission of the publisher [4, 5])

magnitude of the decrease in adsorption energy was largest for the early 3*d* transition metals and smallest for the late 3*d* transition metals.

The O_2 reduction reaction were carried out on platinum monolayers deposited on polycrystalline alloy films of the type Pt_3M (M = Ni, Co, Fe, and Ti) [14]. The Pt_3M alloys showed in (Fig 4a), were annealed to 1000 K under ultrahigh-vacuum (UHV) conditions; analysis of the low-energy ion-scattering spectra indicated that pure Pt constitutes the first surface layer. The surface enrichment of Pt atoms results from a surface segregation phenomenon, whereby one of the alloy's components (in this case Pt) enriches the surface region [15]. UHV experimental analyses and theory revealed that the strong enrichment of Pt in Pt_3M alloy systems is counterbalanced by the depletion of Pt in the first two or three layers beneath the surface, giving a concentration profile that oscillates around the bulk value [16]. The *d*-band center of these alloy films was measured by synchrotron-based high-resolution photoemission spectroscopy, a methodology described in a

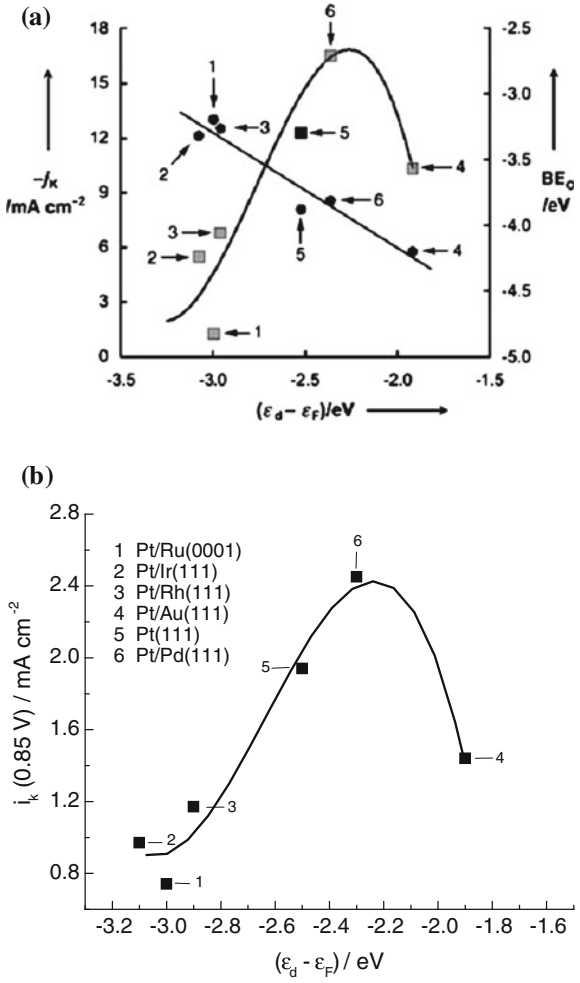

Fig. 3 Kinetic currents (j_K; *square* symbols) at 0.8 V for O_2 reduction on platinum monolayers in a 0.1 mol L^{-1} $HClO_4$ (**a**) and on NaOH 0.1 mol L^{-1} solution (**b**) on the different Pt monolayers, as functions of the electrocatalyst *d*-band center. The current data for Pt(111) in (**a**) is obtained from ref [18]. Labels: *1* Pt_{ML}/Ru(0001), *2* Pt_{ML}/Ir(111), *3* Pt_{ML}/Rh(111), *4* Pt_{ML}/Au(111), *5* Pt(111), *6* Pt_{ML}/Pd(111). (Published with permission of the publisher [4, 5])

previous publication [17]. Figure 4b plots the obtained results of the electrocatalytic activity for the ORR (A/eV) versus the position of the *d*-band center at 0.9 V [14]. It exhibits a classical volcano-shaped dependence, agreeing very well with the activity predicted from DFT calculations (black curve), and with the results for Pt monolayer deposited on different single-crystal substrates, as discussed above.

According to the Sabatier's principle, a good catalyst has to strike a balance between two competing influences [19–21]. The competing influences in the ORR mechanism [22–24] seems to be the first charge-transfer step, or O_2 adsorption with simultaneous charge and proton transference, which is the rate-determining step on pure platinum. The exchange of a second electron with the addition of another proton forms two OH species or hydrogen peroxide (H_2O_2) (in acid media). The latter can escape into the solution phase and terminate the reaction in

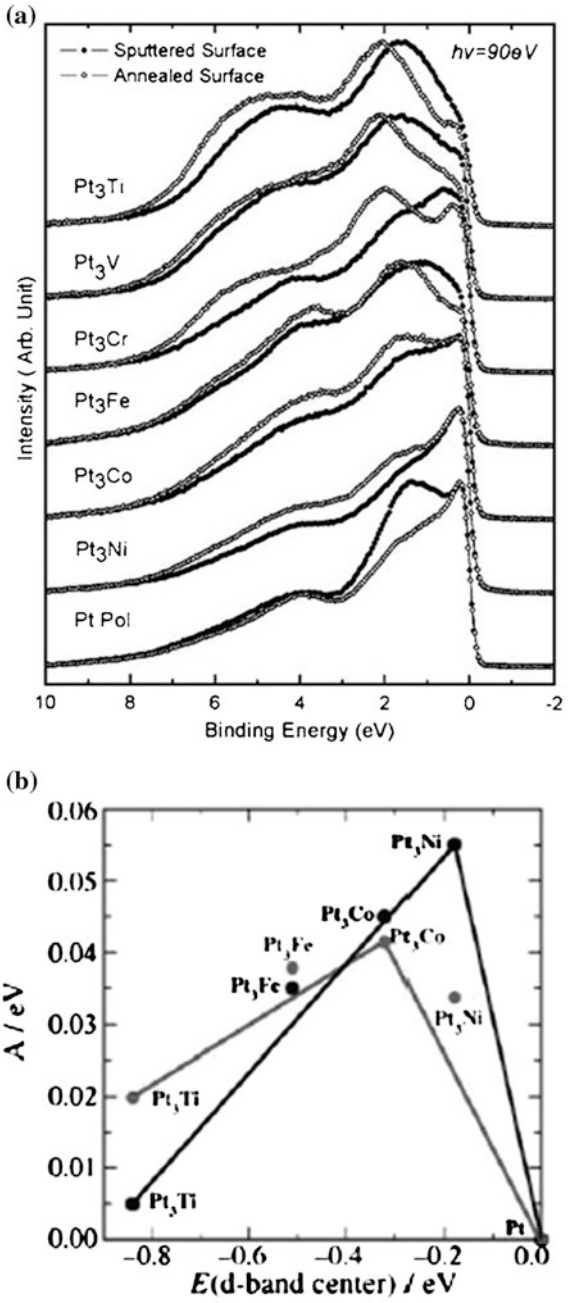

Fig. 4 (**a**) The background-subtracted VB (valence band) spectra of each Pt_3M polycrystalline alloy versus the pure Pt reference after ion sputtering and thermal annealing, respectively (**b**) activity versus the experimentally measured *d*-band center relative to platinum. The activity predicted from DFT simulations is shown in black, and the measured activity is in gray. (Published with permission of the Publishers [14, 17])

a two-electron process. An additional exchange of two electrons and two protons in reactions with OH or H_2O_2 completes the four-electron reduction of O_2 to H_2O. The O_2 reduction reaction via 4 electrons must involve the breaking of the O–O bond (whether in O_2, HO_2, or H_2O_2) and the formation of an O–H bond. As it discussed above, a more reactive surface, such as one characterized by a higher lying ε_d, tends to bind adsorbates more strongly [13], thus enhancing the kinetics of the dissociation reactions. On the other hand, a surface with a lower lying ε_d tends to bind adsorbates more weakly, facilitating the formation of bonds in the reaction adsorbates. So, it is expected that the ε_d of the most active platinum monolayer should have an intermediate value.

Regarding the Geometric Effect, compressive strain tends to down-shift ε_d in energy, whereas tensile strain has the opposite effect, as revealed by DFT studies [6, 7, 13]. The platinum monolayers on Ru(0001), Rh(111), and Ir(111) are compressed compared to Pt(111), whereas Pt_{ML}/Au(111) is stretched by more than 4 %. However, the position of the ε_d depends also on the Electronic Effect, in which the magnitude of the ε_d shift depends on the intensity of the electronic interaction between the platinum monolayer and its substrate [25]. This indicates that Pt_{ML}/Ru(0001), Pt_{ML}/Ir(111), and Pt_{ML}/Rh(111) are less active for O_2 reduction than platinum because of breaking the O–O bond is more difficult on their surfaces than on Pt(111), while the kinetics of hydrogenation of the oxygen atoms may be hindered on Pt_{ML}/Au(111) due to its stronger binding of oxygen atoms or oxygen-containing fragments and, therefore, it is less active than Pt(111). These properties of Pt monolayer on different substrates result in the volcano dependence of kinetic currents as a function of ε_d [4, 5].

In addition, slow rates of O or OH hydrogenation cause an increased in the O or OH surface coverage. This results in a block of the active sites for the O_2 adsorption, dissociation, or hydrogenation.

Therefore, the results evidence that Pt_{ML}/Pd(111) possesses a better balance between the kinetics of the two opposite steps (Eqs. 11 and 12) compared to that of Pt(111), suggesting that Pt_{ML}/Pd(111) is close to the position of an optimum compromise or an optimum balance. Experimentally, Adzic et al. [3] reported that the superior ORR catalytic activity of Pt_{ML}/Pd(111) could be associated with reduced OH coverage, which was observed by in situ XANES (*X-ray Absorption Near Edge Structure*). This result agrees with DFT findings that the binding energy of OH is weaker on Pt_{ML}/Pd(111) than on Pt(111) surfaces.

In the case of the Pt_3M polycrystalline alloys [14], the activity versus the position of the metal d states relative to the Fermi level also resulted in a Volcano plot. Pt_3Ni and Pt_3Co presented higher activities when compared to Pt_3Ti, Pt_3Fe or even pure Pt. It was also evidenced that the increased activity of these alloys in relation to Pt was due to a reduced Pt-oxygen species interaction, which in turns accelerates hydrogenation step. Thus, in both cases, it was observed that Pt binds oxygen a little too strong. So, in order to conduct the Pt-based catalyst closer to the optimum compromise between the two opposite steps, its reactivity for binding oxygen should be slightly reduced.

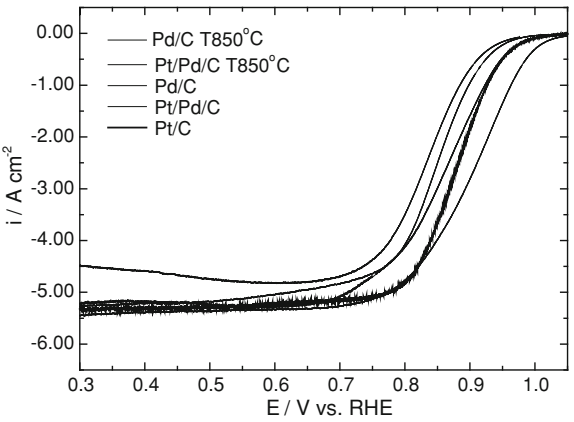

Fig. 5 Comparison of polarization curves for O_2 reduction on Pt monolayer deposited on Pd/C and on Pd/C T850 °C and on the pure substrates. The electrode geometric area is 0.163 cm^2. Published with permission of the publisher [27]

2.2 Nanoparticle

Pd seems to be the best substrate for Pt electrocatalyst. Therefore, several works aimed at synthesizing Pt monolayers on carbon-supported Pd nanoparticles. A suitable and efficient method was developed by the Adzic'group, and involves a galvanic displacement of a UPD Cu monolayer by a Pt monolayer [10]. The formation of this *core–shell* structure/composition can be evidenced and determined by HRTEM (*high resolution transmission electron microscopy*) of the nanoparticle, and using HAADF-STEM (*high-angle annular dark-field scanning transmission electron microscopy*), as demonstrated recently [26].

Oxygen reduction polarization curves obtained on Pt monolayer deposited on carbon-supported Pd nanoparticles in alkaline electrolyte are presented in Fig. 5 [27]. The results for the ORR on Pd/C (2 nm) and thermally treated Pd/C (higher particle size $\sim$10 nm) were included for comparison. It can be noted that the ORR activity of the Pt_{ML}/Pd/C is much higher than that of Pd/C, but more importantly, it is higher than that of Pt/C. The Pt content on the Pt_{ML}/Pd/C material, calculated using the charge associated to the deposition of a Cu monolayer by UPD on Pd/C (after correcting for the double layer charging), revealed that the Pt loading on the *core–shell* nanoparticle was seven times lower than that on Pt/C. This higher mass activity (current for the ORR per mass of Pt) of the Pt_{ML}/Pd/C material is a substantial achievement for practical and/or commercial application of such type of electrocatalysts.

Although this Pt_{ML}/Pd/C material presents a considerable reduction of the Pt mass, it still contains large amount of Pd. So, an additional reduction of the total noble metal mass is advantageous. Using non-noble metals as a core facilitates the reduction of the noble metal's content, while maintaining the full activity of a Pt monolayer by choosing an appropriated *core*. The choice of the metals constituting the *shell* and *core* can be based on considering the segregation properties of the two metals, and their electronic- and strain-inducing effects on the Pt monolayer.

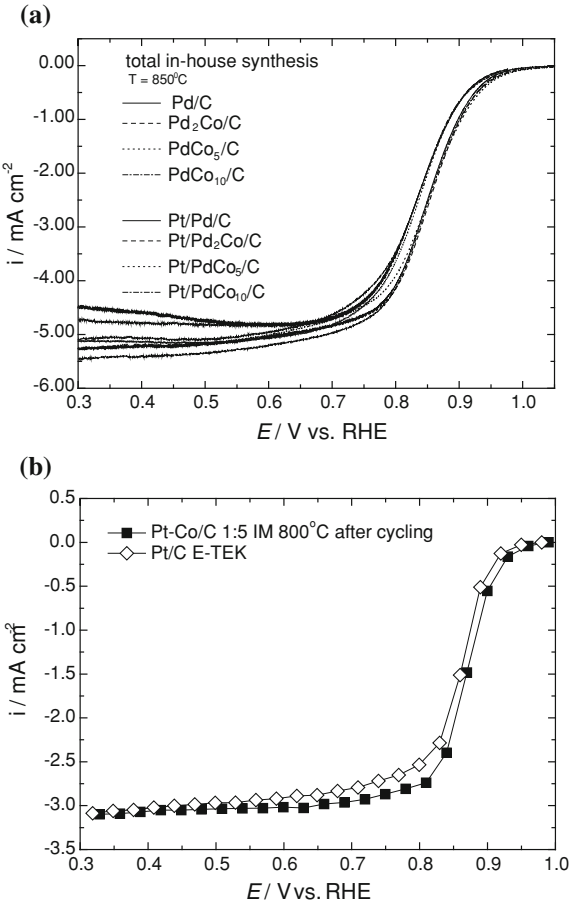

Fig. 6 (**a**) Comparison of polarization curves for O_2 reduction on Pt monolayer deposited on the PdCo/C T = 850 °C with different atomic ratios and on the pure substrates in 0.1 NaOH electrolyte, and at 0.005 V s^{-1}. (**b**) Oxygen reduction on Pt–Co/C alloy electrocatalyst obtained after cycling the material in 0.5 mol L^{-1} H_2SO_4 solution, compared to that on Pt/C E-TEK; the electrolyte was 1.0 mol L^{-1} KOH, and the curves were obtained in steady state condition. Published with permission of the publishers [27, 28]

The O_2 reduction on Pt monolayer deposited on carbon-supported PdCo *core–shell* nanoparticles was studied by Lima and Adzic [27]. These carbon-supported PdCo/C *cores* have Pd surface segregated atoms, which was induced by thermal treatment under a H_2 atmosphere at 850 °C. In this work, the Pt monolayer was prepared by the Cu UPD method [10] onto PdCo/C *core–shell* surface. Figure 6 presents the polarization curves for the O_2 reduction reaction on the Pt monolayer deposited on PdCo/C presenting different Pd/Co atomic ratios. Although their half-wave potentials are below those of Pt_{ML}/Pd/C due to their lower surface area (higher particle size due to the thermal treatment), an important and surprising fact is that the half-wave potentials for O_2 reduction remain essentially constant for different Pd/Co atomic ratios (even for the lowest Pd content). This correspondence may reflect surface enrichment by Pd due to the surface segregation of Pd atoms in the substrate particles [6, 7]. The limiting current densities for all electrocatalysts are close to that of Pt/C. So, the results presented in the Fig. 6a

indicate that the behavior of the ORR is very similar on Pt/C and on the investigated Pt monolayer catalysts [5, 12].

As discussed before, Stamenkovic et al. [14] analyzed the activity towards the ORR of several Pt-3d-metal alloys, and the plot of activity versus d-band center showed a "volcano" dependency, with Pt–Co/C situated on the top of this curve. So, it becomes interesting, considering the practical point of view, to synthesize carbon-supported Pt–Co nanoparticles, presenting low Pt content, and with a Pt-enriched surface. This was the focus of a previous published work [28], where Pt–Co/C nanoparticles were synthesized by reducing the metal ions in H_2 atmosphere, followed by thermal treatment at high temperatures. However, the Pt surface enrichment is difficult to be achieved for this composition (Pd has a higher tendency to segregate on Co), and so, a large amount of the non-noble metal atoms was still present on the surface particle alloys. In acid electrolyte, these Co atoms at the surface may suffer dissolution, resulting in a Pt-enriched surface. However, on alkaline electrolyte, the non-noble metal may form an oxide or hydroxide phase at the catalyst surface, introducing a "screening" effect [29] on neighboring Pt atoms, lowering the number of Pt sites for the oxygen reduction reaction (site blocking). The screening effect may overcome any electronic effect induced by the Co atoms, and this can explain the lower or similar activity of the Pt–Co/C catalysts compared to Pt/C obtained on previous works in alkaline media [9].

In order to overcome this problem, after the thermal treatment of the Pt–Co/C (1:5 atomic ratio) nanoparticles [28], this material was electrochemically cycled in sulfuric acid electrolyte in order to remove (dissolve) the remaining Co atoms on the nanoparticle surface. Figure 6b shows the polarization curves for the O_2 reduction after cycling the Pt–Co/C material in H_2SO_4 electrolyte. The ORR curve on the commercial Pt/C E-TEK (20 wt %) was included for comparison. As it can be observed, the half-wave potentials of these curves clearly indicate higher activity for the cycled alloy catalyst. The higher activity obtained for the Pt–Co/C catalyst, after the Co dissolution from the particle surface, seems to be a consequence of three aspects: (i) increased surface area; (ii) lower "screening effect"; (iii) modification in the 5*d*-band properties of the surface Pt atoms, mainly caused by lattice mismatch and by a electronic coupling of the Pt in the *shell* and Co atoms in the beneath layer. A lattice mismatch of the Pt atoms on the Pt-rich surface and the Pt–Co alloy core may exist, caused by the Pt–Pt bond contraction due to the presence of the Co atoms, which have atomic radii lower than that of Pt. However, this may conduct to a small compressive strain in the Pt surface layer and, probably, this effect contributes little to the changes on the Pt 5*d*-band properties. On the other hand, the electronic interaction of the Pt and Co atoms (ligand effect) leads to a significant lowering of the Pt *d*-band center. This effect conducts to a faster electro-reduction of oxygenated intermediates (O–H bond formation) and/or a decrease on the Pt-oxides coverage from water activation (lower site blocking effect), in both cases inducing an increase of the ORR kinetics. So, the role of Co atoms is, principally, to promote the increase of the catalyst surface area, after their leaching from the surface, and to lower the Pt *d*-

band center, as a result of the electronic interaction of the Pt atoms at the catalyst surface, and the Co atoms in the inner layers.

Regardless considerable recent advances have been achieved in the ORR electrocatalystic activity of nanoparticles, including increased specific activity (A cm^{-2}—total surface area), and increased mass activity (A g^{-1}—active metal—Pt), the stability of these electrocatalysts during the fuel cell operation is of vital importance. One central problem is the substantial loss of the Pt surface area over time in PEMFC during the stop-and-go, and upon holding at constant potentials for extended period of time. A important step forward was accomplished demonstrating that platinum oxygen reduction fuel cell electrocatalysts can be stabilized against dissolution under potential cycling regimes by modifying Pt nanoparticles with gold clusters [30]. This was ascribed to the decreased oxidation of Pt nanoparticles covered by Au in comparison with the oxidation of pure Pt, as it evidenced by in situ XAS (*X-ray Absorption Spectroscopy*).

In the particular case of *core–shell* electrocatalysts, the stability of the core has to be considered. Recently, it was reported a new design of the *core–shell* catalyst consisting of double shells instead of a single one. The two shells were made on a Pd nanoparticle core, with the outermost shell being a Pt_{ML} and the one underneath being an alloy sublayer of $(Pd\text{-}Au)_{ML}$ [31]. This *core–shell* catalyst was obtained by performing Cu UPD twice on an Pd/C catalyst and the Pd:Au atomic composition was varied. The ORR curves obtained on the Pt monolayers deposited on PdAu sublayers with different compositions is presented in Fig. 7a. Analyzing the half-wave potentials, it can be seem the following order of activity: $Pt_{ML}/Pd_{90}Au_{10} > Pt_{ML}/Pd_{95}Au_5 > Pt_{ML}/Pd_{80}Au_{20} > Pt_{ML}/Pd_{100}$.

The presence of Pd-Au alloys sublayer may conduct to lateral strain (compressive and tensile) and radial contraction (compressive strain), which result in an activity improvement for the ORR, and, in that case, the optimal alloy composition was 10 at.% Au. Furthermore, the interaction of the substrate with Pt_{ML} could result in an electronic effect on the ORR activity through charge redistribution. The formation of PtOH is significantly prohibited for the Pt_{ML} on Pd nanoparticles when compared to that of Pt nanoparticles, as observed by in situ XAS and cyclic voltammetry [12]. Therefore, as hydroxyl formation is considered as a major factor affecting ORR activity because of site blocking effect by OH, the increased activity for the O_2 reduction has an important contribution from the reduced coverage by OH on the Pt sites. So, in this case, the Au in the sublayer of the Pt_{ML}/PdAu catalysts may have contributed to the reduction of surface oxidation, leading to improved ORR activity of the catalysts.

The stability of the catalysts was tested using $Pt_{ML}/Pd_{90}Au_{10}$, which was the best electrocatalyst. Its ORR activities are shown in Fig. 7b before and after 5,000 cycles at 1,600 rpm. As can be observed, the catalyst has almost no loss in ORR activity, demonstrating that the catalyst is practically stable. Surface oxidation may lead to catalyst dissolution, and so, the stabilization of the catalyst may be due to the reduction of surface oxidation from Au in the sublayer, due to the fact that Au may play an important role in protecting low-coordination sites from being oxidized [32]. Therefore, the Au in the Pd-Au alloy may have improved the

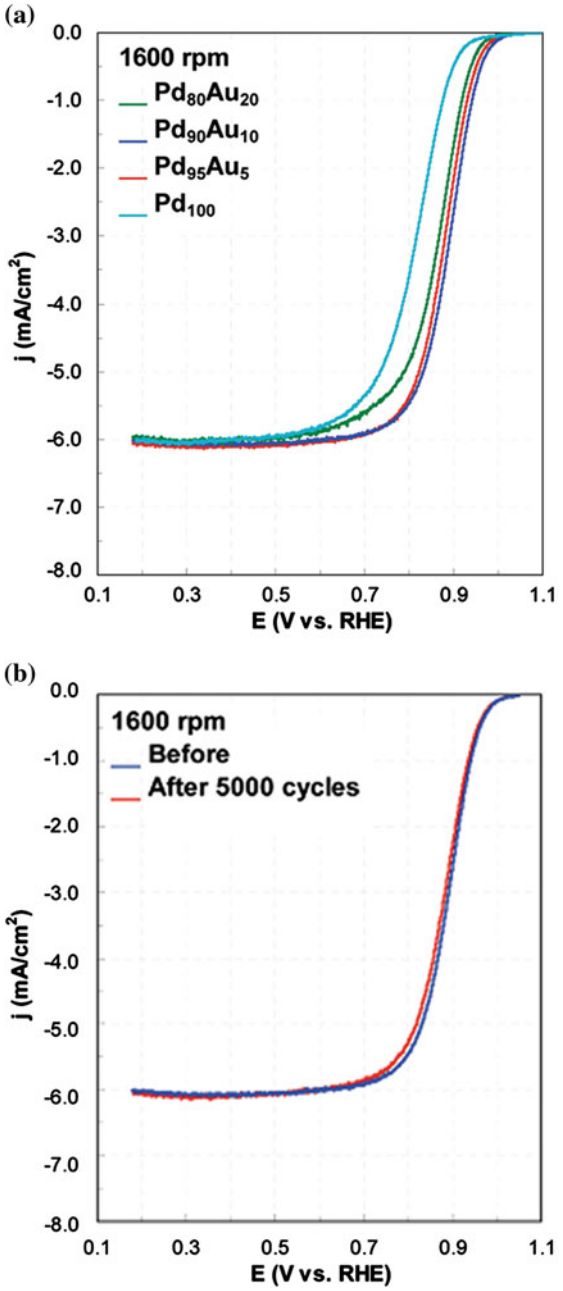

Fig. 7 (**a**) ORR activities of different catalysts obtained with electrode rotating speed at 1,600 rpm in 0.1 M HClO4, showing the best activity with an alloy sublayer of $Pd_{90}Au_{10}$ and the worst without a sublayer; (**b**) Stability of ORR of the catalyst with $Pd_{90}Au_{10}$ alloy sublayer, showing a small deactivation of the catalyst after 5,000 cycles. Published with the permission of the publisher [31]

catalysts by affecting the lattice contraction (both lateral and radial) and preventing some specific sites of Pt_{ML} from oxidation.

3 Ethanol Electro-Oxidation

Ethanol is an interesting fuel for practical application on direct alcohol/air fuel cells, mainly for small electronic devices. The advantages of the ethanol are: (i) it is a liquid fuel available at low cost (this is principally the case of Brazil, where the production is already well established); (ii) easily handled, transported and stored; (iii) lower toxicity, (iv) relatively high theoretical density of energy (8.0 kWh kg^{-1}) when compared to that of gasoline (10–11 kWh kg^{-1}) [33].

3.1 Acid Media

The thermodynamic potential of the total ethanol oxidation reaction (EOR), which is the reaction that takes place at the anode of Direct Ethanol Fuel Cells (DEFCs), is:

$$CH_3CH_2OH + 3H_2O \rightarrow 2CO_2 + 12H^+ + 12\ e^- \quad E_1^0 = 0.084V \tag{14}$$

Where the reaction at cathode is the oxygen reduction (2):

$$3O_2 + 12H^+ + 12\ e^- \rightarrow 6H_2O \quad E_2^0 = 1.229V \tag{15}$$

Resulting in a global reaction (3):

$$CH_3CH_2OH + 3O_2 \rightarrow 2CO_2 + 3H_2O \quad E_{eq}^0 = E_2^0 - E_1^0 = 1.145V \tag{16}$$

Thus, the total or the complete ethanol oxidation, forming CO_2 and H_2O, involves the transference of 12 electrons (97.3 kJ mol^{-1}) [34] per ethanol molecule, with $E_{eq}^0 = 1.145$ V, where E_{eq}^0 is the equilibrium standard potential (vs. SHE—S*tandard Hydrogen Electrode*). For this system, the theoretical thermodynamic efficiency is of 97 %. However, due to the loss by incomplete alcohol oxidation, the efficiency drops to around 40 % [33].

The ethanol electro-oxidation reaction has a relative complex mechanism. A good electrocatalyst for achieving the total ethanol oxidation has to facilitate bond breakings (C–H, C–O and C–C) and to facilitate bond formations (oxygen addition). As most of the investigated electrocatalysts do not satisfy these features, the ethanol electro-oxidation follows parallel reaction pathways forming, mainly, acetaldehyde, acid acetic and CO_2 at much lower extention [35–38], and some adsorbed reaction intermediates, such as CO_{ad} and C_xH_x adsorbed (hydrocarbon fragments with one or two carbon) [35, 36, 39–41], which will be discussed below.

In order to investigate the reaction mechanism and to determine the reaction products, spectroscopic and spectrometric techniques, such as in situ FTIR (*Fourier Transform Infra-red Spectroscopy*) [34, 42, 43], and *on-line* DEMS (*Differential Electrochemistry Mass Spectrometry*) [44], correlated with electrochemical techniques, such as cyclic voltammetry and chronoamperometry [37], have been currently utilized. In a previous published work, some researchers have shown a high dependence on the crystallographic surface orientation of the electrocatalyst [41, 45], and on the ethanol *bulk* concentration [46–48]. Leung et al. [43] investigated the ethanol electro-oxidation pathways on *well*-ordered Pt(111) surface *versus* disordered Pt(111) (higher density of defects), and on polycrystalline Pt by in situ FTIR. They observed that acetic acid and acetaldehyde were the main reaction products. Also, there was a little amount of CO_2 on ordered Pt(111) than on disordered Pt(111). In addition, the CO_{ad} degree of coverage was higher on disordered and polycrystalline Pt surface than on the Pt(111) surface. After that, Colmati et al. [41] studied the reaction on stepped Pt single crystal electrodes by electrochemical methods and by in situ FTIR. For this purpose, two different series of crystallographic surfaces were investigated: 1-(111) terraces with (100) monoatomic steps and, 2-(111) terraces with (110) monoatomic steps. The electrochemical behaviors of the two investigated crystallographic surfaces were significantly different. As discussed by the authors [41], the surface formed by (111) terraces with (100) monoatomic steps showed no activity alteration in relation to Pt(111) single-crystal. On the other hand, the surface formed by (111) terraces with (110) monoatomic steps presented a two-fold effect on the ethanol electro-oxidation: 1-it showed that the step catalyzes the C–C bond breaking followed by the oxidation of the adsorbed intermediates, like CO_{ad}, formed below 0.7 V (vs. RHE); and 2-the steps also catalyzes the ethanol oxidation to acetic acid and acetaldehyde at higher potentials (above 0.7 V vs. RHE).

Using in situ FTIR, Camara and Iwasita [48] showed a strong dependence of the reaction product distribution as a function of the ethanol concentration on polycrystalline Pt, and this result is presented in Fig. 8 [48]. It can be noted that, at low ethanol concentrations (0.01–0.05 mol L^{-1} of ethanol), the main products were CO_2 and acetic acid. In the case of high ethanol concentrations (above 0.2 mol L^{-1} of ethanol), acetaldehyde was the dominant product. In addition, the authors reported that low CO_2 and acetic acid formation, at high ethanol concentration, was probably due to the limited availability of free Pt sites for water adsorption, which is the oxygen specie-donor in the oxidation process. This increase in the CO_2 formation was also explained by a transport effect, namely an increasing tendency for re-adsorption and further oxidation of incomplete oxidation products at lower concentrations. So, higher ethanol concentration leads an overall partial oxidation reaction, in which the ethanol electro-oxidation follow parallel pathways forming by-products such as acetaldehyde and acetic acid.

Considering the previous published investigations using on-line DEMS, in situ FTIR, and electrochemical techniques, it can be proposed a simplified mechanism for ethanol oxidation on Pt-based electrocatalysts [34, 37, 38, 41, 43, 45, 47–49]:

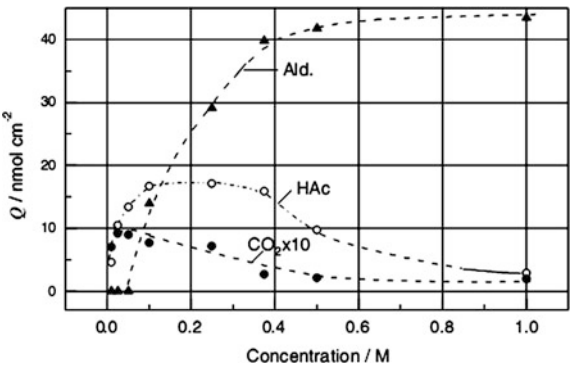

Fig. 8 Amount (Q) of CO_2, acetic acid and acetaldehyde after 10 min of polarization at 0.5 V for different concentrations of ethanol in 0.1 mol L^{-1} $HClO_4$. CO_2 (*full circle*), acetic acid (*empty circle*) and acetaldehyde (*triangle*), respectively. (Published with permission of Elsevier [48])

$$C_2H_5OH + Pt(H_2O) \rightarrow Pt(C_2H_5OH_{ad}) + H_2O \quad (17)$$

$$Pt(C_2H_5OH_{ad}) + Pt \rightarrow Pt(CO_{ad}) + Pt(CH_{x-ad}) + xH^+ + xe^- \quad (18)$$

$$Pt(C_2H_5OH_{ad}) \rightarrow Pt(CH_3CHO) + 2H^+ + 2e^- \quad (19)$$

$$Pt(H_2O) \rightarrow Pt(OH) + H^+ + e^- \quad (20)$$

$$Pt(CH_3CHO) + Pt(OH) \rightarrow CH_3COOH + H^+ + e^- + 2Pt \quad (21)$$

$$Pt(CO_{ad}),\ Pt(CH_x) + Pt(OH) \rightarrow CO_2 + Pt + xH^+ + xe^- \quad (22)$$

where, Pt-$C_2H_5OH_{ad}$, Pt-CO and Pt-$CH_{x\text{-}ad}$ are adsorbed intermediates on Pt surface as: ethanol, carbon monoxide and hydrocarbon fragments, respectively. These steps (17–22) do not necessarily represent the sequential ethanol electro-oxidation.

In order to obtain an efficient electrochemical conversion of the ethanol molecules to CO_2, experimental variables such as temperature [50], and the nature of the nanostructured electrocatalyst [51] has been studied. The ethanol electro-oxidation on carbon-supported Pt/C catalyst was studied by Sun et al. [50] have determined, quantitatively, the amount of CO_2 produced over a wide range of reaction temperatures using by *on-line* DEMS with a dual thin layer flow cell [50]. The electrochemical measurements showed that the faradaic current and CO_2 formation rate, performed at 3 bar overpressure, revealed significant effects of temperature, and ethanol concentration on the reaction efficiency. Elevated values of electrochemical conversion efficiency to CO_2 were obtained for high temperature, low concentration and low electrode overpotentials (nearby 90 % current efficiency for CO_2 formation at 100 °C, 0.01 mol L^{-1}, 0.48 V vs. RHE). On the other hand, at high ethanol concentrations (0.1 mol L^{-1}), high potentials or low temperatures, the current efficiency for CO_2 dropped to values of a few percent.

As discussed by the authors [50], at room temperature, CO_2 formation in the positive-going scan is essentially due to oxidation of CO_{ad} pre-formed at lower potentials. In the negative-going scan, the CO_2 formation is totally inhibited. With

increasing temperature, the pre-formed CO_{ad} can be oxidized at increasingly lower potential, allowing subsequent bulk oxidation to CO_2 via C–C bond breaking, and subsequent oxidation of the resulting $C_{1,ad}$ species in the positive-going scan to CO_2. In the negative-going scan, C–C bond breaking can occur at potentials where subsequent oxidation of the resulting fragments is still possible, and the latter reaction extends to lower potentials, where C–C bond breaking is increasingly active, until the surface is saturated with adsorbed $C_{1,ad}$ fragments again.

Aiming at increasing the Pt electrocatalytic activity and the rate of CO_2 production, Lima et al. [52] and Camara et al. [53] studied the EOR by in situ FTIR on Pt-Ru bimetallic electrocatalysts. The results showed an increase in the overall reaction kinetics when compared to that of pure Pt. This fact was associated to the formation of Ru-OH species (O-donor) at low potentials, conducting the Pt–CO/Ru-OH and Pt-CH_x/Ru-OH coupling. Nevertheless, the efficiency to remove the adsorbed intermediates (probably Pt–CO and Pt-CH_x) was low, resulting in the formation of acetaldehyde and acetic acid as main reaction products.

On the other hand, electrocatalysts composed by the combination between Pt and Rh have shown higher formation of CO_2 when compared to that for other Pt-based bimetallic materials [35, 36, 51–54]. The results showed that the addition of rhodium atoms produces a significant decrease in the acetaldehyde yield, compared to pure platinum electrodes, even at ambient temperature (25 °C). This behavior was attributed to the higher activity of the Rh atoms in relation to Pt for the dissociative ethanol adsorption, resulting in a C–C bond breaking [55]. Although few is known about of the rhodium's role for the ethanol electro-oxidation, one explanation for the decreased acetaldehyde amount could be related to the existence of more availability of Pt-Rh active sites for the C–C bond breaking upon ethanol adsorption at lower potential. However, as in the case of Pt, CO_2 is detected only in the positive-going scan. This also means that the CO_2 is produced only due to the oxidation of the reaction adsorbed intermediate species. Furthermore, this change in the reaction route, or in the CO_2/acetaldehyde ratio, is still very low, and does not conducted to an efficient oxidation of *bulk* ethanol to CO_2, as required for application on fuel cells operating at ambient temperature.

An efficient electrocatalyst for the total electro-oxidation to CO_2 must present a balance between two competitive steps: bond breaking and bond formation (fast stripping of the adsorbed species) [19]. So, the challenge is to develop nanostructured electrocatalysts that allow controlling those effects by modifying the electronic structure or the chemical reactivity of the active metals. In this direction, the *core–shell* structure has show to be a promising kind of electrocatalyst. This is because of two important characteristics of such structure: (1) they allow electronic "modulation" of the atoms at metal surface, through two major effects: (i)—*Electronic* [25]: interaction between the electronic bands of the composing metals, and (ii)—*Geometric* [6]: due to the presence of defects and lattice mismatch between the metals in the *shell* and in the *core* of the nanoparticle. So, this structure allows the change of the adsorption strength of the reacting molecules [25, 56], thus changing the catalytic activity; (2) they present a relatively higher mass-activity (Faradaic current per unit of mass of the active metal, A g^{-1}) due to

the presence of the active noble metal only on the particle surface. Therefore, if the particle *core* is a non-noble metal, this kind of electrocatalyst becomes attractive for commercial application due to its reduced cost.

Notably, this type of nanostructure is recent in the electrocatalysis area, and it possesses a particularly strong electronic modification of the active metal when compared to that of bimetalic alloy materials [56, 57]. These nanostructured materials would provide a change in the behavior of the ethanol electro-oxidation reaction in relation to the commonly employed nanoparticles such as Pt–Sn [58], Pt-Ru [52, 53] and Pt–Rh [35, 54] alloys.

Kowal et al. [36] studied the ethanol electro-oxidation on Pt–Rh/SnO_2/C nanoparticles. The ternary Pt–Rh/SnO_2/C electrocatalyst was synthesized by the *cation-adsorption-reduction-galvanic-displacement method*, resulting in a *core–shell* structure [36]. The electrochemical measurements showed that the current density obtained for the ternary electrocatalyst was more than two orders of magnitude larger than that of commercial Pt/C. In addition, in situ FTIR experiments showed that the material presents a high activity for the C–C bond breaking. The authors suggested that, in this material, the C–C bond is broken directly, not following the acetaldehyde step. In addition, Adzic et al. [51] have investigated the ethanol electro-oxidation on Pt–Rh-SnO_2/C material with different atomic ratios. The results showed lower onset potential and higher Faradaic current for the composition of Pt:Rh:Sn = 3:1:4. These ternary-electrocatalysts presented, effectively, a higher rate for CO_2, in relation to that of pure Pt/C.

In a recent work [59], Lima et al. have investigated the ethanol oxidation products on *core–shell* nanoparticles formed by a carbon-supported Au *core*, and with a *shell* composed by the combination of Pt, Rh, and Ru atoms. The results for the Faradaic current, and ion current signals for acetaldehyde (m/z = 29), and for CO_2 (m/z = 22) for the different electrocatalysts are presented in Fig. 9. The curves show similar onset potentials for all investigated nanoparticles. At high potential values, Pt/C shows higher current densities, which evidences superior overall reaction rate at high overpotential. Although Pt/C has presented higher current densities, it shows larger formation of acetaldehyde. Interestingly, for the Rh/Pt/Au/C material, the curves evidenced some increase of the CO_2 production, and a reduction of the acetaldehyde formation. These results are in agreement with some other investigations using Pt–Rh alloys [52, 54], where the presence of Rh in the electrocatalyst surface induces higher CO_2/acetaldehyde ratio, when compared to materials composed of pure Pt or by bimetallic Pt–Ru.

Therefore, it is important to mention that these results showed that *core–shell* nanoparticles can be developed containing only a fractional amount of Pt, having higher mass-specific activity than Pt/C. Also, it was demonstrated that the overall reaction rate could be hampered by increasing the Pt *shell* thickness (not shown here), and the electrocatalyst efficiency could be improved by adjusting the particle *shell* composition. However, the activity and efficiency of this type of electrocatalyst has also to be tested in other reaction conditions of ethanol concentration and reaction temperature.

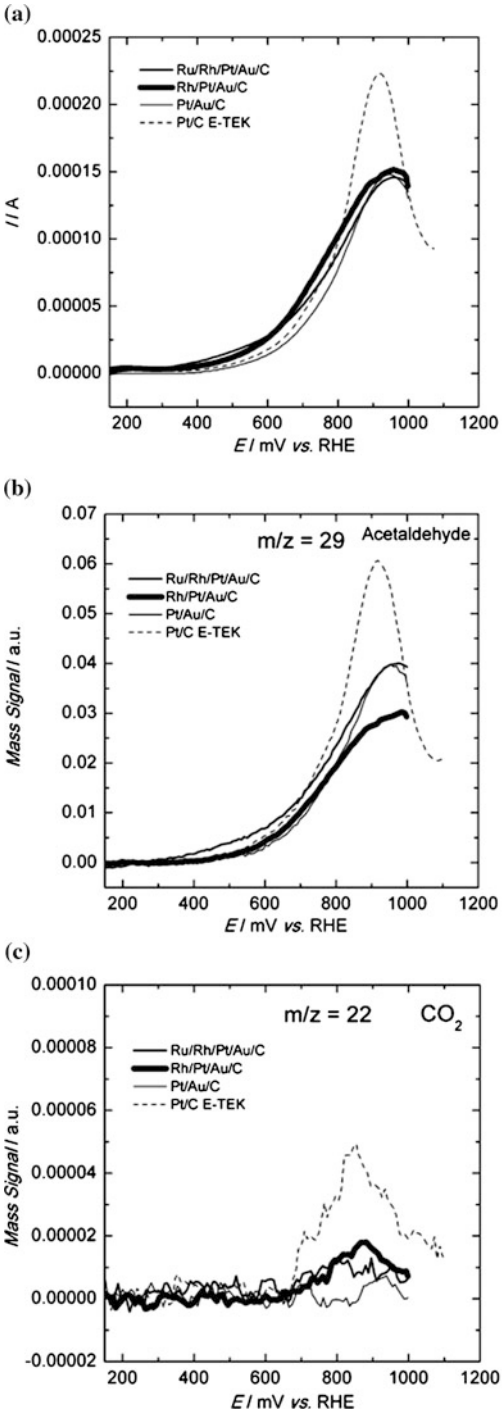
(a)
Ru/Rh/Pt/Au/C
Rh/Pt/Au/C
Pt/Au/C
Pt/C E-TEK
I / A
E / mV vs. RHE
(b)
m/z = 29
Acetaldehyde
Mass Signal / a.u.
(c)
m/z = 22
CO2

◀ **Fig. 9** DEMS experiments for the ethanol electro-oxidation reaction (positive scan) catalyzed by the different electrocatalysts: (**a**) faradaic currents; (**b**) ion currents for the acetaldehyde formation (m/z = 29, CHO +); and (**c**) ionic currents for CO_2 formation (m/z = 22, CO_2^{2+}), in 0.5 mol L^{-1} C_2H_5OH/0.5 mol L^{-1} $HClO_4$ solution. Scan rate of 10 mV s^{-1}. Published with the permission of the publisher [59]

3.2 Alkaline Electrolyte

The investigations of the ethanol electro-oxidation in alkaline electrolyte have been increased due to the possibility of using less noble, or non-noble metals [56, 60–63]. Indeed, the oxidation of small organic molecules are easier in alkaline than in acid media [64, 65]. Meanwhile, even in alkaline electrolyte, the *bulk* ethanol electro-oxidation is difficult and, so, the main products of the ethanol electro-oxidation at the ambient temperature are acetic acid/acetate, which results in Faradaic efficiency of 33 % [64].

Rao et al. [65] studied the ethanol electro-oxidation products in an *Alkaline Membrane Electrode Assembly* catalyzed by carbon-supported Pt nanoparticles, using on-line FC-DEMS (*Fuel Cell Differential Electrochemical Mass Spectrometry*). The results, presented in Fig 10, showed that the ethanol electro-oxidation undergoes considerably more CO_2 formation than that in acidic electrolyte, using the same Pt-catalyzed electrode anode in the positive-ongoing scan. For acid media, the Faradaic efficiency (FE) to CO_2 was only 2 %. However, for the alkaline electrolyte, the same anode and conditions (at 0.8 V vs. RHE, 60 °C and 0.1 mol L^{-1} ethanol), the FE was around 55 % (Fig. 10). This was a indirect indication that the C–C bond breaking and the oxidative removal rates of adsorbed intermediate in alkaline electrolyte are significantly higher than in acid media. Accordingly, Bayer et al. [64, 66] have investigated the ethanol electro-oxidation on Pt/C by on-line DEMS in acid and alkaline electrolyte using a flow cell. The results showed that the CO_2/acetaldehyde ratio is higher in alkaline than in acid media.

Although the mechanism of ethanol electro-oxidation in alkaline media is not entirely understood, the results evidence that, as observed in acid media, most of the CO_2 comes from the oxidation of adsorbed intermediates produced in the previous lower potential excursions. So, the CO_2 does not come from the *bulk* ethanol oxidation, at least in the range of temperatures below 60 °C. Even though many other experiments are needed in order to comprehend the higher efficiency in the positive-going scan, this is one very important feature that justifies further investigations in order to reach higher activity for *bulk* ethanol electro-oxidation.

Recently, some works have demonstrated that Pd/C has a particular high electrocatalytic activity for the overall ethanol electro-oxidation in alkaline electrolyte [67, 68]. The EOR presented fast kinetics of dehydrogenation, in which the reaction adsorbed intermediates were oxidized by the neighboring adsorbed Pt-OH species, which were formed by the OH-ions from the electrolyte. Liang et al. [67], based on electrochemical measurements, proposed a simplified mechanistic for ethanol oxidation on Pd/C, as follow:

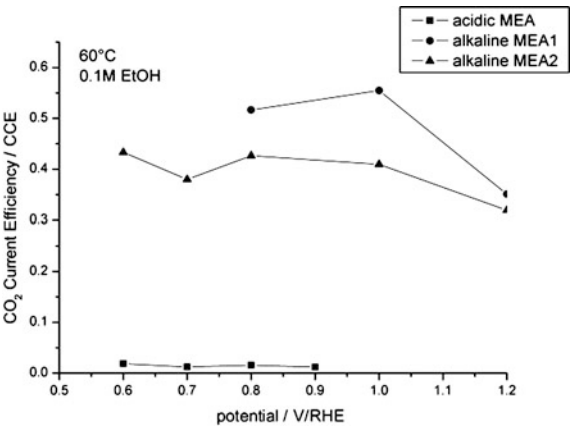

Fig. 10 Comparation between the acidic and alkaline MEAs with Pt as catalyst for CO_2 (FE) at 60 °C. Published with permission of Elsevier [65]

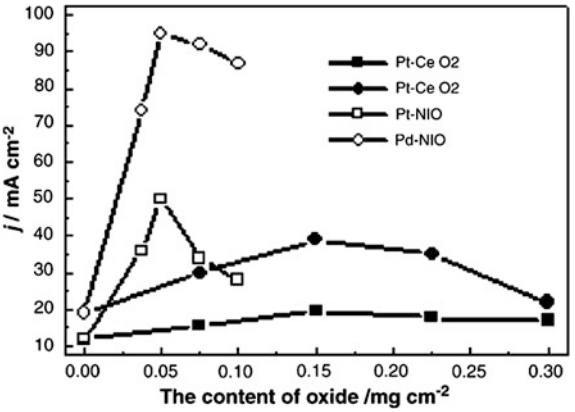

Fig. 11 Effect of the content of oxide on Pt/C and Pd/C catalysts for ethanol electro-oxidation in 1.0 mol L^{-1} KOH solution containing 1.0 M ethanol with a sweep rate of 0.05 V s^{-1}, Pt or Pd loading: 0.3 mg cm^{-2}. Published with permission of the publisher [72]

$$Pd - H_2O + CH_3CH_2OH \rightarrow Pd - CH_3CH_2OH \quad (10)$$

$$Pd - CH_3CH_2OH \ + 3OH^- \rightarrow Pd - CH_3CO \ + 3H_2O + 3e^- \quad (11)$$

$$Pd - CH_3CO + Pd - OH \rightarrow Pd - CH_3COOH + Pd \quad (12)$$

$$Pd - CH_3COOH + OH^- \rightarrow Pd + CH_3COO^- + H_2O \quad (13)$$

where, the ethoxy formation (Pd-CH_3CO) is a strongly adsorbed intermediate, and its oxidation is the determining step of reaction (12). Importantly, the mechanism proposed for the oxidation involves the formation of acetic acid as final product. On the other hand, on Pd/C electrocatalyst, acetaldehyde, and carbon dioxide are also discussed as reaction products [69, 70].

Zhou et al. [70] studied the ethanol electro-oxidation on polycrystalline Pd electrocatalyst by in situ FTIR spectroscopy, in alkaline electrolyte. The authors observed a low conversion of ethanol to CO_2 (around 2.5 % at −0.6 to 0.0 V vs. SCE, 0.1 mol L^{-1} NaOH + 0.1 mol L^{-1} ethanol), and argued that the C–C bond

breaking is more facile on Pd than on Pt under the same conditions. In fact, bridge-bonded CO (CO_B) was observed, suggesting the indirect pathway for CO_2 formation (via adsorbed CO_{ad}).

Preliminary on-line DEMS measurements in alkaline electrolyte for the ethanol electro-oxidation on Pd/C catalyst, in our laboratory, [71] showed a higher CO_2/acetaldehyde ratio compared to that on Pt/C, in two different alkali concentrations (0.01–0.5 mol L^{-1} of ethanol). This was ascribed to the formation of reactive intermediates such as CH2CHO- anion, in which the C-C bond is less shielded, resulting in a higher amount of CO2.

The use of non-noble metal oxides in combination with active noble metals has also been investigated in alkaline electrolyte. Xu et al. [72] have studied the electrocatalytic activity of materials composed by Pt and Pd nanoparticles supported on NiO/C and CeO_2/C, and the obtained results are presented in Fig. 11. The results showed that Pd/C has a higher catalytic activity and better steady-state performance for ethanol electro-oxidation than Pt/C. The activity of the electrocatalysts decreases in the order: Pd–NiO/C > Pd–CeO_2/C > Pt–NiO/C > Pt–CeO_2/C > commercial E-TEK PtRu/C ≈ Pd/C > Pt/C. The authors argued that the higher activities could be ascribed to the OH_{ad} species, which can be easier formed on the oxide surface. This can oxidize CO-like poisoning species on Pt and Pd to CO_2 or other products, releasing active sites on Pt and Pd for further electrochemical reaction.

4 Conclusions

4.1 Oxygen Reduction

The results presented in this text showed that the activity of different single crystal surfaces, of nanoparticles of the same metals, and of Pt monolayer on single crystal supports correlates well with the metals' *d*-band center for the ORR in acid and alkaline solutions. The O_2 reduction activity of these electrode surfaces showed a volcano-type dependency on the *d*-band center of the metal catalyst. In acid and alkaline solutions, the electrocatalyst surfaces exhibit the optimum balance between the kinetics of O–O bonding breaking and the electro-reduction of the oxygenated intermediates or O–H formation. The highest activity was obtained for Pt monolayer deposited on Pd substrates. *Core–shell* electrocatalysts have two main advantages (i) reduce the amount of the total Pt loading; (ii) they offer the possibility of a significant alteration of the Pt electronic structure, which can enhance the reactivity of Pt atoms. The studies of long-term stability showed that the addition of Au, forming a PdAu sublayer showed increased catalyst stability during potential cycling. This was associated to the role of the Au atoms in protecting the Pt and/or Pd low-coordination sites from being oxidized.

4.2 Ethanol Oxidation

The experimental results showed in this chapter indicated that, on Pt, the overall reaction rate and the rate for CO_2 formation increase significantly with increasing reaction temperature, and with decreasing ethanol concentration. The increase with temperature seems to be related to the decrease in the activation energy. The increase of CO_2 formation as the ethanol concentration is decreased was ascribed to the increased amount of water molecules in the ethanol vicinities, which favor the oxygen addition on the reaction intermediates. However, in order to achieve practicable current densities for direct ethanol fuel cells, the ethanol concentration should be increased. In this case, the experimental results indicated a drastic decrease in the reaction efficiency, with only few percent of CO_2 production. The results also showed that the addition of Rh atoms to the Pt-based electrocatalysts leaded to a higher electrochemical conversion efficiency or higher CO_2/acetaldehyde production ratios in relation to pure Pt in the same alcohol concentration.

In the particular case of the ethanol electro-oxidation in alkaline electrolyte, mass spectrometry measurements indicated higher CO_2 formation than in the case of acidic electrolyte, with the same anode electrocatalyst. However, below 60 °C, the CO_2 comes from the oxidation of adsorbed intermediates formed in pre-excursions to lower potentials, instead of from the oxidation of *bulk* ethanol molecules. Pd-based electrocatalysts presented higher electrocatalytic activity than Pt.

Acknowledgments D.A. Cantane (No. 2009/11073-3) and F.H.B. Lima (No. 2008/05156-0) acknowledge support from Fundação de Amaparo à Pesquisa do Estado de São Paulo—FAPESP, Brazil.

References

1. Yeager E (1984) Electrocatalysts for O2 reduction. Electrochim Acta 29(11):1527–1537
2. Kinoshita K (1992) Electrochemical oxygen technology. Wiley-Interscience, New York 431
3. Adzic R (1998) Recent advances in the kinetics of oxygen reduction. In: Lipkowski J, Ross PN (eds) Electrocatalysis, Wiley-VCH, New York, p 197
4. Zhang J, Vukmirovic MB, Xu Y, Mavrikakis M, Adzic RR (2005) Controlling the catalytic activity of platinum- monolayer electrocatalysts for oxygen reduction with different substrates. Angew Chem Int Ed 44:2132–2135
5. Lima F, Zhang J, Shao M, Sasaki K, Vukmirovic M, Ticianelli E, Adzic R (2007) Catalytic activity-d-band center correlation for the O2 reduction reaction on platinum in alkaline solutions. J Phys Chem C 111(1):404–410
6. Hammer B, Nørskov JK (2000) Theoretical surface science and catalysis–calculations and concepts. Adv Catal 45:71–129
7. Greeley J, Nørskov JK, Mavrikakis M (2002) Electronic structure and catalysis on metal surfaces. Annu Rev Phys Chem 53(1):319–348
8. Mukerjee S, Srinivasan S, Soriaga MP, McBreen J (1995) Effect of preparation conditions of Pt alloys on their electronic, structural, and electrocatalytic activities for oxygen reduction-XRD, XAS, and electrochemical studies. J Phys Chem 99(13):4577–4589

9. Lima FHB, Ticianelli EA (2004) Oxygen electrocatalysis on ultra-thin porous coating rotating ring/disk platinum and platinum-cobalt electrodes in alkaline media. Electrochim Acta 49(24):4091–4099
10. Brankovic S, Wang J, Adzic R (2001) Pt submonolayers on Ru nanoparticles: a novel low Pt loading, high CO tolerance fuel cell electrocatalyst. Electrochem Solid-State Lett 4:A217
11. Adzic RR, Zhang J, Sasaki K, Vukmirovic MB, Shao M, Wang J, Nilekar AU, Mavrikakis M, Valerio J, Uribe F (2007) Platinum monolayer fuel cell electrocatalysts. Top Catal 46(3):249–262
12. Zhang J, Mo Y, Vukmirovic MB, Klie R, Sasaki K, Adzic RR (2004) Platinum monolayer electrocatalysts for O2 reduction: Pt monolayer on Pd (111) and on carbon-supported Pd nanoparticles. J Phys Chem B 108(30):10955–10964
13. Kitchin JR, Nørskov JK, Barteau MA, Chen J (2004) Role of strain and ligand effects in the modification of the electronic and chemical properties of bimetallic surfaces. Phys Rev Lett 93(15):156801
14. Stamenkovic V, Mun BS, Mayrhofer KJJ, Ross PN, Markovic NM, Rossmeisl J, Greeley J, Nørskov JK (2006) Changing the activity of electrocatalysts for oxygen reduction by tuning the surface electronic structure. Angew Chem 118(18):2963–2967
15. Ruban A, Skriver HL, Nørskov JK (1999) Surface segregation energies in transition-metal alloys. Phys Rev B 59(24):15990
16. Bardi U, Atrei A, Zanazzi E, Rovida G, Ross P (1990) Study of the reconstructed (001) surface of the $Pt_{80}Co_{20}$ alloy. Vaccum 41(1–3):437–440
17. Mun BS, Watanabe M, Rossi M, Stamenkovic V, Markovic NM, Ross PN Jr (2005) A study of electronic structures of Pt_3 M (M = Ti, V, Cr, Fe, Co., Ni) polycrystalline alloys with valence-band photoemission spectroscopy. J Chem Phys 123:204717-1–204717-4
18. Markovic N, Gasteiger H, Grgur B, Ross P (1999) Oxygen reduction reaction on Pt (111): effects of bromide. J Electroanal Chem 467(1–2):157–163
19. Somorjai GA, Li Y (2010) Introduction to surface chemistry and catalysis. Wiley, New York
20. Chorkendorff I, Niemantsverdriet JW, Wiley J (2003) Concepts of modern catalysis and kinetics, vol 138. Wiley Online Library, Weinheim
21. Nørskov JK, Bligaard T, Logadottir A, Bahn S, Hansen LB, Bollinger M, Bengaard H, Hammer B, Sljivancanin Z, Mavrikakis M (2002) Universality in heterogeneous catalysis. J Catal 209(2):275–278
22. Clouser S, Huang J, Yeager E (1993) Temperature dependence of the Tafel slope for oxygen reduction on platinum in concentrated phosphoric acid. J Appl Electrochem 23(6):597–605
23. Yeager E, Gervasio D, Razaq M, Razaq A, Tryk D (1993) Dioxygen reduction in various acid electrolytes. Serb J Chem Soc 57:819
24. Sidik RA, Anderson AB (2002) Density functional theory study of O_2 electroreduction when bonded to a Pt dual site. J Electroanal Chem 528(1–2):69–76
25. Sasaki K, Wang J, Balasubramanian M, McBreen J, Uribe F, Adzic R (2004) Ultra-low platinum content fuel cell anode electrocatalyst with a long-term performance stability. Electrochim Acta 49(22–23):3873–3877
26. Gong K, Su D, Adzic RR (2010) Platinum-monolayer shell on AuNi 0.5 Fe nanoparticle core electrocatalyst with high activity and stability for the oxygen reduction reaction. J Am Chem Soc 132(41):14364–14366
27. Lima FHB, Zhang J, Shao M, Sasaki K, Vukmirovic M, Ticianelli E, Adzic R (2008) Pt monolayer electrocatalysts for O_2 reduction: PdCo/C substrate-induced activity in alkaline media. J Solid State Electrochem 12(4):399–407
28. Lima FHB, De Castro JFR, Santos LGRA, Ticianelli EA (2009) Electrocatalysis of oxygen reduction on carbon-supported Pt-Co nanoparticles with low Pt content. J Power Sources 190(2):293–300
29. Obradovic M, Grgur B, Vracar LM (2003) Adsorption of oxygen containing species and their effect on oxygen reduction on Pt_3Co electrode. J Electroanal Chem 548:69–78
30. Zhang J, Sasaki K, Sutter E, Adzic R (2007) Stabilization of platinum oxygen-reduction electrocatalysts using gold clusters. Science 315(5809):220

31. Xing Y, Cai Y, Vukmirovic MB, Zhou WP, Karan H, Wang JX, Adzic RR (2010) Enhancing oxygen reduction reaction activity via Pd- Au alloy sublayer mediation of Pt monolayer electrocatalysts. J Phys Chem Lett 1:3238–3242
32. Wang C, van der Vliet D, More KL, Zaluzec NJ, Peng S, Sun S, Daimon H, Wang G, Greeley J, Pearson J (2011) Multimetallic Au/$FePt_3$ nanoparticles as highly durable electrocatalyst. Nano Lett 11(3):919–926
33. Lamy C, Lima A, LeRhun V, Delime F, Coutanceau C, Leger JM (2002) Recent advances in the development of direct alcohol fuel cells (DAFC). J Power Sources 105(2):283–296
34. Iwasita T, Nart F (1997) In situ infrared spectroscopy at electrochemical interfaces. Prog Surf Sci 55(4):271–340
35. De Souza JPI, Queiroz SL, Bergamaski K, Gonzalez ER, Nart FC (2002) Electro-oxidation of ethanol on Pt, Rh, and PtRh electrodes. A study using DEMS and in situ FTIR techniques. J Phys Chem B 106(38):9825–9830
36. Kowal A, Li M, Shao M, Sasaki K, Vukmirovic M, Zhang J, Marinkovic N, Liu P, Frenkel A, Adzic R (2009) Ternary Pt/Rh/SnO2 electrocatalysts for oxidizing ethanol to CO_2. Nat Mater 8(4):325–330
37. Iwasita T, Pastor E (1994) A DEMS and FTIR spectroscopic investigation of adsorbed ethanol on polycrystalline platinum. Electrochim Acta 39(4):531–537
38. Xia X, Liess HD, Iwasita T (1997) Early stages in the oxidation of ethanol at low index single crystal platinum electrodes. J Electroanal Chem 437(1–2):233–240
39. Souza JPI, Queiroz SL, Nart FC (2000) The use of mass spectrometry in electrochemical measurements-the DEMS technique. Quim Nova 23(3):384–391
40. Jiang L, Colmenares L, Jusys Z, Sun G, Behm R (2007) Ethanol electro-oxidation on novel carbon supported Pt/SnOx/C catalysts with varied Pt: Sn ratio. Electrochim Acta 53(2):377–389
41. Colmati F, Tremiliosi-Filho G, Gonzalez ER, Berná A, Herrero E, Feliu JM (2009) The role of the steps in the cleavage of the C–C bond during ethanol oxidation on platinum electrodes. Phys Chem Chem Phys 11(40):9114–9123
42. Gao P, Chang SC, Zhou Z (1989) Electro-oxidation pathways of simple alcohols at platinum in pure nonaqueous and concentrated aqueous environments as studied by real-time ftir spectroscopy. J Electroanal Chem 272(1–2):161–178
43. Leung LWH, Chang SC, Weaver MJ (1989) Real-time FTIR spectroscopy as an electrochemical mechanistic probe: electro-oxidation of ethanol and related species on well-defined Pt (111) surfaces. J Electroanal Chem 266(2):317–336
44. Bruckenstein S, Gadde RR (1971) Use of a porous electrode for in situ mass spectrometric determination of volatile electrode reaction products. J Am Chem Soc 93:793–794
45. Colmati F, Tremiliosi-Filho G, Gonzalez ER, Berná A, Herrero E, Feliu JM (2008) Surface structure effects on the electrochemical oxidation of ethanol on platinum single crystal electrodes. Faraday Discuss 140:379–397
46. Cantane DA, Gonzalez ER (2009) Mechanistic aspects of ethanol electro-oxidation in unsupported platinum nanoparticles. ECS Trans 25:1161–1168
47. Giz MJ, Camara GA (2009) The ethanol electro-oxidation reaction at Pt (1 1 1): the effect of ethanol concentration. J Electroanal Chem 625(2):117–122
48. Camara G, Iwasita T (2005) Parallel pathways of ethanol oxidation: the effect of ethanol concentration. J Electroanal Chem 578(2):315–321
49. Lai SCS, Koper MTM (2008) Electro-oxidation of ethanol and acetaldehyde on platinum single-crystal electrodes. Faraday Discuss 140:399–416
50. Sun S, Halseid MC, Heinen M, Jusys Z, Behm RJ (2009) Ethanol electro-oxidation on a carbon-supported Pt catalyst at elevated temperature and pressure: a high-temperature/high-pressure DEMS study. J Power Sources 190(1):2–13
51. Adzic RR, Li M, Kowal A, Sasaki K, Marinkovic N, Su D, Korach E, Liu P (2010) Ethanol oxidation on the ternary Pt–Rh–SnO_2/C electrocatalysts with varied Pt: Rh: Sn ratios. Electrochim Acta 55(14):4331–4338

52. Lima FHB, Gonzalez ER (2008) Ethanol electro-oxidation on carbon-supported Pt-Ru, Pt-Rh and Pt-Ru-Rh nanoparticles. Electrochimica Acta 53(6):2963–2971
53. Camara G, De Lima R, Iwasita T (2005) The influence of PtRu atomic composition on the yields of ethanol oxidation: a study by in situ FTIR spectroscopy. J Electroanal Chem 585(1):128–131
54. Lima FHB, Profeti D, Lizcano-Valbuena W, Ticianelli EA, Gonzalez ER (2008) Carbon-dispersed Pt-Rh nanoparticles for ethanol electro-oxidation. Effect of the crystallite size and of temperature. J Electroanal Chem 617(2):121–129
55. Houtman C, Barteau M (1991) Divergent pathways of acetaldehyde and ethanol decarbonylation on the Rh (111) surface. J Catal 130(2):528–546
56. Kristian N, Wang X (2008) Ptshell-Aucore/C electrocatalyst with a controlled shell thickness and improved Pt utilization for fuel cell reactions. Electrochem Commun 10(1):12–15
57. Shao M, Sasaki K, Marinkovic NS, Zhang L, Adzic RR (2007) Synthesis and characterization of platinum monolayer oxygen-reduction electrocatalysts with Co-Pd core-shell nanoparticle supports. Electrochem Commun 9(12):2848–2853
58. Colmati F, Antolini E, Gonzalez ER (2008) Effect of thermal treatment on phase composition and ethanol oxidation activity of a carbon supported $Pt_{50}Sn_{50}$ alloy catalyst. J Solid State Electrochem 12(5):591–599
59. Lima FHB, Profeti D, Chatenet M, Riello D, Ticianelli EA, Gonzalez ER (2010) Electro-oxidation of ethanol on Rh/Pt and Ru/Rh/Pt sub-monolayers deposited on Au/C nanoparticles. Electrocatalysis 1(1):72–82
60. Antolini E, Gonzalez ER (2010) Alkaline direct alcohol fuel cells. J Power Sources 195(11):3431–3450
61. Wang Y, Nguyen TS, Liu X, Wang X (2010) Novel palladium-lead (Pd-Pb/C) bimetallic catalysts for electro-oxidation of ethanol in alkaline media. J Power Sources 195(9):2619–2622
62. Xu C, Hu Y, Rong J, Jiang SP, Liu Y (2007) Ni hollow spheres as catalysts for methanol and ethanol electro-oxidation. Electrochem Commun 9:2009–2012
63. He Q, Mukerjee S, Shyam B, Ramaker D, Parres-Esclapez S, Illán-Gómez M, Bueno-López A (2009) Promoting effect of CeO_2 in the electrocatalytic activity of rhodium for ethanol electro-oxidation. J Power Sources 193(2):408–415
64. Bayer D, Berenger S, Joos M, Cremers C, Tübke J (2010) Electrochemical oxidation of C_2 alcohols at platinum electrodes in acidic and alkaline environment. Int J Hydrogen Energy 35:12660–12667
65. Rao V (2007) Investigation of the ethanol electro oxidation in alkaline membrane electrode assembly by differential electrochemical mass spectrometry. Fuel Cells 7(5):417–423
66. Bayer D, Cremers C, Baltruschat H, Tübke J (2010) Ethanol stripping in alkaline medium: a DEMS study. ECS Trans 25:85–93
67. Liang Z, Zhao T, Xu J, Zhu L (2009) Mechanism study of the ethanol oxidation reaction on palladium in alkaline media. Electrochim Acta 54(8):2203–2208
68. Wang E, Xu J, Zhao T (2010) Density functional theory studies of the structure sensitivity of ethanol oxidation on palladium surfaces. J Phys Chem C 114(23):10489–10497
69. Fang X, Wang L, Shen PK, Cui G, Bianchini C (2010) An in situ fourier transform infrared spectroelectrochemical study on ethanol electro-oxidation on Pd in alkaline solution. J Power Sources 195(5):1375–1378
70. Zhou ZY, Wang Q, Lin JL, Tian N, Sun SG (2010) In situ FTIR spectroscopic studies of electro-oxidation of ethanol on Pd electrode in alkaline media. Electrochim Acta 55:7995–7999
71. Cantane DA, Ambrosio WF, Lima FHB (2011) Ethanol electro-oxidation catalyzed by Pt/C, Rh/C, and Pt overlayers on Rh/C. Effect of ethanol concentration and temperature. Electrocatalysis (Submitted)
72. Xu C, Tian Z, Shen P, Jiang SP (2007) Ethanol electrooxidation on Pt/C and Pd/C catalysts promoted with oxide. J Power Sources 164:527–531

Nanocomposites from V_2O_5 and Lithium Ion Batteries

Fritz Huguenin, Ana Rita Martins and Roberto Manuel Torresi

Abstract In this chapter, V_2O_5 xerogel and nanocomposites of V_2O_5 and polymers as well as the charge storage properties are described and discussed, aiming their use as cathode for lithium ion batteries. First, the different synthesis methods are presented, emphasizing the sol–gel methods via vanadates and vanadium alkoxides. Structural aspects are briefly mentioned to a better comprehension of lithium ion insertion/deinsertion, which influence on the electrochemical properties, and consequently, on the charge capacity of electrodes formed of V_2O_5. Nanostructured materials such as nanorolls, nanobelts, nanowires, and ordered nanorods arrays have been prepared and studied to increase the specific capacity, energy density, and power density. Moreover, the intimate contact between the nanocomposite components can also guarantee the enhancement of these properties so that these materials can be used in lithium ion batteries. Intermolecular interactions are also investigated to explain the performance of these positive electrodes. Various polymers have been used in these nanomaterials to increase the electronic conductivity as well as the ionic diffusion, and/or electrochemical stability.

F. Huguenin (✉) · A. R. Martins
Departamento de Química, Faculdade de Filosofia, Ciências e Letras de Ribeirão Preto, Universidade de São Paulo, Ribeirão Preto–SP 14040-901, Brazil
e-mail: fritz@ffclrp.usp.br

R. M. Torresi
Instituto de Química, Universidade de São Paulo, CP 26077, São Paulo–SP 05513-970, Brazil

F. L. de Souza and E. R. Leite (eds.), *Nanoenergy*,
DOI: 10.1007/978-3-642-31736-1_6,

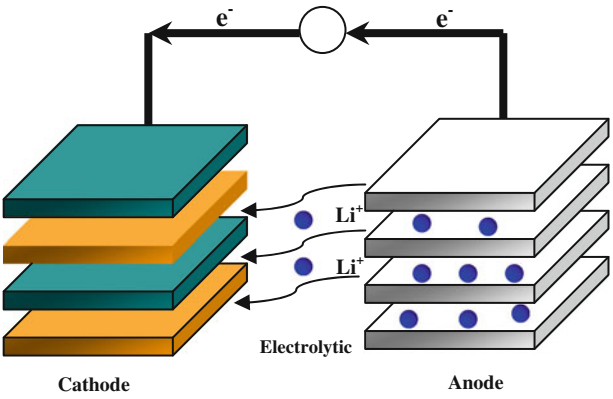

Fig. 1 Schematic representation of lithium-ion batteries during the discharge step

1 Introduction

The properties of metallic lithium, such as its equivalent weight ($M = 6.94$ g mol^{-1}), specific gravity ($\rho = 0.53$ g cm^{-1}), and electropositivity (≈ -3.04 V *versus* SHE) has motivated the development of lithium-ion batteries, which present high energy densities [1, 2]. Moreover, the discovery of inorganic materials that allow for the chemically reversible insertion/extraction of lithium ions into their structures, denominated intercalation materials, has also contributed to this development.

In these batteries, the chemical energy is converted into electrical energy via the discharge step, followed by conversion of the electrical energy into chemical energy via the charge step. The anode (negative electrode) is the source of lithium ions, which migrate and diffuse through the electrolyte toward the cathode (positive electrode) during the discharge step (Fig. 1).

The first generation of lithium batteries emerged in the 70s, together with the primary (non-rechargeable) batteries. The positive electrodes usually consisted of particulate transitions metals oxides (TMO) or chalcogeneous materials of millimetric dimension, meanwhile the negative electrodes were composed of metallic lithium. The half-reactions involved in these electrodes can be represented by the following reactions:

$$M + xLi^+ + xe^- \rightleftarrows Li_xM \text{ (positive electrode)} \quad (1)$$

$$Li^+ + e^- \rightleftarrows Li^0 \text{ (negative electrode)} \quad (2)$$

where M is a host matrix for lithium ion intercalation/deintercalation during the discharge/charge step. Electrons are generated due to the oxidation reaction at the negative electrode, flowing through the external circuit and bringing forth work. They are injected into the conduction band of the positive electrode, which must provide an electrical potential far greater than that of the negative electrode. An

outer power source is used between the electrodes for the charge step, so that the reaction is reversed.

According to equation

$$\Delta G = -n F \Delta E \quad (3)$$

where ΔG is the reaction free energy, n is the number of electrons involved per mol of consumed reactants, F is the Faraday constant, and ΔE is the potential difference between the positive (cathode) and negative (anode) electrodes of the battery and is related to the chemical potential difference between the electrodes. As this difference becomes larger and a material with lower weight or volume is employed, the supplied energy density should be greater. Moreover, these devices are associated with the global reaction rate, especially when they are used in applications requiring high power densities and current, as in the case of electric vehicles (EV). Therefore, the intercalation electrodes should offer high ionic and electronic conductivity to minimize their internal resistance. Another factor limiting the performance of lithium-ion batteries is the inner lithium-ion diffusion coefficient in solid matrices, which controls the insertion/extraction rates [3]. Depending on the material selected for the cathode, power sources with higher energy density can be obtained [4–12].

In the beginning, secondary lithium batteries were comprised of TiS_2 cathodes and metallic lithium anodes, which gave an acceptable performance; i.e., high chemical reversibility that allowed cycling for over 1,100 cycles [13]. However, the cell curtailment resulting from formation of dendritic lithium could result in hazardous explosions. From 1977 to 1979 button cells composed of LiAl anodes and TiS_2 cathodes were commercialized by Exxon as part of watches and other tiny devices [10, 14]. The safety of the cells was improved through the use of a LiAl anode. However, alloy electrodes held out only a restricted number of cycles resulting in extreme volume changes during the process. In the meanwhile, intercalation materials were becoming significantly advanced.

Due to the safety concerns surrounding the use of metallic lithium, researchers have striven to find optional approaches including modifications within the electrolyte and the negative electrode. A first attempt was to substitute metallic lithium for a second insertion material. Then, the lithium-ion technology was demonstrated at the late 1980s and early 1990s. The presence of lithium in its ionic rather than its metallic state solved the dendritic issue surrounding the use of lithium and, at least in principle, lithium-ion cells are intrinsically safer than metallic lithium cells. To compensate the increased potential in the negative electrode, high-potential insertion compounds can be selected to compose the positive electrode, and the layered-type transition-metal disulfides are shifted to the three-dimensional or layered-type transition-metal oxides.

The first lithium-ion batteries were commercialized by Sony® in 1991, after the discovery of the highly reversible and low voltage Li intercalation/deintercalation process in carbonaceous material. In these batteries, lithium ions were stored into graphite anodes (Li_xC_6) that were then intercalated into $LiCoO_2$ electrodes during

the discharge step [15, 16] with specific energy density around 180 W h Kg^{-1} under a potential discharge of approximately 3.8 V. High current densities (10 mA cm^{-2}) can be achieved in this case, thank to the diffusivity of lithium ions in the $LiCoO_2$ electrodes (diffusion coefficient values close to 5×10^{-9} cm^2 s^{-1}) [17]. Despite the significant increase in energy density per volume unit ($\approx$400 W h l^{-1}) and mass ($\approx$170 mA h g^{-1}), new materials have been investigated since they were made commercially available because of the scarcity, cost and toxicity of cobalt.

To be used as electrodes in batteries, these materials must have some basic features. For instance, they must be easy to oxidize and reduce, and they must have high cyclability, high voltage, high capacity of charge storage per mass and volume units, high ionic and electronic conductivity. Moreover, they must be inexpensive and exhibit low toxicity. Advances in solid state chemistry and innovations in the development of new materials have improved battery performance, which is intrinsically related to the properties of the materials comprising the positive and negative electrodes. Within this context, nanostructured materials have effectively contributed to the performance of lithium-ion batteries because of their small size, which enhances the insertion/extraction rates and thus increases their charge transfer capacity.

2 Vanadium Pentoxide

Among various TMOs studied as cathodes for use in lithium-ion batteries V_2O_5 must be mentioned. This oxide displays suitable structural and electrochemical properties for Li^+ insertion/extraction [18–23]. As can be observed below, the V_2O_5 xerogel and its nanocomposites are the focus of the present review, although it is inevitable to mention crystalline V_2O_5, which was one of the earliest studied oxides and has been exploited for 30 years [24].

The layered structure of crystalline V_2O_5 with weak vanadium–oxygen bonds between its layers is already known as well as its capacity to react by an intercalation mechanism. The oxide basic unit is an octahedral VO_6 which share the edges to form a double chain and can be distorted to a square pyramid with a short vanadyl bond and a very long V–O bond. It is observed an alternation among the apexes of the VO_5 pyramids in an up–up-down–down sequence, with the third rows being unoccupied as a consequence of the corner sharing of the double chains. Lithium insertion within the structure of the layered V_2O_5 is rather complex. Initial lithium intercalation into the structure results in the formation of the α-phase ($x < 0.01$) and then the ε-phase ($0.35 < x < 0.7$), in which the layers are more folded. The δ-phase is obtained at $x = 1$, where one layer changes rapidly out of two layers. Nevertheless, significant structural changes can occur if more than one lithium is discharged, giving rise to the γ-phase and enabling cycles in the $0 \leq x \leq 2$ range. Figure 2 shows that the VO_5 square pyramids in the α-, ε-, and δ-phases, which compose V_2O_5, are set in rows with apexes in an up–up-down arrangement. The

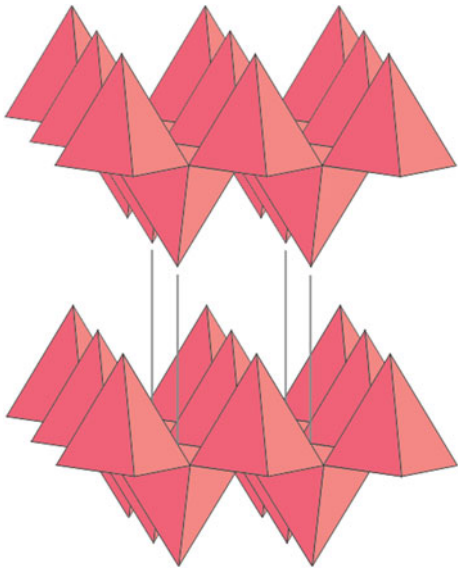

Fig. 2 Structure of crystalline V_2O_5. Adapted with permission from M. S. Whittingham, Chem Rev 104 (2004) 4271 [10]. Copyright 2011 American Chemical Society

structural behavior comes to up-down-up-down in the highly folded γ-phase and, as long as more lithium is discharged, a rock-salt architecture is formed and the ω-$Li_3V_2O_5$ phase arises. This latter phase has a tetragonal structure and becomes a rock-salt structure with the formula $Li_{0.6}V_{0.4}O$ [10]. In addition, the cycling capacity of the initial vanadium oxide phase is quickly lost, making it uninteresting for practical applications.

As a result of the intercalation of 0.5 Li per vanadium, the specific capacity around 147 mA h g^{-1} is comparable to that of $LiCoO_2$, which is also able to cycle 0.5 Li with no irreversible phase changes. However, $LiCoO_2$ demonstrates much better cycling stability and performance at high current densities as compared to V_2O_5. Furthermore, a profound discharge results in significantly lower amount of cycled lithium, a consequence of kinetic limitations due to a rise in current density [25].

In the gel form, vanadium oxides present improved reactivity. The V_2O_5 xerogel can be produced from inorganic or organometallic precursors and remains stable for long periods when placed under adequate conditions. It has already been reported that vanadium alkoxides $VO(OR)_3$ (R = Bu, t-Am) are good precursors that react through hydrolysis and condensation processes [20]. Also, V_2O_5 gels can be prepared outright from the oxide. Crystalline V_2O_5 reacts vigorously with hydrogen peroxide, resulting in a red gelatinous product [26]. V_2O_5 gels can also be produced by spilling the molten oxide heated at 800 °C into water [27]. Moreover, amorphous V_2O_5 can be hydrated, resulting in the formation of V_2O_5 gels [28]. Alternatively, the amorphous oxide can be produced by splat-cooling of the molten oxide and hydration, which has been described as the thickening of a polymeric network in a solvent. Pulverization of the amorphous oxide powder with water results in the formation of gels. Further addition of water yields sols. V_2O_5

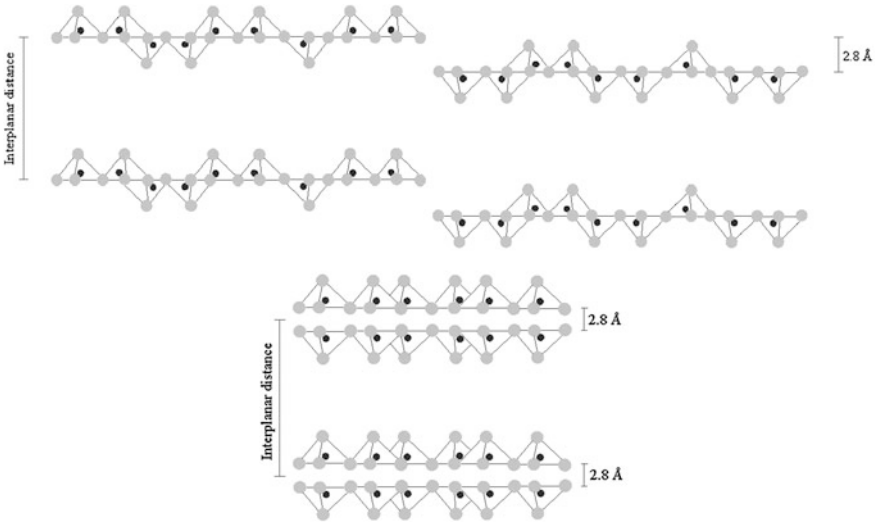

Fig. 3 Schematic representation of V_2O_5 xerogel: single (*upper*) and bilayer (*down*) structural models. Adapted with permission from M. Giorgetti, S. Passerini, W. H. Smyrl, Inorg Chem 39 (2000) 1514 [38]. Copyright 2011 American Chemical Society

films prepared by vapor deposition or even vanadium oxide spheres dissolved in water displays a similar behavior, resulting in gels or colloidal solutions [29, 30]. As will be subsequently detailed, vanadium pentoxide gels can be prepared by a most reliable technique based on the hydrolysis and condensation of vanadates or vanadium alkoxides.

When a metavanadate aqueous solution is passed through a proton exchange resin, a pale yellow solution of decavanadic acid ($[H_2V_{10}O_{28}]^{4-}$) is obtained. It is demonstrated in ^{51}VNMR spectra of V^{5+} solutions that barely two V^{5+} species, $[H_2V_{10}O_{28}]^{4-}$ and $[VO_2]^+$, are observed before gelation occurs, in solution round pH $\approx$ 2. Some neutral species form as an intermediate whilst the decavanadate anion dissociates into the $[VO_2]^+$ cation and one of these neutral species could be written as $[VO(OH)_3(OH_2)_2]^0$. This precursor presents octahedral geometry with the H_2O molecules coordinated to vanadium on the axial and equatorial plane, on opposite direction to vanadyl group (V = O) and hydroxyl group (OH), respectively. The subsequent condensation process occurs only on the equatorial plane due to the absence of V–OH groups on the axial direction, creating two-dimensional V_2O_5 bilayers perpendicular to the substrate and soaked into amorphous regions [31–33]. The condensation reactions (Eqs. 4–6) and the V_2O_5 xerogel structure are shown below (Fig. 3). In reason of some H_2O molecules coordinate to vanadium atom on axial position and other establishes hydrogen bonds with V = O groups, the distance between the oxide planes varies with the intercalated H_2O amount, approximately estimated in 11,55 Å to $V_2O_5 \bullet 1{,}8H_2O$ [31, 34].

$$\mathrm{VOH} + \mathrm{VOH} \rightarrow \mathrm{VOV} + \mathrm{H_2O}\ (\text{Oxolation}) \tag{4}$$

$$\mathrm{VOH} + \mathrm{V(ROH)} \rightarrow \mathrm{VO(H)V} + \mathrm{ROH}\ (\mathrm{Olation}) \tag{5}$$

$$\mathrm{VOH} + \mathrm{V(H_2O)} \rightarrow \mathrm{VO(H)V} + \mathrm{H_2O(Olation)} \tag{6}$$

Metal alkoxides, $VO(OR)_3$ (R = Et, n-Bu, n-Pr, i-Pr), are versatile precursors for the synthesis of sol–gel metal oxides under aqueous conditions [34]. In the presence of excessive water, these alkoxides undergo a hydrolysis process (Eq. 7) and an expansion of metal coordination (V) by nucleophilic addition of two water molecules. Afterwards, polymeric chains are obtained via condensation process.

$$\mathrm{VO(OR)_3} + 3\mathrm{H_2O} \rightarrow \mathrm{VO(OH)_3} + 3\mathrm{ROH(Hydrolysis)} \tag{7}$$

Electron microscopy shows that the gel is constituted of flat ribbons with dimensions round 10^3 Å, 10^3 Å and 10 Å, length x width x thickness, respectively [35, 36]. The behavior of the structure bears close similarity with that of the (*ab*) plane of crystalline V_2O_5 and its arrangement; i.e., pyramidal entities of orthorhombic V_2O_5 with 3.6 Å periodicity along the *b* axis [20]. In the stacking direction (*c* axis), a 2.8 Å amplitude is induced in the ribbon corrugation between the fibrils. The stacking of the ribbons is illustrated in Fig. 3 and corresponds to the structure that emerges when the gel is deposited onto a substrate. The ribbon has a thickness of 8.75 Å. Livage has proposed a model using a single layer. However, Oka et al. have put forward a different model entailing a bilayer for characterization of the ribbon structure in the xerogel [37]. This model can be seen in Fig. 3, where the V_2O_5 sheets face each other at a 2.8 Å distance.

The electrical properties of the $V_2O_5 \bullet nH_2O$ xerogels have been extensively researched due to the conductive nature of these materials. However, the conductivity of these materials varies significantly, approximately from 10^{-7} to $10^0\ \Omega^{-1}\ cm^{-1}$, depending on many parameters such as the preparation method, employed precursors, gel aging time, and thickness of the sample [39–44]. This conductivity has a mixed character involving electronic and ionic transport that are respectively proportional to the water concentration and the vanadium oxidation state [45]. The electrons skipping between the V^{4+} and V^{5+} sites are responsible for the electronic conductivity [46]. However, strong electron–phonon coupling decreases the mobility of charge carriers, with values in the order of 10^{-5}–10^{-6} $cm^2\ V^{-1}\ s^{-1}$ [34]. In the presence of excess water and acidic dissociation of V–OH groups occurs at the oxide/water interface, generating a significant amount of charged H_3O^+ species (pH $\approx$ 2) [31], as shown in equation (8).

$$\mathrm{V-OH} + \mathrm{H_2O} \Leftrightarrow \mathrm{V-O^-} + \mathrm{H_3O^+} \tag{8}$$

Analysis of the electrochemical properties of V_2O_5 suggests that this oxide is an excellent candidate for use as cathode in lithium-ion batteries, with a redox potential greater than 3 V (*vs.* Li/Li^+), specific energy density close to 600 W h Kg^{-1}, and specific capacity around 250 A h Kg^{-1} [47, 48]. Lithium insertion/extraction taking place during the electrochemical process can be described by the following equation:

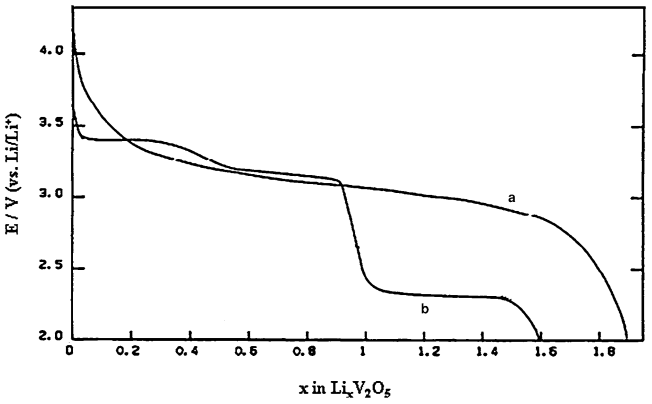

Fig. 4 Potential versus stoichiometric ratio between the amount of lithium ion and V_2O_5 (x in $Li_xV_2O_5$) for **a** V_2O_5 xerogel and **b** orthorhombic V_2O_5. Adapted from Ref. [47]

$$V_2O_5 + xLi^+ + xe^- \leftrightarrow Li_xV_2O_5 \tag{9}$$

where Li^+ compensates the electronic charge involved in the steps of vanadium reduction and oxidation to form vanadium bronze [49]. Four electrons and 4 Li^+ are involved in this process for each V_2O_5 species in the case of xerogel materials [48]. However, owing to some limitations such as slow diffusion of the intercalating ions into the structure and low electronic conductivity of V_2O_5, only reduction of V^{+5} sites to V^{+4} is usually observed (Fig. 4).

Other studies [21, 47, 50] have reported that the diffusion coefficient (D) values can vary between 10^{-9} and 10^{-17} cm^2 s^{-1}, depending on the amount of inserted lithium ions. Thus, considerable effort has been made in attempt to raise the rate of lithium-ion diffusion and electronic conductivity of these cathodes. For example, Parente et al. have described a substantial increase in the lithium-ion diffusion rate by synthesizing V_2O_5 xerogel on synthetic nickel fibers [51]. Dong et al. have used the *sticky carbon* method to obtain higher ionic pore accessibility [52]. Other synthetic routes are being employed in order to obtain new structures and morphologies. For instance, V_2O_5 thin films obtained by spin-coating allow for insertion of 3 to 4 equivalents of Li^+ ions [48, 53–55]. This optimization has been attributed to the amorphous nature and low anisotropy of these materials. In many cases, powdered carbon black is utilized as a conductive agent, to connect metal oxide particles. Passerini et al. have added carbon black in the early stages of V_2O_5 gelation, thereby ensuring higher charge capacity, possibly related to loss of long-range structural ordination [56]. However, carbon black is electrochemically inactive, limiting the ability of the cathode to store charge. Le et al. have held a supercritical drying process for V_2O_5 gels, which produced an amorphous material with very high porosity, thus reducing the diffusional path length. As a consequence, the overall reaction was no longer limited by diffusional processes [54,

57]. These aerogels thus have extremely high charge capacity (560 A h Kg^{-1}) and energy density (1,700 W h Kg^{-1}) [23, 55, 57].

Vanadium pentoxide may undergo some structural changes in the presence of organic solvents. One example is the intercalation of propylene carbonate (PC) in interplanar region by replacing the water molecules and resulting in larger distance between the 001 layers [58]. In situ X-ray diffraction (XRD) analysis of the material subjected to Li^+ intercalation revealed reversible structural changes [47], with layer stacking being destroyed during lithium ion insertion and formed during the detachment process. However, there is a significant decrease in the specific capacity when the electrode is subjected to several charge/discharge cycles. This fact is attributed to mechanical stress in the structure and/or dimensional changes caused by expansion/contraction of the layers due to insertion/extraction of solvent and ions.

3 Nanomaterials

Several research groups from different areas have shown the importance of miniaturization. For instance, it allows for the fast operating speed involving objects designed on a nanometric scale. In fact, the time required for a given system to perform a specific function can be minimized by displacement of electrons, ions, and molecules in a diminished space [59]. Moreover, physical forces that are negligible in the macroscopic world can become decisive in nanometric materials, allowing molecular self-ordering [60]. In addition, the conductivity parallel to the interfaces of a composite can significantly rise when the thickness of the layers components reach very low values, leading to an overlap of the charge spaces [61]. Thus, the design of nanoscale materials may contribute to the optimization and emergence of new properties, enabling the use of these systems for various applications in the fields of optics, electronics, catalysis, biotechnology, and solid state electrochemistry [62–66].

The development of nanostructured electrodes has led to the better performance of lithium-ion batteries, since they ensure higher current and energy densities. In nanostructured systems, the distances which lithium ions must cover are dramatically decreased, thus reducing the free diffusional path, so that lithium ions are able to enter and exit the structure more rapidly. Considering that the time taken for ion intercalation is proportional to the square size of the particle, the current values can significantly increase with the use of nanostructured electrodes.

The intercalation properties can be significantly improved by new developments in the synthesis and characterization of vanadium oxide nanostructures such as nanorolls, nanobelts, nanowires, and ordered nanorods arrays [67]. The galvanostatic discharge performance of V_2O_5 nanorods (with 115 mm diameter and 2 mm length) has been compared to that of a thin film electrode with the same geometric area and equal V_2O_5 mass [68]. The Li^+ storage capacity at low discharge rates (C/20) was equivalent for both the nanostructured and thin film

electrodes. Nonetheless, at high discharge rate, a higher capacity was demonstrated for the nanostructured electrode as compared to the thin film one. More specifically, the capacity was three and four times higher for the nanostructured electrode at a rate of 200 C and above 500 C, respectively, as compared to the thin film electrode.

Spahr et al. have synthesized and analyzed V_2O_5 nanotubes, which represent a new structure for cathode materials for use in lithium-ion batteries with smaller diffusion lengths [69]. An initial high capacity of 300 mA h g^{-1} was demonstrated for the V_2O_5 nanotube arrays, almost twice as high as the initial capacity of 140 mA h g^{-1} observed for the V_2O_5 film. The large surface area and short diffusion distance of the nanotube array were responsible for this improvement, but in the second and third cycles the capacity of the nanostructured material decayed to 200 mA h g^{-1} and 180 mA h g^{-1} respectively. In further cycles the decrease was less pronounced and a stable capacity of 160 mA h g^{-1} was reached after the sixth cycle, which still was 30 % higher than that of the V_2O_5 film. The nanotube array presented a more drastic decay than the film during cycling possibly as a result to the structural flexibility and fragility [70].

The discharge capacities and cyclic performance of platelet and fibrillar-structured V_2O_5 films prepared by solution methods have been compared to those of the conventional, simple structured film. The behavior of these structured V_2O_5 films varied depending on the orientation: the platelet film which is comprised of V_2O_5 particles with sizes of 20–30 nm, presented a random orientation while the fibrillar film displayed randomly oriented fibers, most of which protrude from the substrate surface. Comparing the initial discharge value of the plain V_2O_5 film (260 mA h g^{-1}) with the initial discharged capacities of platelet and fibrillar-structured V_2O_5 films (1,240 and 720 mA h g^{-1}, respectively) it is clear that the latter capacities were far higher than the former. As a result of the reduced distance of Li^+ diffusion, which avoids the situation in which lithium ions are concentrated in the electrode, and of the poor V_2O_5 interlayer cross-linking, of which promotes intercalation of larger quantities of lithium ions, high discharge capacity values were achieved. However, these nanostructured V_2O_5 films suffered degradation during the electrochemical tests [71].

Bearing in mind, the importance of interfaces for electrochemistry, researchers are developing new systems based on nanocomposites, which are characterized by the nanometric particle size and/or distance between their constituents [72, 73]. Some physical–chemical characteristics of composite materials, which are unique due to the interactions established between the components' phases, can be optimized with the aid of nanoscience. Actually, the design of these materials can maximize short-range interactions between the components, generating synergistic effects in the properties of the system. Thus, another way to optimize the electrochemical properties of V_2O_5 is to polymers into its lamellar space.

Some one- and bi- dimensional matrices, consisting of layers, channels, or tunnels, or which are completely amorphous, represent a class of materials made of flexible pores whose size can be adapted to other dimensions of the intercalating species. Given these characteristics, the scientific community has designed and

investigated new materials obtained by inclusion of organic polymers into inorganic matrices, to form composites with an intimate contact with their constituents on a scale between the classical molecular and microscopic scales [74–82]. There are several methods for the preparation of these nanohybrids, including: polymerization of monomeric molecules in the inorganic matrix through chemical, thermal, or photo-induced treatment in situ; of the previously formed polymer intercalation; use of self-assembly technique; and intercalated redox polymerization where the monomers are oxidized by the host matrix, which in turn is reduced and thus promotes formation of a polymer within its structure [83].

One of the most often investigated inorganic matrices is the V_2O_5 xerogel. The interaction between its lamellae is weak enough to allow for the merge of chemical species with different sizes [20, 34]. Moreover, its facile synthesis by the sol–gel methodology, allow for their preparation at low temperatures, which has encouraged several research groups to develop and analyze nanocomposites based on V_2O_5 and organic polymers [19–21, 84]. One reason for the development of these systems is the optimization of energy storage properties, considering the potential use of this oxide as cathode for lithium ion batteries. With a view to maximizing the energy density and specific capacity, electronic conducting polymers (ECPs) can be interspersed in the xerogel thereby offering an alternative conductive path; facilitating the access of electrons to the vanadium ions, and uniting electrically isolated particles. Besides this role, ECPs still participate in the redox process, directly contributing to increasing the battery capacity, as opposed to the carbon powder normally employed in the cathodes. Furthermore, the presence of ECPs can modify the morphology, porosity, and electrostatic interaction between the lithium ions and the oxygen atoms of the host matrix, thus maximizing ion mobility and consequently optimizing the performance of the electrochemical device [85–92].

Kanatzidis et al. were the first researchers to synthesize and characterize nanocomposites consisting of V_2O_5 and ECPs [93, 94], which contributed to a better understanding of the polymerization processes of organic molecules interspersed in a TMO matrix. Polymerization of aniline intercalated in the V_2O_5 xerogel resulted in interlayer distance expansion from 11.55 to 13.94 Å, due to the replacement of the H_2O molecules with the aniline polymer (PANI) [95]. Equation (10) shows the overall reaction process, where it is assumed that aniline oxidation triggers a polymerization process accompanied by reduction of the V^{+5} ions. However, molecular oxygen also participates in the reaction, providing an increase in the length of the polymeric chain and partial re-oxidation of the vanadium ions.

$$x(C_6H_5NH_2) + V_2O_5 + (y/2)O_2 \rightarrow (C_6H_4NH)_xV_2O_5^{(2x-2y)-} + yH_2O + (2x - 2y)H^+ \quad (10)$$

The aniline intercalation/polymerization process was investigated by insertion of the $C_6H_5NH_3I$ salt into the inorganic matrix under inert atmosphere [96], thus enabling oxidation of the iodide ions by V_2O_5 and preventing polymerization of the anilinium ion monomers ($C_6H_5NH_3^+$) in the interlayer. Subsequent exposure of

the material to ambient air resulted in PANI formation in the inorganic host matrix which was unexpected, since anilinium ion monomers are not oxidized to polyaniline in the presence of atmospheric oxygen. This suggests that V_2O_5 acted as a catalyst in the polymerization stage, which in turn was associated with electron transfer to molecular oxygen.

The insertion of a conductive path parallel to the V_2O_5 chains caused significant changes in electronic transport, since the charge transport in these materials is commanded by the spatial charge effects at the interface located between the conductive phase (PANI) chains and the oxide [97]. Thank to the hydrogen bonds formed between the oxygen atom of V_2O_5 and the hydrogen atoms of PANI (NH $\cdots$ OV), chains are held together due to a rise in the interfacial area, thereby leading to an even greater effect on electronic conductivity [96]. The intimate contact between the components can be observed from the Electron Paramagnetic Resonance spectra, indicating proximity (<10 Å) between the PANI *polaron* and the V^{4+} paramagnetic centers [96]. Electrostatic interactions between these polymers have been clearly observed in self-assembled hybrids, for which Raman and UV-visible spectra enable visualization of electronic transfer from PANI to the oxide during stacking of the monolayers, while the level balance of Fermi was maintained [98, 99]. Furthermore, X-ray photoelectron spectra have suggested short-range interactions between PANI and V_2O_5 through binding between the nitrogen and oxygen atoms bond (Fig. 5) [97].

Depending on the amount polymer, morphology, and chain length of the polymer, the electronic conductivity of these nanocomposites can be elevated by about 4 degrees of magnitude as compared to that of the V_2O_5 xerogel. Conductivity in the order of 0.1 S cm^{-1} at room temperature can be achieved after an aging period of 18 months [96]. However, despite the high conductivity value, other preparation methods can be used, in order to ensure faster growth of the macromolecules and consequent achievement of obtain high electronic conductivity in shorter aging periods. One example is PANI intercalation into an array of mesoporous V_2O_5/Mg in atmospheric air [100], which has also given a nanocomposite with an electrical conductivity (10^{-2} S cm^{-1}) of around 4 orders of magnitude higher than that of xerogel after 2 months of aging, approximately. This relatively short time, is attributed to the larger size of the pores, which facilitated diffusion of the polymeric chains into the inorganic solids, and allowed for faster growth of macromelecules.

The first studies involving lithium ion intercalation into these nanocomposites were carried out by Nazar et al. [101], who demonstrated the potential use of these materials as cathodes for lithium-ion batteries. After an oxidative treatment based on O_2, seeking re-oxidation of V^{4+} centers formed during the synthesis stage, a specific capacity of 165 A h kg^{-1} was obtained for the nanocomposite $[PANI]_{0.4}V_2O_5$ in 0.5 M $LiClO_4$/PC. This result evidenced that the charging capacity of the nanohybrid is greater than the sum of the capacities of its components, corresponding to a gain of approximately 40 % as compared to the V_2O_5 xerogel. This optimization of electric charge storage properties is assigned to a larger ionic transport rate, since the presence of the ECP weakers the interaction between the V_2O_5 oxygen atoms and lithium ions, while increasing their mobility

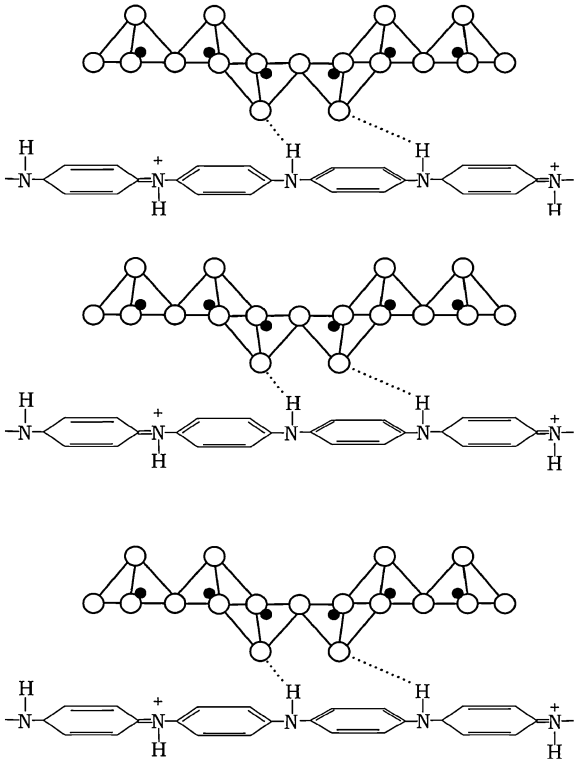

Fig. 5 Schematic representation of PANI/V_2O_5 nanocomposite

[101, 102]. In a study on the oxidative treatment of PANI/V_2O_5 nanohybrids based on O_2 at different temperatures [103], the influence of PANI, molecular oxygen, and heat treatment capacity was verified. The V_2O_5 xerogel exhibited a specific capacity (124 A h kg^{-1}) lower than that of $[PANI]_{0.6}V_2O_5$ (161 A h kg^{-1}), which was maximized when the nanocomposite was exposed to O_2 at 30 and 80 °C, with values of 220 and 302 A h kg^{-1}, respectively.

Although the reaction mechanism was not investigated in these nanocomposites, determination of the chemical species present in the hybrid materials consisting of PANI and V_2O_5 crystalline particles following the charge/discharge steps provided good insight into the effect of the interaction between PANI and the oxide on the charge compensation process. On the basis of elemental analysis of the composites (V_2O_5 comprised 85 % of the total mass), quantity of anions was six times lower (0.07 mol of Cl^- and ClO_4^- per mole of aniline) than that usually seen in a PANI film (0.4 mol of Cl^- per mole of aniline) [104]. These experimental results were attributed to the presence of negative charges on the V_2O_5 particles, which acted as counter-anions for the ECP in the oxidized state. However, these assignments are not conclusive, since participation of the PANI redox process in the presence of V_2O_5 has not been confirmed.

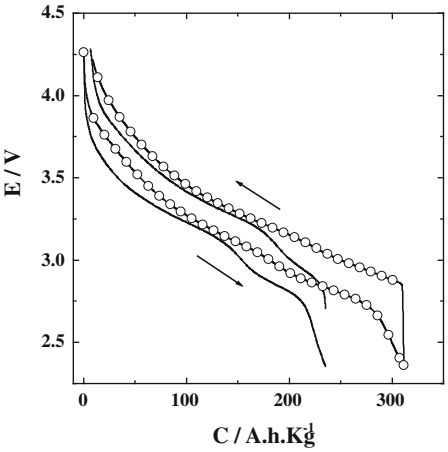

Fig. 6 **a** Chronopotentiometric curves for V_2O_5 (———) and $[PANI]_{0.3}V_2O_5$ (—◯—◯—) in 0.5 M $LiClO_4$, j = 10 μA cm^{-2}. Sample mass: 12 μg. Adapted from Ref. [105]

Huguenin et al. have employed another method for the preparation of nanocomposites from V_2O_5 xerogel and PANI, namely in situ oxidative polymerization of aniline in the V_2O_5 dispersion [105]. Electrochemical impedance was measured by these authors and a value of 2×10^{-11} cm^2 s^{-1} for the lithium ion diffusion coefficient was found and compared to the value of 3×10^{-12} cm^2 s^{-1} for V_2O_5. The V_2O_5/PANI nanocomposite exhibited higher lithium ion diffusion coefficient and larger electronic conductivity as compared to the V_2O_5 xerogel, a result of the increased charge capacity (313 A h Kg^{-1} for $[PANI]_{0.3}V_2O_5$ and 234 A h Kg^{-1} for V_2O_5), as presented in Fig. 6. These researchers also conducted measurements using an electrochemical quartz crystal microbalance (EQCM), and they proposed that a parallel solvent (propylene carbonate) transport occurred during the charge compensation process in V_2O_5. In contrast with the expected result, knowing that PANI charge compensation occurs by anion transport [106], it has been observed that the charge compensation proceeds with lithium ion and solvent transport in the V_2O_5/PANI nanocomposite in an average of 5 % on a molar basis (i.e. 0.05 mol of propylene carbonate per mole of Li^+). This can be related to mingling of the PANI and V_2O_5 chains at molecular level which enables PANI to be oxidatively doped. Nevertheless, only anionic vanadium oxide chains are present as anions during formation of the nanocomposite, so it is possible that the electroneutrality condition for the p-doped PANI is achieved by charge compensation from the firm anionic sites on the vanadium oxide lattice when the nanocomposite microstructure is initially established. In accordance with the observed results, charge compensation for PANI should occur via lithium ion transport, since the anionic sites on the vanadium oxide lattice should have no mobility.

In some cases, the ionic transport during redox exchange can be significantly improved by manipulation of the ionic transport, so that charge compensation is predominantly achieved by lithium ion movement. This happens when PANI is employed as a cathode material in lithium ion batteries. This improvement in the properties of PANI results in reduction of the demand for excess supporting electrolyte and increased in energy density for the cathode. Moreover, it is known that solvent transport, and therefore volumetric changes within the thin film systems, biases the film life cycle. For instance, in the case that $LiClO_4$/PC was utilized as supporting electrolyte, V_2O_5/PANI nanocomposites demonstrated higher electrochemical stability as well as greater charge capacity than the V_2O_5 xerogel after several charge/discharge cycles [105, 107].

Raman spectroscopy measurements carried out in situ on the poly(N-propane sulfonic acid aniline) PSPAN/V_2O_5 nanohybrid have attested to the oxidation and reduction of the PSPAN component during its redox cycling, although the electrochemical profile of the PSPAN in the presence of the V_2O_5 component remains unknown [108]. In contrast to the V_2O_5/PANI nanocomposite, only lithium ion participated in the charge compensation process in the PSPAN/V_2O_5 nanocomposite, hence avoiding anion and solvent contribution and accounting for the lower specific capacity as compared to that of the V_2O_5/PANI nanocomposite. In situ EQCM and cyclic voltammetry measurements have revealed the major participation of lithium ions. Taking into consideration the mass conservation principles and the electroneutrality during the redox process, determination of the electron, cation, anion and solvent flux was feasible. Thus, once there was no significant modification in the composition in the presence of small volume of the electrolyte, which served as a path for lithium ion transport, these cathodes can be utilized in high energy secondary batteries. Moreover, the minimum insertion/extraction of solvent minimized expansion/contraction of the structure, resulting in enhanced electrode cycling [108, 109]. Nevertheless, the lithium ion diffusion coefficient values are virtually the same for PSPAN/V_2O_5 and V_2O_5 [108].

The reasons for subtle difference among the diffusion coefficients of the PSPAN/V_2O_5, V_2O_5/PANI, and V_2O_5 host matrices were elucidated by ultraviolet–visible (UV–VIS), Fourier transform infrared (FTIR), and nuclear magnetic resonance (NMR) experiments. Several previously published works have proposed that the $Li^+ \cdots O = V$ is more shielded interaction in the PANI/V_2O_5 material, which would explain higher lithium ion diffusion rate observed for the PANI/V_2O_5 nanocomposite as compared to the V_2O_5 and the PSPAN/V_2O_5 nanocomposites.

The band-gap energies related to the electronic transition from O 2p to V 3d was detected in the UV–VIS absorption spectra of both the oxidized and reduced states ($E = 0.4$ V and $E = -1.0$ V, respectively) of the V_2O_5 xerogel and the $[PANI]_{0.3}V_2O_5$ nanocomposite. This corresponds to a shift from 2.40 to 2.75 eV for the V_2O_5 xerogel and from 2.15 to 2.20 eV for the $[PANI]_{0.3}V_2O_5$ nanocomposite. The shift in the band-gap energy is lower for the $[PANI]_{0.3}V_2O_5$ nanocomposite as compared to the V_2O_5 xerogel because PANI induces a partial shield between the lithium ions and the oxygen atoms of V_2O_5, thus resulting in a tiny reduction in the O 2p band as compared to the V 3d band [105, 110].

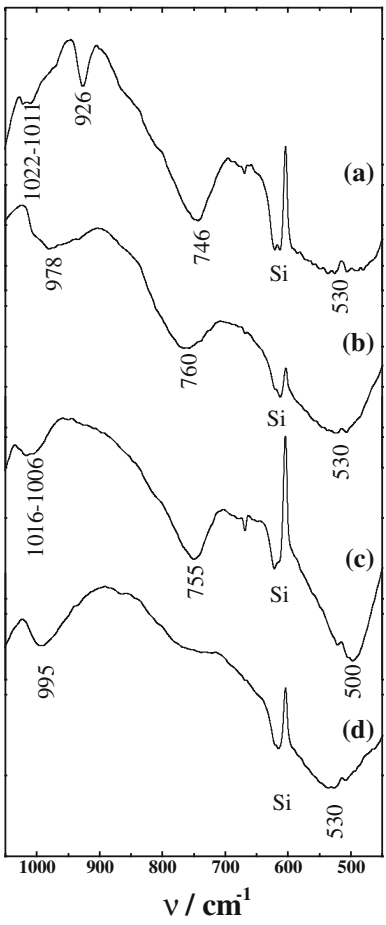

Fig. 7 FTIR spectra of **a** oxidized and **b** reduced V_2O_5, and **c** oxidized and **d** reduced $[PANI]_{0.3}V_2O_5$. Adapted from Ref. [111]

Huguenin et al. have carried out a characterization of the V_2O_5 xerogel and V_2O_5/PANI by Fourier transform infrared (FTIR) analyses, which elucidated another aspect surrounding the molecular level interaction. Figure 7 brings the FTIR spectra for the V_2O_5 xerogel, $Li_{1.3}V_2O_5$ xerogel, $[PANI]_{0.3}V_2O_5$, and $Li_{1.3}[PANI]_{0.3}V_2O_5$ [111]. The doublet wavenumbers at 1,022 and 1,011 cm^{-1} corresponds to the V = O vibrations for the V_2O_5, and it shifts to about 978 cm^{-1} for $Li_{1.3}V_2O_5$. Moreover, when $[PANI]_{0.3}V_2O_5$ is reduced, the doublet shifts from 1,016–1,006 to 995 cm^{-1}. The shift is smaller for $Li_{1.3}[PANI]_{0.3}V_2O_5$ as compared to $Li_{1.3}V_2O_5$ because of a partial blinding prompted by PANI in the $Li^+ \cdots O = V$ interactions, which is due to an innermost contact between the organic and inorganic components. These data corroborated with literature reports describing that the $NH \cdots O = V$ hydrogen bonds and the electrostatic interactions between PANI and V_2O_5 are responsible for hindering the interactions between the lithium ions and the vanadyl groups [96, 98, 99].

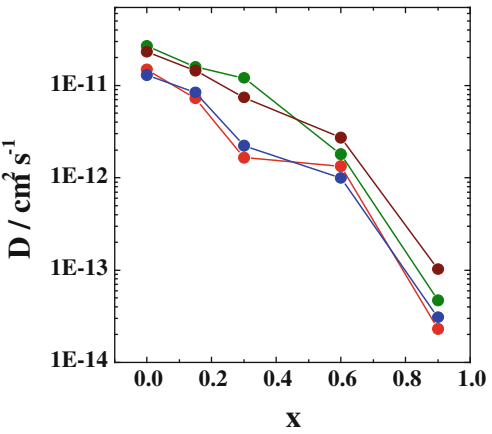

Fig. 8 Logarithm of lithium ion diffusion coefficient as a function of x for (•) $Li_xV_2O_5$ xerogel, (•) $Li_x[PANI]_{0.3}V_2O_5$, (•) $Li_x[PSPAN]_{0.3}V_2O_5$, and (•) $Li_x[Ppy]_{0.3}V_2O_5$. Adapted with permission from F. Huguenin, R. M. Torresi, J Phys Chem C 112 (2008) 2202 [114]. Copyright 2011 American Chemical Society

Solid-state nuclear magnetic resonance (NMR), particularly magic angle spinning (MAS), better elucidated the $Li^+ \cdots O$ interaction for the $Li_xV_2O_5$, $Li_x[PANI]_{0.3}V_2O_5$, and $Li_x[PSPAN]_{0.3}V_2O_5$ nanocomposites at the molecular level [112]. The ^7Li MAS NMR spectra displayed a wide peak for $Li_xV_2O_5$ as a consequence of the presence of lithium ions in bulk sites. This peak shifted upfield as more lithium ions were intercalated, indicating that the oxygen atoms shielded the lithium ions from the magnetic field as a result of a more difficult access to the inner bulk sites [112, 113]. In contrast, for the $Li_x[PANI]_{0.3}V_2O_5$ nanocomposite the wide peak was shifted downfield, a consequence of less effective shielding from the magnetic field due to the smaller amount of lithium. These results confirmed the partial blinding effect of PANI on the interactions between the lithium ions and the oxygen atoms of V_2O_5. The ^7Li MAS NMR spectra for the poly(N-propane sulfonic acid) (PSPAN)/V_2O_5 nanocomposite was also analyzed, so that the influence of oxygen atoms on shielding of lithium ions from the magnetic field could be understood [112]. As the amount of intercalated lithium ions increased the wide peak due to $Li_x[PSPAN]_{0.3}V_2O_5$ slightly shifted upfield. This change occurred in the same direction as that observed for the $Li_xV_2O_5$. It is noteworthy that the difference between PSPAN and PANI lies on the presence of the sulfonic propane group in the former, so the intercalated lithium ions can interact with the oxygen atoms, which allows for a partial blinding effect on the interaction between the lithium ions and the oxygen atoms of V_2O_5. Finally, the difference between the shifts detected for the nanostructures consisting of PSPAN, PANI, and V_2O_5 as well as the difference in the lithium diffusion coefficient values were analyzed (Fig. 8).

Ppy/V_2O_5 nanocomposites are also good candidates for use as cathodes in batteries of high energy density. However, depending on the preparation method, these materials may exhibit high coulombic irreversibility [115]. One way to facilitate extraction of ions from the host matrix and enhance the charge capacity is to employ a supercritical drying process based on CO_2 and organic solvents, which raises the porosity of the nanocomposite [116]. Depending on the utilized

conditions, it is possible to reversibly merge up to 3.5 mol of Li^+ to a mole of material in these hybrid aerogels, which represents a 40 % increase as compared to V_2O_5 aerogels. Another approach that can be used to optimize the electrochemical performance is to employ thin films, which give rise to high specific capacity and coulombic reversibility under application of a high current/mass ratio [117].

Distribution of the ECP in the inorganic matrix interferes with the structural, electrical and electrochemical properties of these electrodes which can be controlled depending on the preparation method [118]. When the V_2O_5 gel was exposed to Ppy dispersion, microcomposites were formed. The short-range interactions between components of these microcomposites were restricted, thereby minimizing the synergistic effects on the energy storage properties. When pyrrole was polymerized in the presence of the V_2O_5 xerogel, nanohybrid materials were formed, and the amount of Ppy necessary to produce percolation of a conductive path was much smaller than in the case of the microcomposite. However, there were Ppy aggregates in the films, which diminished the homogeneity of the conductive phase in the inorganic matrix. When the organic and inorganic precursors were polymerized simultaneously, homogeneous nanocomposites with higher specific capacities were generated, attesting to the influence of intimate contact between the ECP and V_2O_5 on these hybrid materials. Effects between the components caused by the interfaces have also been observed by Demets et al., who analyzed modified electrodes deposited on V_2O_5, Ppy/V_2O_5 nanocomposites, and V_2O_5 deposited on Ppy [119]. These authors commented on the different electrical and electrochemical behaviors of these materials and showed the importance of the nature, composition, and architecture of the film regarding the materials' properties.

A two-component nanocomposite constituted of conducting polymers (polyaniline, polypyrrole, and polythiophene) and vanadium oxide has been prepared by a mechanochemical method developed by Posudievsky et al. [120]. The nanocomposite based on polypyrrole exhibited the greatest capacity. The structure stability of this nanocomposite was demonstrated by cycling at a current of ≈ 0.2 A g^{-1}, and its capacity was retrieved at lower current cycling. As a result of the higher lithium ion diffusion rate and the default of film passivation on the surface of the nanoparticles, lithium ion intercalation in the nanocomposites was more effective than its intercalation into the V_2O_5 xerogel. The stacking of the conducting polymer and the inorganic compound in the nanocomposite material can be related to the stability during extended charge/discharge cycles, higher discharge capacity, and enhanced diffusion coefficient of the lithium ions.

The morphology of the host matrix also interfered in lithium ion intercalation. In fact, during the copolymerization process, the Ppy chains inhibited the growth of V_2O_5 chains, resulting in a low planning degree and larger pore size (160 Å) as compared to the xerogel (80 Å), which facilitated ion intercalation [103]. Addition of surfactants (nonylphenol EON2) to the V_2O_5 xerogel also elicited an increase in structural disorder, resulting in elevated charge capacity and allowing for the merge of 2.7 mol of Li^+ per mole of V_2O_5 in the nanocomposite against 1.6 mol of Li^+ in the xerogel [50]. The increase in the flatness of the nanocomposites

consisting of poly(3,4-ethylenedioxythiophene) (PEDOT)/V_2O_5, which is due to larger interlayer spacing, was considered one of the reasons for higher specific capacity as well as elevated electronic conductivity [121, 122].

Depending on the medium, the high oxidation potential of V_2O_5 can cause undesired reactions with the electrolyte, culminating in the passivation of the electrode surface. Because Ppy has a lower oxidation potential, the polymer can cover the metal oxide particles and thus prevent degradation reactions from taking place in the electrolyte solution. As noted by Kuwabata et al., coating of crystalline V_2O_5 particles with Ppy assured a high cyclability of the composite, and avoided the possible reactions between V_2O_5 and poly(methyl methacrylate) (PMMA) [123].

The reverse micelle method has been applied for preparation of V_2O_5 and V_2O_5/PANI nanofibers. The cycling behavior of the V_2O_5/PANI nanofibers was greater as compared to the V_2O_5. Moreover, there was higher capacity impairment for V_2O_5 nanofibers during cycling. It was found that V_2O_5/PANI nanofibers with a 30 % PANI molar ratio exhibited a stable capacity of about 300 mA h g^{-1}. The morphology of V_2O_5 and V_2O_5/PANI nanofibers during charge/discharge cycles was examined by scanning electron microscopy (SEM), and it was found that the morphology of the V_2O_5 nanofibers changed after 10 charge/discharge cycles, whilst morphology of the V_2O_5/PANI nanofibers was preserved after the electrochemical cycling. Thus, the presence of the polymer within the nanohybrid material may have stabilized the capacity via homogeneous distribution during cycling [124].

Another method for obtaining nanofibers is to react the V_2O_5/PANI nanocomposite and hexadecylamine after the hydrothermal treatment, which usually gives V_2O_5/PANI nanofibers with dimensions varying from 1 to 10 μm length and 15–300 nm width. Electrochemical measurements evidenced a specific capacity of about 150 A h k/g during the 10 initial cycles. Moreover, electrochemical impedance spectroscopy estimated the apparent diffusion coefficient in about 1×10^{-12} cm^2/s^{-1}. In contrast, replacing hexadecylamine with sodium cations by submitting the nanofibers through a reflux treatment led to an apparent diffusion coefficient that was at least three orders magnitude higher as compared to the vanadium oxide template [125].

Searching for a better performance, ECPs and other redox polymers have been used in the preparation of new nanocomposites based on V_2O_5. An example is the use of functionalized polymers such as poly(aniline-*co*-N-(4-sulfophenylacetic) aniline (PAPS), whose solubility in H_2O renders homogeneous nanocomposites with better defined stoichiometry as compared to PANI/V_2O_5. However, despite the increase in conductivity promoted by this polymer, the electrochemical stability was lower as compared to the xerogel. Indeed, this electrode became electroinactive after 30 voltammetry cycles in 0.1 M $LiClO_4$/acetonitrile [126]. The synthesis and characterization of other nanocomposites consisting of poly(3-decylpyrrole) (P3DP) or poly(hexadecylpyrrole) (P3HDP) and V_2O_5 has been described by F. Huguenin et al. [127]. Compared to the Ppy/V_2O_5 nanocomposite, the P3DP/V_2O_5 and P3HDP/V_2O_5 nanocomposites demonstrated greater

electrochemical stability. Possibly, this was a result of the side-chain of the P3DP and P3HDP polymers, which guaranteed higher specific capacity for the P3DP/V_2O_5 and P3HDP/V_2O_5 nanocomposites (115 Ah/Kg and 106 Ah/Kg, respectively), as compared to the Ppy/V_2O_5 nanocomposite (50 Ah/Kg), after 50 electrochemical cycles. Wang G et al. have described intercalation of poly(N-[5-(8-hydroxyquinoline)methyl]aniline) into the V_2O_5 xerogel (PNQA/V_2O_5), a hybrid that was synthesized by the in situ intercalative polymerization method [128]. The authors found that aging in air atmosphere facilitated PNQA chain growth between the V_2O_5 lamellae, resulting in increased electrical conductivity: 1.9×10^{-4} S cm^{-1} for the PNQA/V_2O_5 hybrid versus 4.2×10^{-6} S cm^{-1} for the V_2O_5 xerogel.

The slow redox coupling of thiol-disulfide makes poly[2,5-dimercapto(1,3,4-thiadiazole)] (PDTT) unfeasible for application in batteries [129]. Meanwhile, hybrid systems formed from the polymerization of the dimer 2,5-dimercapto1,3,4-thiadiazole (diDMcT) inserted into the V_2O_5 structure exhibited increased charge in relation to the oxide [130], which was attributed to the reduction and oxidation of the organic polymer PDTT, for which the reductive cleavage of S–S bond was facilitated in the inorganic matrix. Nevertheless, after several voltammetry cycles the charge capacity resemble that of V_2O_5, while molecules of dimercapto-1,3,4-thiadiazole (DMcT) produced during reduction of the oligomers diffused out of the host matrix. Considering the good performance of PANI/V_2O_5 nanocomposites, Park et al. intercalated PDMcT and PANI into the inorganic matrix [131]. Although the specific capacity of this ternary material (220 A h kg^{-1}) was lightly higher than that of the xerogel (205 A h kg^{-1}), the binary materials are still considered a better alternative as energy source.

Poly(ethylene oxide) (PEO) is another interesting polymer because of its ion conductivity, a result of its alkali-metal ions complexes, and the PEO/V_2O_5 nanocomposite has been demonstrated to lead to interesting lithium ion intercalation and display relevant photochemical and electrical properties [132–135]. Investigations into electrochromic processes and electrical conductivity have shown enhanced charge capacity and reversibility due to lithium ion insertion/extraction. The inserted (Q_c) and extracted (Q_a) charge densities of PEO/V_2O_5 film for the 10^{th} cycle as measured in the study of Jin A et al. [136] were 18.1 and 17.9 m C cm^{-2}, respectively, which are about two orders of magnitude higher than those of the V_2O_5 xerogel film (9.6 and 9.8 m C cm^{-2}, respectively). Reversibility was calculated by the ratio between the inserted and extracted charge densities (Q_a/Q_c), and revealed a greater reversibility value (98.9 %) was achieved for PEO/V_2O_5 as compared to the V_2O_5 xerogel (98 %).

The layer-by-layer technique has already been described in the literature and can be applied to the manufacture of these nanocomposites [137, 138]. This method can result in the spontaneous formation of nanoarchitectures thank to the ionic attraction between oppositely charged materials. Furthermore, some physical–chemical properties of the film can be tailored by controlling film thickness, uniformity and composition. Additionally, an improvement of the ionic mobility and the diffusion rate can be achieved by generation of an electrostatic shield between the chemical species involved in the diffusion bounce. The highest

negative charge sites bounce into the host matrices as a result of innermost contact between the polymer chains and the metal oxide [114]. Although the interaction vanadyl group and the lithium ion led to a diminished ionic mobility and energy dissipation during the electro-insertion process, the layer-by-layer technique allowed for organic polymer adsorption onto strategic sites of the V_2O_5, promoting shielding of the ion–dipole interaction [139, 140].

The layer-by-layer (LbL) technique can improve the charge storage capacity, giving rise to new electrochromic effects and even control of the ionic conductivity. Therefore, several works on the manipulation of V_2O_5/PANI nanocomposites at molecular level using this technique have been developed. The amount of PANI participating in the redox processes can be controlled by shifting the film structure at the molecular level, so that the chromogenic properties of PANI on the nanometric scale can be obtained, whilst the intrinsic electrochemical properties of the V_2O_5 xerogel are retained. By controlling the absorption of V_2O_5/PANI LbL films onto a cast PANI film, the properties of the nanoarchitectures are achieved. A study involving immersion of the PANI-V_2O_5/PANI system into a $LiClO_4$/propylene carbonate (PC) solution has been conducted by varying the immersion time. The EQCM technique enabled monitoring of the mass gain/loss (Δm) as a function of the charge as well as control of the insertion/extraction species. Thus, the charge compensation process as a consequence of the shift from anionic to cationic contributions resulted in mass reduction and enhancement of the specific capacity of secondary lithium batteries.

In addition, Huguenin F. et al. have studied nanoarchitectures of V_2O_5/chitosan/PEO (V_2O_5/blend) obtained by addition of 1 % chitosan to the PEO dispersion. It was found that chitosan was only effective regarding assistance in the manufacturing of the films [140]. Indeed, the V_2O_5/blend performed better in comparison to V_2O_5/chitosan (8.03 m C cm^{-2} and 3.41 m C cm^{-2}, respectively), which was attributed to a larger number of electrochemically active sites and an increase in the diffusion rate of lithium ions within the host matrix, as determined from electrochemical and spectroelectrochemical measurements [141]. The enhanced diffusion process arose from the complexation of lithium ions with the oxygen atoms of PEO, guaranteeing higher charge capacity during the charge/discharge steps.

4 Conclusions

When it is employed positive electrode in lithium ion batteries, the V_2O_5 xerogel poses some limitations, which made it uninteresting for workable applications. Nanocomposites constituted of conducting polymers and V_2O_5 have been demonstrated to be an alternative to the V_2O_5 xerogel for electrochemical energy storage. The preparation and investigation of novel manufacture nanoarchitectured systems from these components can overcome these restrictions, improving some features that are essential for lithium ion batteries, such as stability, charge

transport, energy density, specific capacity, and control of solvent insertion. Furthermore, studies on lithium ion insertion can significantly contribute to further applications such as electrochromic devices and sensors.

Acknowledgments Financial support from FAPESP, CNPq, and Capes is gratefully acknowledged.

References

1. Cheng F, Tao Z, Liang J, Chen J (2008) Chem Mater 20:667
2. Tarascon J-M, Armand M (2001) Nature 414:359
3. Bruce PG, Scrosati B, Tarascon J-M (2008) Angew Chem Int Ed 47:2930
4. Wang Y, Cao G (2008) Adv Mater 20:2251
5. Liu C, Li F, Ma LP, Cheng H-M (2010) Adv Mater 22:E28
6. Li H, Wang Z, Xeng L, Huang X (2009) Adv Mater 21:4593
7. Guo Y-G, Hu J-S, Wan L-J (2008) Adv Mater 20:2878
8. Balaya P, Bhattacharyya AJ, Jamnik J, Zhukovkii YF, Kotomin EA, Maier J (2006) J Power Sources 159:171
9. Armand M, Tarascon J-M (2008) Nature 451:652
10. Whittingham MS (2004) Chem Rev 104:4271
11. Tarascon J-M (2010) Philosophical Transactions of the Royal Society A: Mathematical. Physics & Engineering Science 368:3227
12. Brodd RJ, Bullock KR, Leising RA, Middaugh RL, Miller JR, Takeuchi E (2004) J Electrochem Soc 151:K1
13. Whittingham MS (1976) Science 192:1126
14. Rao BML, Francis RW, Christopher HA (1977) J Electrochem Soc 124:1490
15. Nagaura T, Tozawa K (1990) Prog Batteries Solar Cells 9:209
16. Ozawa K (1994) Solid State Ion 69:212
17. Goodenough JB, Mizuchima K (1981) U.S. Patent 4,302,518
18. Ohzuku T (1995) Lithium batteries: new materials, developments and perspectives. In: Pistoia G (ed), vol. 5, 2a Ed, p 239, Elsevier, Amsterdam
19. Tarascon JM, Armand M (2001) Nature 414:359–367
20. Livage J (1991) Chem Mater 3:578
21. Pereira-Ramos JP, Baffier N, Pistoia G (1995) Lithium batteries: new materials, developments and perspectives. In: Pistoia G (ed), vol. 5, 2a Ed, p 281, Elsevier, Amsterdam
22. Manthiram A, Kim J (1998) Chem Mater 10:2895
23. Owens BB, Smyrl WH, Xu JJ (1999) J Power Sources 81:150
24. Whittingham MS (1976) J Electrochem Soc 123:315
25. Chernova NA, Roppolo M, Dillon AC, Whittingham MS (2009) J Mater Chem 19:2526
26. Ostermann W (1922) Wiss Ind Hamburg 1:17
27. Müller E, Chem Z (1911) Ind Kolloide 8:302
28. Gharbi N, R'Kha C, Ballutaud D, Michaud M, Livage J, Audiere JP, Shiffmacher G, Non-Cryst J (1981) Solids 46:247
29. Sanchez C, Livage J, Audière JP, Madi A, Non-Cryst J (1984) Solids 65:285
30. Kittaka S, Sasaki S, Ogawa N, Uchida N (1988) J Solis State Chem 76:40
31. Livage J (1999) Coord Chem Rev 190:391
32. Legendre JJ, Livage J (1983) J Colloid Interface Sci 94:75
33. Pelletier O, Davidson P, Bourgaux C, Coulon C, Regnault S, Livage J (2000) Langmuir 16:5295
34. Livage J, Henry M, Sanchez C (1988) Prog Solid St Chem 18:259

35. Legendre JJ, Livage J (1983) J Coll Int Sci 94:75
36. Legendre JJ, Livage J (1983) J Coll Bit Sci 94:84
37. Yao T, Oka Y, Yamamoto N (1992) Mater Res Bull 116:279
38. Giorgetti M, Passerini S, Smyrl WH (2000) Inorg Chem 39:1514
39. Bullot J, Gallais O, Gauthier M, Livage J (1980) Appl Phys Lett 36:986
40. Bullot J, Cordier P, Gallais O, Gauthier M, Livage J (1981) Phys Stat Sol 68:357
41. Sanchez C, Morineau R, Livage J (1983) Phys Stat Sol 76:661
42. Sanchez C, Babonneau F, Morineau R, Livage J (1983) Phil Mag B 47:279
43. Livage J (1996) Solid States Ion 86:935
44. Anaissi FJ Demets GJ–F, Alvarez EB, Politi MJ, Toma HE (2001) Electrochim Acta 47:441
45. Bardoux P, Morineau R, Livage J (1988) Solid State Ion 27:221
46. Bullot J, Cordier P, Gallais O, Gauthier M, Non-Cryst J (1984) Solids 68:135
47. Baddour R, Pereira-Ramos JP, Messina R, Perichon J (1991) J Electroanal Chem 314:81
48. Tipton AL, Passerini S, Owens BB, Smyrl WH (1996) J Electrochem Soc 143:3473
49. Park H–K, Smyrl WH Ward MD (1995) J Electrochem Soc 142:1068
50. Mège S, Levieux Y, Ansart F, Savariault JM, Rousset A (2000) J Appl Electrochem 30:657
51. Parent MJ, Passerini S, Owens BB, Smyrl WH (1999) J Electrochem Soc 146:1346
52. Dong W, Rolison DR, Dunn B (2000) Electrochem Solid State Lett 3:457
53. Park HK, Smyrl WH (1994) J Electrochem Soc 141:L25
54. Le DB, Passerini S, Tipton AL, Owens BB, Smyrl WH (1995) J Electrochem Soc 142:L102
55. Owens BB, Passerini S, Smyrl WH (1999) Electrochim Acta 45:215
56. Passerini S, Smyrl WH, Berrettoni M, Tossici R, Rosolen M, Marassi R, Decker F (1996) Solid State Ion 90:5
57. Le DB, Passerini S, Guo J, Ressler J, Owens BB, Smyrl WH (1996) J Electrochem Soc 143:2099
58. Lemordant D, Bouhaouss A, Aldebert P, Baffier N (1986) J Chim Phys 83:105
59. Hupp J (2001) Interface 10:21
60. Lu Y, Lang Y, Sellinger A, Lu M, Huang J, Fan H, Haddad R, Lopez G, Burns AR, Sasaki DY, Shelnutt J, Brinker CJ (2001) Nature 410:913
61. Chadwick AV (2000) Nature 408:925
62. Nazar LF, Goward G, Leroux F, Duncan M, Huang H, Kerr T, Gaubicher J (2001) Intern. J Inorg Mater 3:191
63. Bourgeat-Lami E (2002) J Nanosci Nanotech 2:1
64. Maia DJ, De Paoli MA, Alves OL, Zarbin AJG, das Neves S Quim Nova 23 (2000) 204
65. Gimenez IF, Alves OL, Brazil J (1999) Chem Soc 10:167
66. Kryszewski M (2000) Synthetic Met 109:47
67. Wang Y, Cao G (2006) Chem Mater 18:2787
68. Patrissi CJ, Martini CR (1999) J Electrochem Soc 146:3176
69. Spahr ME, Bitterli PS, Nesper R, Haas O, Novák P (1999) J Electrochem Soc 145:2780
70. Wang Y, Takahashi K, Shang H, Cao G (1995) J Phys Chem B 109:3085
71. Lee K, Wang Y, Cao GZ (2005) J Phys Chem B 109:16700
72. Gangopadhyay R, De A (2000) Chem Mater 12:608
73. Kerr TA, Wu H, Nazar LF (1996) Chem Mater 8:2005
74. Nazar LF, Wu H, Power WP (1993) J Mater Chem 5:1985
75. Kanatzidis MG, Marcy HO, McCarthy WJ, Kannewurf CR, Marks TJ (1989) Solid States Ion 32:594
76. Maia DJ, Das Neves S, Alves OL, De Paoli MA (1999) Synth Met 102:1153
77. Maia DJ, Alves OL, De Paoli MA (1997) Synth Met 90:37
78. Wu CG, DeGroot DC, Marcy HO, Schindler JL, Kannewurf CR, Bakas T, Papaefthymiou V, Hirpo W, Yesinowski JP, Liu YJ, Kanatzidis MG (1995) J Am Chem Soc 117:9229
79. Liu YJ, Kanatzidis MG (1995) Chem Mater 7:1525
80. Vaia RA, Vasudevan S, Krawiec W, Scanlon LG, Giannelis EP (1995) Adv Mater 7:154
81. Oriakhi CO, Lerner MM (1996) Chem Mater 8:2016
82. Kerr TA, Leroux F, Nazar LF (1998) Chem Mater 10:2588

83. Schöllhorn R (1996) Chem Mater 8:1747
84. Lev O, Wu Z, Bharathi S, Glezer V, Modestov A, Gun J, Rabinovich L, Sampath S (1997) Chem Mater 9:2354
85. Harreld J, Wong HP, Dave BC, Dunn B, Nazar LF (1998) J Non-Cryst Solids 225:319
86. Lira-Cantú M, Gómez-Romero P (1999) J Solid State Chem 147:601
87. Oliveira HP, Graeff CFO, Brunello CA, Guerra EM (2000) J Non-Cryst Solids 273:193
88. Posudievsky OY, Biskulova SA, Pokhodenko VD (2004) J Mater Chem 14:1419
89. Guerra EM, Brunello CA, Graeff CFO, Oliveira HP (2002) J Solid State Chem 168:134
90. Demets GJF, Toma HE (2003) Electrochem Commun 5:73
91. Yatabe T, Matsubayashi G (1996) J Mater Chem 6:1849
92. Wang J, Gonsalves KE (1999) J Comb Chem 1:216
93. Kanatzidis MG, Wu C-G, Marcy HO, Kannewurf CR (1989) J Am Chem Soc 111:4139
94. Wu CG, Kanatzidis MG, Marcy HO, DeGroot DC, Kannewurf CR (1989) Polim Mater Sc. Eng 61:969
95. Liu YJ, DeGroot DC, Schindler JL, Kannewurf CR, Kanatzidis MG (1993) J Chem Soc Chem Commun 3:593
96. Wu C-G, DeGroot DC, Marcy HO, Schindler JL, Kannewurf CR, Liu Y-J, Hirpo W, Kanatzidis MG (1996) Chem Mat 8:1992
97. Somani PR, Marimuthu R, Mandale AB (2001) Polymer 42:2991
98. Ferreira M, Zucolotto V, Huguenin F, Torresi RM, Oliveira ON Jr (2002) J Nanosci Nanotech 2:29
99. Ferreira M, Huguenin F, Zucolotto V, da Silva JEP, de Torresi SIC, Temperini MLA, Torresi RM, Oliveira ON Jr (2003) J Phys Chem B 107:8351
100. Li ZF, Ruckenstein E (2002) Langmuir 18:6956
101. Leroux F, Koene BE, Nazar LF (1996) J Electrochem Soc 143:L181
102. Leurox F, Goward G, Power WP, Nazar LF (1997) J Electrochem Soc 144:3886
103. Lira-Cantú M, Gómez-Romero P (1999) J Electrochem Soc 146:2029
104. Kuwabata S, Idzu T, Martin CR, Yoneyama H (1998) J Electrochem Soc 145:2707
105. Huguenin F, Torresi RM, Buttry DA (2002) J Electrochem Soc 149:A546
106. Varela H, Torresi RM (2000) J Electrochem Soc 147:665
107. Lira-Cantú M, Gómez-Romero P (1999) Int J Inorg Mat 1:111
108. Huguenin F, Torresi RM, Buttry DA, da Silva JEP, de Torresi SIC (2001) Electrochem Acta 46:3555
109. Varela H, Huguenin F, Malta M, Torresi RM (2002) Quim Nova 25:287
110. McKinnon WR (1995) In: Solid State Electrochemistry; Bruce PG (ed) Cambridge University Press, Cambridge p 163
111. Huguenin F, Ticianelli EA, Torresi RM (2002) Electrochim Acta 47:3179
112. Holland GP, Yarger JL, Buttry DA, Huguenin F, Torresi RM (2003) J Electrochem Soc 150:A1718
113. Holland GP, Buttry DA, Yarger YL (2002) Chem Mater 14:3875
114. Huguenin F, Torresi RM (2008) J Phys Chem C 112:2202
115. Goward GR, Leroux F, Nazar LF (1998) Electrochim Acta 43:1307
116. Wong HP, Dave BC, Leroux F, Harreld J, Dunn B, Nazar LF (1998) J Mater Chem 8:1019
117. Huguenin F, Girotto EM, Torresi RM, Buttry DA (2002) J Electroanal Chem 536:37
118. Harreld JH, Dunn B, Nazar LF (1999) Int J Inorg Mater 1:135
119. Demets GJF, Anaissi FJ, Toma HE (2000) Electrochim Acta 46:547
120. Posudievsky OY, Kozarenko OA, Dyadyun VS, Jorgensen SW, Spearot JA, Koshechko VG, Pokhodenko VD (2011) J Power Sources 196:3331
121. Murugan AV, Kale BB, Kwon C-W, Campet G, Vijayamohanan K (2001) J Mater Chem 11:2470
122. Kwon CW, Murugan AV, Campet G, Portier J, Kale BB, Vijaymohanan K, Choy JH (2002) Electrochem Commun 4:384
123. Kuwubata S, Tomiyori M (2002) J Electrochem Soc 149:A988
124. Ponzio EA, Benedetti TM, Torresi RM (2007) Electrochim Acta 52:4419

125. Malta M, Torresi RM (2005) Electrochim Acta 50:5009
126. Chun-Guey W, Jiunn-Yih H, Shui-Sheng H (2001) J Mater Chem 11:2061
127. Huguenin F, Girotto EM, Ruggeri G, Torresi RM (2003) J Power Sources 114:133
128. Wang GC, Zhao J, Li XW, Li CZ, Yuan WK (2008) Synth Met 159:366
129. Liu M, Visco SJ, De Jonghe LC (1991) J Electrochem Soc 138:1891
130. Shouji E, Buttry DA (1999) Langmuir 15:669
131. Park NG, Ryu KS, Park YJ, Kang MG, Kim DK, Kang SG, Kim KM, Chang SH (2002) J Power Sources 103:273
132. Liu YJ, Schindler JL, Degroot DC, Kannewurf CR, Hirpo W, Kanatzidis MG (1996) Chem Mat 8:525
133. Ruiz-Hitzky E, Aranda P, Casal B (1992) J Mater Chem 2:581
134. Chen W, Xu Q, Hu YS, May LQ, Zhu QY (2002) J Mater Chem 12:1926
135. Jin AP, Zhu QY, Chen W, Volkov VL, Zakharova GS, Liu HX, Zhou J, Xu Q (2007) Solid State Phenom 124:363
136. Jin A, Chen W, Zhou Q, Yang Y, Volkov VL, Zakharova GS (2008) Solid State Ion 179:1256
137. Lutkenhaus JL, Hammond PT (2007) Soft Mater 3:804
138. Galiote NA, Huguenin F (2007) J Phys Chem C 111:14911
139. Huguenin F, Ferreira M, Zucolotto V, Nart FC, Torresi RM, Oliveira ON (2004) Chem Mater 16:2293
140. Huguenin F, Santos DS, Bassi A, Nart FC, Oliveira ON (2004) Adv Func Mater 14:985
141. Huguenin F, Nart FC, Gonzalez ER, Oliveira ON (2004) J Phys Chem B 108:18919

Magnesium Alloys as Anode Materials for Ni-MH Batteries: Challenges and Opportunities for Nanotechnology

Sydney Ferreira Santos, Flavio Ryoichi Nikkuni and Edson Antonio Ticianelli

Abstract New developments on portable electronics, electrical vehicles, and hybrid electrical vehicles have been creating a demand for secondary batteries with larger energy densities than those commercially available. In this scenarios the development of nickel-metal hydride (Ni-MH) rechargeable batteries with improved energy densities is mandatory to achieve the present needs and also to face the tough competition with other technologies such as Li-ion batteries and low temperature fuel cells. The production of such batteries is closely related to the development of novel hydrogen storage materials which can be successfully achieved through the incorporation of new finds of nanotechnology. In this chapter, some fundamental aspects concerning Ni-MH cells and their component materials are introduced. Moreover, recent developments on anode materials, its challenges and perspectives are overviewed. On this subject, special emphasis is given for the nanostructured Mg alloys which are promising candidates for this application.

1 Introduction

The commercialization of Ni-MH batteries started at late eighties. Presently, these cells are largely used in portable electronics such as digital cameras and their annual production is over one billion of units. These batteries have also been used in hybrid electrical vehicles and electrical vehicles [1].

S. F. Santos (✉)
CECS, Universidade Federal do ABC, Rua Santa Adélia 166-CEP, Santo André-SP 09210-170, Brazil
e-mail: sydney.ferreira@ufabc.edu.br

F. R. Nikkuni · E. A. Ticianelli
IQSC, Universidade de São Paulo, Av. Trab. São-carlense 400-CEP, São Carlos-SP 13560-970, Brazil

F. L. de Souza and E. R. Leite (eds.), *Nanoenergy*,
DOI: 10.1007/978-3-642-31736-1_7,

Table 1 Comparison between Ni-MH, Ni-Cd, and Li-ion sealed cells

Property	Ni-Cd	Ni-MH	Li-ion
Energy density	Fair	Good	Excellent
Power density	Excellent	Very good	Very good
Low temperature operation	Excellent	Very good	Very good
Charge retention	Fair	Fair	Very good
Charge acceptance	Very good	Very good	Excellent
Efficiency	Good	Good	Excellent
Life	Good	Good	Excellent

Concerning the market of secondary cells, Ni-MH batteries have Ni-Cd and Li-ion cells as main competitors. Comparing to Ni-Cd batteries, Ni-MH-type cells have larger volumetric and gravimetric energy densities. Furthermore, the absence of cadmium in Ni-MH cells is advantageous from the environmental point of view due to the high toxicity of this element. Due to the aforesaid, Ni-MH batteries replaced Ni-Cd cells in large extent.

Conversely, Ni-MH batteries have been experiencing a hard competition with Li-ion batteries which quickly increased their share market and nowadays are predominant for several applications such as cell phones, notebooks, portable players among others. These batteries have larger energy densities (volumetric and gravimetric) than Ni-HM ones.

Table 1 compares some key features of Ni-MH, Ni-Cd, and Li-ion cells [2]. In terms of price, Ni-MH cells are situated between Ni-Cd (less expensive) and Li-ion (more expensive) counterparts.

In the market of portable energy sources, Ni-MH batteries have to compete not only with other types of batteries, as aforementioned, but also with emerging technologies such as low temperature fuel cells and super-capacitors. Another driving force for improvements in Ni-MH cells is the continuous development in portable electronics (longer operating times, color screens, Wi-Fi technology, etc.) which generates an increasing demand for energy sources with larger energy densities. In the case of Ni-MH batteries, the development of cells with larger energy densities is mainly related to the development of novel anode materials with larger hydrogen storage capacities. In addition to this property, anode materials need to be stable over repeated cycles of electrochemical charge and discharge of hydrogen in a strong alkaline electrolyte. This aggressive environment is very restrictive concerning the material which can be used for this application.

In the following sections, the main concepts on Ni-MH cells are introduced. Moreover, the anode materials used in commercial Ni-MH cells and those which are currently under investigation are reviewed.

2 Principles of Nickel-Metal Hydride Batteries

A Ni-MH cell is an electrochemical device for energy storage. These cells are classified as secondary cells since they can be charged again after the complete exhaustion of the cell (i.e., after all the reactants have been converted in product species, the electrochemical reaction can be reverted). These cells are composed by three main parts: a positive electrode (cathode), a negative electrode (anode), and an electrolyte. The cathode is the NiOOH compound, the anode is a hydrogen storage alloy, and the electrolyte is a concentrated solution of KOH. A Ni-MH cell is schematically represented in Fig. 1 [3–6].

The electrochemical reactions that take place during the Ni-MH cell operation are shown bellow. The reactions are reversible and the direction from left to right indicates charging, whereas the opposite direction indicates discharging [3–6].

In the cathode side, the reaction that takes place is:

$$Ni(OH)_2 + OH^- \leftrightarrow NiOOH + H_2O + e^- \quad E = 0.52\ \text{V} \tag{1}$$

while the reaction in anode side is:

$$M + H_2O + e^- \leftrightarrow MH + OH^- \quad E = 0.83\text{V} \tag{2}$$

Then, the overall cell reaction is:

$$Ni(OH)_2 + M \leftrightarrow NiOOH + MH \quad E = 1.35\ \text{V} \tag{3}$$

In a Ni-MH cell, the upper limit of the theoretical discharge capacity is controlled by the reversible hydrogen storage capacity of the alloy electrode. Therefore, the development of novel hydrogen storage materials with larger storage capacities is fundamental for attaining cells with higher energy densities.

The hydrogen storage materials used in Ni-MH cells are typically intermetallic compounds. Further information on these materials such as their composition and crystal structures are giving in the following section.

In hydride forming materials, hydrogen is up taken into their crystal structures, firstly forming an interstitial solid solution (α phase) for low concentration of hydrogen. In this phase, hydrogen is randomly distributed in available interstitial sites throughout the crystal structure. When the limit of solubility is exceed a new phase started to nucleate into the microstructure. This phase is a metal hydride (β phase). In this phase hydrogen occupy periodically the available interstitial sites in crystal structure. These two phases are represented schematically in Fig. 2.

Due to its small atomic size, hydrogen exhibits large limits of solubility in metals to form interstitial solid solutions when compared to other light elements (N, C, O, B). Conversely, even the limits of solubility of hydrogen in metals are small when compared to the solubility observed in substitutional solid solutions with extensive solubility (i.e., those solid solutions which follows the so called "Hume-Rothery rules" [7]). The limited solubility of interstitial elements in metals arises from the high elastic strain imposed by solute atoms to the host

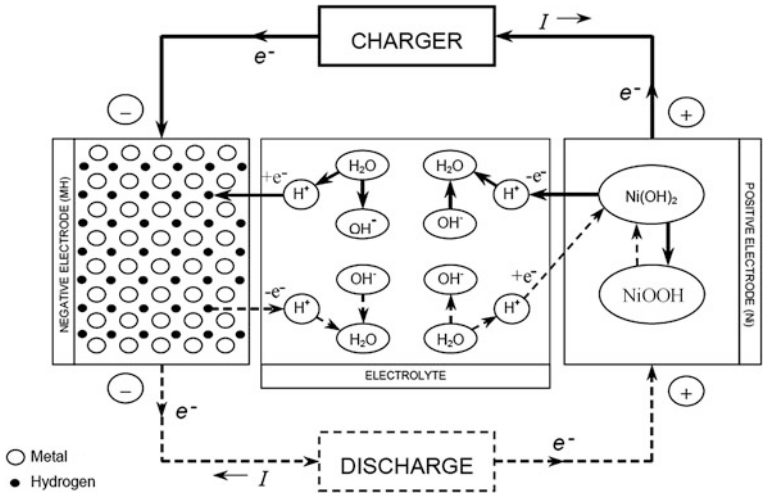

Fig. 1 Schematic representation of a Ni-MH cell. Full line represents the electrical circuit during charging while the doted line represents the circuit during discharging [3, 4]

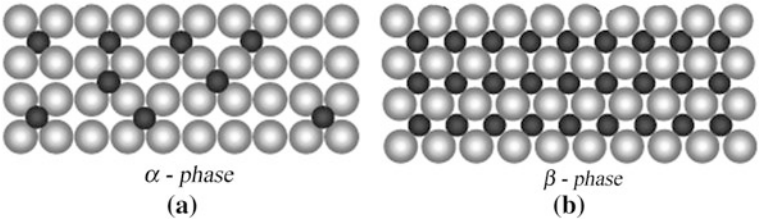

Fig. 2 Schematic representation of the atomic arrangement for (**a**) interstitial solid solution (α-phase) and (**b**) metal hydride (β-phase)

lattice. Even hydrogen (the smallest interstitial atom) is much larger then the interstitial spaces in host lattice. This difference in volume size is the origin of the elastic strain. In extensive substitutional solid solutions the elastic strain fields around the solute atoms are much lower.

When a metal with positive heat of mixing with hydrogen is submitted to a hydrogen atmosphere, it absorbs the atoms of this element until reaching the equilibrium with the gaseous atmosphere. If the pressure is increased, more hydrogen will be absorbed until reaching a new equilibrium condition. Thus, for each pressure (p) there is a certain amount of hydrogen which can be absorbed in equilibrium condition (c). This behavior is known as Sievert's law and it can be mathematically represented by the following expression:

$$c = k.\sqrt{p} \tag{4}$$

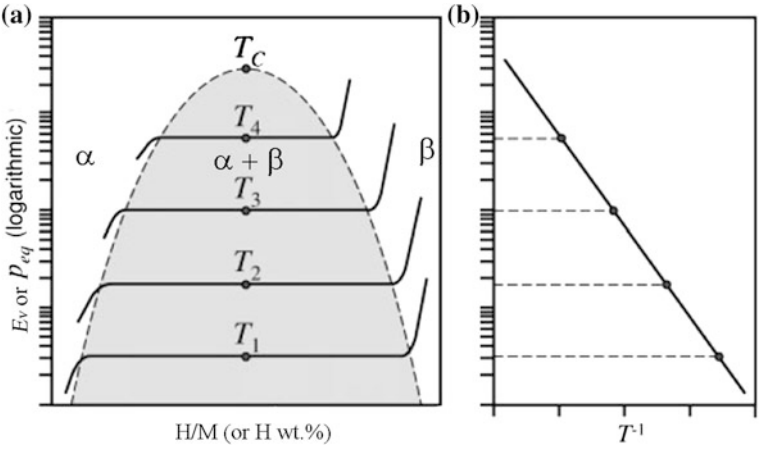

Fig. 3 Schematic representation of some PCI curves (**a**) and the corresponding van't Hoff plot (**b**) [3]

Where c means the hydrogen concentration in the metal, p is the equilibrium pressure of H_2, and k is a constant which depends on temperature (Sievert's constant).

When the material is hydrogenated under a gas phase atmosphere at constant temperature, pressure—composition isotherms (PCI) can be determined for this material. These isotherms can be measured for different temperatures, as illustrated in Fig. 3a [3].

As aforementioned, in solid solution composition range, hydrogen metal interaction follows the Sievert's Law and the hydrogen content is function of the pressure. When the maximum solubility at a given temperature is attained further hydrogen absorption results on the formation of a new phase named metal hydride.

In equilibrium condition, the transformation from interstitial solid solution (usually denominated α-phase) to hydride (β-phase) takes place under constant pressure. This pressure is the equilibrium pressure of hydride formation (or equilibrium pressure of absorption) and corresponds to the plateaus of pressure observed for the *pressure-composition* isotherms in Fig. 3a for different temperatures. As represented in this Fig. 3a, increasing the temperature a higher equilibrium pressure is attained. Under desorption, the same reaction takes place but the equilibrium pressure of desorption is lower than that of absorption. Ideally, the plateau pressure of hydride formation/decomposition is flat. This behavior is assumed to the occupation of energetically equivalent interstitial sites by hydrogen atoms. But, in several cases, a slopping plateau is observed during (de)hydriding. This behavior can by ascribed to a few reasons. On of these reasons is the presence of internal stresses developed from dislocation pile-ups. This accumulation of defects is generated from the sudden volume change associated to the hydride formation/decomposition. Slopping plateau can also be caused by internal oxide precipitates. In the case of alloys and intermetallic compounds, the slopping plateau can be originated from chemical inhomogeneities [8].

From a set of PCI curves, it is possible to obtain the thermodynamic properties of the hydride, through the van't Hoff equation, expressed as:

$$\ln P_{eq} = \frac{\Delta H}{R \cdot T} - \frac{\Delta S}{R} \tag{5}$$

From the linearization of this equation (Fig. 3b), one can obtain the values of enthalpy (ΔH) and entropy (ΔS) of $\alpha \rightarrow \beta$ reaction. The ΔS term mostly corresponds to the change from molecular hydrogen to dissolved solid hydrogen, i.e. it is nearly the standard entropy of hydrogen and does not depend on the nature of the metal. The term ΔH depends on the metal hydrogen bond [3, 9, 10]. These values can be obtained from a set of PCI curves of absorption or desorption. P_{eq}, R, and T are the equilibrium pressure of absorption or desorption (plateau pressure), the ideal gas constant and the absolute temperature, respectively [3, 9].

The equilibrium pressure for gaseous hydrogenation can be correlated to the electrochemical potential (E_v) of the hydride electrode through the equation

$$E_v = -\frac{1}{2} \cdot \frac{RT}{F} \ln P_{H_2} - \delta E_{ref} \tag{6}$$

Where F is the Faraday constant ($F = 9.6487 \times 10^4$ C/mol), P_{H2} is the hydride dissociation pressure, and T the absolute temperature. E_v is measured with reference to the standard reference electrode. Thus, if other reference electrode is used, δE_{ref} is added to the value of E_v (for instance, −0.926 for Hg/HgO reference electrode) [3, 4].

2.1 Conventional Alloy Electrodes

There are many alloys that form metal hydrides. For hydrogen storage purposes, the metal hydrides should have large reversible hydrogen storage capacities and adequate thermodynamic properties. But, in the case of anode application, the hydride—forming alloy should have additionally:

(i) Adequate corrosion resistance in concentrated alkaline electrolyte;
(ii) Stability over repeated cycles of electrochemical charge/discharge;
(iii) High electro catalytic activity and reversibility of the electrode reaction;
(iv) Easy activation.

Development of materials suitable to fulfill completely this set of requirements is a challenging task. Presently, there are two different types of alloys used as anode materials in commercial Ni-MH batteries: AB_5 and AB_2 alloys.

The AB_5 alloys are based on the $LaNi_5$ intermetallic compound which have $CaCu_5$ compound as prototype structure and space group P6/mmm. A detailed description of the crystallography of these alloys is beyond the scope of this

chapter and further useful information on this subject can be obtained from Wronsky [6] and references therein.

The investigations on the use of intermetallic compounds as anode materials started in early seventies but only in late eights the minimum requirements for practical application were achieved [11]. Few years latter, the commercial production of Ni-MH batteries started having a $LaNi_5$-based alloy as anode material. These alloys have been used up to the present days in commercial Ni-MH cells.

In this alloys both elements La and Ni are partially replaced by other metals in order to improve the electrode performance.

In commercial alloys, La is usually replaced by mischmetal, a commercial mixture of rare earths (La, Ce, Nd, and Pr), aiming to decrease the cost of raw material. The hydrogen storage properties of mischmetal-containing AB_5 alloys are strongly affected by the mischmetal composition. For example, mischmetal with high content of Ce causes an increase in plateau pressure and hysteresis in pressure-composition isotherm loops [6]. This later means that the difference between the plateau pressure of absorption and plateau pressure of desorption increased. This is usually an undesired feature for metal hydrides designed for technological applications but it is a more serious problem for those hydrides aimed for hydrogen storage tanks.

Partial substitution of Ni is also performed with the purpose of improving the reaction kinetics, increase the corrosion resistance, and adjust the plateau pressures of hydrogen absorption and desorption of the alloys.

The substitution of Ni by elements such as Sn and mainly Co can improve the kinetic properties and increase both cycle life and discharge capacity [12, 13]. These beneficial effects have been attributed to the increase in the unit cell parameter and reduction in cell volume expansion during hydriding. Both features lead to the decrease in pulverization of the alloy under galvanostatic cycling. This pulverization process takes place due to successive volume expansion and contraction caused by hydride formation and decomposition resulting on the generation and accumulation of defects and, consequently, fractures of the particles and formation of fresh surfaces which are more sensitive to corrosion when exposed to electrolyte. This process results in continuous loss of active material by corrosion.

In spite of these positive effects of Co addition, alternatives to this element have been searched due to its high cost.

Replacement of Al for Ni increases the cycle-life performance of the electrodes through the formation of a protective passive film. Other common substitute for Ni is Mn which decreases the plateau pressures of hydride formation and decomposition maintaining the same hydrogen storage capacity [6, 12–14].

The commercial Ni-MH cells make use of multi-component alloys as anode materials, with several substitutes for both A and B elements. As a common feature, the commercial alloys need relatively large amounts of cobalt to present satisfactory electrode performances, despite the inconvenience of its high cost. A typical example of composition of AB_5 alloy electrode is $MmNi_{3.55}Mn_{0.4}Al_{0.3}Co_{0.75}$ (in at

%), where Mm means mischmetal. This alloy contains over 10 % of Co which ensure good durability for the electrode. Conversely, Co is an expensive alloying element been responsible by approximately 40 % of the cost of raw material [15, 16].

Concerning the AB_5 alloys, the main constraint is related to the low discharge capacity displayed by these alloys, which absorb nearly 1.2–1.4 wt % of H, depending on composition. These hydrogen storage capacities can lead to discharge capacities nearly 370 mA.h/g. The experimental results indicate capacities nearly 300 mA.h/g. This discrepancy has been attributed to the pulverization.

The AB_2 alloys used in electrode applications are multi-element pseudo-binary alloys, having ZrV_2 and $ZrMn_2$ compounds as prototypes for hydrogen storage. The ZrV_2 compound has structure C14 hexagonal while the $ZrMn_2$ compound has structure C15 cubic. These two phases present high hydrogen storage capacities. Other phases that typically appear in such alloys are the C36 hexagonal, with poor hydrogen storage capacity, and a BCC solid solution with high hydrogen storage capacity [6]. The C14, C15, and C36 structures are members of a group of intermetallic compounds denoted Laves phases. Some useful crystallographic information can be obtained in Wronsky [6] and references therein.

The discharge capacity of AB_2 alloys is typically larger than those of the AB_5 counterparts, reaching values around 390 mA.h/g. Conversely, AB_2 alloys exhibit lower electrocatalytic activity, poorer activation behavior, and higher costs than AB_5 counterparts, limiting their utilization [1, 6, 17].

Concerning the synthesis of AB_2 and AB_5 alloys, they are typically produced by melting under controlled atmosphere. The preferential processing routes are arc-melting and induction melting. In the first one, chunks of pure elements are place into the furnace chamber which is repeatedly evacuated and filled with an inert gas (argon, in general) to ensure a low partial pressure of oxygen. Thus an electrical arc between the metal chunks and a non-consumable tip of tungsten is produced and it allows to reach high temperatures (over 2000 ^{o}C) promoting the fusion and intermixing of pure elements. The obtained ingots are usually turned up-side down and re-melted few times to achieve homogenization of the chemical composition. This arc-melting furnaces usually have a water cooled copper base were the raw material is places and melted avoiding the necessity of crucibles, a potential source of contamination. On the other hand, dendritic segregation is usually observed for arc-melted alloys and in some cases subsequent high temperature annealing is necessary to achieve the desired microstructure. In the case of induction melting, similar procedures for cleaning the atmosphere are employed. In this case, the melting is usually carried out in crucibles and the selection of the crucible material is an important task in order to avoid or minimize the contamination of the cast ingot. Conversely, the magnetic agitation promoted by the magnetic field generated by the induction coil can promote a refining of the microstructure and homogenization at some extent.

2.2 Mg Alloy Electrodes

Magnesium-based materials (alloys and composites) are very attractive for hydrogen storage applications due to a set of promising properties of Mg, such as:

(i) High volumetric and gravimetric hydrogen storage capacities;
(ii) Low density;
(iii) Availability;
(iv) Relative low cost.

For instance, Mg and Mg_2Ni when fully hydrided (i.e. converted to MgH_2 and Mg_2NiH_4, respectively) can reach gravimetric hydrogen storage capacities of 7.6 and 3.6 wt %, respectively. As mentioned in previous section, the commercially used AB_5-type alloys can only reach up to 1.4 wt % of hydrogen.

Not withstanding the abovementioned encouraging properties, the slow kinetics of hydrogen absorption/desorption has been a major drawback to apply Mg—based materials in hydrogen storage applications. Moreover, the poor corrosion resistance of magnesium in alkaline solution is a major problem for electrochemical applications.

Polycrystalline magnesium and magnesium alloys can only absorb and release hydrogen at high temperatures and usually with slow kinetics. In pure Mg and Mg-Ni alloys, for example, the room temperature electrochemical (de)hydrogenation is negligible. For this reason, only after the development of highly metastable magnesium alloys (i.e., alloys with amorphous or nanocrystalline structures) these materials started to be considered for anode applications. The main investigated Mg alloys for anode application are those of the Mg-Ni system. Alloys of this system are mostly synthesized by mechanical alloying even though other routes are also possible. For Mg alloys, routes involving fusion introduce a considerable degree of complexity because Mg easily evaporates and it is very reactive with oxygen and moisture, especially in liquid state. In mechanical alloying, powders of pure Mg and Ni are placed together, in appropriate stoichiometry, in a milling vial with a certain number of balls and milled by a pre-defined period of time. Before milling, the vial is evacuated and filled with argon in order to prevent the oxidation during processing. The impact of the balls against small powder agglomerates during milling promotes repeated events of cold welding and fracture. After certain time, the particles become mixtures of deformed Mg and Ni regions with lamellar-like microstructures. The large amount of Mg/Ni interfaces and structural defects (vacancies, dislocations, staking faults, etc.) generated by plastic deformation create short-circuits for inter-diffusion, promoting atomic mixture of the metallic elements through a solid state reaction. This is the typical behavior observed for mechanical alloying of soft elements [3, 18].

Depending on the type of mill, material to be processed, and its application, a number of other processing variables need to be settled, such as: (i) ball-to-powder weight ration (ii) number of balls (iii) diameter of the balls (iv) in some cases, the milling speed, etc. A deeper description of the mechanical alloying process is far

beyond the scope of the present chapter and there is a vast literature for consulting on this subject [18–20]. One of the most interesting and complete source of information is the classical review article of Suryanarayana [18] which deals with all relevant aspects of mechanical alloying and correlated techniques.

The mechanical alloying of Mg-Ni binary system can generate a variety of different microstructures, depending on the selected stoichiometry, processing parameters, etc. This process is mainly indicated to obtain alloys with metastable microstructures such as: extended solid solutions (i.e. solid solutions into which the limit of solubility in equilibrium is exceed), fully amorphous alloys, nanocrystalline alloys (single or multi-phase), and mixtures of amorphous and nanocrystalline phases. The processing parameters adopted during mechanical alloying will define all the microstructural and morphological features of the synthesized alloys and therefore will greatly affect the electrochemical properties of the final product.

Liu et al. [21] investigated the Mg_xNi_{100-x} alloy series, with x ranging from 10 to 90 at %. These authors reported that fully amorphous alloys were obtained between 30 and 70 at % of Mg and yielded the best electrochemical properties among this series. The highest value of discharge capacity was achieved by the $Mg_{50}Ni_{50}$ alloy (387 mAh/g), but its cycle—life performance was very poor. After nine cycles the discharge capacity was only 35 % of the initial one. Similar behavior has been reported for MgNi binary alloys by other authors [22, 23].

Investigations on the surface chemical composition of Mg-Ni alloys have been performed trying to understand their electrochemical performances. Surface and subsurface analysis of the $Mg_{50}Ni_{50}$ alloy, by combining X-ray photoelectron spectroscopy (XPS), Auger electron spectroscopy (AES), and Ar^+ sputtering, indicated that at top surface Mg prevail in oxidized state and Ni in metallic state [22]. Penetrating the subsurface, there was observed an enrichment of Ni up to about 60 at %. The good electrocatalytic activity of this alloy was ascribed to this Ni-rich subsurface layer which could act as a catalyst for the electrochemical reactions [22].

In a study of Zhang et. al. [23] three different compositions of Mg-Ni amorphous alloys were investigated. The larger value for the maximum discharge capacity was 490 mAh/g for the $Mg_{50}Ni_{50}$ alloy. The maximum discharge capacity decreased for larger amounts of Ni (370 mAh/g for $Mg_{40}Ni_{60}$ and 200 mAh/g for $Mg_{33}Ni_{67}$). Conversely, the increase in Ni content improved the cycling performance of the electrodes. Surface analyses indicated that Mg prevails in oxidized state on top surface for all three compositions while Ni remains mostly in metallic state for the $Mg_{50}Ni_{50}$ composition. Increasing Ni content resulted in a higher Ni oxidized/Ni metallic ratio which can be related to the decrease of the maximum discharge capacity. Moreover, subsurface analyses indicate an increase of the thickness of Ni subsurface layer for the alloys with larger Ni content.

The aforementioned experimental results on Mg-Ni alloys highlights the necessity of improving their electrochemical properties, mainly their cycling performances in order to obtain alloys suitable for practical applications. There are several strategies

that have been investigated aiming to optimize the electrochemical properties of Mg-Ni alloys. These strategies can be sub-divided in two main groups:

(i) Modification of surface chemical composition,
(ii) Modification of bulk chemical composition.

The former group comprises all routes where only the surface is modified and the center of the particle remains unchanged. These routes include all types of coatings, lixiviation and etching of Mg-Ni particle surfaces.

The second group of strategies comprises modification of chemical composition in full particles' volume. This is typically the case of addition of alloying elements which takes place during the synthesis of the alloy.

Concerning the modification of the surface chemical composition, the modified surface (usually coated with some type of protective layer) must prevent or minimize the corrosion of the alloy electrode but can not hinder the absorption and release of hydrogen. Moreover, the modified surface should present high electrocatalytic activity and mechanical stability. One of the most investigated methods of modifying the chemical composition of alloy electrodes is the *electroless deposition* which allows the particles of the hydrogen-absorbing alloy to be completely covered with a metal or compound with good corrosion resistance. In this technique the coating is performed by immersing the active material (hydrogen absorbing alloy) or the working electrode in a Becker with a chemical solution containing the coating precursor (usually salts of the element to be deposited). Thus the reaction takes place on the surface of the hydrogen storage alloy in the presence of a reducing agent. For instance, a bath containing $CuSO_4$ (0.16 g/ml) and H_2SO_4 (pH = 4–5) has been employed for Cu electroless deposition on hydrogen-absorbing alloy electrodes [24]. The electroless deposition usually presents improvements on the high rate dischargeability, decreasing of cyclic degradation, lowering the charge transfer resistance, and lowering the charge/discharge overpotential in AB_5-type alloys [24–27]. But, in the case of Mg-Ni alloys, the experimental results have not been so promising like those obtained for the AB_5 counterparts. Rongeat et al. [28] performed the electroless coating of the $Mg_{50}Ni_{50}$ alloy with a fine and dense chromate coating and observed a constant discharge capacity of the coated electrode for the first two cycles. After that, a decay of the discharge capacity similar to that observed for the uncoated one was reported. This behavior was attributed to the rupture of the coating layer caused by the huge mechanical stresses on this layer due to the large volume expansion promoted by hydriding. These explanation is not complete satisfactory since AB_5 alloys also experience pronounced volume expansion due to hydride formation and their electrochemical performance is improved in a larger extent by electroless deposition. This highlights that further investigation is still necessary to understand the different performances attained by electroless coated AB_5 and Mg-Ni alloys.

Another technique for modifying the surface chemical composition of the alloy electrodes is *mechanical coating* which consists of dispersing a coating element by short milling times in a parent Mg-Ni alloy to promote the improvement on its

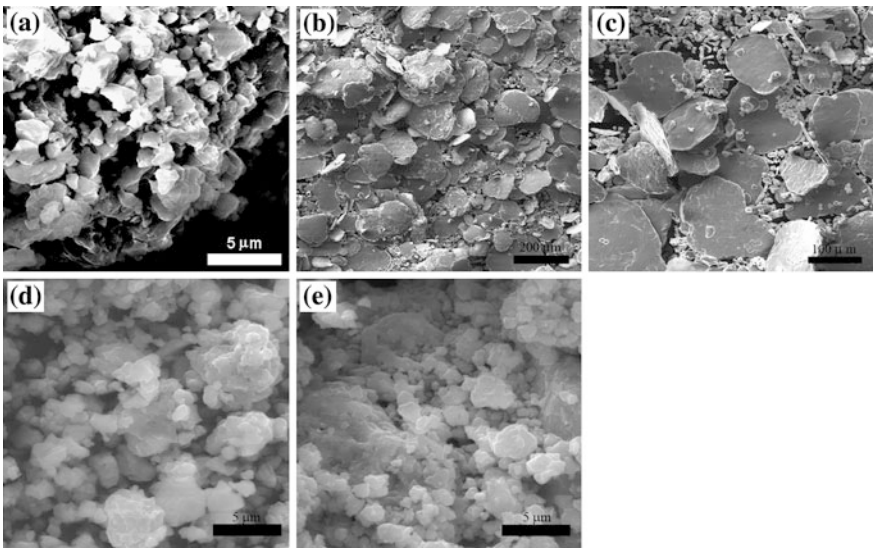

Fig. 4 SEM images of (**a**) ball-milled and uncoated Mg-Ni alloy; (**b**) Ni coating, prepared by ball-milling pure Ni granulates; (**c**) Ni-5 % Al coating, prepared by ball-milling Ni and Al powders in appropriate stoichiometry; (**d**) Mg-Ni coated with Ni by mechanical coating; and (**e**) Mg-Ni coated with Ni-5 %Al by mechanical coating [29]

corrosion resistance [28, 29]. Differently of electroless deposition, mechanical coating does not form a compact and continuous layer on the particle surface of the Mg-Ni alloy. This feature probably makes the coating obtained by this technique less sensitive to the expansion caused by hydride formation. Conversely, the particles are not fully protected against the contact with the electrolyte and protected from corrosion. Figure 4 shows the scanning electron microscopy (SEM) images of the coating materials used for mechanical coating of a Mg-Ni alloy, the uncoated (bare) Mg-Ni alloy and Mg-Ni coated alloys [29]. Figure 4a shows the morphology of the ball-milled bare alloy. This alloy has a relatively equiaxial particle shape with sizes ranging from 1 to 5 µm. In Fig. 4b and c the microstructures of the coating materials can be observed. There is a clear morphological difference between the coating materials and bare alloy. For the coating materials, two types of morphologies can be observed: (i) small agglomerates of fine and rounded particles, in small amount; and (ii) a large amount of flattened particles. The morphology of Mg-Ni bare alloy is probably due to a equilibrium between cold welding and fracture events during ball-milling while the morphology of coating materials suggest a predominance of deformation and cold welding. Figure 4d and e show the microstructures of the Mg-Ni alloy coated by Ni and Ni-5 % Al, respectively. The resulting nano composites have similar morphologies, composed by fine spherical particles. Flattened particles are no longer observed. This feature can be ascribed to the low fraction of coating materials (5 wt %) and to an effective coating of the Mg-Ni particles.

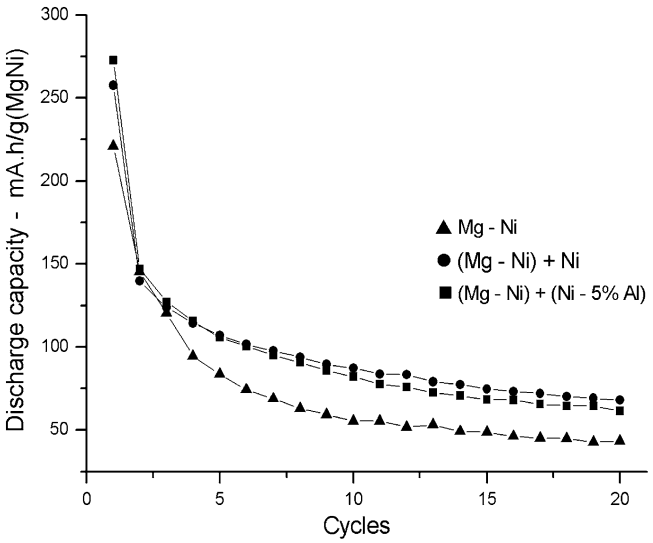

Fig. 5 Discharge capacity versus number of cycles of bare, Ni coated, and Ni-5 %Al coated $Mg_{50}Ni_{50}$ alloys [29]

The X-ray diffraction patterns for the coating materials (not shown here) indicate that Al was only partially solubilized in Ni-Al coating material. The amount of solubilized Al was estimated to about 2.2 at % [29].

Figure 5 shows curves of discharge capacity as a function of the number of cycles of bare nanostructured $Mg_{50}Ni_{50}$ and two coated $Mg_{50}Ni_{50}$ alloys (one coated with 5 wt % of Ni and the other with 5 wt % of Ni-Al alloy) [29]. The coating materials were dispersed by 1 h of further milling in a planetary ball-mill. It is possible to see that mechanical coating improved both the maximum discharge capacity and the cycle-life performance of the electrodes, but in a limited extent. The results indicate that more extensive investigations on processing/coating parameters are still necessary in order to optimize the electrode performances.

As aforementioned, modifications of the surface chemical composition can lead to improvements of the electrode performance of Mg-Ni alloys but until now the best electrochemical results were reported for modifications of the bulk chemical composition of the alloy electrodes, i.e. addition of alloying elements to the binary Mg-Ni system. Thus, a number of ternary and quaternary alloys have been investigated and some of than have showed remarkable improvements on the electrochemical properties when compared to the binary counterparts. Some of these metallic elements improve the cycle-life performance of the electrodes while reducing their maximum discharge capacities. This behavior is observed for instance for Co, Al, Si, Cu, W, Ti, Mn, among others [28–31]. In a previous report [31] we investigated the effect of Cr, Co, Nb, Ti, and V additions on the electrochemical properties of the nanostructured $Mg_{50}Ni_{50}$ alloy. It was observed increases in maximum discharge capacities for the additions of Zr, Nb, and Cr

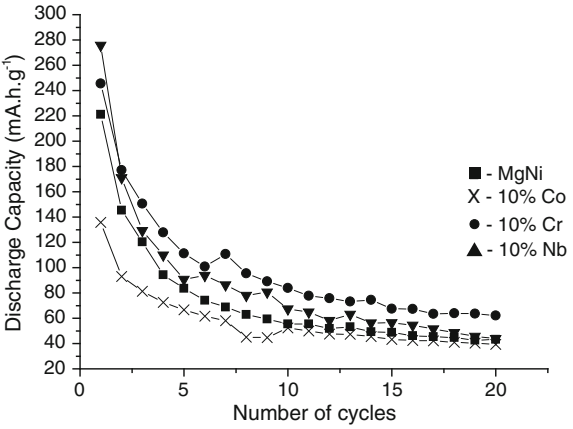

Fig. 6 Discharge capacity as a function of the number of cycles of the Mg-Ni, Mg-Ni-Co, Mg-Ni-Cr and Mg-Ni-Nb alloys

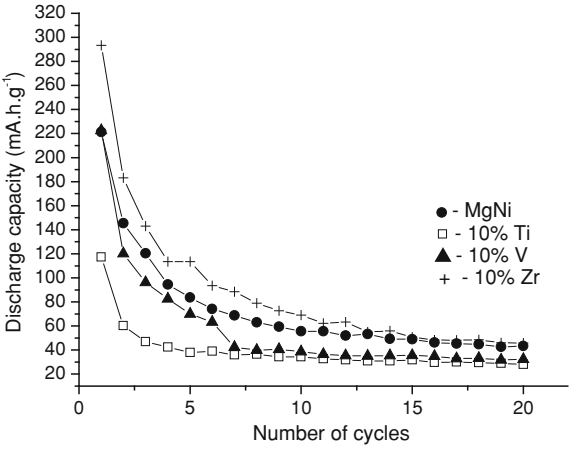

Fig. 7 Discharge capacity as a function of the number of cycles of the Mg-Ni, Mg-Ni-Ti, Mg-Ni-V and Mg-Ni-Zr alloys

metals, given rise to the ternary $Mg_{45}Ni_{45}M_{10}$ alloys (where M is the added metal). Additions of Zr and Nb decreased the cycle-life performance when compared to the binary alloy while Cr slightly increased this property. These results of discharge capacity vs. cycling number are shown is Figs. 6 and 7.

Some promising results have been reported for amorphous alloys of the Mg-Ni-Ti and Mg-Ni-Al systems, which presented a limited decrease of the maximum discharge capacity and improvements of cycle-life performance [28]. Mg-Ni-V system also presented interesting electrode performances [32]. In alloys of this system the same capacity of $Mg_{50}Ni_{50}$ alloy and improved cycle-life performance were achieved [32]. In the case of Ti addition, it was observed by surface analysis the formation TiO_2 on top surface of the alloy particles and also decrease in $Mg(OH)_2$ formation rate [33]. These results indicate a preferential oxidation of Ti on the surface of the particles creating a thin layer of TiO_2. This passive film might protect the bulk particle against corrosion improving the cycle-life performance of the electrodes.

Rare earths have been investigated too as alloying elements for Mg-Ni alloy electrodes. Huang et al. [34] investigated the effect of Nd addition and reported that the maximum discharge capacity increased for the alloys with larger contents of this element. When the amount of Nd was in the range of 10–15 mol %, the maximum discharge capacity was close to 580 mAh/g. Moreover, the maximum discharge capacity after 20 cycles of charge/discharge was 80 % of the initial one. This retained capacity is larger than those observed for Mg-Ni binary alloys. The effect of La addition on the structure and electrode performance of the Mg_2Ni alloy synthesized by melting-spinning technique (i.e. a technique of rapid solidification which allows obtaining thin metallic ribbons, in the range of tens of micrometers of thickness, with metastable microstructures) was reported by Ren et al. [35]. Using the same processing parameters, these authors observed that Mg_2Ni alloy presented a nanocrystalline structure and the addition of La favored the formation of amorphous phase. This behavior indicates that La addition increased the glass—forming ability of the Mg-Ni alloy. It was also observed that the increase in La content improved the maximum discharge capacity and cycle—life performance of the electrodes.

Noble metals also have attracting attention as alloying elements for the Mg-Ni alloys. The most investigated of these metals is Pd [36–38]. As a general trend, it has been reported that Pd additions promoted increase in cycle—life performances. To avoid a decay of the maximum discharge capacity, the amount of Pd in the alloy should be low. As an example, Ma et al. [37] reported improvement in cycle—life performance by ball-milling $(Mg_{50}Ni_{50}) + 6$ mol % of Pd. The maximum discharge capacities reported for both unalloyed and Pd—added alloys was almost the same. Similar results were reported by Souza et al. [39] for the $Mg_{49.5}Ni_{49.5}Pt_1$ (in at %) ball-milled alloy.

Recently, Mg-Ni-based quaternary alloys have been investigated. Depending on the alloying elements, further improvements can be obtained by these quaternary systems when compared with the ternary ones. Figure 8 shows the curves of discharge capacity versus number of cycles for some quaternary $Mg_{51}Ti_4Ni_{43}M_2$ alloys (in at %) where M is the alloying element [40]. From these results, it is possible to observe that the best electrode performances were attained by Pd and Pt additions. The elaboration of multi-element alloys (i.e., at least four components in the system) for electrode applications open a wide range of possibilities concerning the designing of microstructures in order to obtain a material with optimized electrochemical properties.

In Fig. 9 the effects of Ti and Pt on the electrochemical properties of the $Mg_{55}Ni_{45}$ alloy can be observed [41]. The addition of Pt significantly increased the maximum discharge capacity and improved the cycle-life of the alloy. A partial replacement of Ti for Mg resulted in further improvements of these electrochemical properties. From these results, one can see that the addition of both Ti and Pt simultaneous resulted the best electrode performance. Concerning the cycling stability, the major target of this investigation, the decrease in degradation rate for these quaternary alloys can be ascribed to different protection mechanisms acting simultaneously. As abovementioned, Ti decreases the corrosion rate of Mg

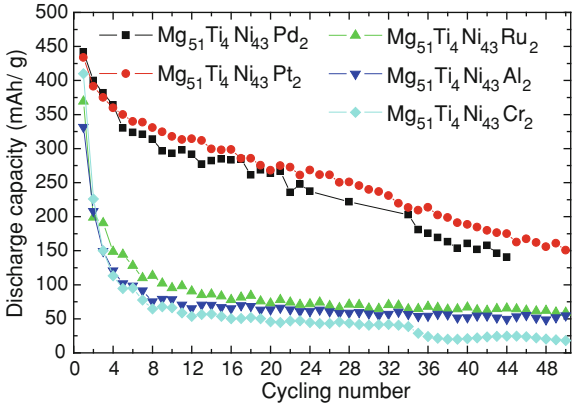

Fig. 8 Discharge capacities versus cycling number of $Mg_{51}Ti_4Ni_{43}M_2$ alloys [40]

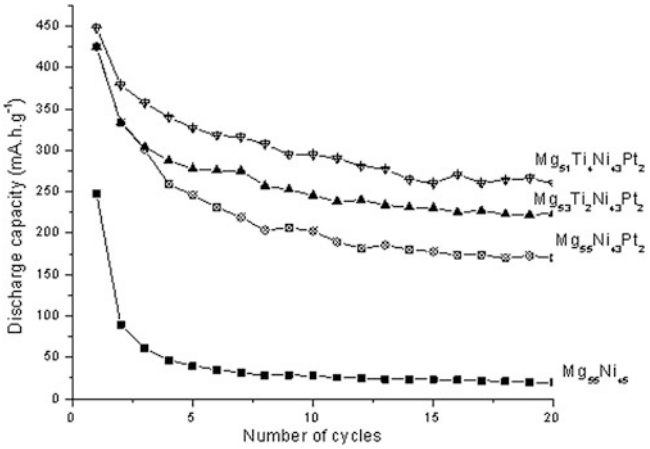

Fig. 9 Discharge capacities versus cycling number of $Mg_{55}Ni_{45}$ and Pt-containing alloys [41]

through the formation of a protective layer of TiO_2 on the particle's surface. In the case of Pt, the protective behavior can be ascribed to a displacement of the corrosion potential reinforcing the cathodic character of the alloy in a similar way of that reported for Ti-Pd and Ti-Pt alloys [42, 43].

In other investigation of our group, the effect of partial substitution of noble metals for Ni in the $Mg_{49}Ti_6Ni_{45}$ was carried out [40]. The alloys were synthesized by mechanical alloying with nominal composition of $Mg_{49}Ti_6Ni_{45-X}NM_X$, where NM means Pd or Pt and assume values of 2 and 4 at %. The structure of the alloys was characterized by X-ray diffraction (XRD) and transmission electron microscopy (TEM).

Figure 10 shows the XRD patterns of the abovementioned alloys [40]. It is possible to observe the presence of broadened peaks in all samples due to reduced crystallite sizes and strain generated by ball-milling. The Mg_2Ni and $MgNi_2$

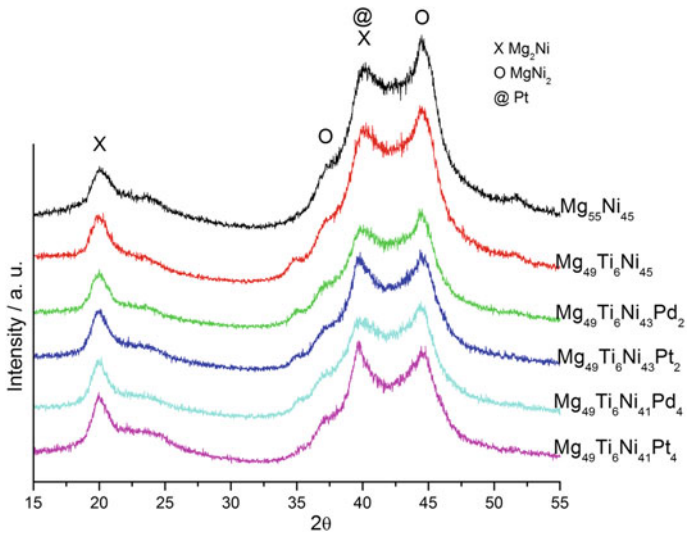

Fig. 10 XRD patterns of $Mg_{55}Ni_{45}$, $Mg_{49}Ti_6Ni_{45-x}MN_x$ alloys [40]

intermediate phases were identified in all samples while there is evidence of Pt phase in the alloys containing this element.

Figures 11, 12, 13, 14 show the results of transmission electron microscopy (TEM) for $Mg_{49}Ti_6Ni_{45-x}MN_x$ alloys [40]. It can be observed that all alloys presented microstructures composed of nanocrystalline phases dispersed on an amorphous matrix. The average crystallite size is bellow 10 nm. In the case of Pt-containing alloys, the fraction of amorphous phase is apparently larger than that of Pd-containing alloys.

There was not observed the presence of Pt and Pd—based intermediate phases, however evidences of these elements in unalloyed state were indicated by XRD and selected area electron diffraction (SAED).

The curves of discharge capacity *versus* cycling number for the $Mg_{49}Ti_6Ni_{45-x}NM_x$ alloys are presented in Fig. 15 [40]. From these results, it is noticeable the improvements on the electrode performance of the alloys due to the addition Ti and Pd/Pt. There are some differences between the electrochemical behavior of the alloys containing Pd and Pt. In the case of Pd, the increase of this element from 2 to 4 at % resulted in substantial improvement in cycle-life performance but only a slight decrease of the maximum discharge capacity. In the case of Pt, the improvement of cycling stability was less pronounced when the amount of this metal increase from 2 to 4 at %. Moreover, the decrease of the maximum discharge capacity was more pronounced. These results indicated a better electrode performance for the alloys containing Pd, specially the $Mg_{49}Ti_6Ni_{41}Pd_4$ one.

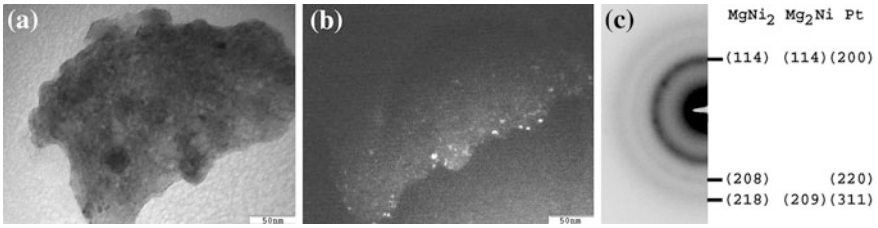

Fig. 11 *Bright field image* (**a**), *dark field image* (**b**), and selected area electron diffraction pattern (**c**) of the $Mg_{49}Ti_6Ni_{43}Pt_2$ alloy [40]

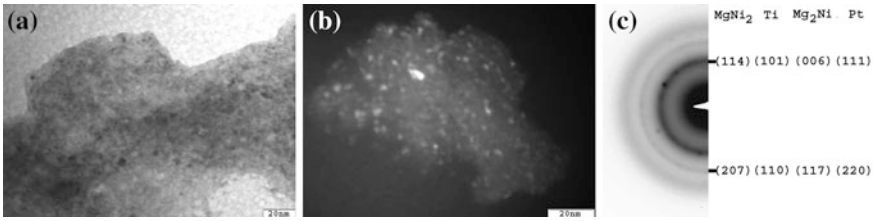

Fig. 12 *Bright field image* (**a**), *dark field image* (**b**), and selected area electron diffraction pattern (**c**) of the $Mg_{49}Ti_6Ni_{41}Pt_4$ alloy [40]

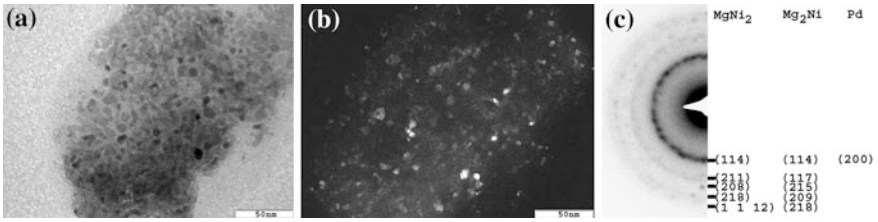

Fig. 13 *Bright field image* (**a**), *dark field image* (**b**), and selected area electron diffraction pattern (**c**) of the $Mg_{49}Ti_6Ni_{43}Pd_2$ alloy [40]

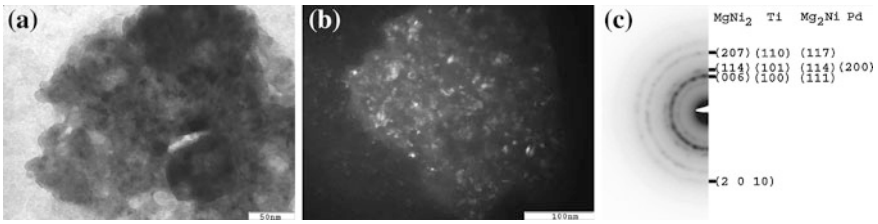

Fig. 14 *Bright field image* (**a**), *dark field image* (**b**), and selected area electron diffraction pattern (**c**) of the $Mg_{49}Ti_6Ni_{41}Pd_4$ alloy [40]

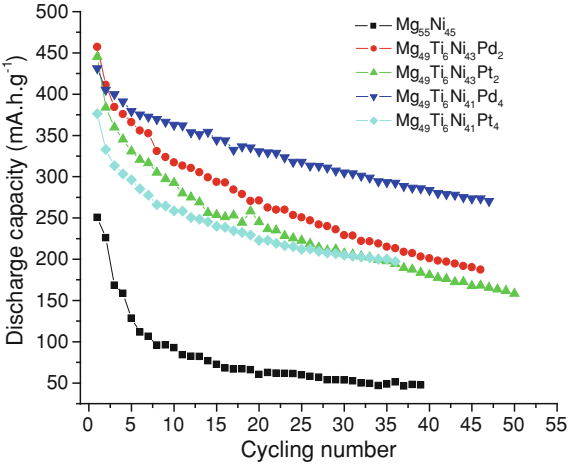

Fig. 15 Discharge capacities versus cycling number of $Mg_{55}Ni_{45}$ and $Mg_{49}Ti_6Ni_{45-x}NM_X$ [40]

3 Concluding Remarks

In the last 10 years the search for new anode materials for Ni-MH batteries was intensified. The results obtained by quaternary systems having a transition metal and a noble metal as alloying elements for Mg-Ni—based nanostructured alloys can be considered very promising but further improvements are necessary to allow the technological use of such materials. Until now, the number of quaternary alloys investigated is very small. Moreover, a more detailed understanding of the correlation between the electrochemical properties and microstructures is necessary to obtain alloys with optimized electrode performances. This goal can be accomplished only with systematic investigation of these multi-element alloys and their mechanisms of degradation. Moreover in quaternary alloys other transition metals different of Ti need to be investigated, such as Al, Cr and V, among others. One approach to drive the directions of the investigations in quaternary alloys is to select alloying elements from those which presented interesting results in ternary alloys. Furthermore, the study of quaternary alloys with rare earths as alloying elements instead of transition metals was not explored so far.

There is also a lack of investigations concerning the processing routes of hydrogen storage alloys for anode applications. The investigated alloys are mostly synthesized by mechanical alloying and the processing parameters of this route have not been sufficiently investigated. Moreover, other processing techniques almost have not been investigated. Only few manuscripts on Mg—based ternary alloys synthesized by melt-spinning (a technique of rapid solidification for obtaining amorphous/nanostrutured alloys in form of thin ribbons) have been reported. Furthermore, new processing techniques of severe plastic deformation started to be investigated for hydrogen storage alloys applied in solid state hydrogen storage but almost nothing have been done for electrode applications. An interesting feature of the techniques of severe plastic deformation is to produce

alloys with refined grain sizes (nanostructure, in general) but with lower surface areas than those synthesized by mechanical alloying. Theoretically, this feature could produce alloys with fast hydrogen diffusion coefficients (due to the large volume of nano-grain boundaries) and lower corrosion rates than mechanical alloying counterparts (due to their smaller surface areas).

The abovementioned issues are only few examples on the potentiality of nanotechnology to create new hydrogen storage materials suitable for anode applications.

References

1. Fetcenko MA, Ovshinsky SR, Reichman B, Young K, Fierro C, Zallen A, Mays W, Ouchi T (2007) Recent advances in NiMH battery technology. J Power Sources 165:544–551
2. Linden D, Reddy TB (2002) Handbook of batteries, 3rd edn. McGraw-Hill, New York
3. Santos SF, Ishikawa TT, Ticianelli EA (2009) Fundamentals and technological applications of hydrogen—absorbing Mg amorphous alloys. In: Telle JR, Pearstine NA (eds) Amorphous materials: research, technology and applications. Nova Science Publishers, pp 219–237, New York
4. Harding battery handbook for quest®, Rechargeable cells and battery packs (2004), One Energy Centre Shores, MI. www.hardingenergy.com
5. Notten PHL, Ouwerkerk M, van Hal H, Beelen D, Keur D, Zhuo J, Feil H (2004) High energy density strategies: from hydride-forming materials research to battery integration. J Power Sources 129:45–54
6. Wronski ZS (2001) Materials for rechargeable batteries and clean hydrogen energy sources. Int Mater Reviews 46:1–49
7. Smallman RE, Bishop RJ (1999) Modern physical metallurgy and engineering materials: science, processing and applications, 6th edn, Butterworth Heinemann, Boston
8. Park CN, Luo S, Flanagan TB (2004) Analysis of sloping plateaux in alloys and intermetallic hydrides I: diagnostic features. J Alloys Compd 384:203–207
9. Huot J (2010) Metal hydrides. In: Hirscher M (ed) Handbook of hydrogen storage. Willey-VCH, Weinheim
10. Schlapbach L, Zuttel A (2001) Hydrogen—storage materials for mobile applications. Nature 414:253–258
11. Reilly JJ, Adzic GD, Johnson JR, Vogt T, Mukerjee S, McBreen J (1999) The correlation between composition and electrochemical properties of metal hydride electrodes. J Alloys Compd 293–295:569–582
12. Ambrosio RC, Ticianelli EA (2002) Effect of cobalt on the physicochemical properties of a simple LaB5 metal hydride alloy. J Power Sources 110:73–79
13. Lin Q, Zhao S, Zhu DJ, Song B, Mei Z (2003) Investigation of hydriding properties and structure of MlNI5-Snx system. J Alloys Compd 351:91–94
14. Liu J, Yang Y, Li Y, Yu P, He Y, Shao H (2007) Comparative study of $LaNi_{4.7}M_{0.3}$ by powder microelectrode technique. Int J Hydrogen Energy 32:1905–1910
15. Ayari M, Paul-Boncour V, Lamloumi J, Percheron-Guégan A, Guillot M (2005) Study of the aging of $LaNi_{3.55}Mn_{0.4}Al_{0.3}(Co_{1-x}Fe_x)_{0.75}$ ($0 \leq x \leq 1$) compounds in Ni–MH batteries by SEM and magnetic measurements. J. Magnetism and Magnetic Mater. 288:374–383
16. Ben Moussa M, Abdellaoui M, Mathlouthi H, Lamloumi J, Percheron-Guégan A (2008) Electrochemical properties of the $MmNi_{3.55}Mn_{0.4}Al_{0.3}Co_{0.75-x}Fe_x$ ($x = 0.55$ and 0.75) compounds. J Alloys Compd 458:410–414

17. dos Santos AR, Ambrosio RC, Ticianelli EA (2004) Electrochemical and structural studies on nonstoichiometric AB_2-type metal hydride alloys. Int J Hydrogen Energy 29:1253–1261
18. Suryanarayana C (2001) Mechanical alloying and milling. Prog. Mat. Sci. 46:1–184
19. Murty BS, Ranganathan S (1998) Novel materials synthesis by mechanical alloying/milling. Int Mater Reviews 43:101–141
20. El-Eskandarany MS (2001) Mechanical alloying for fabrication of advanced engineering materials. Noyes Publications, Norwich
21. Liu W, Wu H, Lei Y, Wang Q, Wu J (1997) Amorphization and electrochemical hydrogen storage properties of mechanically alloyed Mg–Ni. J Alloys Comp 252:234–237
22. Zhang SG, Yorimitsu K, Nohara S, Morikawa T, Inoue I, Iwakura C (1998) Surface analysis of an amorphous MgNi alloy prepared by mechanical alloying for use in nickel–metal hydride batteries. J Alloys Compd 270:123–126
23. Zhang SG, Hara Y, Morikawa T, Inoue I, Iwakura C (1999) Electrochemical and structural characteristics of amorphous $MgNi_x$ ($x \geq 1$) alloys prepared by mechanical alloying. J Alloys Compd 293:552–555
24. Feng F, Northwood DO (2004) Effect of surface modification on the performance of negative electrodes in Ni/MH batteries. Int J Hydrogen Energy 29:955–960
25. Ambrosio RC, Ticianelli EA (2005) Studies on the influence of palladium coatings on the electrochemical and structural properties of a metal hydride alloy. Surf Coating Tech 197:215–222
26. Deng C, Shi P, Zhang S (2006) Effect of surface modification on the electrochemical performances of $LaNi_5$ hydrogen storage alloy in Ni/MH batteries. Mater Chem Phys 98: 514–518
27. Ambrosio RC, Ticianelli EA (2005) Electrochemical and X-ray absorption spectroscopy studies of copper coatings on a hydrogen storage alloy. J. Electroanalytical Chem. 574: 251–260
28. Rongeat C, Grosjean MH, Ruggeri S, Dehmas M, Bourlot S, Marcotte S, Roué L (2006) Evaluation of different approaches for improving the cycle life of MgNi-based electrodes for Ni-MH batteries. J Power Sources 158:747–753
29. Santos SF, de Castro JFR, Ishikawa TT, Ticianelli EA (2008) Effect of Mechanical coating with Ni and Ni-5 % Al on the structure and electrochemical properties of the Mg-50 % Ni alloy. J Mater Sci 43:2889–2894
30. Liu W, Wu H, Lei Y, Wang Q, Wu J (1997) Effects of substitution of other elements for nickel in mechanically alloyed $Mg_{50}Ni_{50}$ amorphous alloys used for nickel—metal hydride batteries. J Alloys Compd 261:289–294
31. Santos SF, de Castro JFR, Ishikawa TT, Ticianelli EA (2007) Effect of transition metal additions on the electrochemical properties of a MgNi-based alloy. J Alloys Compd 434: 756–759
32. Iwakura C, Shyn-ya R, Miyanohara K, Nohara S, Inoue H (2001) Effects of Ti–V substitution on electrochemical and structural characteristics of MgNi alloy prepared by mechanical alloying. Electrochem Acta 46:2781–2786
33. Han SC, Lee PS, Lee JY, Zuttel A, Schlapbach L (2000) Effects of Ti on the cycle life of amorphous MgNi-based alloy prepared by ball milling. J Alloys Compd 306:219–226
34. Huang L-J, Tang J-G, Wang Y, Liu J-X, Wu DC (2009) Effects of microstructure on the electrode properties of melt–spun Mg-based amorphous alloys. J Alloys Compd 485:186–191
35. Ren HP, Zhang YH, Li BW, Zhao DL, Guo SH, Wang XL (2009) Influence of the substitution of La for Mg on the microstructure and hydrogen storage characteristics of $Mg_{20-x}La_xNi_{10}$ ($x = 0 - 6$) alloys. Int J Hydrogen Energy 34:1429–1436
36. Yamaura SI, Kim HY, Kimura H, Inoue A, Arata Y (2002) Electrode properties of rapidly solidified $Mg_{67}Ni_{23}Pd_{10}$ amorphous alloy. J Alloys Compd 347:239–243
37. Ma T, Hatano Y, Abe T, Watanabe K (2004) Effects of Pd addition on electrochemical properties of MgNi. J Alloys Compd 372:251–258
38. de Castro JFR, Santos SF, Ishikawa TT, Ticianelli EA (2007) Structural and electrochemical characterization of Mg-Ni-Pd alloy electrodes. Proceedings of the Brazilian MRS Meeting, Natal

39. Souza EC, de Castro JFR, Ticianelli EA (2006) A new electrode material for nickel-metal hydride batteries: MgNiPt alloy prepared by ball-milling. J Power Sources 160:1425–1430
40. Nikkuni FR, Santos SF, Ticianelli EA (2010) Effects of Pd and Pt additions on the structure and electrochemical performance of Mg-Ti-Ni alloy electrodes. Proceedings of the Brazilian MRS Meeting, Ouro Preto
41. de Castro JFR, Santos SF, Nikkuni FR, Ishikawa TT, Ticianelli EA (2010) Structural and electrochemical characteristics of $Mg_{(55-x)}Ti_xNi_{(45-y)}Pt_y$ metal hydride electrodes. J Alloys Compd 498:57–61
42. Nakagawa M, Matsuya S, Udoh K (2001) Corrosion behavior of pure titanium and titanium alloys in fluoride-containing solutions. Dental Mater J 20:305–314
43. Nakagawa M, Matsuya S, Udoh K (2002) Effects of fluoride and dissolved oxygen concentrations on the corrosion behavior of pure titanium and titanium alloys. Dental Mater J 21:83–92